Morphological instabilities of vicinal surfaces during epitaxial growth

Lucas Benoit-Maréchal

INSTITUT POLYTECHNIQUE DE PARIS

NNT : 2021IPPAX132

Thèse de doctorat

Morphological instabilities of vicinal surfaces during epitaxial growth

Thèse de doctorat de l'Institut Polytechnique de Paris
préparée à École polytechnique

École doctorale n°626 École doctorale de l'Institut Polytechnique de Paris (EDIPP)
Spécialité de doctorat : Mécanique des fluides et des solides, acoustique.

Thèse présentée et soutenue à Palaiseau, le 17/12/2021, par

LUCAS BENOIT--MARÉCHAL

Composition du Jury :

Mathis Plapp Directeur de recherche CNRS, École polytechnique (Laboratoire de Physique de la Matière Condensée)	Président
Vesselin Tonchev Associate Professor, Sofia University, Faculty of Physics (Meteorology and Geophysics)	Rapporteur
Axel Voigt Director and Professor, Technische Universität Dresden (Institute of Scientific Computing)	Rapporteur
Eliot Fried Professor, Okinawa Institute of Science and Technology (Mathematics, Mechanics, and Materials Unit)	Examinateur
Michel Jabbour Professeur, École polytechnique (Laboratoire de Mécanique des Solides)	Directeur de thèse
Pere Roca I Cabarrocas Directeur de recherche CNRS et Professeur, École polytechnique (Laboratoire de Physique des Interfaces et des Couches Minces)	Co-directeur de thèse
Nicolas Triantafyllidis Professeur, École polytechnique (Laboratoire de Mécanique des Solides)	Invité (Co-encadrant)

MORPHOLOGICAL INSTABILITIES OF VICINAL SURFACES DURING EPITAXIAL GROWTH

Lucas BENOIT–MARÉCHAL: *Morphological isntabilities of vicinal surfaces during epitaxial growth*, December 2021.

CONTENTS

ABSTRACT

The study of step dynamics on vicinal surfaces is a long-standing problem in crystal growth, dating back to the seminal work of Burton, Cabrera, and Frank (BCF) in 1951. On these surfaces, the crystal grows by step flow, i.e., by propagation of the atomic steps, which may develop instabilities breaking the regularly spaced, straight-step initial configuration. Step bunching corresponds to situations where steps coalesce together resulting in an alternating pattern of bunches and wide atomic terraces, and step meandering to situations where the initially straight steps exhibit a distinct waviness.

Using nonequilibrium thermodynamics and the formalism of configurational forces, we derive a generalized Gibbs–Thomson relation for the step chemical potential which natively accounts for the contribution of the elastic bulk and incorporates the necessary coupling between the diffusion fields on adjacent terraces (the *chemical effect*). This leads to a free-boundary problem that generalizes the BCF model for the governing equations of step flow where full account is taken of the dynamics terms. In doing so, we circumvent the quasistatic approximation that prevails in the existing literature.

Through comprehensive numerical simulations, scaling laws governing the coarsening behaviour of step bunches are identified. Taking the discrete-to-continuum limit of the step-flow equations leads to a nonlinear partial differential equation that describes the macroscopic evolution of the surface profile, from which we recover the numerically obtained scaling laws. Importantly, we demonstrate that the chemical and dynamical effects can account for the onset of step bunching and for the scaling laws experimentally observed in the coarsening regime.

In the context of a general stability analysis, we discuss the influence on step bunching and step meandering of all the mechanisms independently, as well as their interplay, and we demonstrate the significant impact of the chemical and dynamical effects on stability, even in the slow deposition/evaporation regime where the dynamics were deemed negligible. Consequently, we set forth the possible coexistence of bunching and meandering, in contrast with the BCF model which predicts that the two instabilities are mutually exclusive.

In light of these findings, we show that the chemical and dynamical effects offer interesting alternative explanations to account for the step instabilities observed in some experiments, notably in the setting of electromigration under extreme deposition flux for which we correctly predict the unexplained step pairing instability. A full accounting of the stability reversals observed on Si(111) under electromigration remains an open problem as the chemical and dynamical effects do not modify the stability dependence on the direction of the current.

RÉSUMÉ

L'étude de la dynamique des marches sur les surfaces vicinales est un problème de longue date dans le domaine de la croissance cristalline, qui remonte aux travaux précurseurs de Burton, Cabrera et Frank (BCF) en 1951. Sur ces surfaces, le cristal croît par écoulement de marches, qui peuvent développer des instabilités rompant la configuration initiale de marches droites et équidistantes. La mise en paquet correspond à des situations où les marches coalescent, tel que se développe à la surface un motif de larges terrasses séparées par des paquets de marches, et le méandrage à des situations où les marches initialement rectilignes développe une ondulation distinctive.

En utilisant le formalisme de la thermodynamique hors-équilibre et des forces configurationnelles, nous établissons une relation de Gibbs–Thomson généralisée pour le potentiel chimique des marches qui incorpore le couplage nécessaire entre les champs de diffusion de terrasses adjacentes (l'effet chimique) et inclut la contribution du substrat élastique. Celle-ci généralise l'approche usuelle de la littérature qui se limite souvent à des marches rectilignes et postule d'emblée une énergie d'interaction dipolaire entre les marches. Nous aboutissons finalement à un problème à frontière libre qui généralise le modèle BCF, et où les termes dynamiques sont pleinement pris en compte. Ce faisant, nous contournons l'approximation quasi-statique qui prévaut dans la littérature existante.

Les lois d'échelle régissant le mûrissement de la mise en paquet sont identifiées par simulation numérique et sont extrêmement robustes. La limite continue des équations de l'écoulement de marches conduit à une équation aux dérivées partielles non-linéaire qui décrit l'évolution macroscopique du profil de la surface, et dont les coefficients diffèrent de ceux reportés dans la littérature puisqu'ils incluent les effets chimique et dynamique. Via une analyse asymptotique multi-échelles, nous pouvons extraire analytiquement de cette équation aux dérivées partielles des lois d'échelle qui corroborent celles obtenues numériquement. De ce fait, nous soulignons que l'identification des préfacteurs des lois d'échelle offre une piste intéressante pour la détermination des paramètres microscopique de la surface vicinale (tels que le taux de couverture à l'équilibre ou le coefficient d'attachement/détachement) à partir de grandeurs macroscopiques (comme la taille des paquets). Enfin, et c'est un des résultats clés de notre travail, nous démontrons que les effets chimique et dynamique à eux seuls suffisent à expliquer la mise en paquet ainsi que les lois d'échelle observées expérimentalement pour leur mûrissement. En d'autres termes, en prenant en compte tous les mécanismes requis, sans en négliger a priori, nous sommes capables d'expliquer les résultats expérimentaux dans un cadre unifié, sans avoir besoin d'introduire d'effets supplémentaires tel que l'effet Ehrlich–Schwoebel (ES) inverse.

Avec pour dessein une analyse générale de la stabilité, nous discutons de l'influence de chaque mécanisme, agissant indépendamment ou de concert, sur

les instabilités de mise en paquet et de méandrage, et nous démontrons l'impact significatif des effets chimique et dynamique sur la stabilité, et ce, même dans le régime de déposition/évaporation lente où les termes dynamiques étaient considérés comme négligeables. Nous mettons aussi en évidence la possible coexistence des instabilités de mise en paquet et de méandrage, contrairement au modèle BCF qui prévoit que les deux instabilités sont mutuellement exclusives. Par ailleurs, étant donné que les effets chimique et dynamique partagent certaines caractéristiques communes avec l'effet Ehlrich–Schwoebel inverse, nous proposons qu'ils puissent en quelque sorte être interprétés comme un effet ES inverse effectif, réconciliant ainsi les théories qui requièrent un effet ES inverse pour déclencher l'instabilité et l'invraisemblance de l'existence d'une telle barrière énergétique dans les faits.

À la lumière de ces résultats, nous montrons que les effets chimique et dynamique offrent des alternatives intéressantes pour expliquer les instabilités observées dans certaines expériences. Dans le cadre de l'électromigration avec un courant remontant (step-up) sous un flux de déposition extrême, nous prédisons correctement l'instabilité d'appariement des marches auparavant inexpliquée. En présence d'un courant descendant (step-down), nous montrons qu'une transition d'une instabilité de mise en paquet à une instabilité de méandrage est possible en jouant sur la largeur des terrasses, en accord avec l'expérience. Enfin, en réexaminant la relation mesurée expérimentalement entre le champ électrique critique (c'est-à-dire le champ requis pour déclencher la mise en paquet) et la largeur des terrasses, nous établissons une valeur robuste pour le coefficient d'attachement/détachement, très peu sensible aux valeurs des autres paramètres, qui place la surface dans un régime intermédiaire entre le régime cinétiquement limité et le régime limitée par la diffusion de surface, avec une tendance vers ce dernier, en accord avec la littérature. Toutefois, une explication complète des inversions de stabilité observées sur Si(111) sous électromigration reste un problème ouvert car les effets chimique et dynamique n'affectent pas la dépendance de la stabilité à la direction du courant d'électromigration.

FOREWORD

The thesis work presented here was undertaken at École polytechnique between the *Laboratoire de Mécanique des Solides (LMS)* and the *Laboratoire de Physique des Interfaces et des Couches Minces (LPICM)* under the supervision of Professor Michel Jabbour and Professor Nicolas Triantafyllidis from the mechanics laboratory, and Professor Pere Roca i Cabarrocas from the physics laboratory.

It was financed by the *Ministère de l'Enseignement Supérieur et de la Recherche et de l'Innovation* through the AMX program of *École Polytechnique*.

Some of the results presented here have already been published as:

Guin, L., M. E. Jabbour, L. Shaabani-Ardali, L. Benoit-Maréchal, and N. Triantafyllidis (2020). "Stability of Vicinal Surfaces: Beyond the Quasistatic Approximation." In: *Physical Review Letters* 124.3, p. 036101. DOI: 10.1103/PhysRevLett.124.036101,

Benoit–Maréchal, L., M. E. Jabbour, and N. Triantafyllidis (2021). "Scaling Laws for Step Bunching on Vicinal Surfaces: Role of the Dynamical and Chemical Effects." In: *Physical Review E* 104.3, p. 034802. DOI: 10.1103/PhysRevE.104.034802.

1 INTRODUCTION

The term *epitaxy*, coined by Royer (1928) from the Greek roots *epi* (above) and *taxis* (order), refers to a type of crystal growth which consists in growing a crystalline layer upon a crystalline substrate that imposes its order. If the layer and substrate are different materials, one speaks of *heteroepitaxy*, whereas the term *homoepitaxy* is used when the two materials are identical, which is the situation of interest here.

Typically, and as will be the case in the present approach, the film is grown from a vapor, but liquid-phase epitaxy or solid-phase epitaxy are also possible. Three primary growth modes may be identified — Volmer-Weber (island formation), Frank-van-der-Merwe (layer-by-layer), and Stransk-Krastanov (hybrid) — based on thermodynamic considerations (Bauer, 1958), and therefore apply to growth near thermodynamic equilibrium. For further details, the reader is referred to Michely and Krug (2012).

In this work, we are concerned with out-of-equilibrium growth conditions, such that the surface evolution is not only governed by the energetics of the crystal but also by the kinetics of deposition/evaporation, which play a decisive role. Consequently, we focus our attention on homoepitaxial layer-by-layer growth. Indeed, as this mode corresponds to the thermodynamic prediction, any deviation from perfect layer-by-layer growth must have a kinetic origin, thus furnishing an ideal framework for studying the kinetics of growth in thin film.

To promote this mode over the others, the epitaxial growth is performed not on high-symmetry crystallographic planes but on surfaces deliberately misoriented from one: the *vicinal surfaces*, as shown in Figure 1.1. Such surfaces present as a staircase of atomically smooth terraces separated by atom-high steps. If the width of the terraces, i. e., the distance between steps, is smaller than the nucleation length, adatoms diffusing on the terraces will reach a

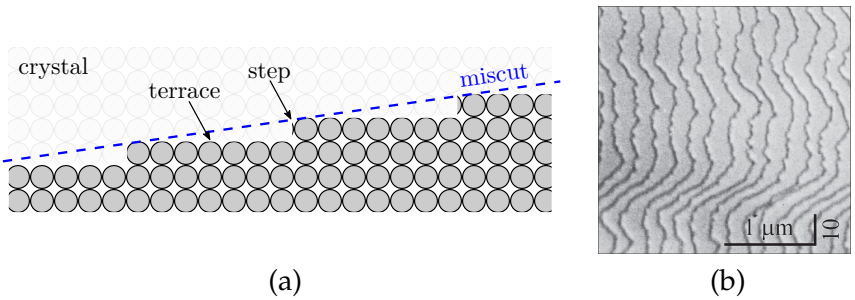

Figure 1.1: (a) Schematic of a crystal cut forming a vicinal surface. (b) Reflection electron microscopy image of an array of monoatomic steps on Si(111) (reprinted from Latyshev et al. (2017) with permission from Elsevier).

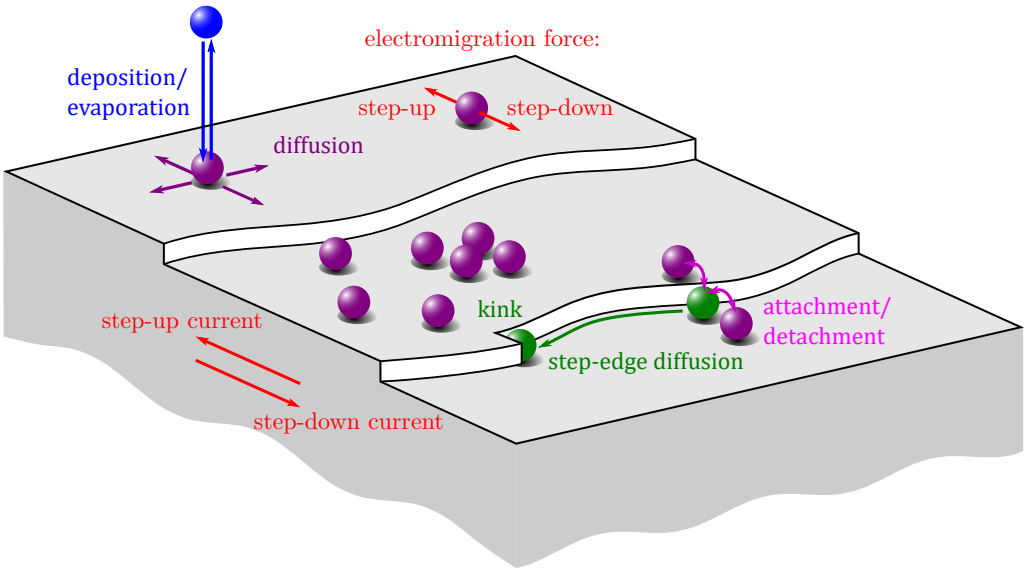

Figure 1.2: Microscopic processes underlying atomic step dynamics. Adatoms are shown in purple, step atoms in green and the vapor atom in blue.

step and attach to it (because it provides an energetically-favorable *kink* site) before they nucleate. As a result, the steps propagate forward, achieving a layer-by-layer growth called the *step-flow regime*.

ATOMIC PROCESSES OF STEP FLOW To lay the foundation for the derivation of the governing equations of step flow, we review the different microscopic processes underlying the step dynamics depicted in Figure 1.1:

1. *Deposition/evaporation:* When an atom from the vapor reaches the surface, it has a chance to get adsorbed and become an *adatom* ("adsorbed atom"). Reciprocally, an adatom may re-evaporate to the gas phase. Depending on the balance between the deposition and evaporation rates, the net evolution of the crystal will correspond to either growth or sublimation. At sufficiently low temperature, the evaporation probability is so low that a pure deposition regime can be assumed. Conversely, experiments of crystal annealing in vacuum correspond to pure evaporation.

2. *Diffusion on terraces:* The adatoms move by diffusion on the terraces.

3. *Attachment/detachment to steps:* When an adatom reaches a step, it has some probability to attach to it, thus advancing the step front.

4. *Step-edge diffusion:* More precisely, adatoms attach to (and detach from) steps at kink sites (see Figure 1.2) after diffusing along the step edges.

5. *Electromigration:* In the presence of an electric field, adatoms experience a drift, which is referred to as electromigration, that biases the diffusion process in one direction. This corresponds to experimental situations where the substrate is heated by circulating a direct electric current of typically a few amperes through it. To explain this drift, adatoms

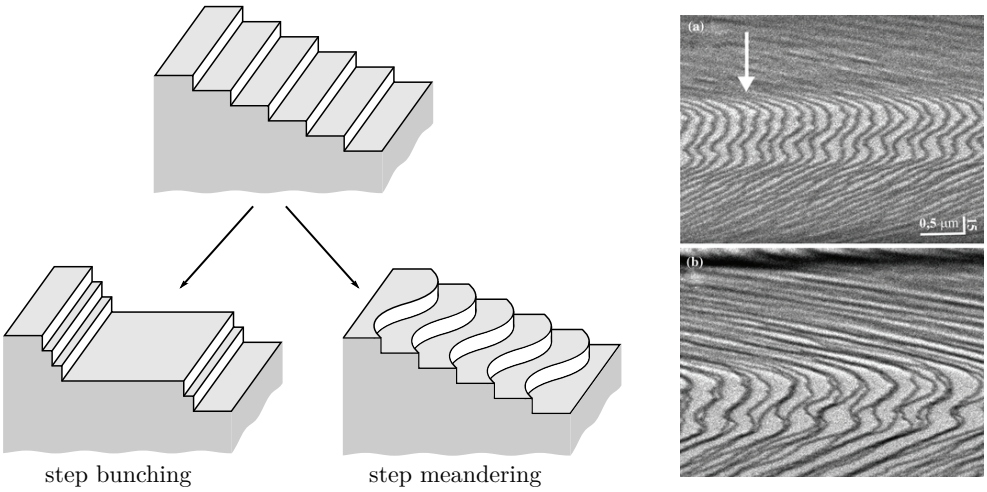

Figure 1.3: (left) Schematic for the two principal step instabilities. (right) Reflection electron microscope image of Si(111) at 900°C: (top) regular atomic steps and (bottom) initial stage of step bunches (reprinted from Kosolobov and Latyshev (2011) with permission from Springer). Note that the aspect ratio of 30:1 between vertical and horizontal directions makes the steps appear wavy while they are essentially straight.

are endowed with an effective charge q_e, which makes them subject to an electrostatic force (Stoyanov, 1991). Experimental estimates place this effective charge in the range of one hundredth to one tenth of the elementary charge (Fu et al., 1997; Liu et al., 1998; Thürmer et al., 1999; Homma and Aizawa, 2000; Pierre-Louis and Métois, 2004).

In addition, a *permeability* mechanism is sometimes invoked, notably to explain the reversals of stability observed in electromigration experiment on Si(111) (Métois and Stoyanov, 1999; Pierre-Louis, 2003), whereby adatoms may directly cross a step without attaching to it when the kink density is too low (Liu et al., 1996; Stoyanov, 1998). However, while this hypothesis allows to predict the existence of an instability, many inconsistencies remain unsolved (e. g., the effective charge prediction or the permeability reversals explanation). Moreover, it has been shown that fast step kinetics and high permeability are essentially indistinguishable (Pierre-Louis, 2003) and could in fact be two ways of modeling the same physical process (Guin, 2018). Therefore, we do not consider permeable steps in the present investigation.

OBSERVATIONS OF STEP INSTABILITIES In the standard case of step flow growth, all the steps propagate at the same velocity and therefore maintain their original equidistant configuration (e. g., MBE growth of Si(111) $-$ 7 $\times$ 7 at 650°C, see Omi et al. (2005)). However, under certain conditions, this uniform propagation breaks down, and some steps, or portions of steps, may accelerate while others slow down, leading to the two main types of instabilities observed on vicinal surfaces (Figure 1.3):

1. *Step bunching*, when straight atomic steps propagate at different velocities, eventually coalescing together in an alternating pattern of high step-density regions (the *bunches*) and wide flat terraces.

2. *Step meandering*, when portions of the same step propagate at different velocities, leading the initially straight steps to become wavy.

MODELS OF STEP FLOW The study of instabilities and subsequent nonlinear evolution of vicinal surfaces is crucial to our understanding of the microscopic mechanisms governing crystal growth in the step-flow regime. Not only of fundamental interest, it also paves the way for such applications as the nanopatterning of semiconductor surfaces (Ronda and Berbezier, 2004; Wise et al., 2005).

There exist three main approaches to model step flow, corresponding to three different scales of study.

1. *Kinetic Monte Carlo (KMC) simulations*, whereby all kinetic processes (diffusion on terraces and along steps, deposition/evaporation from/to the vapor, attachment/detachment at the step) are modeled with corresponding energies and hopping rates. Being the closest representation of the actual physical motion of adatoms, this method allows to easily model nontrivial mechanisms such as diffusion anisotropy or surface reconstruction, in very good agreement with experimental observations (Šmilauer and Vvedensky, 1995; Mysliveček et al., 2002). On the downside, Monte Carlo simulations are computationally expensive.

2. *Continuum step model*, whereby adatoms are described on terraces through an adatom density ρ (number of adatoms per unit area), and steps are seen as moving smooth interfaces across which the adatom density is discontinuous, leading to the formulation of a free boundary problem. Relative to the KMC simulations, this approach provides a more synthetic view of the surface evolution (the individual motions of adatoms are now described in terms of fluxes), and thus requires less computational power, while giving comparable results (Misbah et al., 2010).

3. *Continuum evolution equation*, whereby the surface is described by a continuous height function, abandoning the resolution of the step discreteness. This approach results in one compact, although highly nonlinear, partial differential equation to which the tools of calculus may be applied to derive many fundamental properties of step flow growth.

In the present work, we focus on the derivation of a thermodynamically consistent *continuum step model* in Chapter 2, which we also coarse-grain into a *continuum evolution equation* for the analysis of the coarsening behavior of step bunching in Chapter 3.

STEP GOVERNING EQUATIONS The free boundary problem of the continuum step model accounts for the step dynamics via a reaction-diffusion equation for adatoms on each terrace, supplemented by two boundary conditions at the

step, and an interface motion equation that describes the movement of steps. Denoting F the deposition flux and ν the evaporation rate, the form of the reaction-diffusion equation is generally accepted as:

$$\partial_t \rho = \nabla^2 \rho + F - \nu \rho, \tag{1.1}$$

although we show that it implicitly assumes near-equilibrium crystal growth, which corresponds to the linearization of its far-from-equilibrium counterpart derived in Chapter 2. On the other hand, the boundary conditions are subject to more discussions as they depend on which mechanisms are incorporated in the model, and often rely on physically sensible phenomenological arguments.

Historically, in the first formulation by Burton et al. (1951), the boundary conditions simply expressed the equilibrium of the terrace adatoms with the reservoir of atoms constituted by the steps, i. e.,

$$\rho = \rho_{eq}^*, \tag{1.2}$$

along the steps, where ρ_{eq}^* is the equilibrium adatom density. As this is essentially equivalent to infinitely fast kinetics at the steps, these boundary conditions where modified by Chernov (1961) and Schwoebel (1969) to account for the finite kinetics of attachment/detachment, as well as their possible asymmetry. Indeed, depending on whether adatoms reach the step from the upper or lower terrace, they do not have the same chance of incorporation. This is usually due to the presence of an extra energy barrier that upper terrace adatoms need to overcome to attach to the step: the *Ehrlich–Scwhoebel barrier*. Including curvature effects, much like in the classical formulation of the Gibbs–Thomson relation, the corresponding boundary conditions read:

$$\pm \mathcal{D} (\nabla \rho)^{\pm} \cdot \mathbf{n} = \kappa_{\pm} (\rho^{\pm} - \rho_{eq}^* + \tilde{\gamma} K), \tag{1.3}$$

where $\mathcal{D}$ is the coefficient of diffusion on terraces, $\mathbf{n}$ the step normal, $\tilde{\gamma}$ the step stiffness, K the step curvature, κ_- (κ_+) the kinetic coefficients for the attachment/detachment of adatoms from the upper (lower) terraces, and ρ^- (ρ^+) the limit value of adatom density at the upper (lower) side of the step. Further classical refinements include elastic interactions between steps and electromigration (see Chapter 2).

By contrast with these previous approaches, we strive to derive constitutive relations in consistency with the principles of thermodynamics, following the approach developed by Jabbour (2005) and Cermelli and Jabbour (2005). Based on nonequilibrium thermodynamics, this method, which we review and extend to include elasticity in Chapter 2, leads to modified boundary conditions with a term that couples the adatom diffusion fields on adjacent terraces in the form of a jump in the adatom density across the step, which we refer to as the *chemical effect*. Moreover, an advection term $\pm \rho^+ v_\perp$ (with $v_\perp$ the normal velocity of the step) is also required on the left hand side of (1.3), that takes into account the motion of the step through the adatom density field. With the transient term $\partial_t \rho$ in the reaction-diffusion equation, we refer to these terms collectively as the *dynamical effect*. While their contribution is predominantly neglected in the

literature,[1] these two effects have a significant impact on the stability of the vicinal surface and cannot be neglected *a priori*, as shown in a one-dimensional setting by Guin et al. (2020, 2021b).

STABILITY ANALYSES OF THE STEP FLOW MODEL The study of step instabilities relies on analyzing the stability of the step governing equations against perturbations of the principal solution. There are two aspects:

1. The *linear stability analysis*, which predicts the onset of instabilities.
2. The long-term, post-instability, evolution of the surface morphology.

In this work, we extend the results of Guin et al. (2021a,b) to the two-dimensional setting for the linear stability analysis, and to the post-instability regime in the one-dimensional setting.

In the literature, the stability analysis is generally conducted under the so-called quasistatic approximation, whereby the dynamical effect is deemed negligible for low enough deposition/evaporation rates. This approach, which we develop in Section 4.3, has the advantage of permitting an analytical treatment of the linear stability analysis, which yields closed-form expressions for the growth rate of the perturbation and allows to study in detail the effect of each mechanism and their interplay.

However, as was shown in Guin (2018) and Guin et al. (2020, 2021a), the quasistatic approximation is not well justified, even in the regime of low deposition/evaporation rates. Because of the transient term in the reaction-diffusion equation, it is no longer possible to obtain a closed-form solution for the adatom density in the general case, and a more involved numerical treatment is required for the linear stability analysis, based on an *Arbitrary Lagrangian-Eulerian* formulation inspired by fluid-structure interaction problems in hydrodynamics (Guin et al., 2020). The dynamical effect proves to be a stabilizing/destabilizing mechanism of its own. For straight steps, under deposition, it has a destabilizing effect in the kinetically limited regime, and a stabilizing effect in the diffusion-limited regime (the effects are reversed under evaporation). In Section 4.4, we extend these preliminary results to the general two-dimensional setting, where steps are not restricted to a rectilinear shape.

Likewise, in the context of long-term evolution, the dynamical effect is seldom taken into account, as it imposes the resolution of a coupled system of equations, and the chemical effect is not considered, being a relatively recent addition to the framework of the continuum step model. In Chapter 3, we present extensive numerical simulations from which we extract scaling laws for characteristic length scales of the step bunches. Comparison with experimental results on $\mathrm{Si}(111) - 7 \times 7$ (Omi et al., 2005) shows that the dynamical and chemical effects can provide a novel explanation for the observed coarsening behavior of bunches. To further our understanding of step bunching, we also

1 A few works have studied the influence of the dynamical effect, often in a simplified setting as in Ghez et al. (1993), Keller et al. (1993), Ranguelov and Stoyanov (2007), and Dufay et al. (2007), more rarely accounting for all dynamics terms as in Gillet et al. (2000) and Bänsch et al. (2004). Cermelli and Jabbour (2007) and Chen (2019) studied the influence of the chemical effect.

provide the nonlinear partial differential equation governing the evolution of the surface height derived from a consistent coarse-graining of the one-dimensional continuum step model.

OUTLINE This thesis is organized as follows. We present in Chapter 2 the governing equations of step-flow growth with our starting point a thermodynamically consistent generalization of the BCF model that relies on a clear separation between general balance laws, derived in Section 2.1, and constitutive relations, made explicit in Section 2.2. Special attention is given to the contribution of bulk elasticity in Section 2.3. Section 2.4 summarizes the results of the previous sections, recording the working set of equations for step-flow epitaxy used in the rest of the thesis.

Chapter 3 is dedicated to the investigation of step bunching beyond the linear-stability regime. The numerical resolution process is detailed in Section 3.2, along with the resulting scaling laws for the coarsening process. The continuum limit, whereby a continuous function is used to describe the surface height, is derived in Section 3.3 via Taylor expansions with respect to the terrace size. In Section 3.4, the exponents that enter the scaling laws are extracted analytically and compared to the ones obtained numerically.

The step meandering analysis is developed in Chapter 4. After establishing the framework for a general linear stability analysis in Section 4.2, we discuss the effect of each mechanism and their interplay, under the quasistatic approximation in Section 4.3, and in the general case, including dynamics terms, in Section 4.4. A comparison to some experimental results follows in Section 4.5.

The last Chapter 5 is devoted to the problem of electromigration. Using a different method for the stability analysis (the so-called *transpiration method*), we derive in Section 5.2 an approximate analytical expression for the growth rate of instabilities, which we use in the subsequent Section 5.4 to reinterpret several experimental results.

2 STEP FLOW EQUATIONS

In this chapter, the governing equations of step flow are derived from the thermodynamics of nonequilibrium processes. This derivation follows the work of Jabbour (2005) and Cermelli and Jabbour (2005), built on the approach presented in Fried and Gurtin (2004) that is based on

1. A global atomic balance as well as adatom balances on the upper and lower terrace that account for surface diffusion and attachment/detachment fluxes at the step.
2. Newtonian balance laws for forces and moments that account for Newtonian stresses in bulk, at the surface, and at the step.
3. An independent balance law for configurational forces that accounts for configurational stresses in bulk, at the surface, and at the step.
4. A mechanical (i. e., isothermal) version of the first two laws of thermodynamics in the form of a free-energy imbalance that accounts for temporal changes in free energy, energy flows due to adatom transport, and power expended by both Newtonian and configurational forces.
5. Thermodynamically consistent constitutive relations.

In most published works (Natori, 1994; Houchmandzadeh and Misbah, 1995; Tersoff et al., 1995; Paulin et al., 2001; Pierre-Louis, 2003; Xiang, 2002; Luo et al., 2016) the study of elastic step-step interactions is limited to straight steps,[1] and the contribution of elasticity is included via a correction to the equilibrium adatom concentration at a step, assuming dipolar interaction between steps based on the seminal work of Marchenko and Parshin (1980). In that regard, two studies stand out, that generalize step-step interactions beyond the usual dipolar representation. Recently, Guin (2018) considered the contribution of elasticity to the step driving force via the J-integral of the energy-momentum tensor, representing the elastic driving force on the mobile elastic singularity that is the step (Eshelby and Mott, 1951). In their treatment of the heteroepitaxial growth of a strained, substitutional, binary alloy, Haußer et al. (2007) describe the growing film as a discrete-continuum atomistically layered structured that captures the contribution of the elastic bulk to the step driving force in the form of the Helmholtz free-energy density of each layer.

Compared to the present theory, we underline that the approach in Guin (2018) does not account, from the outset, for the contribution of the stress field to the energetics of the system, but instead adds it *a posteriori* to the driving force. Besides, it is restricted to the one-dimensional setting of straight steps. On

1 Notable exceptions are Houchmandzadeh and Misbah (1995) and Paulin et al. (2001).

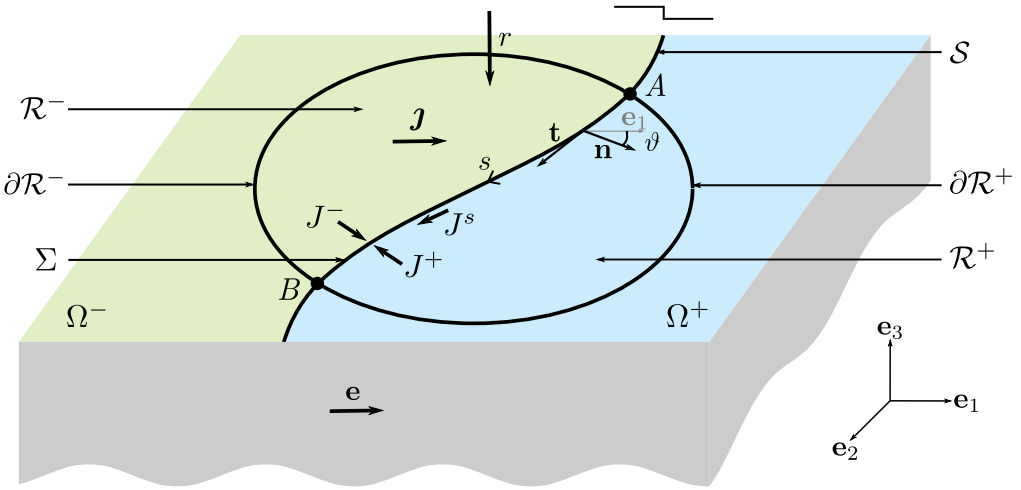

Figure 2.1: Schematic 3D view of atomic terraces separated by an atomic step $\mathcal{S}$ showing the different control surfaces and fluxes.

the other hand, elasticity is an integral part of the derivation we present here in the full two-dimensional setting, in the form of the Newtonian force balance, where surface stress and line traction at the step are also considered. As such, it differs from the approach in Haußer et al. (2007), where only bulk stress is considered. Additionally, while their description of the film as a nanolayered structure is an interesting alternative to our own approach, it introduces a separate mechanical-equilibrium condition for each layer of the film, limiting its practical applications. By contrast, we account for the effect of elasticity via a J-integral, where the derivation of the elastic fields can be reduced to textbook elasticity problems.

2.1 GENERAL PRINCIPLES

In a continuum theory, the step height a is negligible relative to the height of thin film. The step is therefore modeled as a time dependent line defect $\mathcal{S}(t)$ separating the crystal surface Ω into the upper atomic terrace $\Omega^-(t)$ and the lower one $\Omega^+(t)$. The curve $\mathcal{S}(t)$ is parametrized with $\mathbf{x} = \mathbf{x}^s(s,t)$ where s is the arclength parameter oriented such that the lower terrace Ω^+ is locally on the left of $\mathcal{S}$ (see Figure 2.1). Denote by $\mathbf{t}$ the unit tangent to $\mathcal{S}$ and $\mathbf{n}$ the unit normal obtained by a counter-clockwise rotation of $\mathbf{t}$ by $\pi/2$. $\mathbf{n}$ makes an angle ϑ with $\mathbf{e}_1$. The signed curvature K of $\mathcal{S}$ is defined by the following Frénet relation: $\partial_s \mathbf{t} = K\mathbf{n}$, which entails $K = \partial_s \theta$. Let the velocity of the step $\mathbf{v} := \partial_t \mathbf{x}^s$ and denote by $v_\perp := \mathbf{v}\cdot\mathbf{n}$ and $v_\parallel := \mathbf{v}\cdot\mathbf{t}$ its normal and tangential components.

Consider a control surface $\mathcal{R}$ intersected by the step curve $\mathcal{S}$ and let $\Sigma(t) := \mathcal{S}(t) \cap \mathcal{R}$, $\mathcal{R}^-(t) := \mathcal{R} \cap \Omega^-(t)$ and $\mathcal{R}^+(t) := \mathcal{R} \cap \Omega^+(t)$. The boundaries of $\mathcal{R}^-$ and $\mathcal{R}^+$ are decomposed as $\partial\mathcal{R}^- \cup \Sigma$ and $\partial\mathcal{R}^+ \cup \Sigma$, respectively. The end points of Σ (intersection with $\partial\mathcal{R}$) are denoted A and B, chosen such that the arc parameters $s^A(t)$ and $s^B(t)$ of A and B defined by $\mathbf{x}^A(t) = \mathbf{x}^s(s^A(t),t)$ and $\mathbf{x}^B(t) = \mathbf{x}^s(s^B(t),t)$ satisfy $s^A \leqslant s^B$.

2.1.1 *Transport theorems*

SURFACE INTEGRAL Let $\varphi(\mathbf{x},t)$ be a scalar field defined on Ω which experiences a discontinuity at crossing $\mathcal{S}$. For $\mathbf{x}\in\mathcal{S}$, we denote by $\varphi^-(\mathbf{x},t)$ and $\varphi^+(\mathbf{x},t)$ the limit values of φ approaching $\mathcal{S}$ from Ω^- and Ω^+, respectively. The jump of φ as crossing $\mathcal{S}$ is written $[\![\varphi(\mathbf{x},t)]\!] := \varphi^+(\mathbf{x},t) - \varphi^-(\mathbf{x},t)$.

We recall the Reynolds transport theorems (Fried and Gurtin, 2003) for $\mathcal{R}$ (i. e., a fixed domain with a moving discontinuity),

$$\frac{\mathrm{d}}{\mathrm{d}t}\int_{\mathcal{R}}\varphi\,\mathrm{d}a = \int_{\mathcal{R}}\partial_t\varphi\,\mathrm{d}a - \int_{\Sigma}[\![\varphi]\!]v_\perp\,\mathrm{d}s, \tag{2.1}$$

and for $\mathcal{R}^-$ and $\mathcal{R}^+$ taken independently (i. e., time-dependent domains),

$$\frac{\mathrm{d}}{\mathrm{d}t}\int_{\mathcal{R}^\pm}\varphi\,\mathrm{d}a = \int_{\mathcal{R}^\pm}\partial_t\varphi\,\mathrm{d}a \mp \int_{\Sigma}\varphi^\pm v_\perp\,\mathrm{d}s. \tag{2.2}$$

LINE INTEGRAL As $\mathcal{S}$ evolves, the endpoints of Σ move with velocity

$$\mathbf{V}^\alpha(t) := \dot{\mathbf{x}}^\alpha(t) = \dot{s}^\alpha(t)\mathbf{t}^\alpha(t) + \mathbf{v}(s^\alpha(t),t) \quad \text{for } \alpha = A,B, \tag{2.3}$$

where the dot notation is used for the time derivative and $\mathbf{t}^\alpha(t) := \mathbf{t}(s^\alpha(t),t)$ with $\alpha = A,B$ are the tangents at the endpoints. Denote by $V_\parallel^\alpha(t) := \mathbf{V}^\alpha(t)\cdot\mathbf{t}^\alpha(t)$ the tangential velocities for $\alpha = A,B$, which by (2.3) can be rewritten

$$V_\parallel^\alpha(t) = \dot{s}^\alpha(t) + v_\parallel(s^\alpha(t),t). \tag{2.4}$$

Let $\xi(s,t)$ a scalar field defined along $\mathcal{S}$. Introducing the normal time derivative of ξ defined by

$$\overset{\square}{\xi} := \partial_t\xi - v_\parallel\partial_s\xi, \tag{2.5}$$

the transport theorem for a line integral on a portion Σ of $\mathcal{S}$ reads

$$\frac{\mathrm{d}}{\mathrm{d}t}\int_{\Sigma}\xi\,\mathrm{d}s = \int_{\Sigma}(\overset{\square}{\xi} - \xi K v_\perp)\,\mathrm{d}s + \int_{\partial\Sigma}\xi V_\parallel^{\partial\Sigma}. \tag{2.6}$$

where the boundary term denotes

$$\int_{\partial\Sigma}\xi V_\parallel^{\partial\Sigma} = \xi(s^B(t),t)V_\parallel^B(t) - \xi(s^A(t),t)V_\parallel^A(t). \tag{2.7}$$

Finally, we also record the transport identity (Fried and Gurtin, 2004):

$$\overset{\square}{\vartheta} = \partial_s v_\perp. \tag{2.8}$$

2.1.2 *Mass balance*

Let $\rho(\mathbf{x},t)$ the adatom density, ρ^b the bulk density (assumed constant) and $\boldsymbol{\jmath}(\mathbf{x},t)$ the adatom surface diffusion flux on the atomic terraces, and denote by $r(\mathbf{x},t)$ the net evaporation/deposition flux of adatoms on the terraces.

ADATOM BALANCE ON UPPER AND LOWER TERRACES The balance of adatoms written on the regions $\mathcal{R}^-$ and $\mathcal{R}^+$ independently reads

$$\frac{\mathrm{d}}{\mathrm{d}t}\int_{\mathcal{R}^\pm}\rho\,\mathrm{d}a=\int_{\mathcal{R}^\pm}r\,\mathrm{d}a-\int_{\partial\mathcal{R}^\pm}\boldsymbol{\jmath}\cdot\mathbf{n}_{\partial\mathcal{R}}\,\mathrm{d}\ell-\int_\Sigma J^\pm\,\mathrm{d}s, \tag{2.9}$$

where $J^-(s,t)$ and $J^+(s,t)$ are the net attachment rate of adatoms to the step from the upper and lower terraces, respectively. Using the Reynolds transport theorem (2.2) along with the divergence theorem, (2.9) is rewritten

$$\int_{\mathcal{R}^\pm}\left(\partial_t\rho-r+\nabla\cdot\boldsymbol{\jmath}\right)\mathrm{d}a+\int_\Sigma\left(\mp\rho^\pm v_\perp+J^\pm\pm\boldsymbol{\jmath}^\pm\cdot\mathbf{n}\right)\mathrm{d}s=0, \tag{2.10}$$

Localization of (2.10) on the terraces yields the diffusion equation,

$$\partial_t\rho=r-\nabla\cdot\boldsymbol{\jmath}\quad\text{on }\Omega, \tag{2.11}$$

while localization at the step provides the local mass balances,

$$\begin{cases}J^-=\boldsymbol{\jmath}^-\cdot\mathbf{n}-\rho^-v_\perp,\\ J^+=-\boldsymbol{\jmath}^+\cdot\mathbf{n}+\rho^+v_\perp.\end{cases} \tag{2.12}$$

GLOBAL ATOMIC BALANCE In the above adatom balances, the step is seen as an exterior sink/source term of adatoms for the lower and upper terraces. We now write a global balance of atoms over $\mathcal{R}$, which accounts for the fact that adatoms attaching to the step contribute to the extension of the top crystal layer of the upper terrace. In addition, we introduce a diffusion current of adatoms along the step but neglect the contribution of the step linear density of adatoms to the total number of atoms. Let $J^s(s,t)$ be the scalar diffusive flux along the step (see Figure 2.1, J^s is oriented such that $\mathbf{J}^s=J^s\mathbf{t}$). Accounting for adatom diffusion on terraces and for adsorption/desorption on terraces, the global balance reads

$$\frac{\mathrm{d}}{\mathrm{d}t}\left\{\int_{\mathcal{R}}\rho\,\mathrm{d}a+\int_{\mathcal{R}^-}a\rho^b\,\mathrm{d}a\right\}=\int_{\mathcal{R}}r\,\mathrm{d}a-\int_{\partial\mathcal{R}}\boldsymbol{\jmath}\cdot\mathbf{n}_{\partial\mathcal{R}}\,\mathrm{d}\ell-\int_{\partial\Sigma}J^s. \tag{2.13}$$

Appealing to the Reynolds transport theorems (2.1) and (2.2) and the divergence theorem in the presence of a discontinuity, specifically,

$$\int_{\partial\mathcal{R}}\boldsymbol{\jmath}\cdot\mathbf{n}_{\partial\mathcal{R}}\,\mathrm{d}\ell=\int_{\mathcal{R}}\nabla\cdot\boldsymbol{\jmath}\,\mathrm{d}a+\int_\Sigma[\![\boldsymbol{\jmath}]\!]\cdot\mathbf{n}\,\mathrm{d}s, \tag{2.14}$$

(2.13), combined with (2.9), yields

$$\int_{\mathcal{R}}\left(\partial_t\rho-r+\nabla\cdot\boldsymbol{\jmath}\right)\mathrm{d}a+\int_\Sigma\left[(a\rho^b-[\![\rho]\!])v_\perp+[\![\boldsymbol{\jmath}]\!]\cdot\mathbf{n}+\partial_sJ^s\right]\mathrm{d}s=0. \tag{2.15}$$

With the help of (2.12), localization of (2.15) along the step provides the following step velocity equation:

$$a\rho^bv_\perp=J^-+J^+-\partial_sJ^s\quad\text{along }\mathcal{S}. \tag{2.16}$$

2.1.3 *Newtonian force balance*

Before we can turn to the force and moment balances, we introduce in Figure 2.2 the migrating volume $\mathcal{V}$, bounded by $\mathcal{R} = \mathcal{R}^+ \cup \mathcal{R}^-$ at the surface (with associated velocity field $\mathbf{w}_{\partial\mathcal{R}}$) and $\partial\mathcal{V}$ in the bulk (with associated velocity field $\mathbf{w}_{\partial\mathcal{V}}$).

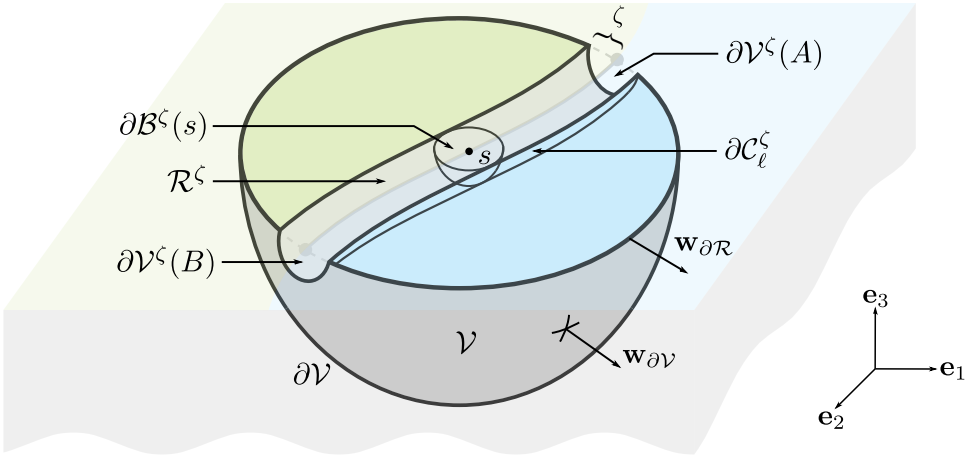

Figure 2.2: Schematic 3D view of the different control volumes considered.

FORCE BALANCE Let $\mathbf{T}$ be the bulk stress tensor, $\mathbf{T}^t$ its surface analog (where the superscript t stands for *terrace*), and $\mathbf{T}^s$ the line traction at the step. In the absence of body forces, the force balance takes the form:

$$\int_{\partial\mathcal{V}} \mathbf{T}\mathbf{n}_{\partial\mathcal{V}}\,\mathrm{d}a + \int_{\partial\mathcal{R}} \mathbf{T}^t\mathbf{n}_{\partial\mathcal{R}}\,\mathrm{d}\ell + \int_{\partial\Sigma} \mathbf{T}^s = \mathbf{0}. \tag{2.17}$$

Since $\mathbf{T}$ is singular at the step, we write the divergence theorem on the control volume $\mathcal{V}$ from which we have excluded a cylindrical tube $\mathcal{C}^\zeta$ of radius ζ enclosing the step with boundaries $\partial\mathcal{C}_\ell^\zeta = \partial\mathcal{C}^\zeta \cap \mathcal{V}$ as lateral surface, $\mathcal{R}^\zeta = \partial\mathcal{C}^\zeta \cap \mathcal{R}$ as top surface, and $\partial\mathcal{V}^\zeta(A)$ and $\partial\mathcal{V}^\zeta(B)$ as front and back faces (see Figure 2.2).[2] In the integrals involving these surfaces, we will denote their corresponding normal vectors by $\mathbf{n}_{\partial\mathcal{C}}$. On that newly defined control volume $\mathcal{V} \setminus \mathcal{C}^\zeta$, we may use the divergence theorem in the usual manner and write

$$\int_{\mathcal{V}\setminus\mathcal{C}^\zeta} \nabla\cdot\mathbf{T}\,\mathrm{d}V = \int_{\partial\mathcal{V}\setminus\partial\mathcal{V}^\zeta} \mathbf{T}\mathbf{n}_{\partial\mathcal{V}}\,\mathrm{d}a + \int_{\mathcal{R}\setminus\mathcal{R}^\zeta} \mathbf{T}|_{\mathcal{R}}\,\mathbf{e}_3\,\mathrm{d}a - \int_{\partial\mathcal{C}_\ell^\zeta} \mathbf{T}\mathbf{n}_{\partial\mathcal{C}}\,\mathrm{d}a. \tag{2.18}$$

We rearrange the last integral on the right-hand side as

$$\begin{aligned}\int_{\partial\mathcal{C}_\ell^\zeta} \mathbf{T}\mathbf{n}_{\partial\mathcal{C}}\,\mathrm{d}a = \int_{\partial\mathcal{C}^\zeta} \mathbf{T}\mathbf{n}_{\partial\mathcal{C}}\,\mathrm{d}a - \int_{\mathcal{R}^\zeta} \mathbf{T}|_{\mathcal{R}}\,\mathbf{e}_3\,\mathrm{d}a \\ - \int_{\partial\mathcal{V}^\zeta(A)} \mathbf{T}\mathbf{n}_{\partial\mathcal{V}}\,\mathrm{d}a - \int_{\partial\mathcal{V}^\zeta(B)} \mathbf{T}\mathbf{n}_{\partial\mathcal{V}}\,\mathrm{d}a,\end{aligned} \tag{2.19}$$

2 We choose a cylindrical tube for convenience, but any family of "regular enough" regions that tends to the step as $\zeta \to 0$ would work equally well.

to conclude that

$$\int_{\mathcal{V}\setminus\mathcal{C}^\zeta} \nabla\cdot\mathbf{T}\,\mathrm{d}V = \int_{\partial\mathcal{V}} \mathbf{T}\mathbf{n}_{\partial\mathcal{V}}\,\mathrm{d}a + \int_{\mathcal{R}} \mathbf{T}|_{\mathcal{R}}\,\mathbf{e}_3\,\mathrm{d}a - \int_{\partial\mathcal{C}^\zeta} \mathbf{T}\mathbf{n}_{\partial\mathcal{C}}\,\mathrm{d}a. \tag{2.20}$$

Thus, if $\lim_{\zeta\to 0}\int_{\partial\mathcal{C}^\zeta}\mathbf{T}\mathbf{n}_{\partial\mathcal{C}}\,\mathrm{d}a$ exists, then $\int_{\mathcal{V}}\nabla\cdot\mathbf{T}\,\mathrm{d}V$ exists as the limit

$$\int_{\mathcal{V}} \nabla\cdot\mathbf{T}\,\mathrm{d}V = \lim_{\zeta\to 0}\int_{\mathcal{V}\setminus\mathcal{C}^\zeta}\nabla\cdot\mathbf{T}\,\mathrm{d}V, \tag{2.21}$$

and we obtain the *generalized divergence theorem*:

$$\int_{\mathcal{V}} \nabla\cdot\mathbf{T}\,\mathrm{d}V = \int_{\partial\mathcal{V}} \mathbf{T}\mathbf{n}_{\partial\mathcal{V}}\,\mathrm{d}a + \int_{\mathcal{R}} \mathbf{T}|_{\mathcal{R}}\,\mathbf{e}_3\,\mathrm{d}a - \int_{\text{step}} \mathbf{T}\mathbf{n}_{\partial\mathcal{C}}\,\mathrm{d}a, \tag{2.22}$$

where

$$\begin{aligned}&\int_{\mathcal{R}} \mathbf{T}|_{\mathcal{R}}\,\mathbf{e}_3\,\mathrm{d}a \text{ is taken in the sense of its Cauchy principal value,}\\ &\int_{\text{step}} \mathbf{T}\mathbf{n}_{\partial\mathcal{C}}\,\mathrm{d}a = \lim_{\zeta\to 0}\int_{\partial\mathcal{C}^\zeta}\mathbf{T}\mathbf{n}_{\partial\mathcal{C}}\,\mathrm{d}a.\end{aligned} \tag{2.23}$$

Similarly the fundamental theorem for line integrals takes the form:

$$\int_{\mathcal{R}} \nabla_{\mathrm{S}}\cdot\mathbf{T}^t\,\mathrm{d}a = \int_{\partial\mathcal{R}}\mathbf{T}^t\mathbf{n}_{\partial\mathcal{R}}\,\mathrm{d}\ell - \int_\Sigma [\![\mathbf{T}^t(\mathbf{x}^s(s,t),t)]\!]\mathbf{n}\,\mathrm{d}s, \tag{2.24}$$

with:

$$\begin{aligned}&\nabla_{\mathrm{S}} = \nabla - \mathbf{n}(\mathbf{n}\cdot\nabla) \text{ the surface gradient, for a surface of normal } \mathbf{n},\\ &\int_{\mathcal{R}}\nabla_{\mathrm{S}}\cdot\mathbf{T}^t\,\mathrm{d}a \text{ defined in terms of its Cauchy principal value,}\\ &\text{and } \mathbf{T}^t \text{ is assumed smooth along the surface up to the step.}\end{aligned} \tag{2.25}$$

Substitution of (2.22) and (2.24) into (2.17) yields, after localization:

$$\begin{cases}\nabla\cdot\mathbf{T} = \mathbf{0} & \text{in the bulk,}\\ -\mathbf{T}|_{\mathcal{R}}\,\mathbf{e}_3 + \nabla_{\mathrm{S}}\cdot\mathbf{T}^t = \mathbf{0} & \text{on } \Omega,\\ \int_s \mathbf{T}\mathbf{n}_{\partial\mathcal{B}}\,\mathrm{d}a + [\![\mathbf{T}^t]\!]\mathbf{n} + \partial_s\mathbf{T}^s = \mathbf{0} & \text{along } \mathcal{S},\end{cases} \tag{2.26}$$

where we have defined

$$\int_s \mathbf{T}\mathbf{n}_{\partial\mathcal{B}}\,\mathrm{d}a = \lim_{\zeta\to 0}\int_{\partial\mathcal{B}^\zeta(s)}\mathbf{T}\mathbf{n}_{\partial\mathcal{B}}\,\mathrm{d}a, \tag{2.27}$$

with $\partial\mathcal{B}^\zeta(s)$ a closed half-sphere of radius ζ centered at the curvilinear abscissa s (see Figure 2.2).[3]

3 Again, a half-sphere is chosen for convenience, but any family of "regular enough" regions that tends to the point of curvilinear abscissa s as $\zeta\to 0$ would work.

MOMENT BALANCE Using index notation, we write:

$$\mathbf{a} \times \mathbf{b} = \epsilon_{ijk} a_i b_j \mathbf{e}_k,$$

with ϵ_{ijk} the Levi–Civita symbol.[4] We use roman letters for indices in $\{1,2,3\}$ and Greek letters for indices in $\{1,2\}$. Relative to the origin, the moment balance takes the form

$$\int_{\partial\mathcal{V}} \mathbf{x} \times \mathbf{T}\mathbf{n}_{\partial\mathcal{V}} \,\mathrm{d}a + \int_{\partial\mathcal{R}} \mathbf{x} \times \mathbf{T}^t \mathbf{n}_{\partial\mathcal{R}} \,\mathrm{d}\ell + \int_{\partial\Sigma} \mathbf{x} \times \mathbf{T}^s = \mathbf{0}, \tag{2.28}$$

or, in index notation,

$$\int_{\partial\mathcal{V}} \epsilon_{ijk} x_i T_{j\ell} n_\ell^{\partial\mathcal{V}} \,\mathrm{d}a + \int_{\partial\mathcal{R}} \epsilon_{\alpha jk} x_\alpha T_{j\delta}^t n_\delta^{\partial\mathcal{R}} \,\mathrm{d}\ell + \int_{\partial\Sigma} \delta_{3k} \epsilon_{\alpha\beta k} x_\alpha T_\beta^s = 0. \tag{2.29}$$

The divergence theorem applied to the surface $\mathcal{R}$ and to the volume $\mathcal{V}$ respectively, allows us to write:

$$\begin{aligned} \int_{\mathcal{R}} \frac{\partial}{\partial x_\delta}(\epsilon_{\alpha jk} x_\alpha T_{j\delta}^t) \,\mathrm{d}a = &\int_{\partial\mathcal{R}} \epsilon_{\alpha jk} x_\alpha T_{j\delta}^t n_\delta^{\partial\mathcal{R}} \,\mathrm{d}\ell \\ &- \int_\Sigma \epsilon_{\alpha jk} x_\alpha^s [\![T_{j\delta}^t(\mathbf{x}^s(s,t),t)]\!] n_\delta \,\mathrm{d}s \end{aligned} \tag{2.30}$$

and

$$\begin{aligned} \int_{\mathcal{V}} \frac{\partial}{\partial x_\ell}(\epsilon_{ijk} x_i T_{j\ell}) \,\mathrm{d}V = &\int_{\partial\mathcal{V}} \epsilon_{ijk} x_i T_{j\ell} n_\ell^{\partial\mathcal{V}} \,\mathrm{d}a + \int_{\mathcal{R}} \epsilon_{\alpha jk} x_\alpha T_{j3}|_{\mathcal{R}} \,\mathrm{d}a \\ &- \int_{\text{step}} \epsilon_{ijk} x_i T_{j\ell} n_\ell^{\partial\mathcal{C}} \,\mathrm{d}a. \end{aligned} \tag{2.31}$$

Further, using $(2.26)_{1,2}$,

$$\begin{cases} \dfrac{\partial}{\partial x_\delta}(\epsilon_{\alpha jk} x_\alpha T_{j\delta}^t) = \epsilon_{\alpha jk} x_\alpha \; T_{j3}|_{\mathcal{R}} + \epsilon_{\alpha jk} T_{j\alpha}^t, \\ \dfrac{\partial}{\partial x_\ell}(\epsilon_{ijk} x_i T_{j\ell}) = \epsilon_{ijk} T_{ji}. \end{cases} \tag{2.32}$$

Finally,

$$\begin{aligned} &\int_{\text{step}} \epsilon_{ijk} x_i T_{j\ell} n_\ell^{\partial\mathcal{C}} \,\mathrm{d}a = \lim_{\zeta\to 0} \int_{\partial\mathcal{C}^\zeta} \epsilon_{ijk} (x_i^s + \zeta n_i^{\partial\mathcal{C}}) T_{j\ell} n_\ell^{\partial\mathcal{C}} \,\mathrm{d}a \\ &= \int_{\text{step}} \epsilon_{\alpha jk} x_\alpha^s T_{j\ell} n_\ell^{\partial\mathcal{C}} \,\mathrm{d}a + \epsilon_{ijk} \lim_{\zeta\to 0} (\zeta \int_{\partial\mathcal{C}^\zeta} n_i^{\partial\mathcal{C}} T_{j\ell} n_\ell^{\partial\mathcal{C}} \,\mathrm{d}a) \\ &= \int_{\text{step}} \epsilon_{\alpha jk} x_\alpha^s T_{j\ell} n_\ell^{\partial\mathcal{C}} \,\mathrm{d}a, \end{aligned} \tag{2.33}$$

4 Also known as the permutation symbol, ϵ_{ijk} is 1 if (i,j,k) is an even permutation (i. e., $(1,2,3)$, $(2,3,1)$, or $(3,1,2)$), -1 if it is an odd permutation (i. e., $(1,3,2)$, $(2,1,3)$, or $(3,2,1)$), and 0 if any index is repeated.

where we have assumed that $\mathbf{T}$ is "regular enough" that $\lim_{\zeta\to 0}\int_{\partial\mathcal{C}^\zeta} n_i^{\partial\mathcal{C}} T_{j\ell} n_\ell^{\partial\mathcal{C}}\,\mathrm{d}a$ exists. After substitution of the above identities into (2.28), localization, with the help of $(2.26)_3$, then yields:

$$\begin{cases} \epsilon_{ijk}T_{ji} = 0 & \text{in the bulk,} \\ \epsilon_{\alpha jk}T^t_{j\alpha} = 0 & \text{on } \Omega, \\ \epsilon_{3\alpha\beta}t_\alpha T^s_\beta = 0 & \text{along } \mathcal{S}. \end{cases} \tag{2.34}$$

In other words,

$$\begin{cases} \mathbf{T} = \mathbf{T}^\intercal, \\ T^t_{31} = T^t_{32} = 0; \quad T^t_{12} = T^t_{21}, \\ \mathbf{T}^s = T^s\mathbf{t}. \end{cases} \tag{2.35}$$

Note that the last column T^t_{i3} is irrelevant because $\mathbf{T}^t$ is contracted with an in-plane vector. As such, and without loss of generality, $\mathbf{T}^t$ is a symmetric tensor with $T^t_{i3} = T^t_{3i} = 0$.

2.1.4 *Configurational force balance*

Following Gurtin (1995), we augment the mass balances and Newtonian force balance with a *configurational* force balance, as this formalism allows a unified treatment of problems with multiple phases or defects. Like Newtonian *deformation* forces describe the response of a body to deformation, configurational *accretive* forces are associated with the addition and deletion of material points at the boundary of a portion of a body. Indeed, two kinematics govern the problem: one associated with the material velocity, to which Newtonian forces are conjugate; and another associated with the step propagation velocity, to which configurational forces are conjugate; each kinematic system being subject to a balance law. For configurational forces, the general balance law is assumed to take the form:

$$\int_{\partial\mathcal{V}} \mathbf{C}\mathbf{n}_{\partial\mathcal{V}}\,\mathrm{d}a + \int_{\partial\mathcal{R}} \mathbf{C}^t\mathbf{n}_{\partial\mathcal{R}}\,\mathrm{d}\ell + \int_\Sigma \mathbf{g}\,\mathrm{d}s + \int_{\partial\Sigma} \mathbf{C}^s = \mathbf{0}, \tag{2.36}$$

where $\mathbf{C}$ is the bulk configurational stress tensor, that acts in response to the exchange of material at the boundary; $\mathbf{C}^t$ the surface configurational stress tensor, a generalization of surface tension that acts in response to increases in interfacial area or changes in the orientation of the interface; $\mathbf{C}^s$ the step configurational stress vector, a generalization of line tension; and $\mathbf{g}$ the step configurational internal force. By contrast with the Newtonian force balance, which involves external forces, the configurational force balance involves an internal force, associated with the exchange of adatoms, at the step, between the crystallized bulk and the terraces.

$$\begin{cases} \nabla\cdot\mathbf{C} = \mathbf{0} & \text{in the bulk,} \\ -\,\mathbf{C}|_{\mathcal{R}}\,\mathbf{e}_3 + \nabla_S\cdot\mathbf{C}^t = \mathbf{0} & \text{on } \Omega, \\ \displaystyle\int_s \mathbf{C}\mathbf{n}_{\partial\mathcal{B}}\,\mathrm{d}a + [\![\mathbf{C}^t]\!]\mathbf{n} + \mathbf{g} + \partial_s\mathbf{C}^s = \mathbf{0} & \text{along } \mathcal{S}. \end{cases} \tag{2.37}$$

Letting $\mathbf{C}^s = \sigma\mathbf{t} + \tau\mathbf{n}$ and $g = \mathbf{g}\cdot\mathbf{n}$, the normal component of this last equation is:

$$\int_s \mathbf{n}\cdot\mathbf{C}\mathbf{n}_{\partial\mathcal{B}}\,\mathrm{d}a + \mathbf{n}\cdot[\![\mathbf{C}^t]\!]\mathbf{n} + g + \partial_s\tau + \sigma K = 0, \tag{2.38}$$

where we have used the identity $\partial_s\mathbf{t} = K\mathbf{n}$. Since $\mathbf{g}\cdot\mathbf{t}$ is indeterminate, the tangential component of (2.37)$_3$ is inconsequential to the theory (Fried and Gurtin, 2003).

2.1.5 *Dissipation inequality*

EXTERNAL POWER EXPENDITURES By definition, we assume that configurational forces expend power in consort with transfers of material, and take $\mathbf{w}_{\partial\mathcal{V}}$, $\mathbf{w}_{\partial\mathcal{R}}$, and $\mathbf{V}_{\partial\Sigma}$ to be appropriate power-conjugate velocities for $\mathbf{C}\mathbf{n}_{\partial\mathcal{V}}$, $\mathbf{C}^t\mathbf{n}_{\partial\mathcal{R}}$, and $\mathbf{C}^s$, respectively (Gurtin, 1995, 2000; Fried and Gurtin, 2004).

Classically, for a control volume $\mathcal{V}$, the Newtonian traction $\mathbf{T}\mathbf{n}$ would be power-conjugate to the velocity $\dot{\mathbf{u}}$. However, when migrating, $\partial\mathcal{V}$ has no intrinsic material description, and the appropriate power-conjugate velocity should instead be the induced velocity field $\overline{\mathbf{w}} = \dot{\mathbf{u}} + (\nabla\mathbf{u})\mathbf{w}$, i. e., the motion velocity following $\partial\mathcal{V}$ as described by $\mathbf{w}$. Invoking an analogous argument for the surface and line tractions, the external power expended on $\mathcal{R}\cup\partial\mathcal{V}$ takes the form:

$$\begin{aligned}\mathcal{W}(\mathcal{V}) = &\int_{\partial\mathcal{V}} \mathbf{T}\mathbf{n}_{\partial\mathcal{V}}\cdot\overline{\mathbf{w}}_{\partial\mathcal{V}}\,\mathrm{d}a + \int_{\partial\mathcal{V}} \mathbf{C}\mathbf{n}_{\partial\mathcal{V}}\cdot\mathbf{w}_{\partial\mathcal{V}}\,\mathrm{d}a\\ &+ \int_{\partial\mathcal{R}} \mathbf{T}^t\mathbf{n}_{\partial\mathcal{R}}\cdot\overline{\mathbf{w}}_{\partial\mathcal{R}}\,\mathrm{d}\ell + \int_{\partial\mathcal{R}} \mathbf{C}^t\mathbf{n}_{\partial\mathcal{R}}\cdot\mathbf{w}_{\partial\mathcal{R}}\,\mathrm{d}\ell\\ &+ \int_{\partial\Sigma} \mathbf{T}^s\cdot\overline{\mathbf{V}}_{\partial\Sigma} + \int_{\partial\Sigma} \mathbf{C}^s\cdot\mathbf{V}_{\partial\Sigma},\end{aligned} \tag{2.39}$$

where $\overline{\mathbf{w}}_{\partial\mathcal{V}} = \dot{\mathbf{u}} + (\nabla\mathbf{u})\mathbf{w}_{\partial\mathcal{V}}$, $\overline{\mathbf{w}}_{\partial\mathcal{R}} = \dot{\mathbf{u}} + (\nabla_{\mathrm{S}}\,\mathbf{u})\mathbf{w}_{\partial\mathcal{R}}$, and $\overline{\mathbf{V}}_{\partial\Sigma} = \overset{\square}{\mathbf{u}} + (\partial_s\mathbf{u})V^{\parallel}_{\partial\Sigma}$. After substitution,

$$\begin{aligned}\mathcal{W}(\mathcal{V}) = &\int_{\partial\mathcal{V}} \Big[\mathbf{T}\mathbf{n}_{\partial\mathcal{V}}\cdot\dot{\mathbf{u}} + \Big((\nabla\mathbf{u}^{\mathsf{T}})\mathbf{T}\mathbf{n}_{\partial\mathcal{V}} + \mathbf{C}\mathbf{n}_{\partial\mathcal{V}}\Big)\cdot\mathbf{w}_{\partial\mathcal{V}}\Big]\,\mathrm{d}a\\ &+ \int_{\partial\mathcal{R}} \Big[\mathbf{T}^t\mathbf{n}_{\partial\mathcal{R}}\cdot\dot{\mathbf{u}} + \Big((\nabla_{\mathrm{S}}\,\mathbf{u}^{\mathsf{T}})\mathbf{T}^t\mathbf{n}_{\partial\mathcal{R}} + \mathbf{C}^t\mathbf{n}_{\partial\mathcal{R}}\Big)\cdot\mathbf{w}_{\partial\mathcal{R}}\Big]\,\mathrm{d}\ell\\ &+ \int_{\partial\Sigma} \mathbf{T}^s\cdot\overline{\mathbf{V}}_{\partial\Sigma} + \int_{\partial\Sigma} \mathbf{C}^s\cdot\mathbf{V}_{\partial\Sigma}.\end{aligned} \tag{2.40}$$

We require that our theory be independent of the choice of parametrization for the velocity fields $\mathbf{w}_{\partial\mathcal{V}}$ and $\mathbf{w}_{\partial\mathcal{R}}$. Given that a change in parametrization affects the tangential component of the velocity fields, but leaves the normal component unaltered, invariance of (2.40) under reparametrization is equivalent to the requirement that, for all tangential fields $\mathbf{t}_{\partial\mathcal{V}}$ and $\mathbf{t}_{\partial\mathcal{R}}$,

$$\begin{cases}\Big((\nabla\mathbf{u}^{\mathsf{T}})\mathbf{T}\mathbf{n}_{\partial\mathcal{V}} + \mathbf{C}\mathbf{n}_{\partial\mathcal{V}}\Big)\cdot\mathbf{t}_{\partial\mathcal{V}} = 0, & (2.41)\\ \Big((\nabla_{\mathrm{S}}\,\mathbf{u}^{\mathsf{T}})\mathbf{T}^t\mathbf{n}_{\partial\mathcal{R}} + \mathbf{C}^t\mathbf{n}_{\partial\mathcal{R}}\Big)\cdot\mathbf{t}_{\partial\mathcal{R}} = 0. & (2.42)\end{cases}$$

For a migrating control volume with associated velocity field $\mathbf{w}$, the expression for the velocity $\mathbf{V}^\alpha$ ($\alpha = A, B$) becomes

$$\mathbf{V}^\alpha = \dot{s}^\alpha(t)\mathbf{t} + \mathbf{v}(s^\alpha(t)) + \frac{w_\perp \mathbf{t}}{\mathbf{t}\cdot\mathbf{n}_{\partial\mathcal{R}}}. \tag{2.43}$$

Note that it only depends on the normal component of $\mathbf{w}$, which is why no constraint is imposed on $\mathbf{C}^s$ at this stage. Then, since $\mathcal{V}$ is arbitrary, $\Big((\nabla\mathbf{u}^\intercal)\mathbf{T} + \mathbf{C}\Big)\mathbf{n}_{\partial\mathcal{V}}$ and $\Big((\nabla_S\,\mathbf{u}^\intercal)\mathbf{T}^t + \mathbf{C}^t\Big)\mathbf{n}_{\partial\mathcal{R}}$ must be parallel to $\mathbf{n}_{\partial\mathcal{V}}$ and $\mathbf{n}_{\partial\mathcal{R}}$, respectively, so that

$$\begin{cases} (\nabla\mathbf{u}^\intercal)\mathbf{T} + \mathbf{C} = \pi\mathbf{I}, \\ (\nabla_S\,\mathbf{u}^\intercal)\mathbf{T}^t + \mathbf{C}^t = \pi^t\mathbf{I}. \end{cases} \tag{2.44}$$

The external power expenditure expression (2.40) takes the form

$$\begin{aligned} \mathcal{W}(\mathcal{V}) = &\int_{\partial\mathcal{V}} \mathbf{T}\mathbf{n}_{\partial\mathcal{V}}\cdot\dot{\mathbf{u}}\,\mathrm{d}a + \int_{\partial\mathcal{V}} \pi w^\perp_{\partial\mathcal{V}}\,\mathrm{d}a \\ &+ \int_{\partial\mathcal{R}} \mathbf{T}^t\mathbf{n}_{\partial\mathcal{R}}\cdot\dot{\mathbf{u}}\,\mathrm{d}s + \int_{\partial\mathcal{R}} \widehat{\pi} w^\perp_{\partial\mathcal{R}}\,\mathrm{d}\ell \\ &+ \int_{\partial\Sigma} \mathbf{T}^s\cdot\overline{\mathbf{V}}_{\partial\Sigma} + \int_{\partial\Sigma} \mathbf{C}^s\cdot\mathbf{V}_{\partial\Sigma} \end{aligned} \tag{2.45}$$

We now focus on the work of the Newtonian tractions. Starting with the bulk term, we have, by the divergence theorem:

$$\int_{\partial\mathcal{V}} \mathbf{T}\mathbf{n}_{\partial\mathcal{V}}\cdot\dot{\mathbf{u}}\,\mathrm{d}a + \int_{\mathcal{R}} \mathbf{T}|_{\mathcal{R}}\,\mathbf{e}_3\cdot\dot{\mathbf{u}}\,\mathrm{d}a - \int_{\text{step}} \mathbf{T}\mathbf{n}_{\partial\mathcal{C}}\cdot\dot{\mathbf{u}}\,\mathrm{d}a\,\mathrm{d}s = \int_{\mathcal{V}} \nabla\cdot(\mathbf{T}^\intercal\dot{\mathbf{u}})\,\mathrm{d}V, \tag{2.46}$$

where $\nabla\cdot(\mathbf{T}^\intercal\dot{\mathbf{u}}) = \cancel{(\nabla\cdot\mathbf{T})}\cdot\dot{\mathbf{u}} + \mathbf{T}\cdot\dot{\overline{\nabla\mathbf{u}}}$. Adding and subtracting $(\nabla\mathbf{u})v_\perp\mathbf{n}$ in the step integral, and recalling that $\overset{\square}{\mathbf{u}} = \dot{\mathbf{u}} + (\nabla\mathbf{u})v_\perp\mathbf{n}$:

$$\begin{aligned} \int_{\partial\mathcal{V}} \mathbf{T}\mathbf{n}_{\partial\mathcal{V}}\cdot\dot{\mathbf{u}}\,\mathrm{d}a = &\int_{\mathcal{V}} \mathbf{T}\cdot\dot{\boldsymbol{\varepsilon}}\,\mathrm{d}V - \int_{\mathcal{R}} \mathbf{T}|_{\mathcal{R}}\,\mathbf{e}_3\cdot\dot{\mathbf{u}}\,\mathrm{d}a + \int_{\text{step}} \mathbf{T}\mathbf{n}_{\partial\mathcal{C}}\cdot\overset{\square}{\mathbf{u}}\,\mathrm{d}a \\ &- \int_{\text{step}} v_\perp\mathbf{n}\cdot((\nabla\mathbf{u}^\intercal)\cdot\mathbf{T})\mathbf{n}_{\partial\mathcal{C}}\,\mathrm{d}a, \end{aligned} \tag{2.47}$$

where, $\mathbf{T}$ being symmetric by $(2.35)_2$, $\mathbf{T}\cdot\dot{\overline{\nabla\mathbf{u}}} = \mathbf{T}\cdot\dot{\boldsymbol{\varepsilon}}$. Next, for the surface boundary $\partial\mathcal{R}$ term:

$$\int_{\partial\mathcal{R}} \mathbf{T}^t\mathbf{n}_{\partial\mathcal{R}}\cdot\dot{\mathbf{u}}\,\mathrm{d}s - \int_{\Sigma} [\![\mathbf{T}^t\mathbf{n}\cdot\dot{\mathbf{u}}]\!]\,\mathrm{d}\ell = \int_{\mathcal{R}} \nabla_S\cdot((\mathbf{T}^t)^\intercal\dot{\mathbf{u}})\,\mathrm{d}a, \tag{2.48}$$

where, by $(2.26)_2$, $\nabla_S\cdot((\mathbf{T}^t)^\intercal\dot{\mathbf{u}}) = \mathbf{T}|_{\mathcal{R}}\,\mathbf{e}_3\cdot\dot{\mathbf{u}} + \mathbf{T}^t\cdot\dot{\overline{\nabla_S\,\mathbf{u}}}$. Adding and subtracting $(\nabla_S\,\mathbf{u})v_\perp\mathbf{n}$ in the brackets:[5]

$$\begin{aligned} \int_{\partial\mathcal{R}} \mathbf{T}^t\mathbf{n}_{\partial\mathcal{R}}\cdot\dot{\mathbf{u}}\,\mathrm{d}\ell = &\int_{\mathcal{R}} \Big[\ \mathbf{T}|_{\mathcal{R}}\,\mathbf{e}_3\cdot\dot{\mathbf{u}} + \mathbf{T}^t\cdot\dot{\boldsymbol{\varepsilon}}^t\Big]\,\mathrm{d}a \\ &+ \int_{\Sigma} [\![\mathbf{T}^t\mathbf{n}]\!]\cdot\overset{\square}{\mathbf{u}}\,\mathrm{d}s - \int_{\Sigma} v_\perp\mathbf{n}\cdot[\![(\nabla_S\,\mathbf{u}^\intercal)\mathbf{T}^t\mathbf{n}]\!]\,\mathrm{d}s, \end{aligned} \tag{2.49}$$

5 ∇ or ∇_S does not matter *in fine* as it is contracted with $\mathbf{T}^t\mathbf{n}$ in the plane.

where $\boldsymbol{\varepsilon}^t = \frac{1}{2}\left(\nabla_S \mathbf{u}|_{\mathcal{R}} + \nabla_S \mathbf{u}^\intercal|_{\mathcal{R}}\right)$ is the interfacial strain tensor, and $\mathbf{T}^t$ being symmetric, $\mathbf{T}^t \cdot \overline{\dot{\nabla_S \mathbf{u}}} = \mathbf{T}^t \cdot \dot{\boldsymbol{\varepsilon}}^t$. We have also used the fact that $[\![\overset{\square}{\mathbf{u}}]\!] = 0$, which stems from the continuity condition

$$\mathbf{u}((\mathbf{x}^S)^+(s,t),t) = \mathbf{u}((\mathbf{x}^S)^-(s,t),t) \tag{2.50}$$

differentiated with respect to time. Finally, for the line term, introducing the interfacial strain

$$\mathbf{e}^s = (\nabla \mathbf{u})\mathbf{t} = \partial_s \mathbf{u} = \gamma \mathbf{n} + \varepsilon^s \mathbf{t}, \tag{2.51}$$

with γ the interfacial shear strain and ε^s the interfacial tensile strain, we get

$$\int_{\partial\Sigma} \mathbf{T}^{\mathbf{s}} \cdot \overset{\square}{\mathbf{u}} = \int_\Sigma \left[(\partial_s T^s) \cdot \overset{\square}{\mathbf{u}} + \mathbf{T}^s \cdot (\overset{\square}{\mathbf{e}^s} - K v_\perp \mathbf{e}^s) \right] \mathrm{d}s, \tag{2.52}$$

where the identity $\partial_s \overset{\square}{\mathbf{u}} = \overset{\square}{\mathbf{e}^s} - K v_\perp \mathbf{e}^s$ is used. Substituting (2.47), (2.49), and (2.52) back into (2.45), and using $(2.26)_3$, we conclude:

$$\begin{aligned}
\mathcal{W}(\mathcal{V}) = &\int_{\mathcal{V}} \mathbf{T} \cdot \dot{\boldsymbol{\varepsilon}} \,\mathrm{d}V + \int_{\mathcal{R}} \mathbf{T}^t \cdot \dot{\boldsymbol{\varepsilon}}^t \,\mathrm{d}a + \int_\Sigma \mathbf{T}^s \cdot \overset{\square}{\mathbf{e}^s} \,\mathrm{d}s - \int_\Sigma T^s \varepsilon^s K v_\perp \,\mathrm{d}s \\
&- \int_{\text{step}} v_\perp \mathbf{n} \cdot \left[((\nabla \mathbf{u}^\intercal) \cdot \mathbf{T}) \mathbf{n}_{\partial\mathcal{C}} + [\![(\nabla_S \mathbf{u}^\intercal) \mathbf{T}^t \mathbf{n}]\!] \right] \mathrm{d}a \\
&+ \int_{\partial\mathcal{V}} \pi w^\perp_{\partial\mathcal{V}} \,\mathrm{d}a + \int_{\partial\mathcal{R}} \pi^t w^\perp_{\partial\mathcal{R}} \,\mathrm{d}\ell + \int_{\partial\Sigma} \left[T^s \varepsilon^s V_\parallel^{\partial\Sigma} + \mathbf{C}^s \cdot \mathbf{V}_{\partial\Sigma} \right].
\end{aligned} \tag{2.53}$$

FREE-ENERGY IMBALANCE Denote by

$$\mathcal{F}(\mathcal{R}) = \int_{\mathcal{R}} \mu^v r \,\mathrm{d}a - \int_{\partial\mathcal{R}} \mu(\boldsymbol{\jmath} - \rho \mathbf{w}_{\partial\mathcal{R}}) \cdot \mathbf{n}_{\partial\mathcal{R}} \,\mathrm{d}\ell - \int_{\partial\Sigma} \mu^s J^s \tag{2.54}$$

the energy intake that accompanies the flow of atoms into or out of $\mathcal{R}$ by adsorption/desorption on the terraces, as well as diffusion across $\partial\mathcal{R}$ and along Σ (bulk diffusion is neglected), where μ^v is the vapor chemical potential (taken, for simplicity, to be constant), $\mu(\mathbf{x},t)$ the chemical potential of adatoms on terraces, and μ^s the chemical potential of adatoms attached to the step. Using (2.11) and (2.12), we rewrite

$$\begin{aligned}
\mathcal{F}(\mathcal{R}) = &\int_{\mathcal{R}} \left[\mu \partial_t \rho - (\mu - \mu^v) r - \boldsymbol{\jmath} \cdot \nabla \mu \right] \mathrm{d}a + \int_{\partial\mathcal{R}} \mu \rho w^\perp_{\partial\mathcal{R}} \,\mathrm{d}\ell \\
&+ \int_\Sigma \Big[(\mu^+ - \mu^s) J^+ + (\mu^- - \mu^s) J^- \\
&\quad - (a \rho^b \mu^s + [\![\mu\rho]\!]) v_\perp - J^s \partial_s \mu^s \Big] \,\mathrm{d}s.
\end{aligned} \tag{2.55}$$

In addition, in the presence of an electric field $\mathbf{e} = -\nabla\Phi$, assuming adatoms behave as particles with an effective charge q_e, we denote by

$$\mathcal{W}_{\mathcal{L}}(\mathcal{R}) = -\int_{\mathcal{R}} q_e (\nabla\Phi) \cdot \boldsymbol{\jmath} \,\mathrm{d}a - \int_\Sigma q_e (\nabla\Phi) \cdot \mathbf{J}^s \,\mathrm{d}s \tag{2.56}$$

the work of the Lorentz force. In an isothermal setting, the energy imbalance and entropy imbalance combine to deliver the free-energy imbalance:

$$\frac{\mathrm{d}}{\mathrm{d}t}\left(\int_{\mathcal{V}}\psi^b(\mathbf{x},t)\,\mathrm{d}V+\int_{\mathcal{R}}\psi(\mathbf{x},t)\,\mathrm{d}a+\int_{\Sigma}\psi^s(\mathbf{x}^s(s,t),t)\,\mathrm{d}s\right)\leqslant\mathcal{W}(\mathcal{V})+\mathcal{F}(\mathcal{R})+\mathcal{W}_{\mathcal{L}}(\mathcal{R}),\quad(2.57)$$

with ψ^b the bulk free energy (per unit volume), ψ the terrace free energy (per unit area) and ψ^s the step free energy (per unit length).

At this point, we also need the following transport identity for the bulk free energy ψ^b

$$\frac{\mathrm{d}}{\mathrm{d}t}\int_{\mathcal{V}}\psi^b\,\mathrm{d}V=\int_{\mathcal{V}}\partial_t\psi^b\,\mathrm{d}V+\int_{\partial\mathcal{V}}\psi^b w^{\perp}_{\partial\mathcal{V}}\,\mathrm{d}a-\int_{\text{step}}v_{\perp}\mathbf{n}\cdot\psi^b\mathbf{n}_{\partial\mathcal{C}}\,\mathrm{d}a.\quad(2.58)$$

Using transport identities (2.1) and (2.58), the LHS reduces to:

$$\begin{aligned}&\int_{\mathcal{V}}\partial_t\psi^b\,\mathrm{d}V+\int_{\mathcal{R}}\partial_t\psi\,\mathrm{d}a+\int_{\Sigma}\left[\overset{\square}{\psi^s}-([\![\psi]\!]+\psi^sK)v_{\perp}\right]\mathrm{d}s\\&-\int_{\text{step}}v_{\perp}\mathbf{n}\cdot\psi^b\mathbf{n}_{\partial\mathcal{C}}\,\mathrm{d}a+\int_{\partial\mathcal{V}}\psi^b w^{\perp}_{\partial\mathcal{V}}\,\mathrm{d}a+\int_{\partial\mathcal{R}}\psi w^{\perp}_{\partial\mathcal{R}}\,\mathrm{d}\ell+\int_{\partial\Sigma}\psi^s V^{\partial\Sigma}_{\parallel}.\end{aligned}\quad(2.59)$$

Substituting (2.53), (2.55), (2.56), and (2.59) in (2.57), we obtain, using the relations (2.8), (2.38), and (2.44):

$$\begin{aligned}&\int_{\partial\mathcal{V}}(\psi^b-\pi)w^{\perp}_{\partial\mathcal{V}}\,\mathrm{d}a+\int_{\partial\mathcal{R}}(\psi-\mu\rho-\pi^t)w^{\perp}_{\partial\mathcal{R}}\,\mathrm{d}\ell+\int_{\partial\Sigma}(\psi^s-(\sigma+T^s\varepsilon^s))V^{\partial\Sigma}_{\parallel}\\&+\int_{\mathcal{V}}\left[\partial_t\psi^b-\mathbf{T}\cdot\dot{\boldsymbol{\varepsilon}}\right]\mathrm{d}V+\int_{\mathcal{R}}\left[\partial_t\psi-\mathbf{T}^t\cdot\dot{\boldsymbol{\varepsilon}}^t-\mu\partial_t\rho+(\mu-\mu^v)r+\boldsymbol{\jmath}\cdot\nabla\mu_e\right]\mathrm{d}a\\&+\int_{\Sigma}\Big[\overset{\square}{\psi^s}-\mathbf{T}^s\cdot\overset{\square}{\mathbf{e}^s}-\tau\overset{\square}{\vartheta}-(a\rho^b\mu^s-g)v_{\perp}\\&\qquad-(\mu^+-\mu^s)J^+-(\mu^--\mu^s)J^-+J^s\partial_s\mu^s_e\Big]\mathrm{d}s\leqslant0,\end{aligned}\quad(2.60)$$

where we denote $\mu_e:=\mu+q_e\Phi$ the electrochemical potential of adatoms and $\mu^s_e:=\mu^s+q_e\Phi$ the electrochemical potential of step adatoms. Then, invoking the arbitrariness of the velocity fields $w^{\perp}_{\partial\mathcal{V}}$, $w^{\perp}_{\partial\mathcal{R}}$, and $V^{\partial\Sigma}_{\parallel}$, the following relations must hold:

$$\begin{cases}\pi=\psi^b,\\ \pi^t=\psi-\mu\rho,\\ \sigma=\psi^s-T^s\varepsilon^s,\end{cases}\quad(2.61)$$

which yields the final dissipation inequality:

$$\begin{aligned}&\int_{\mathcal{V}}\left[\partial_t\psi^b-\mathbf{T}\cdot\dot{\boldsymbol{\varepsilon}}\right]\mathrm{d}V+\int_{\mathcal{R}}\left[\partial_t\psi-\mathbf{T}^t\cdot\dot{\boldsymbol{\varepsilon}}^t-\mu\partial_t\rho+(\mu-\mu^v)r+\boldsymbol{\jmath}\cdot\nabla\mu_e\right]\mathrm{d}a\\&+\int_{\Sigma}\Big[\overset{\square}{\psi^s}-\mathbf{T}^s\cdot\overset{\square}{\mathbf{e}^s}-\tau\overset{\square}{\vartheta}-(a\rho^b\mu^s-g)v_{\perp}\\&\qquad-(\mu^+-\mu^s)J^+-(\mu^--\mu^s)J^-+J^s\partial_s\mu^s_e\Big]\mathrm{d}s\leqslant0.\end{aligned}\quad(2.62)$$

Hence, away from the surface, the bulk dissipation inequality has the form:

$$\partial_t \psi^b - \mathbf{T} \cdot \dot{\boldsymbol{\varepsilon}} \leqslant 0, \tag{2.63}$$

where localization arguments, as pertaining to an arbitrary control volume, have been invoked and $\mathbf{w} = \mathbf{0}$ assumed. At the surface but away from the step, the terrace dissipation inequality reads:

$$\partial_t \psi - \mathbf{T}^t \cdot \dot{\boldsymbol{\varepsilon}}^t - \mu \partial_t \rho + (\mu - \mu^v) r + \boldsymbol{\jmath} \cdot \nabla \mu^e \leqslant 0, \tag{2.64}$$

where the arbitrariness of $\mathcal{R}$ permits localization and $\mathbf{w} = \mathbf{0}$ is assumed. Finally, at the step, the dissipation inequality can be written as:

$$\overset{\square}{\psi}^s - T^s \overset{\square}{\varepsilon}^s - \tilde{\tau} \overset{\square}{\vartheta} - \mathfrak{G} v_\perp - (\mu^+ - \mu^s) J^+ - (\mu^- - \mu^s) J^- + J^s \partial_s \mu^s_e \leqslant 0, \tag{2.65}$$

where $\tilde{\tau} = \tau - T^s \gamma$ is the reduced configurational shear, $\mathfrak{G} = a \rho^b \mu^s - g$ the thermodynamic driving force, and we have used the identities $\overset{\square}{\mathbf{n}} = -\overset{\square}{\vartheta} \mathbf{t}$ and $\overset{\square}{\mathbf{t}} = \overset{\square}{\vartheta} \mathbf{n}$ to compute $\overset{\square}{\mathbf{e}}^s = (\overset{\square}{\gamma} + \varepsilon^s \overset{\square}{\vartheta}) \mathbf{n} + (\overset{\square}{\varepsilon}^s - \gamma \overset{\square}{\vartheta}) \mathbf{t}$.

2.2 CONSTITUTIVE RELATIONS

2.2.1 *Thermodynamic restrictions*

Following the Coleman-Noll procedure (Coleman and Noll, 1963), the dissipation inequalities (2.63), (2.64) and (2.65), valid for any admissible process, furnish restrictions on the constitutive relations. Assume ψ^b to be a function of $\boldsymbol{\varepsilon}$, $\psi^b := \psi^b(\boldsymbol{\varepsilon})$, by (2.63) the bulk stress reads

$$\mathbf{T} = \partial_{\boldsymbol{\varepsilon}} \psi^b. \tag{2.66}$$

Likewise, assume ψ to be a function of $\boldsymbol{\varepsilon}^t$ and ρ, $\psi := \psi(\boldsymbol{\varepsilon}^t, \rho)$, by (2.64) the surface stress and the adatom chemical potential read

$$\begin{cases} \mathbf{T}^t = \partial_{\boldsymbol{\varepsilon}^t} \psi, \\ \mu = \partial_\rho \psi. \end{cases} \tag{2.67}$$

Finally, assume ψ^s to be a function of ε^s and ϑ, $\psi^s := \psi^s(\varepsilon^s, \vartheta)$, by (2.65) the line traction and reduced configurational shear read:

$$\begin{cases} T^s = \partial_{\varepsilon^s} \psi^s, \\ \tilde{\tau} = \partial_\vartheta \psi^s. \end{cases} \tag{2.68}$$

Assuming the dissipative fluxes at the step to depend linearly on the thermodynamic forces, we write, in the most general case:

$$\begin{pmatrix} J^s \\ J^+ \\ J^- \\ v_\perp \end{pmatrix} = \mathbf{L} \begin{pmatrix} -\partial_s \mu^s_e \\ \mu^+ - \mu^s \\ \mu^- - \mu^s \\ \mathfrak{G} \end{pmatrix}, \tag{2.69}$$

where, by (2.64) and (2.65), $\mathbf{L} \in \mathbb{R}^{4\times4}$ is positive semi-definite. Restricting our attention to the most simple case of negligible couplings,[6] we can write the deposition/evaporation rate as

$$r = -\gamma_v(\mu - \mu^v), \tag{2.70}$$

and the different fluxes as

$$\begin{cases} \jmath = -\rho M(\nabla\mu_e), \\ J^s = -M^s\partial_s\mu_e^s, \\ J^+ = \gamma_+(\mu^+ - \mu^s), \\ J^- = \gamma_-(\mu^- - \mu^s), \end{cases} \tag{2.71}$$

where, by (2.64) and (2.65), γ_v, M, M^s, and $\gamma_\pm$ are all scalar positive coefficients. Lastly, from (2.65) we assume the following linear *kinetic relation*, with positive coefficient b, between the velocity $v_\perp$ and thermodynamic driving force $\mathfrak{G}$ at the step:

$$v_\perp = b\mathfrak{G}. \tag{2.72}$$

Using the configurational force balance at the step (2.38),

$$g = -\mathbf{n}\cdot\int_s \mathbf{C}\mathbf{n}_{\partial\mathcal{B}}\,\mathrm{d}a - \mathbf{n}\cdot[\![\mathbf{C}^t]\!]\mathbf{n} - \partial_s\tau - \sigma K, \tag{2.73}$$

and using the definition of the reduced configurational shear, we have, by differentiation:

$$\partial_s\tau = \partial_s\tilde{\tau} + (\partial_s T^s)\gamma + T^s(\partial_s\gamma). \tag{2.74}$$

Moreover, from the constitutive relation (2.68),

$$\partial_s\tilde{\tau} = \partial_{s\vartheta}\psi^s = (\partial_s\varepsilon^s)(\partial_\vartheta T^s) + K\partial_{\vartheta\vartheta}\psi^s. \tag{2.75}$$

Hence, substituting (2.73), (2.74), and (2.75) in the thermodynamic driving force:

$$\begin{aligned}\mathfrak{G} = a\rho^b\mu^s + \mathbf{n}\cdot\int_s \mathbf{C}\mathbf{n}_{\partial\mathcal{B}}\,\mathrm{d}a + \mathbf{n}\cdot[\![\mathbf{C}^t]\!]\mathbf{n} + K(\psi^s + \partial_{\vartheta\vartheta}\psi^s - T^s\varepsilon^s) \\ + (\partial_s\varepsilon^s)(\partial_\vartheta T^s) + \partial_s(T^s\gamma).\end{aligned} \tag{2.76}$$

2.2.2 *Step chemical potential*

As the step velocity is already prescribed by (2.16), (2.76) can be seen as a generalized Gibbs–Thomson relation furnishing the step chemical potential,

$$\mu^s = -\frac{1}{a\rho^b}\Big(\mathfrak{f} + \mathbf{n}\cdot[\![\mathbf{C}^t]\!]\mathbf{n} + \tilde{\gamma}K + (\partial_s\varepsilon^s)(\partial_\vartheta T^s) + \partial_s(T^s\gamma) - \frac{v_\perp}{b}\Big), \tag{2.77}$$

6 We investigate in Appendix A the effect of a coupling between the fluxes $J^\pm$ and the thermodynamic forces $(\mu^\pm - \mu^s)$.

with

$$\begin{cases} \mathfrak{f} := \mathbf{n} \cdot \int_s \mathbf{C}\mathbf{n}_{\partial\mathcal{B}} \, \mathrm{d}a, \\ \tilde{\gamma} := \psi^s + \partial_{\theta\theta}\psi^s - T^s\varepsilon^s. \end{cases} \tag{2.78}$$

If we neglect surface stress and line traction, in line with the existing literature, the relation simplifies to

$$\mu^s = -\frac{1}{a\rho^b}\left(\mathfrak{f} + [\![\omega]\!] + \tilde{\gamma}K - \frac{v_\perp}{b}\right), \tag{2.79}$$

with $\omega := \psi - \mu\rho$ the adatom grand canonical potential. Compared to the classical Gibbs–Thomson relation

$$\mu^s = -\frac{1}{a\rho^b}\tilde{\gamma}K, \tag{2.80}$$

one can see that with the nonequilibrium thermodynamics approach we adopt here, full account is taken of:

1. the energetics of the global system {crystal monolayer+step+adatom layer} via the coupling of diffusion fields on adjacent terraces $[\![\omega]\!]$,
2. the dissipation related to the finite velocity of the step $-v_\perp/b$, akin to kinetic undercooling in solidification problems (Davis, 2001),
3. the contribution of the elastic bulk to the driving force via the elastic fields generated by the steps on the vicinal surface $\mathfrak{f}$.

2.2.3 *Choice of a free energy*

The restrictions on the constitutive relations derived in Section 2.2.1 need to be completed by a constitutive assumption for the adatom free-energy density. Assume the adatom layer over terraces to be an ideal gas, its free energy reads

$$\psi(\rho) = \rho k_B \mathsf{T}\left(\ln\left(\frac{\rho}{\rho^*_{eq}}\right) - 1\right), \tag{2.81}$$

where ρ^*_{eq} is the equilibrium adatom density, whose physical meaning is further explained below. By (2.67), we have

$$\mu(\rho) = k_B \mathsf{T} \ln\left(\frac{\rho}{\rho^*_{eq}}\right). \tag{2.82}$$

Noting that $\mu(\rho^*_{eq}) = 0$, it appears that ρ^*_{eq} is the *adatom density in equilibrium with a straight isolated step*. Indeed, in such a situation, by (2.77), the step chemical potential reduces to 0 (cf. $K = 0$, $[\![\psi - \mu\rho]\!] = 0$ since in equilibrium $\rho = \rho^*_{eq}$ over all Ω, and $v_\perp = 0$ at equilibrium) and $\mu(\rho^*_{eq}) = 0$ is then the expression of equilibrium of the adatom layer with the step reservoir.

Using the free energy assumption, we explicit some of the constitutive relations (2.71) and (2.77). Letting $\mathcal{D} = k_B \mathsf{T} M$ and $\mathcal{D}^s = k_B \mathsf{T} M^s$, in the most simple

case where we neglect the step-edge deformation and stress, and the surface stress, these constitutive relations are rewritten as

$$\begin{cases} \jmath = \mathcal{D}\left[-\nabla\rho + \dfrac{q_e\rho}{k_B\mathsf{T}}\mathbf{e}\right], \qquad r = \gamma_v\left[\mu^v - k_B\mathsf{T}\ln\left(\dfrac{\rho}{\rho^*_{eq}}\right)\right], \\ J^s = -\mathcal{D}^s\partial_s\left[-\dfrac{1}{a\rho^b}\left(\dfrac{\mathfrak{f}}{k_B\mathsf{T}} - [\![\rho]\!] + \dfrac{\tilde{\gamma}}{k_B\mathsf{T}}K - \dfrac{v_\perp}{k_B\mathsf{T}b}\right) + \dfrac{q_e}{k_B\mathsf{T}}\Phi\right], \\ J^\pm = \gamma_\pm\left[k_B\mathsf{T}\ln\left(\dfrac{\rho^\pm}{\rho^*_{eq}}\right) + \dfrac{1}{a\rho^b}\left(\mathfrak{f} - k_B\mathsf{T}[\![\rho]\!] + \tilde{\gamma}K - \dfrac{v_\perp}{b}\right)\right]. \end{cases} \tag{2.83}$$

2.3 ELASTIC INTERACTIONS BETWEEN STEPS

This section is dedicated to the derivation of the elastic contribution $\mathfrak{f}$ to the driving force that appears in the step chemical potential (2.77). Note that, for simplicity, we will assume that the elasticity and diffusion problems are uncoupled. After showing how the steps can be equivalently represented as force dipoles acting on a flat surface (in the absence of a far field stress), we establish the following identity for two dipoles A and B, with associated dipolar tensors $\mathbf{d}^A$ and $\mathbf{d}^B$, interacting at distance $\mathbf{x}^0$, for an arbitrary control volume $\mathcal{V}$ enclosing only dipole B:

$$\int_{\partial\mathcal{V}\cup\mathcal{R}} C_{ij}n_j \,\mathrm{d}a = d^B_{jk}u^A_{k,ij}(\mathbf{x}^0). \tag{2.84}$$

In Section 4.2.2, the above result is used to compute explicitly the step-step interaction for infinitesimally perturbed meanders in the context of linear stability analysis.

2.3.1 *Multipole representation of steps*

A simple continuum representation of the elastic field generated by a step consists in replacing the stepped surface by an elastic half space subjected to a surface distribution of forces $\mathbf{f}^s(x_1, x_2)$ exerted by the step system on the bulk. This distribution of forces is assumed localized on a surface domain $\mathcal{L}$ around the step (Figure 2.3).

The displacement field $\mathbf{u}(\mathbf{x})$ generated by this distribution of forces can be described as a convolution with the appropriate Green's function:

$$u_i(\mathbf{x}) = \int_{\mathcal{L}} G_{ij}(x_1 - x'_1, x_2 - x'_2, x_3) f^s_j(x'_1, x'_2)\,\mathrm{d}x'_1\,\mathrm{d}x'_2, \tag{2.85}$$

with G_{ij} the components of the tensor Green's function for a half-space, given in Appendix B (in the absence of surface stress). Assuming the extent of the region $\mathcal{L}$ is small compared to the distance between steps, we Taylor-expand (2.85):

$$u_i(\mathbf{x}) = \sum_{n\geqslant 0}\frac{(-1)^n}{n!}\left(\int_{\mathcal{L}}(x'_{k_1}\ldots x'_{k_n})f^s_j(x'_1, x'_2)\,\mathrm{d}x'_1\,\mathrm{d}x'_2\right)\frac{\partial^n G_{ij}}{\partial x_{k_1}\ldots\partial x_{k_n}}(\mathbf{x}), \tag{2.86}$$

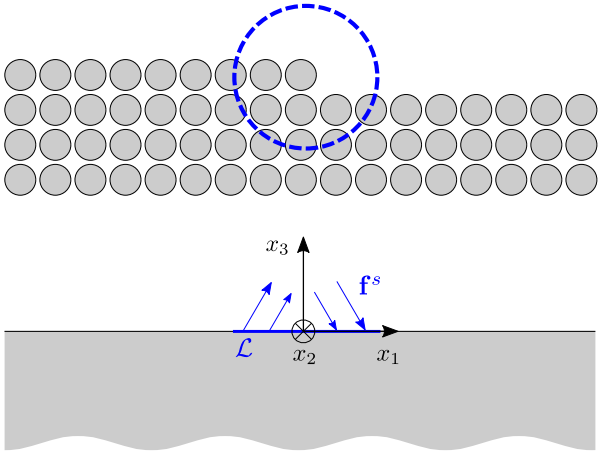

Figure 2.3: Representation in a continuum picture of the effect of a step on the bulk through a surface distribution of forces $\mathbf{f}^s(x_1, x_2)$.

where indices k_i span $\{1, 2\}$. This is the multipole expansion. Correspondingly, the stress associated to this displacement field solves:

$$T_{ij,j} + \sum_{n \geqslant 0} \frac{(-1)^n}{n!} \Big(\int_{\mathcal{L}} (x'_{k_1} ... x'_{k_n}) f_j^s(x'_1, x'_2) \, \mathrm{d}x'_1 \, \mathrm{d}x'_2 \Big) \frac{\partial^n \delta}{\partial x_{k_1} ... \partial x_{k_n}}(\mathbf{x}) = 0, \tag{2.87}$$

with δ Dirac delta function. Integrating (2.87) over $\mathcal{V}$, applying the divergence theorem, and using the properties of the delta function, we obtain:

$$\int_{\partial \mathcal{V} \cup \mathcal{R}} \mathbf{T}\mathbf{n}_{\partial \mathcal{V}} \, \mathrm{d}a + \int_{\mathcal{L}} \mathbf{f}^s(x'_1, x'_2) \, \mathrm{d}x'_1 \, \mathrm{d}x'_2 = 0. \tag{2.88}$$

Along with (2.17), this result suggests:

$$\int_{\mathcal{L}} \mathbf{f}^s(x'_1, x'_2) \, \mathrm{d}x'_1 \, \mathrm{d}x'_2 = - \int_{\partial \mathcal{R}} \mathbf{T}^t \mathbf{n}_{\partial \mathcal{R}} \, \mathrm{d}\ell - \int_{\partial \Sigma} \mathbf{T}^s. \tag{2.89}$$

In the classical derivation of the elastic field induced by a step, surface stress and line tension are neglected. Consequently, the monopole is found to be zero and the dominant contribution is expected to be dipolar. To allow for the computation of an explicit expression for step interactions, we will proceed with this simplification as well. Based on the work of Koguchi (2008), this should have minimal impact on the linear stability analysis. Indeed, the author showed that the influence of surface stress and elasticity is limited to a few tenths of nanometers around the step, while we consider interactions between steps that are typically several nanometers apart. In conclusion, neglecting the higher order moment multipoles, as they are associated with higher order derivatives of the Green's function, which scale as r^{-k}, with $k \geqslant 3$, and thus decay more rapidly than the dipolar contribution, which scales as r^{-2}, we model a portion of a step as a dipolar tensor $\mathbf{d}$ with an associated displacement field:

$$u_i(\mathbf{x}) = -G_{ij,k}(\mathbf{x}) d_{kj}, \tag{2.90}$$

where $d_{kj} = \int_{\mathcal{L}} x_k f_j^s(x'_1, x'_2) \, \mathrm{d}x'_1 \, \mathrm{d}x'_2$.

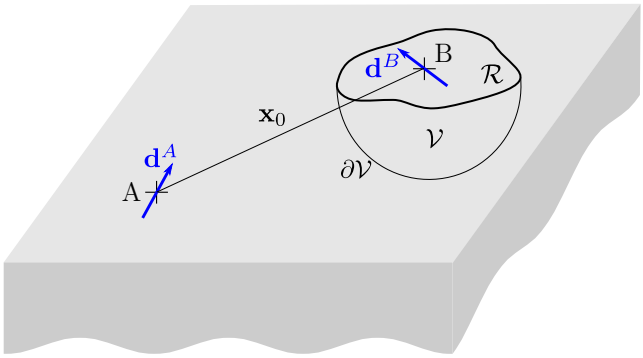

Figure 2.4: Interaction of two dipoles A and B, with associated dipolar tensors $\mathbf{d}^A$ and $\mathbf{d}^B$. The control volume encloses dipole B but not A.

2.3.2 *Interaction of two elastic dipoles*

From (2.44) and (2.61), we recover the classical expression for the configurational bulk stress tensor $\mathbf{C}$

$$\mathbf{C} = \psi^b \mathbf{1} - (\nabla \mathbf{u})^\intercal \mathbf{T}, \tag{2.91}$$

which corresponds to the *Eshelby energy-momentum tensor*. Recalling that $\psi^b = \psi^b(\boldsymbol{\varepsilon})$, its spatial derivative reads

$$\psi^b_{,i} = \boldsymbol{\varepsilon}_{,i} \cdot \mathbf{T}, \tag{2.92}$$

where we have used the identity (2.66): $\mathbf{T} = \partial_{\boldsymbol{\varepsilon}} \psi^b$. Next, the divergence theorem, combined with (2.91) and (2.92), yields:

$$\int_{\partial\mathcal{V}\cup\mathcal{R}} C_{ij} n_j \, \mathrm{d}a = \int_{\mathcal{V}} \left(\varepsilon_{jk,i} T_{jk} - u_{j,ik} T_{jk} - u_{j,i} T_{jk,k} \right) \mathrm{d}V. \tag{2.93}$$

Using the symmetry of $\mathbf{T}$, the first two terms on the right hand side cancel out, and the relation simplifies to:

$$\int_{\partial\mathcal{V}\cup\mathcal{R}} C_{ij} n_j \, \mathrm{d}a = - \int_{\mathcal{V}} u_{j,i} T_{jk,k} \, \mathrm{d}V, \tag{2.94}$$

From (2.87), we have, for $\alpha = A, B$:

$$T^\alpha_{jk,k} - d^\alpha_{kj} \frac{\partial \delta}{\partial x_k} (\mathbf{x} - \mathbf{x}^\alpha) = 0.^7 \tag{2.95}$$

Decomposing the total displacement and stress fields as $\mathbf{u} = \mathbf{u}^A + \mathbf{u}^B$ and $\mathbf{T} = \mathbf{T}^A + \mathbf{T}^B$, it is then immediate to see that

$$\int_{\mathcal{V}} u_{j,i} T^A_{jk,k} \, \mathrm{d}V = 0, \tag{2.96}$$

7 Note that this relation also allows us to verify the self-consistency of our formulation as it immediately shows that $\lim_{\zeta\to 0} \int_{\partial\mathcal{C}^\zeta} \mathbf{T}\mathbf{n}_{\partial\mathcal{C}} \, \mathrm{d}a = 0$ and thus converges.

as dipole A is outside the control volume $\mathcal{V}$. Hence, using the properties of the Dirac delta function, (2.94) reduces to

$$-\int_{\mathcal{V}} u_{j,i}T_{jk,k}\,\mathrm{d}V = d^B_{kj}u^A_{j,ik}(\mathbf{x}^B) + U_{\text{self}}, \tag{2.97}$$

where U_{self} corresponds to the J-integral of an isolated dipole, i. e.,

$$U_{\text{self}} = \int_{\partial\mathcal{V}\cup\mathcal{R}} C^B_{ij}n_j\,\mathrm{d}a. \tag{2.98}$$

In the present setting of dipolar interaction, this "self-energy" integral is not convergent, which violates the assumption used in the derivation of the generalized divergence theorem for the bulk configurational stress tensor. This is consistent with the breakdown of linear elasticity theory near the step, as evidenced by the atomistic simulations of Stewart et al. (1994). To circumvent this core singularity, noticing that the term $d^B_{kj}u^A_{j,ik}(\mathbf{x}^B)$ is not affected by the core behavior of the displacement field for two distant-enough dipoles, we may introduce in the dipolar displacement field a regularized region of finite width centered around the dipole's position, such that the self-energy integral converges to a finite value, dependent on the specific choice of regularization. Finally, because the J-integral only contributes via the step-chemical potential, which is defined up to an additive constant, we may always set

$$U_{\text{self}} = 0 \tag{2.99}$$

via a redefinition of the chemical potential reference. Hence, after centering the origin at dipole A, we obtain

$$\int_{\partial\mathcal{V}\cup\mathcal{R}} C_{ij}n_j\,\mathrm{d}a = d^B_{kj}u^A_{j,ik}(\mathbf{x}^0), \tag{2.100}$$

where $\mathbf{x}^0 = \mathbf{x}^B - \mathbf{x}^A$.

2.4 STEP DYNAMICS MODEL

2.4.1 *Governing equations*

We combine (2.11), (2.12), (2.16), and (2.83) to write the step dynamics governing equations as a partial differential system for ρ over Ω with boundary conditions along $\mathcal{S}$ and a condition on $v_\perp$ for the computation of the motion of $\mathcal{S}$.

$$\begin{cases} \partial_t\rho = \mathcal{D}\,\nabla\cdot\left(\nabla\rho - \dfrac{q_e\rho}{k_B\mathsf{T}}\mathbf{e}\right) + \gamma_v\left[\mu^v - k_B\mathsf{T}\ln\left(\dfrac{\rho}{\rho^*_{eq}}\right)\right], \\ -\rho^- v_\perp - \mathcal{D}\left((\nabla\rho)^- - \dfrac{q_e\rho^-}{k_B\mathsf{T}}\mathbf{e}\right)\cdot\mathbf{n} = J^-, \\ \rho^+ v_\perp + \mathcal{D}\left((\nabla\rho)^+ - \dfrac{q_e\rho^+}{k_B\mathsf{T}}\mathbf{e}\right)\cdot\mathbf{n} = J^+, \\ a\rho^b v_\perp = J^- + J^+ - \partial_s J^s, \end{cases} \tag{2.101}$$

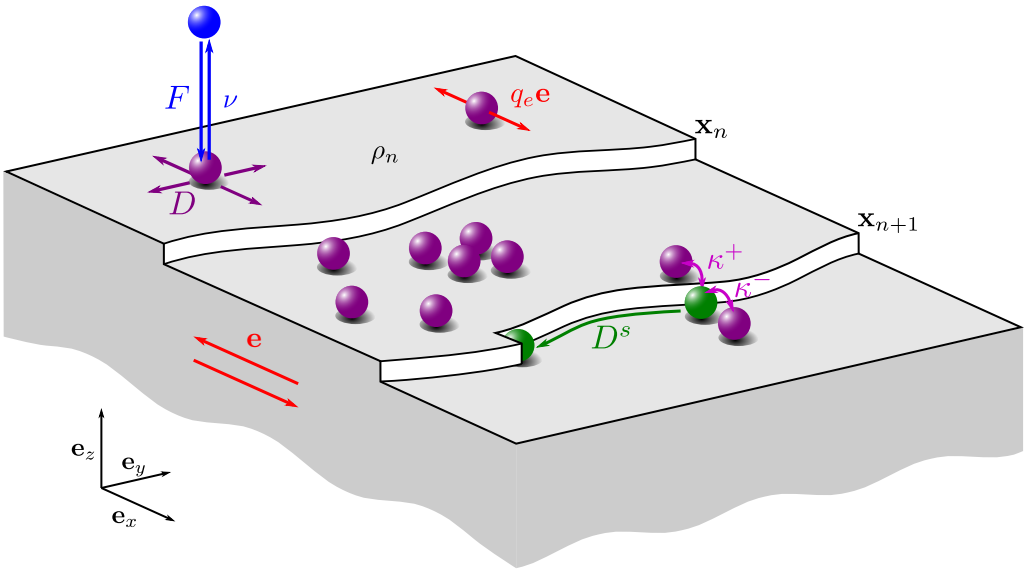

Figure 2.5: Schematic 3D view of the terraces and the different processes taking place at their surface.

with J^+, J^-, and J^s given in (2.83). As shown in Figure 2.5, we denote $\mathbf{x}_n(s,t)$ the position of the n^{th} step, and $\rho_n(\mathbf{x},t)$ the adatom density on the n^{th} terrace (comprised between steps n and $n+1$). We also use subscript n to describe quantities relating to step n, such as its curvature K_n and the elastic interaction with the rest of the steps

$$\mathfrak{f}_n := \mathbf{n}_n \cdot \int_{s_n} \mathbf{C}\mathbf{n}_{\partial\mathcal{C}}\, \mathrm{d}a. \tag{2.102}$$

Assuming small departures of the adatom density from its equilibrium value ($|\rho - \rho^*_{eq}| \ll \rho^*_{eq}$), we linearize $\ln(\rho/\rho^*_{eq}) \simeq (\rho - \rho^*_{eq})/\rho^*_{eq}$. Defining

$$\begin{cases} \nu := \dfrac{k_B \mathsf{T} \gamma_v}{\rho^*_{eq}} \text{ the evaporation rate,} \\ F := \gamma_v(\mu^v + k_B\mathsf{T}) \text{ the deposition flux,} \\ \kappa_\pm := \dfrac{k_B \mathsf{T} \gamma_\pm}{\rho^*_{eq}} \text{ the attachment/detachment kinetic coefficients,} \\ v_n := (\partial_t \mathbf{x}_n) \cdot \mathbf{n} \text{ the normal velocity,} \end{cases} \tag{2.103}$$

the governing equations read

$$\begin{cases} \partial_t \rho_n = \mathcal{D}\,\nabla\cdot\left(\nabla\rho_n - \dfrac{q_e\rho_n}{k_B\mathsf{T}}\mathbf{e}\right) + F - \nu\rho_n, \\ -\rho_n^- v_{n+1} - \mathcal{D}\left((\nabla\rho_n)^- - \dfrac{q_e\rho_n^-}{k_B\mathsf{T}}\mathbf{e}\right)\cdot\mathbf{n} = J^-_{n+1}, \\ \rho_n^+ v_n + \mathcal{D}\left((\nabla\rho_n)^+ - \dfrac{q_e\rho_n^+}{k_B\mathsf{T}}\mathbf{e}\right)\cdot\mathbf{n} = J^+_n, \\ a\rho^b v_n = J^-_n + J^+_n - \partial_s J^s_n, \end{cases} \tag{2.104}$$

with

$$\begin{cases} J_n^- = \kappa_- \left[\rho_{n-1}^- - \rho_{eq}^* + a^2 \rho_{eq}^* \left(\dfrac{\mathfrak{f}_n}{k_B \mathsf{T}} - [\![\rho]\!]_{x_n} + \dfrac{\tilde{\gamma}}{k_B \mathsf{T}} K_n - \dfrac{v_n}{k_B \mathsf{T} b} \right) \right], \\ J_n^+ = \kappa_+ \left[\rho_n^- - \rho_{eq}^* + a^2 \rho_{eq}^* \left(\dfrac{\mathfrak{f}_n}{k_B \mathsf{T}} - [\![\rho]\!]_{x_n} + \dfrac{\tilde{\gamma}}{k_B \mathsf{T}} K_n - \dfrac{v_n}{k_B \mathsf{T} b} \right) \right], \\ J_n^s = \mathcal{D}^s \partial_s \left[a^2 \left(\dfrac{\mathfrak{f}_n}{k_B \mathsf{T}} - [\![\rho]\!]_{x_n} + \dfrac{\tilde{\gamma}}{k_B \mathsf{T}} K_n - \dfrac{v_n}{k_B \mathsf{T} b} \right) - \dfrac{q_e}{k_B \mathsf{T}} \Phi \right], \end{cases} \tag{2.105}$$

where we have used the following notations

$$\begin{cases} \rho_n^- := \rho_n(\mathbf{x}_{n+1}, t), & \rho_n^+ := \rho_n(\mathbf{x}_n, t), \\ (\nabla \rho_n)^- := \nabla \rho_n(\mathbf{x}_{n+1}, t), & (\nabla \rho_n)^+ := \nabla \rho_n(\mathbf{x}_n, t), \\ [\![\rho]\!]_{x_n} := \rho_{n+1}(\mathbf{x}_n, t) - \rho_n(\mathbf{x}_n, t). \end{cases} \tag{2.106}$$

2.4.2 *Nondimensionalization*

We nondimensionalize the free-boundary value problem (2.104) and (2.105) with the initial terrace width $\mathcal{L}_0$ as a characteristic length, ρ_{eq}^* for the adatom density and $\mathcal{L}_0^2/\mathcal{D}$ as a characteristic time, and consequently identify twelve dimensionless parameters in the dimensionless formulation of the problem. The equilibrium adatom coverage is described by

$$\Theta := a^2 \rho_{eq}^*. \tag{2.107}$$

Necessarily, $0 \leqslant \Theta \leqslant 1$, since it represents a fraction of the available lattice sites. The deposition and evaporation of adatoms are characterized by the dimensionless counterpart of F and ν:

$$\overline{F} := \frac{F \mathcal{L}_0^2}{\rho_{eq}^* \mathcal{D}} = \left(\frac{\mathcal{L}_0}{L_d^{dep}} \right)^2, \tag{2.108}$$

which quantifies the ratio of the initial terrace width to the diffusion length under deposition and

$$\bar{\nu} := \frac{\nu \mathcal{L}_0^2}{\mathcal{D}} = \left(\frac{\mathcal{L}_0}{L_d^{eva}} \right)^2, \tag{2.109}$$

that similarly gives the ratio of the initial terrace width to the diffusion length under evaporation. Note that the natural requirement that $\rho \leqslant 1/a^2$ and the more compelling assumption that ρ deviates little from ρ_{eq}^* implies upper bounds on the values of $\overline{F}$ and $\bar{\nu}$ discussed in Appendix D. Next, we introduce the *Péclet number*

$$\mathcal{P} = \frac{V_0 \mathcal{L}_0}{\mathcal{D}}, \tag{2.110}$$

which gives the ratio of step velocity V_0 to a characteristic diffusion velocity $\mathcal{D}/\mathcal{L}_0$, and is central in the discussion of the quasistatic approximation (see

Section 4.3.1). The electromigration force and potential are given by their dimensionless counterparts

$$\bar{\mathbf{e}} := \frac{q_e \mathcal{L}_0}{k_B \mathsf{T}} \mathbf{e} \tag{2.111}$$

and

$$\overline{\Phi} := \frac{q_e \Phi}{k_B \mathsf{T}}. \tag{2.112}$$

Given that the adatom attachment/detachment from above and below are related to similar atomistic mechanisms, they shall have comparable orders of magnitude, hence the kinetic coefficients are rewritten in terms of

$$\bar{\kappa} := \frac{\kappa_- \mathcal{L}_0}{\mathcal{D}}, \tag{2.113}$$

expressing the ratio of the initial terrace width to the attachment/detachment kinetic length $\mathcal{D}/\kappa_-$ associated to the upper terrace (Krug, 2005). $\bar{\kappa}$ is an important parameter that allows to distinguish between the *attachment/detachment limited regime* and the *diffusion limited regime*. These notions refer to the two kinetic processes: attachment/detachment at steps and diffusion on terraces. $\bar{\kappa}$ can be seen as the ratio of a characteristic step attachment/detachment velocity κ_- to a characteristic diffusion velocity $\mathcal{D}/\mathcal{L}_0$. Then, $\bar{\kappa} \ll 1$ corresponds to situations where the attachment/detachment is the limiting kinetic process and conversely $\bar{\kappa} \gg 1$ is associated to cases where the diffusion is limiting.

To quantify the asymmetry of attachment/detachment at steps from the upper and lower terraces, we introduce

$$S := \frac{\kappa_+}{\kappa_-}, \tag{2.114}$$

giving the strength of the Ehrlich-Schwoebel (ES) effect. The case $0 < S < 1$ ($S > 1$) correspond to an inverse (direct) ES effect, while $S = 1$ is for a symmetric attachment/detachment.

Likewise, to quantify the relative strength of surface diffusion and step-edge diffusion, we introduce

$$\Pi := \frac{a^2 \mathcal{D}^s}{\mathcal{L}_0 \mathcal{D}}, \tag{2.115}$$

which can be seen as the ratio of the step-edge diffusion $\mathcal{D}^s$ to a characteristic terrace diffusion velocity $\mathcal{D}\mathcal{L}_0/a^2$. As such, $\Pi \ll 1$ corresponds to situations where the diffusion process is dominated by surface diffusion and $\Pi \gg 1$ is associated to cases where step-edge diffusion is the main diffusion process.

The strength of the elastic dipoles is represented by the dimensionless counterpart of $\mathbf{d}$,

$$\overline{\mathbf{d}} = \sqrt{\frac{a^2}{k_B \mathsf{T} \mathcal{L}_0^3}} \mathbf{d}, \tag{2.116}$$

such that we write the dimensionless step-step interaction as

$$\bar{\mathfrak{f}}_n = \frac{a^2}{k_B \mathsf{T} \mathcal{L}_0^3} \mathfrak{f}_n. \tag{2.117}$$

The step stiffness is rewritten in dimensionless form

$$\bar{\gamma} = \frac{a^2 \tilde{\gamma}}{k_B \mathsf{T} \mathcal{L}_0}, \tag{2.118}$$

and the kinetic coefficient b

$$\bar{b} = \frac{\mathcal{L}_0 k_B \mathsf{T} b}{a^2 \mathcal{D}}. \tag{2.119}$$

Without relabeling the dimensionless time and space variables, the governing equations for the adatom diffusion problem (2.104) and (2.105) read in their dimensionless form

$$\begin{cases} \partial_t \rho_n = \nabla \cdot \left(\nabla \rho_n - \rho_n \bar{\mathbf{e}} \right) + \bar{F} - \bar{v} \rho_n, \\ -\rho_n^- v_{n+1} - \left((\nabla \rho_n)^- - \rho_n^- \bar{\mathbf{e}} \right) \cdot \mathbf{n} = J_{n+1}^-, \\ \rho_n^+ v_n + \left((\nabla \rho_n)^+ - \rho_n^+ \bar{\mathbf{e}} \right) \cdot \mathbf{n} = J_n^+, \\ v_n = \Theta(J_n^- + J_n^+) - \partial_s J_n^s, \end{cases} \tag{2.120}$$

with

$$\begin{cases} J_n^- = \bar{\kappa} \Big(\rho_{n-1}^- - 1 - \Theta(\rho_n^+ - \rho_{n-1}^-) + \bar{\mathfrak{f}}_n + \bar{\gamma} K_n - \dfrac{v_n}{\bar{b}} \Big), \\ J_n^+ = \bar{\kappa} S \Big(\rho_n^+ - 1 - \Theta(\rho_n^+ - \rho_{n-1}^-) + \bar{\mathfrak{f}}_n + \bar{\gamma} K_n - \dfrac{v_n}{\bar{b}} \Big), \\ J_n^s = \Pi \partial_s \Big(- \Theta(\rho_n^+ - \rho_{n-1}^-) + \bar{\mathfrak{f}}_n + \bar{\gamma} K_n - \dfrac{v_n}{\bar{b}} - \bar{\Phi} \Big). \end{cases} \tag{2.121}$$

Note that the term in $1/\bar{b}$ in (2.121) accounts for the dissipation related to the nonequilibrium processes underlying the propagation of the step. Although an experimental estimation of b is out of reach, if we assume the step is in *local thermodynamic equilibrium*, i. e., $\mathfrak{G} = 0$, Equation 2.72 imposes $b \to \infty$ to allow for step motion at finite velocity. Consequently, the contribution of the term in $1/\bar{b}$ to the step governing equation may be neglected.[8]

2.4.3 *Arbitrary Lagrangian-Eulerian formulation*

The problem under consideration being a free boundary problem, the domain of definition of the adatom density is not constant but varies with the steps' positions, which can pose additional difficulties for the linear stability analysis as

8 We also performed numerical simulations with a finite b that showed no visible difference with the limit case $b \to \infty$.

well as the numerical integration of the system. Thus, in order to eliminate this dependence, the system of partial differential equations $(2.120)_{1-3}$ is rewritten on a fixed domain by introducing the *Lagrangian* space variable u related to (x, y) on $(x_n, x_{n+1}) \times \mathbb{R}$ by the diffeomorphism g_n defined by

$$u = g_n(\mathbf{x}, t) := \frac{|\mathbf{x} - \mathbf{x}_n(s,t)|}{\ell_n(s,t)} \text{ where } \ell_n(s_n, t) := |\mathbf{x}_{n+1}(s_{n+1}, t) - \mathbf{x}_n(s_n, t)|. \tag{2.122}$$

If the curvilinear abscissae s_n can be written as single-valued functions of the coordinate y, i. e.,

$$s_n := h_n(y), \tag{2.123}$$

which is guaranteed for small deviations from the straight-step configuration, we can describe the step profiles as functions of the coordinate y instead of the curvilinear abscissae s_n, so that $\mathbf{x}_n = \mathbf{x}_n(y = h_n^{-1}(s_n), t) = x_n(y,t)\mathbf{e}_1 + y\mathbf{e}_2$, where h_n^{-1} designates the reciprocal function of h_n. Consequently, we redefine

$$u = g_n(\mathbf{x}, t) := \frac{x - x_n(y,t)}{\ell_n(y,t)} \text{ where } \ell_n(y,t) := x_{n+1}(y,t) - x_n(y,t), \tag{2.124}$$

and obtain, denoting y-derivatives with primes,

$$\begin{cases} K_n = \dfrac{x_n''}{\sqrt{1 + (x_n')^2}}, \\ \mathbf{n}_n = \dfrac{1}{\sqrt{1 + (x_n')^2}}(\mathbf{e}_1 - x_n'\mathbf{e}_2). \end{cases} \tag{2.125}$$

Let g_n^{-1} be the reciprocal function of g_n, then the *Lagrangian adatom density* $\tilde{\rho}_n$ is defined by

$$\tilde{\rho}_n(u, y, t) := \rho_n(x = g_n^{-1}(u, y, t), y, t), \tag{2.126}$$

on the spatial domain $(0,1) \times \mathbb{R}$ which is now independent of the steps' positions.

Differentiating u:

$$\begin{cases} \partial_t u = -\dfrac{\dot{x}_n + \dot{\ell}_n u}{\ell_n}, \\ \partial_x u = \dfrac{1}{\ell_n}, \\ \partial_y u = -\dfrac{x_n' + \ell_n' u}{\ell_n}, \\ \partial_{yy} u = -\dfrac{x_n'' + \ell_n'' u}{\ell_n} + 2\dfrac{\ell_n'}{\ell_n}\dfrac{x_n' + \ell_n' u}{\ell_n}, \end{cases} \tag{2.127}$$

we explicit the relations between the partial derivatives of ρ_n and $\tilde{\rho}_n$:

$$\begin{cases} \partial_t \rho_n = (\partial_t u)\partial_u \tilde{\rho}_n + \partial_t \tilde{\rho}_n = -\dfrac{\dot{x}_n + \dot{\ell}_n u}{\ell_n}\partial_u \tilde{\rho}_n + \partial_t \tilde{\rho}_n, \\ \partial_x \rho_n = (\partial_x u)\partial_u \tilde{\rho}_n = \dfrac{1}{\ell_n}\partial_u \tilde{\rho}_n, \\ \partial_{xx}\rho_n = \dfrac{1}{\ell_n^2}\partial_{uu}\tilde{\rho}_n, \\ \partial_y \rho_n = (\partial_y u)\partial_u \tilde{\rho}_n + \partial_y \tilde{\rho}_n = -\dfrac{x_n' + \ell_n' u}{\ell_n}\partial_u \tilde{\rho}_n + \partial_y \tilde{\rho}_n, \\ \partial_{yy}\rho_n = (\partial_y u)^2 \partial_{uu}\tilde{\rho}_n + \partial_{yy}\tilde{\rho}_n + 2(\partial_y u)\partial_{uy}\tilde{\rho}_n + (\partial_{yy}u)\partial_u \tilde{\rho}_n. \end{cases} \tag{2.128}$$

Substituting back, (2.120) is rewritten with Lagrangian variables

$$\begin{cases} \ell_n^2 \partial_t \tilde{\rho}_n = [1 + (x_n' + \ell_n' u)^2]\partial_{uu}\tilde{\rho}_n + \ell_n^2 \partial_{yy}\tilde{\rho}_n - 2\ell_n(x_n' + \ell_n' u)\partial_{uy}\tilde{\rho}_n \\ \qquad + \ell_n[\dot{x}_n + \dot{\ell}_n u - x_n'' - \ell_n'' u + 2\ell_n'(x_n' + \ell_n' u)]\partial_u \tilde{\rho}_n + \ell_n^2(\overline{F} - \bar{v}\tilde{\rho}_n), \\ J_{n+1}^- = -\rho_n^- v_{n+1} \\ \qquad - \dfrac{1}{\sqrt{1 + (x_n')^2}}\left[\dfrac{1}{\ell_n}[1 + x_n'(x_n' + \ell_n' u)](\partial_u \tilde{\rho}_n)^- - x_n'(\partial_y \tilde{\rho}_n)^-\right], \\ J_n^+ = \rho_n^+ v_n \\ \qquad + \dfrac{1}{\sqrt{1 + (x_n')^2}}\left[\dfrac{1}{\ell_n}[1 + x_n'(x_n' + \ell_n' u)](\partial_u \tilde{\rho}_n)^+ - x_n'(\partial_y \tilde{\rho}_n)^+\right], \\ v_n = \Theta(J_n^+ + J_n^-) - \Pi\partial_{yy}[-\Theta(\tilde{\rho}_n^+ - \tilde{\rho}_{n-1}^-) + \gamma K_n + \bar{\mathfrak{f}}_n], \end{cases} \tag{2.129}$$

Except for replacing ρ with $\tilde{\rho}$, the definition of J_n^- and J_n^+ is unchanged:

$$\begin{cases} J_n^- = \bar{\kappa}\Big(\tilde{\rho}_{n-1}^- - 1 - \Theta(\tilde{\rho}_n^+ - \tilde{\rho}_{n-1}^-) + \bar{\mathfrak{f}}_n + \bar{\gamma}K_n\Big), \\ J_n^+ = \bar{\kappa}S\Big(\tilde{\rho}_n^+ - 1 - \Theta(\tilde{\rho}_n^+ - \tilde{\rho}_{n-1}^-) + \bar{\mathfrak{f}}_n + \bar{\gamma}K_n\Big). \end{cases} \tag{2.130}$$

2.5 KEY RESULTS

We have derived a thermodynamically consistent generalization of the BCF model for the governing equations of step-flow growth. With our starting point general mass balance laws for the {step+terrace} system, full account is also taken of elasticity in the bulk, at the surface, and at the step, via balance laws for the Newtonian forces and moments. Further, invoking the formalism of *configurational forces*, we introduce a configurational force balance, as postulated by Gurtin (1995) to allow for a unified treatment of problems with multiple phases or defects (e. g., the step line defect separating an upper-terrace adatoms "phase" from the lower-terrace adatoms "phase").

Unlike the prevailing phenomenological approach, we invoke consistency with the second law of thermodynamics, in the form of a free-energy imbalance in the present isothermal setting, to prescribe appropriate constitutive laws relating the thermodynamic fluxes to the associated thermodynamic forces. In particular, we obtain the kinetic relation linking the step velocity to the associated driving force, which, after substitution back in the configurational force balance at the step, yields the generalized Gibbs–Thomson relation for the step chemical potential:

$$\mu^s = -\frac{1}{a\rho^b}\left(\mathfrak{f} + [\![\omega]\!] + \tilde{\gamma}K - \frac{v_\perp}{b}\right),$$

in the absence of surface stress and line traction. Besides the curvature effect from the classical Gibbs–Thomson relation, this expression states that the step chemical potential differs from its bulk counterpart through three additional contributions, stemming from:

1. the energetics of the global system {crystal monolayer+step+adatom layer} via the coupling of diffusion fields on adjacent terraces $[\![\omega]\!]$,
2. the dissipation related to the nonequilibrium processes underlying the propagation of the step $-v_\perp/b$, akin to kinetic undercooling in solidification problems,
3. the elastic bulk via the elastic fields generated by the steps on the vicinal surface $\mathfrak{f} = \mathbf{n}\cdot\int_s \mathbf{C}\mathbf{n}_{\partial\mathcal{B}}\,\mathrm{d}a$, where $C = \psi^b\mathbf{I} - (\nabla\mathbf{u})^\intercal\mathbf{T}$ is the bulk configurational stress tensor, corresponding to the energy-momentum tensor.

This last contribution generalizes the usual approach in the literature that is often limited to the straight-step setting and assumes a dipole-dipole interaction energy between steps from the outset. Then, for the sake of obtaining explicit expressions, we have followed the standard procedure which consists in replacing the stepped surface by a flat surface with an appropriate surface distribution of forces. Applying the multipole expansion to the displacement field induced by this force distribution, we have shown that in order to recover the classical prediction of a dipolar leading order for the step elastic field, line and surface tension must be neglected as they contribute to the monopolar order.

In addition to these contributions, we have also considered the full effect of dynamics, in contract with the BCF model which relies on the quasistatic approximation, by including the transient term $\partial_t\rho$ in the reaction diffusion equation and the *convective* terms $\rho^+ v_\perp$ and $\rho^- v_\perp$ in the boundary conditions.

3

STEP BUNCHING NONLINEAR EVOLUTION

In this chapter, we analyze the nonlinear evolution of a vicinal surface after the onset of the step-bunching instability, specialized to the case without electromigration ($\bar{e} = 0$).

The numerical resolution process and obtained scaling laws are presented in Section 3.2. After taking the discrete-to-continuum limit of the continuum step model in Section 3.3, the resulting nonlinear PDE is used to derive analytical scaling laws in Section 3.4.

3.1 REVIEW OF EXISTING THEORIES

Computing the evolution of the surface profile past the onset of instability is a challenging task. Indeed, the system of governing equations for step-flow growth is a nonlinear coupled free-boundary problem that needs to be solved to large times, for a large number of steps, in order to establish the relevant coarsening laws for the surface. Nonlinear simulations of discrete systems like (2.120) have been carried out in numerous works—e. g., Natori (1994), Sato and Uwaha (1999b), and Chang et al. (2006) with electromigration; Misbah and Pierre-Louis (1996), Sato et al. (2000a), and Krug et al. (2005) without. However, with two exceptions (Gillet, 2000; Ranguelov and Stoyanov, 2007), these analyses are performed under the quasistatic approximation, whereby the dynamical terms $\partial_t \rho_n$ in $(2.120)_1$, $-\rho_n^- v_{n+1}$ in $(2.120)_2$, and $-\rho_n^+ v_n$ in $(2.120)_3$ are deemed negligible for a slow enough deposition rate, i. e., $|\overline{F} - \bar{v}|\Theta \ll 1$ (Michely and Krug, 2012). Under this assumption, the simulation process is greatly simplified as it becomes possible to derive a closed-form expression for the adatom density field. As a result, letting $\mathbf{X} := \{x_n\}_{n\in\mathbb{N}}$, the behavior of the surface can be described by a system of coupled ordinary differential equations of the form:

$$\frac{d\mathbf{X}}{dt} = f(\mathbf{X}). \tag{3.1}$$

which can readily be integrated with conventional time-stepping schemes. However, Guin et al. (2020, 2021a) recently showed that this approximation is erroneous and unjustified: even for a vanishing growth rate, the dynamical effect plays an essential role in the stability of the system. In addition, the classical model also ignores the chemical effect which, again, was shown to have a notable impact on stability (Cermelli and Jabbour, 2007; Guin et al., 2021b).

We now briefly review the two existing works that include the effects of dynamics in the nonlinear simulations of step bunching. Ranguelov and Stoyanov (2007) address the problem of step dynamics in the simplified framework of infinitely fast terrace diffusion ($\mathcal{D} \to \infty$), which allows them to consider a

constant adatom density across a terrace, and slow attachment/detachment kinetics ($\bar{\kappa} \ll 1$). Further, they neglect the advective contribution of the dynamics terms and solely focus on the transient term in the diffusion equation. More precisely, looking at the system in the comoving frame (i. e., introducing the change of variables $\hat{x} = x - x_n$ and $\rho_n(x,t) = \hat{\rho}_n(\hat{x},t)$), the partial time derivative $\partial_t \rho_n$ becomes $\partial_t \hat{\rho}_n - \dot{x}_n \partial_{\hat{x}} \hat{\rho}_n$. We refer to the first term $\partial_t \hat{\rho}_n$ as the transient contribution and to the second term $-\dot{x}_n \partial_{\hat{x}} \hat{\rho}_n$, grouped with the terms $-\rho_n^- \dot{x}_{n+1}$ and $-\rho_n^+ \dot{x}_n$ in the boundary conditions, as the advective contribution. In our simulations, no such approximations are introduced: there is no constraints on the model parameters, all the dynamics terms are considered, and the adatom density profile is resolved during the numerical integration. Additionally, although several snapshots of their numerical simulations are presented, they are essentially illustrative and only aim at highlighting the presence of step-density compression waves, which is the main focus of their work.

As part of his thesis, Gillet (2000) uses spatiotemporal Green functions to solve the integral version of the reaction-diffusion equation, including all the dynamics terms. Following this formalism, the adatom density field is calculated at each time step, and then serves to compute the velocity of steps through the interface motion equation $(2.120)_4$. However, as the main motivation behind his work is the continuum limit of the discrete system of equations, the numerical simulation of the latter is limited to one example with minimal discussion.

In contrast, we strive to conduct simulations over a wide range of parameters which allows us to establish the scaling laws with respect to all model parameters and show the robustness of the power-law coarsening with time. Further, it offers a ground for comparison with the continuum limit, which requires additional assumptions to be derived whose validity can be checked against the discrete simulations. On a final note, neither work take into account the chemical effect, which we include in our analysis given its proven impact on stability.

In view of the existing literature which extensively resorts to the quasistatic approximation and the almost nonexistent works on simulations of the discrete system including the dynamics terms, our objective is to propose a comprehensive overview of step bunching on a vicinal surface, including the dynamical and chemical effects. The results of this extensive simulation process are presented in section Section 3.2. General scaling laws are extracted with respect to each model parameter. Furthermore, in Appendix D, with the aim of completing the general analysis, we estimate for Si(111) values and ranges of the physical parameters, aggregated from several experimental works. On that basis, we show quantitatively in section Section 3.3 that the dynamical effect can explain step bunching without recourse to the debated existence of an inverse Ehrlich-Schwoebel effect.

3.2 NONLINEAR SIMULATIONS OF THE DISCRETE SYSTEM

3.2.1 *One-dimensional equations*

Quantitative studies of step bunching in the absence of electromigration (Omi et al., 2005) are conducted at such temperatures ($< 900^{\circ}$C) that evaporation can be safely neglected (Alfonso et al., 1993; Jung et al., 1994; Cohen et al., 2002). Moreover, since we are concerned in this chapter with the step-bunching instability, which is one-dimensional by essence, we specialize the general system (2.129) and (2.130) derived in Chapter 2 to the case of straight steps in the pure deposition regime with no electromigration:

$$\begin{cases} \chi_a \ell_n^2 \partial_t \tilde{\rho}_n = \partial_{uu}\tilde{\rho}_n + \chi_a \ell_n (\dot{x}_n + \dot{\ell}_n u)\partial_u \tilde{\rho}_n + \ell_n^2(\overline{F} - \bar{\nu}\tilde{\rho}_n), \\ J_{n+1}^- = -\chi_a \rho_n^- \dot{x}_{n+1} - \dfrac{1}{\ell_n}(\partial_u \tilde{\rho}_n)^-, \\ J_n^+ = \chi_a \rho_n^+ \dot{x}_n + \dfrac{1}{\ell_n}(\partial_u \tilde{\rho}_n)^+, \\ \dot{x}_n = \Omega(J_n^+ + J_n^-). \end{cases} \tag{3.2}$$

with

$$\begin{cases} J_n^- = \bar{\kappa}\Big(\tilde{\rho}_{n-1}^- - 1 - \chi_c \Omega(\tilde{\rho}_n^+ - \tilde{\rho}_{n-1}^-) + \bar{\mathfrak{f}}_n\Big), \\ J_n^+ = \bar{\kappa} S\Big(\tilde{\rho}_n^+ - 1 - \chi_c \Omega(\tilde{\rho}_n^+ - \tilde{\rho}_{n-1}^-) + \bar{\mathfrak{f}}_n\Big), \end{cases} \tag{3.3}$$

where we have introduced χ_c and χ_a to follow the impact of the chemical and dynamical effect respectively, so that the standard BCF model corresponds to $\chi_a = \chi_c = 0$ and the full model to $\chi_a = \chi_c = 1$.

For straight steps, the expression for $\mathfrak{f}_n$ is widely available (Marchenko and Parshin, 1980; Stewart et al., 1994; Tersoff et al., 1995) and reads:

$$\mathfrak{f}_n = \frac{a^2}{k_B T \mathcal{L}_0^3} \sum_{r \in \mathbb{Z}^*} \frac{-\alpha_0}{(x_{n+r} - x_n)^3} = \sum_{r \in \mathbb{Z}^*} \frac{-\bar{\alpha}_0}{(x_{n+r} - x_n)^3}, \tag{3.4}$$

where the coefficient α_0 accounting for the dipole-dipole interactions between step is computed in Section 4.2.2. In the context of a numerical study, the infinite sum has to be truncated, and we substitute $\bar{\mathfrak{f}}_n$ with $\bar{\mathfrak{f}}_n(R)$, the step-step interaction of the R nearest neighbors of step n, i. e.,

$$\bar{\mathfrak{f}}_n(R) = \sum_{r \in \{-R,\dots,R\} \setminus 0} \frac{-\bar{\alpha}_0}{(x_{n+r} - x_n)^3}. \tag{3.5}$$

3.2.2 *Numerical method*

The resolution of a free boundary problem may be approached two ways. One may directly solve the discrete system of equations via classical numerical

schemes (such as finite differences or finite elements), tracking explicitly the moving domain boundaries (i. e., the step fronts). Even though this approach is straightforward for a one-dimensional system, it remains computationally expensive due to the size of the system needed to mitigate finite size effects and the coupling between terraces introduced by the chemical effect. A fair amount of optimization is thus required to reach large simulation times for reasonable computation times. As a result, an extension to a two-dimensional treatment seems prohibitively intensive. In that regard, we mention the work of Bänsch et al. (2004) on the simulation of island evolution, who propose an adaptive finite-element method with two independent meshes and element marking.

The second approach relies on the phase-field theory, whereby step flow is governed by a system of two coupled partial differential equations (PDE) for a global adatom density field and an order parameter (the phase field). The latter is constant on the terraces but varies rapidly inside narrow transition regions around the steps (Otto et al., 2003), which allows to forgo explicit tracking of the fronts, thereby alleviating the computational cost (Liu and Metiu, 1994). The main feature of the phase-field model is that it automatically captures such topological changes as island nucleation or step coalescence, making it particularly efficient at predicting the evolution of island shapes in two space dimensions (Torabi et al., 2009; Hu et al., 2012). However, in the present one-dimensional setting and in the absence of nucleation and coalescence, the phase-field model is not more advantageous than the direct numerical resolution of the sharp-interface free boundary problem (3.2).

Therefore, in order to simulate the evolution of a sufficient number of steps while retaining the transient and advective terms in the free boundary problem, we use finite elements to discretize the terraces by the Galerkin method, and solve for the adatom densities and the step positions concomitantly. As we have to work with a finite system numerically, we need to specify the boundary conditions at the edges of the system. Periodic boundary conditions are imposed such that $x_{N_s+1} = x_1 + N_s$, where N_s is the number of steps simulated in the system. Regarding the initial condition, two different configurations are used. Under *natural bunching conditions*, the integration is initiated from a vicinal surface with 500 steps whose deviation from their equidistant equilibrium position follows a uniform distribution in $[-0.1, 0.1]$. After the onset of instability, the surface profile consists of many bunches separated by large terraces (Figure 3.8), whose characteristic length scales coarsen with time. Under *forced bunching conditions*, a number of steps (from 10 to 200) are initially placed in close proximity ($\forall n,\ \ell_n = 0.1$ is arbitrarily chosen) so that, as time progresses, they will relax towards a stable arrangement, providing the actual quasisteady bunch shape.

In the next sections, we review the finite element formulation, and present the results of the two convergence tests that were used to optimize the number of elements per terrace and number of neighbors included in the computation of the step-step elastic interaction.

3.2.2.1 *Discretization using the Galerkin method*

The system is discretized in space following the classical Galerkin method. We multiply $(3.2)_1$ by a weight function ϕ and integrate:

$$\begin{aligned}\int_0^1 (\partial_t\tilde{\rho}_n)\phi\,\mathrm{d}u = \frac{1}{\ell_n^2}\int_0^1 (\partial_{uu}\tilde{\rho}_n)\phi\,\mathrm{d}u + \frac{\dot{x}_n}{\ell_n}\int_0^1 (\partial_u\tilde{\rho}_n)\phi\,\mathrm{d}u \\ + \frac{\dot{\ell}_n}{\ell_n}\int_0^1 (u\,\partial_u\tilde{\rho}_n)\phi\,\mathrm{d}u + \overline{F}\int_0^1 \phi\,\mathrm{d}u.\end{aligned} \tag{3.6}$$

Next, integrating by parts the term with the double derivative:

$$\begin{aligned}\int_0^1 (\partial_t\tilde{\rho}_n)\phi\,\mathrm{d}u = \frac{1}{\ell_n^2}\Big[(\partial_u\tilde{\rho}_n)\phi\Big]_0^1 - \frac{1}{\ell_n^2}\int_0^1 (\partial_u\tilde{\rho}_n)\phi'\,\mathrm{d}u \\ + \frac{\dot{x}_n}{\ell_n}\int_0^1 (\partial_u\tilde{\rho}_n)\phi\,\mathrm{d}u + \frac{\dot{\ell}_n}{\ell_n}\int_0^1 (u\,\partial_u\tilde{\rho}_n)\phi\,\mathrm{d}u + \overline{F}\int_0^1 \phi\,\mathrm{d}u.\end{aligned} \tag{3.7}$$

Finally, introducing the number of nodes per terrace N and shape functions φ_μ,[1] we write

$$\tilde{\rho}_n(u,t) = \sum_{\mu=1}^{N} \breve{\rho}_n^{(\mu)}(t)\varphi_\mu(u) \tag{3.8}$$

and substitute ϕ for an arbitrary φ_ν in (3.7) to obtain the following system at the nth terrace ($n \in \mathbb{N}^*$):

$$\mathbf{M}\dot{\breve{\rho}}\big|_n = \mathbf{A} - \frac{1}{\ell_n^2}\mathbf{D}^{(2)}\breve{\rho}\big|_n + \frac{\dot{x}_n}{\ell_n}\mathbf{D}^{(1)}\breve{\rho}\big|_n + \frac{\dot{\ell}_n}{\ell_n}\mathbf{D}^{(u)}\breve{\rho}\big|_n + \overline{F}\mathbf{B}, \tag{3.9}$$

where $\breve{\rho}\big|_n = \{\breve{\rho}_n^{(\mu)}\}_{\mu\in\{1,\dots,N\}}$. From the boundary conditions $(2.129)_{2,3}$,

$$\begin{aligned}A_\mu =& \frac{1}{\ell_n^2}\Big[(\partial_u\tilde{\rho}_n)\varphi_\mu\Big]_0^1 \\ =& \frac{1}{\ell_n}\Big(-J_{n+1}^- - \tilde{\rho}_n^-\dot{\tilde{x}}_{n+1}\Big)\varphi_\mu(1) - \frac{1}{\ell_n}\Big(J_n^+ - \tilde{\rho}_n^+\dot{\tilde{x}}_n\Big)\varphi_\mu(0),\end{aligned} \tag{3.10}$$

and

$$\begin{cases} M_{\mu\nu} = \displaystyle\int_0^1 \varphi_\mu(u)\varphi_\nu(u)\,\mathrm{d}u, \\ D_{\mu\nu}^{(2)} = \displaystyle\int_0^1 \varphi'_\mu(u)\varphi'_\nu(u)\,\mathrm{d}u, \\ D_{\mu\nu}^{(1)} = \displaystyle\int_0^1 \varphi_\mu(u)\varphi'_\nu(u)\,\mathrm{d}u, \\ D_{\mu\nu}^{(u)} = \displaystyle\int_0^1 u\varphi_\mu(u)\varphi'_\nu(u)\,\mathrm{d}u, \\ B_\mu = \displaystyle\int_0^1 \varphi_\mu(u)\,\mathrm{d}u. \end{cases} \tag{3.11}$$

1 We use Greek letters to denote indices in $\{1,\dots,N\}$, and lower case letters for indices in $\{1,\dots,N_s\}$.

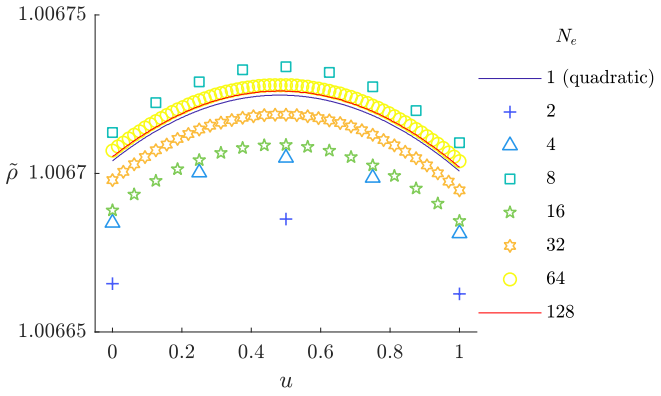

Figure 3.1: Adatom concentration profiles for different values of N_e.

Note the $1/\ell_n^2$ factor associated to $\mathbf{D}^{(2)}$. Once the instability is triggered and steps start coalescing, the terrace width ℓ_n will, by definition, become greatly reduced in the bunches and thus $1/\ell_n^2$ will take extremely high values. As a result, equation (3.9) is a stiff equation which requires special attention to be efficiently integrated. For instance, the commonly used $4th$ order Runge–Kutta explicit scheme will fail as the time step required to maintain the solution's accuracy becomes prohibitively small. Instead, an implicit scheme must be used. We rely on Julia's implementation of Sundials' CVODE routine with Backward Differentiation Formula, which implements a variable step, variable order, multistep method (*The Julia Programming Language* n.d.; *CVODE Solver Description* n.d.).[2] With an implicit scheme, the time steps may be taken much larger than with an explicit scheme, at the cost of more computationally intensive operations at each time step. Indeed, proceeding to the next time step typically requires the computation of the jacobian matrix of the system and its inversion. While the jacobian may be computed numerically with relative efficiency, the associated additional cost for large systems like the one we are interested in would still make the simulations excessively long. To circumvent this issue, we derive the jacobian analytically (see Appendix E) and provide it to the solver for a dramatic increase of the simulation speed.

3.2.2.2 *Convergence analysis*

For a complete optimization of the resolution process, we further need to determine (i) the minimum number of elements per terrace N_e in the finite element discretization, and (ii) the minimum number of nearest neighbors R that need to be included in the calculation of the elastic interaction $\bar{f}_n(R)$, to make the numerical resolution as fast as possible while retaining a good accuracy. All simulations in this section are run with the set of parameters: $\overline{F} = 10^{-4}$, $\bar{\nu} = 0$, $\Theta = 0.02$, $\bar{\kappa} = 10^{-2}$, $\bar{\alpha}_0 = 10^{-5}$, motivated by experimental values for Si (see Appendix D).

2 Matlab's `ode15s` is also used for the preliminary convergence tests

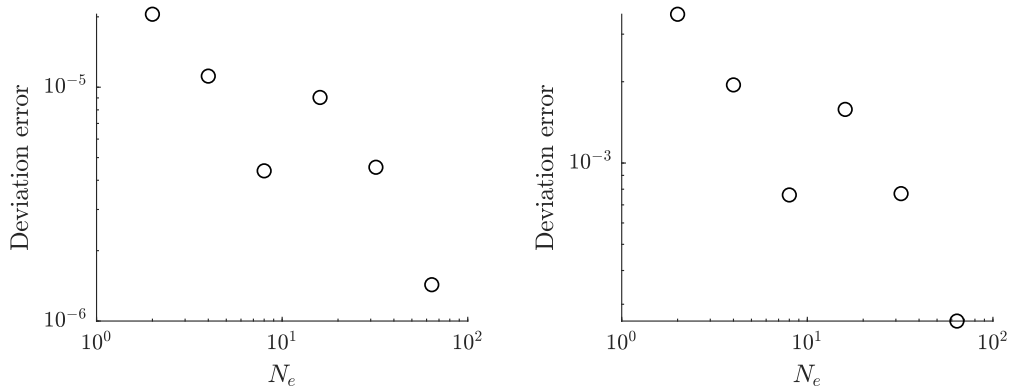

(a) Deviation error of the adatom density field.

(b) Deviation error of the step positions.

Figure 3.2: Dependence on N_e of the deviation error of (a) the adatom density field and (b) the step positions.

NUMBER OF ELEMENTS PER TERRACE We study the convergence with mesh refinement by running simulations under natural bunching conditions, where each terrace is discretized with 2^n elements for $n \in \{1, ..., 7\}$ and a linear shape function is used. An additional simulation is also run where each terrace consists of only one element but a quadratic shape function is used. The results presented are obtained after simulating the deposition of 500 monolayers. The adatom density fields and step positions are used to analyze convergence. As can be checked visually from Figure 3.1, all simulations give extremely close results. Using the simulation with the finest discretization ($N_s = 128$) as reference to obtain quantitative error estimates, we plot the deviation error of the adatom density field and the step positions in Figure 3.2, where we define the deviation error between two functions or vectors as the euclidean norm of their difference.

Because the output of the simulations also depends on the time integration, it is not surprising that the error is not monotonously decreasing. In fact, the time integration algorithm automatically adjusts the time steps to maximize their amplitude while maintaining the integration error below a set threshold. The point of this section is to show that the time stepping error dominates the space discretization error. Indeed, notice that even in the coarsest case, the error remains extremely small, of the order of 2×10^{-5} for the adatom density fields and 3.5×10^{-3} for the step positions, which are the crucial variables for the ulterior study of the coarsening of step bunches. Given that the bunch characteristic length scales are typically of order 10^{-1} and above, we conclude that mesh refinement is unnecessary. Additionally, in terms of computation times, simulations with the linear shape function and the coarsest mesh (two elements, three degrees of freedom per terrace) take as much time to complete as simulations with the quadratic shape function (one element, three degrees of freedom per terrace). Since a parabolic adatom density profile represents the exact solution in the quasistatic case and an approximation to $\mathcal{O}(\mathcal{P}^2)$ in

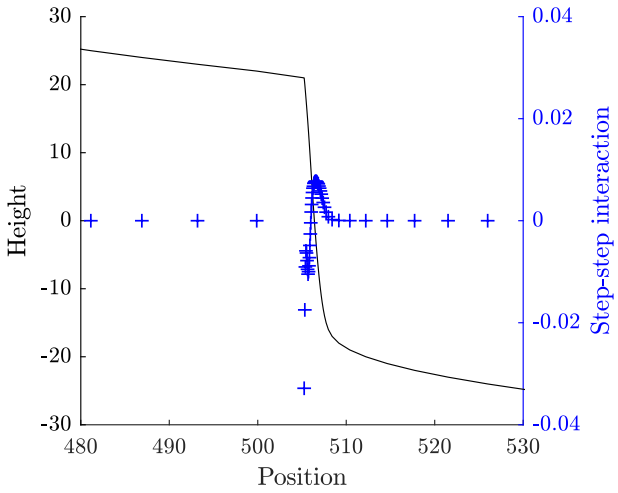

Figure 3.3: Superposition of the bunch profile (left axis, black) with the step-step elastic interaction (right axis, blue). There is virtually no interaction outside the bunched region.

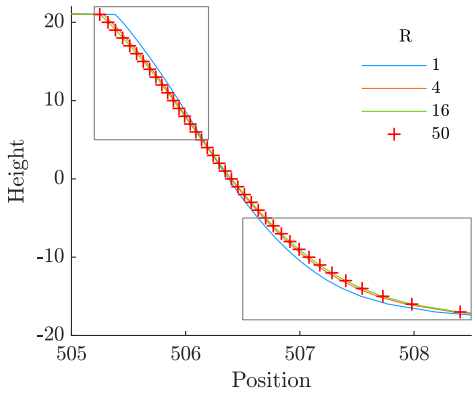

(a) General view of the bunch.

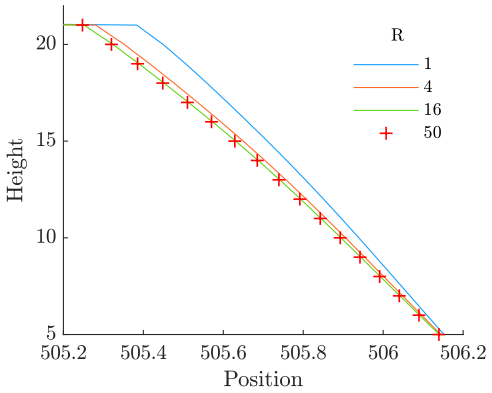

(b) Zoom on the upper edge of the bunch.

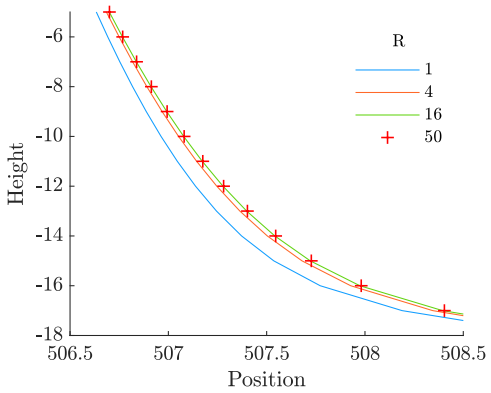

(c) Zoom on the lower edge of the bunch.

Figure 3.4: The relaxed shape of bunches for different values of R.

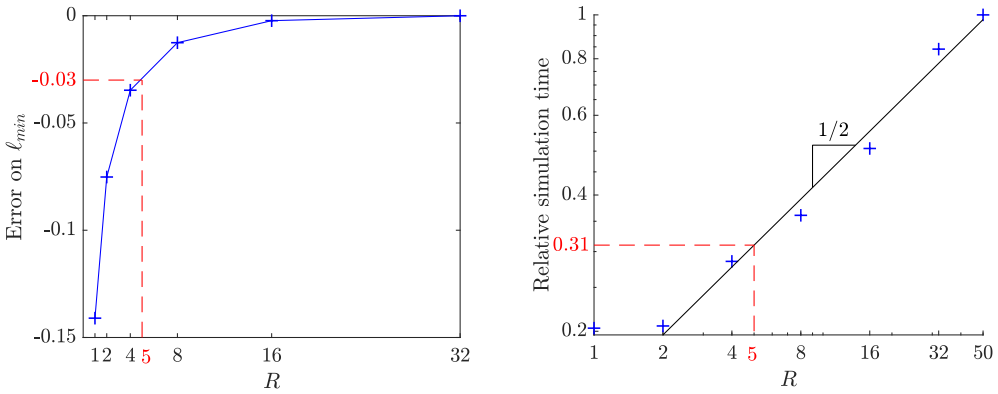

(a) Deviation error on ℓ_{min} (b) Computational cost

Figure 3.5: Dependence on R of (a) the deviation error on ℓ_{min} and (b) the computational cost.

the complete case, we favor the 1-element per terrace discretization with a quadratic shape function to conduct all the simulations presented in this work.

NUMBER OF ELASTICALLY INTERACTING STEPS R To determine the cutoff R on the infinite sum, i. e., the number of nearest neighbors considered in the calculation of the elastic interaction, we run simulations under forced bunching conditions with 50 steps. We focus our attention on a mature bunched morphology and not the initial small bunches because the elastic repulsion scales as the cube of the inverse of the distance between steps, which means that outside of bunches, where steps are far apart, the elastic interactions are negligible (Figure 3.3).

A visual comparison of the bunch profiles for $R = 1$, $R = 4$, $R = 16$, and $R = 50$, suggests that R has a discernible influence on the bunch shape (Figure 3.4). To quantify the difference, we plot the minimal interstep distance in the bunch ℓ_{min} against R (Figure 3.5). ℓ_{min} quickly reaches an asymptote, such that for $R = 9$, the deviation from the asymptotic value (estimated from the case $R = 50$) is less than 1%. Note that as expected, ℓ_{min} increases with R: including more neighbors in the calculation of the elastic repulsion increases its intensity and therefore causes steps to stay further apart. Additionally, we also compare the computational cost of the simulations for the different values of R, and find that it scales as $\sqrt{R}$ (Figure 3.5).

In conclusion, all simulations presented in this work are conducted using only the five nearest neighbors as a good compromise between accuracy and computational strain. Indeed for $R = 5$, the values for ℓ_{min}, whose scaling we ultimately want to establish, are within 3% of the asymptotic value while the simulations run three times faster, compared to the case $R = 50$.

In all the displayed figures, we use the normalized time $\bar{t} = \mathcal{P}t$, which amounts to measuring time in terms of the number of monolayers deposited, thus removing the dependence on the deposition rate. An example of the formation and evolution of step bunches is shown in the spatiotemporal diagram of Figure 3.6, where each line represents a step trajectory. The lines are initially

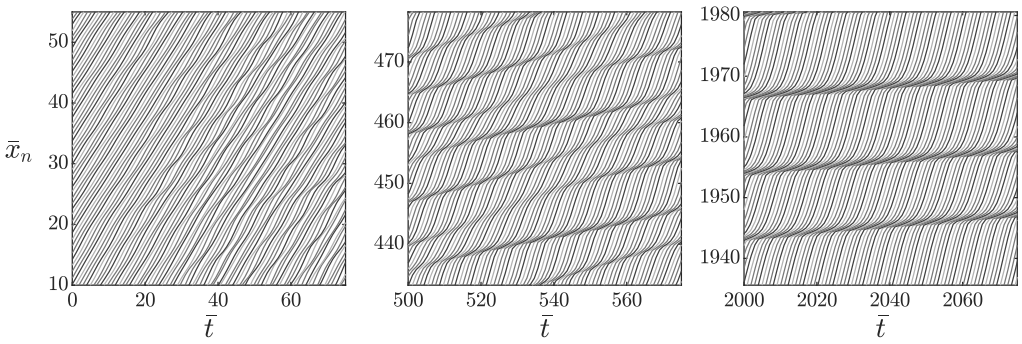

Figure 3.6: Spatiotemporal evolution of a vicinal surface with 500-step periodicity. Each line is a step trajectory. Only 45 steps are shown for clarity. Parameters: $S = 1$, $\Theta = 0.02$, $\overline{F} = 10^{-4}$, $\bar{\kappa} = 10^{-2}$, and $\bar{\alpha}_0 = 10^{-5}$.

straight and parallel as the steps propagate at a constant velocity corresponding to the steady-state solution, until the instability develops (visible already after 20 monolayers) and the lines swerve towards each other as steps start to coalesce. At later times, the bunched structure is clearly visible. Note that step bunching is a dynamic process: a bunch is not a fixed entity which contains identifiable steps, as can be the case under certain electromigration conditions (Sato and Uwaha, 1999b; Homma and Aizawa, 2000; Toktarbaiuly et al., 2018), but rather continually emits and receives steps to and from neighboring bunches, which we refer to as *crossing steps*. Moreover, the number of bunches decreases as they increase in size: this is a direct manifestation of the coarsening process. Finally, bunches move much slower than steps, with a seemingly inverse correlation between their velocity and size.

We also take this opportunity to compare our nonlinear simulations of step dynamics to the linear stability predictions of Guin et al. (2020, 2021a). We focus on the two sets of parameters $(\overline{F}_A, \bar{\kappa}_A) = (10^{-4}, 10^{-1})$ and $(\overline{F}_B, \bar{\kappa}_B) = (10^{-3}, 10^{-1})$, with $S = 1$, $\Theta = 0.02$, $\bar{\alpha}_0 = 10^{-5}$, for which the linear stability analysis predicts the most unstable modes are $k = 0.8335$ and $k = \pi$, respectively. Running the simulations for each set of parameters, we show in Figure 3.7(a) and (b) typical spatiotemporal diagrams of the quantity $x_n - \mathcal{P}t$, i. e., the step positions relative to the steady-state solution. From the spatiotemporal diagram of A, it is quite evident that the most unstable mode is one of step pairing, corresponding to the theoretical prediction of $k = \pi$. Regarding the spatiotemporal diagram of B, it is easy to deduce that the most unstable mode is not step pairing, but determining the actual wavenumber is not immediate. Introducing the average separation Λ between the extrema of $x_n - n - \mathcal{P}t$, i. e., the deviation of the steps from the principal solution, we may calculate k as follows:

$$k = \frac{2\pi}{\Lambda}. \tag{3.12}$$

After averaging over 100 runs (see Figure 3.7(c)), we again find excellent agreement between the numerical simulations $k \simeq 0.83$ and the theoretical prediction $k = 0.8335$, which comforts the validity of both.

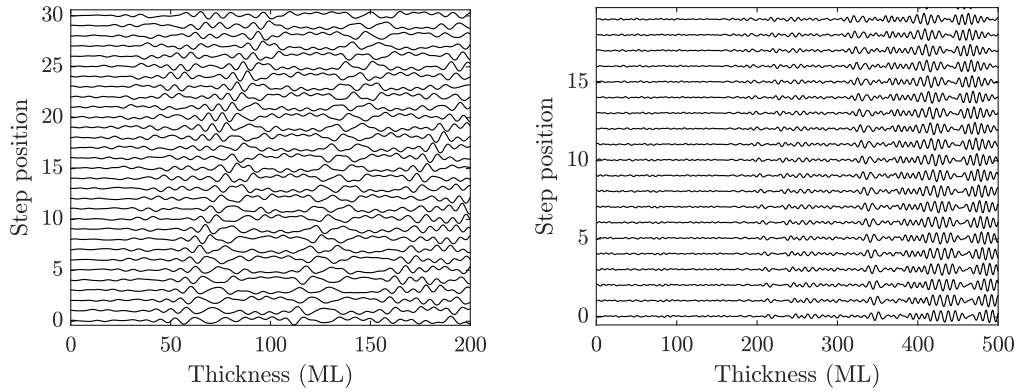

(a) $(\overline{F}, \bar{\kappa}) = (10^{-3}, 10^{-1})$ (b) $(\overline{F}, \bar{\kappa}) = (10^{-4}, 10^{-1})$

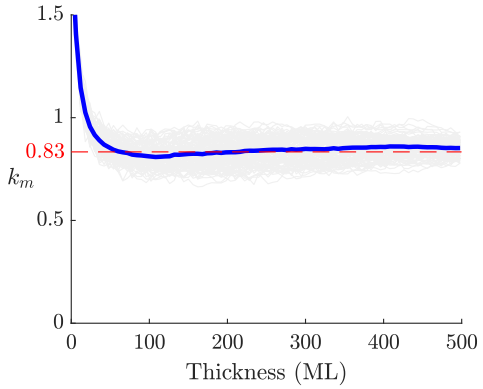

(c) Most unstable wavenumber k computed from the simulations

Figure 3.7: Comparison of the predictions for the most unstable mode from the linear stability analysis and the numerical simulations. (a) and (b) spatiotemporal diagrams of the steps, and (c) most unstable wavenumber computed from the numerical simulations. Parameters: $S = 1$, $\Theta = 0.02$, $\bar{\alpha}_0 = 10^{-5}$.

3.2.3 *Coarsening behavior*

3.2.3.1 *Bunch parameters*

Before proceeding with the quantitative analysis of the coarsening process, we introduce some characteristic parameters to describe the bunched surface. A difference is made between a *bunch*, which corresponds to the high step-density region only, and a *bunch cell*, which comprises a bunch and the terraces running to the next bunch. We denote H the height and W the width of a bunch, ℓ_{min} and ℓ_{max} the narrowest and widest terrace on the surface, and N the number of steps in a bunch cell, which corresponds to the distance between bunches in units of $\mathcal{L}_0$, as shown in Figure 3.8. Since vicinality requires the average slope of the surface to remain constant, $H \sim N$.

Among these parameters, we choose to focus on the scaling of H with $\bar{t}$ and the scaling of ℓ_{min} with N, as they are the most reliable indicators and can be easily computed from theoretical models for comparison. Indeed, monitoring

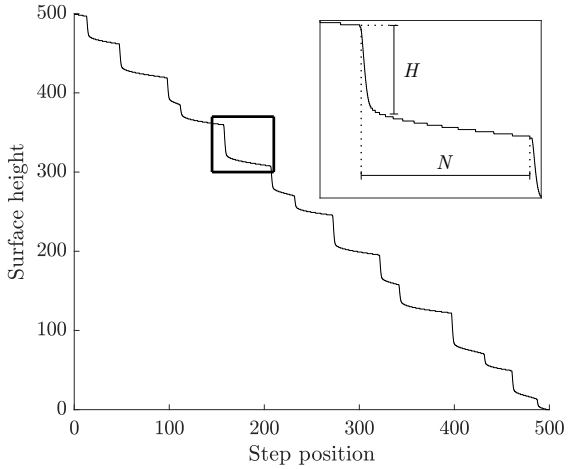

Figure 3.8: Height profile of a surface with 500 steps after deposition of 3×10^4 monolayers. Same parameters as those of Figure 3.6. H is the bunch height and N the distance separating two bunches.

the evolution of bunches requires the introduction of an arbitrary threshold on the interstep distance, which determines whether steps belong to the same bunch or not. While some quantities (e.g., ℓ_{min} and ℓ_{max}) are independent of any threshold, others (e.g., H and W) are sensitive to this choice, especially so because of the asymmetrical distribution of crossing steps between bunches. While there is an abrupt change in the terrace length at the upper edge of the bunch, making the transition with the low step-density region clear cut, at the lower edge, steps gradually depart from the bunch, blurring this transition zone, as observed in Figure 3.8.[3] This asymmetrical distribution of steps around a bunch is not specific to our thermodynamically consistent model. It is also observed in the case of ES-triggered step bunching under evaporation (Krug et al., 2005), in the generic model of Slanina et al. (2005) where the step velocity is a linear combination of the neighboring terrace widths, and in the Cellular Automaton-based model of Krzyżewski et al. (2017).

We verify however that the bunch height is only weakly impacted: as all steps have the same height, the total bunch height is not dramatically modified by a few additional steps at the boundaries of the bunch, especially for large bunches. On the other hand, since terraces further from the bunch center are much wider than terraces close to it, the same additional steps have a considerable impact on the total bunch width. Hence, W is strongly conditioned by the choice of threshold and cannot serve as a reliable indicator of the coarsening process in the presence of crossing steps. Lastly, as the distance between two bunches can be precisely determined as the distance between their respective sharp edges, N is also a robust quantity.

3 This hold true under net deposition conditions. Under net evaporation conditions, the "sharp" and "blurred" edges are reversed.

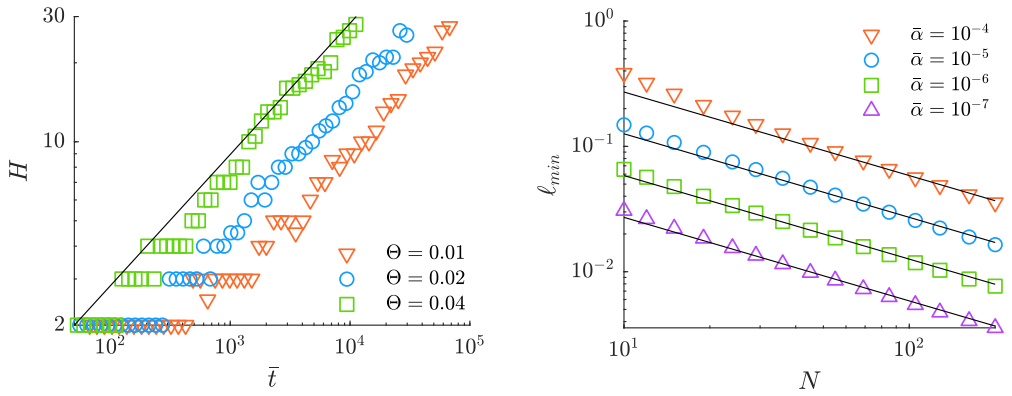

(a) Bunch height H (b) Minimal interstep distance ℓ_{min}

Figure 3.9: Scaling laws for (a) the bunch height H with time $\bar{t}$, and (b) the minimal interstep distance ℓ_{min} with N. The black trend line shows the theoretical predictions $H \sim t^{1/2}$ and $\ell_{min} \sim N^{-2/3}$. Same parameters as those of Figure 3.6.

3.2.3.2 *Scaling laws*

The typical evolution of $H(\bar{t})$ and $\ell_{min}(N)$ are plotted in Figure 3.9, where steps are considered as bunched when their distance is smaller than the initial terrace width (Tonchev, 2012). It is interesting to comment on the nondimensional physical parameters of our model. Based on experiments (Chung and Altman, 2002; Ichimiya et al., 2000), the kinetics of deposition on Si(111) at low temperatures (less than 900°C) is expected to be kinetic-limited ($\bar{\kappa} \ll 1$) for miscut angles greater than 0.2°, and we thus restrict the parameter space to $\bar{\kappa} \leqslant 10^{-1}$. To obey the near-equilibrium hypothesis, additional restrictions are necessary. From the steady-state solution of (3.2), the maximum departure of the adatom density from its equilibrium value can be estimated as $\max(\overline{F}/8, \overline{F}/\bar{\kappa})$ so that the near-equilibrium hypothesis imposes $\overline{F} \ll 10$ and $\overline{F} \ll \bar{\kappa}$. Hence, the latter condition being more restrictive here, $\overline{F} \leqslant \bar{\kappa}/10$ is assumed in our simulations.

In addition, due to the low temperatures, we assume a low equilibrium adatom coverage $\Theta = 0.02$. This value is conservatively low in the sense that it minimizes the strength of the dynamical and chemical effects, as their associated growth rates scale as Θ^2 compared to Θ for the other mechanisms (see Guin (2018) and Chapter 4). Indeed, estimates from the literature place this value closer to 0.04 for Si (Yang and Williams, 1994) and as high as 0.2 for GaAs (Johnson et al., 1996). Finally, the elastic coefficient is set to $\bar{\alpha}_0 = 10^{-5}$. With these restrictions, systematic simulations were conducted every decade for $\overline{F}$ from 10^{-5} to 10^{-2} and $\bar{\kappa}$ from 10^{-4} to 10^{-1}. Additional simulations were conducted with $\overline{F} = 10^{-4}$ and $\bar{\kappa} = 10^{-2}$ for various values of Θ and $\bar{\alpha}_0$ in order to ascertain the scaling with respect to these parameters. From all the simulations

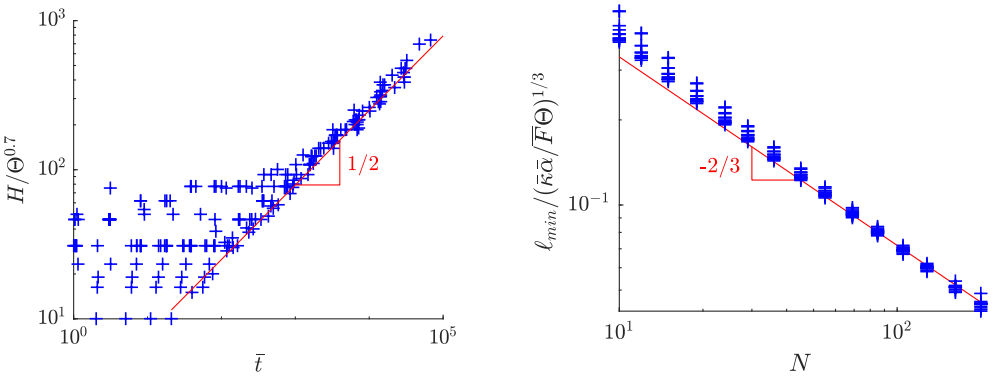

(a) Rescaled bunch height $H/\Theta^{0.7}$ (b) Rescaled minimal interstep distance $\ell_{min}/(\bar{\kappa}\bar{\alpha}_0/\overline{F}\Theta)^{1/3}$

Figure 3.10: Dependence of the rescaled quantities (a) $H/\Theta^{0.7}$ on $\bar{t}$, and (b) $\ell_{min}/(\bar{\kappa}\bar{\alpha}_0/\overline{F}\Theta)^{1/3}$ on N. The theoretical trend lines and their slopes are shown in red.

performed, robust scaling laws emerge, and we find, in the absence of any ES barrier ($S=1$):

$$\begin{cases} H \simeq 2.5\Theta^{0.7\pm0.05}\,\bar{t}^{1/2}, \\ \ell_{min} \simeq 1.55\left(\dfrac{\bar{\kappa}\bar{\alpha}_0}{\overline{F}\Theta}\right)^{1/3} N^{-2/3}. \end{cases} \tag{3.13}$$

The rescaled quantities $H/\Theta^{0.7}$ and $\ell_{min}/(\bar{\kappa}\bar{\alpha}_0/\overline{F}\Theta)^{1/3}$ are plotted in Figure 3.10. Note how, regardless of the physical parameters, all the curves merge into a universal trend.

Systematic quantitative experiments on coarsening without electromigration are scarce. Of the three studies found in the literature, one concerns Si(001) (Schelling et al., 2000), on which adatom diffusion is strongly anisotropic, and another concerns GaAs(001) (Ishizaki et al., 1996), where the surface is grown by metalorganic vapor phase epitaxy, so that precursor interactions need to be taken into account. Since we are interested in investigating the influence of the dynamical and chemical effects on the step bunching instability, effects that are basic to step flow in the sense that they are present irrespective of whether adatom diffusion is anisotropic or not and whether chemical reaction between distinct species occur or not, we only consider Si(111) (Omi et al., 2005), which is the ideal candidate to test our model due to its isotropy and weak (or absent) ES barrier. On this surface, the bunch height and width were monitored and found to grow as t^β and $t^{1/\alpha}$ with $\beta = 0.49\pm0.09$ and $1/\alpha = 0.54\pm0.08$. In the framework of universality classes based on the classical BCF model (Pimpinelli et al., 2002), the destabilizing mechanism leading to the closest match ($\beta=1/\alpha=1/2$) is the iES effect, whose existence remains controversial (Pimpinelli and Videcoq, 2000; Vladimirova et al., 2001; Slanina et al., 2005), with contradictory experimental results (Voigtländer et al., 1995; Ichimiya et al., 1996; Chung and Altman, 2002; Rogilo et al., 2013). Importantly, our simulations of the thermodynamically consistent model reproduce the bunch height scaling

($\beta = 1/2$) without recourse to an iES ($S = 1$). In other words, by accounting for all the necessary mechanisms without *a priori* assumptions, we are able to explain experimental results in a unified framework, without the need to introduce additional effects.

Since there are no experimental studies for the scaling of ℓ_{min} in the absence of electromigration, we are not able to test our prediction. However, we note that the exponent we find is identical to the one obtained in the simulations of Popkov and Krug (2005).

3.3 CONTINUUM EVOLUTION EQUATION

While precious to produce quantitative results, numerical resolutions preclude a more qualitative understanding of the nature of step-bunching. Because the resolution of the discrete system is intractable analytically, the idea is instead to represent the stepped surface profile as a continuous height function, whose temporal evolution is governed by a partial differential equation obtained from taking the continuum limit of the discrete step-flow equations (3.2). This nonlinear PDE that governs the evolution of the surface height allows us to gain insight into the mechanisms responsible for step bunching and explain the coarsening behavior observed in the simulations, by rendering possible the analytical derivation of scaling laws.

3.3.1 *Discrete-to-continuum limit*

We briefly review the different existing works addressing this transition from discrete to continuum. One may employ a general continuum growth equation $\partial_t h = -\nabla j$ (in the absence of desorption from the surface), using system symmetries (Lai and Das Sarma, 1991) or a phenomenological expression (Johnson et al., 1994) to obtain the surface current dependence on the gradients of h. This places step-bunching in a very generic framework of nonlinear models. However, proceeding as such forbids the derivation of the relation between the microscopic and macroscopic parameters.

To remedy that, it is important to start from the microscopic model and homogenize it to a macroscale. In Krug et al. (2005), a hybrid approach is adopted in which the nonlinear elastic repulsion term is treated using a first-order correspondence between finite differences and derivatives, and the remaining terms, which form a linear combination of the adjacent terrace widths in the model considered, are coarse-grained through a Fourier transform (Krug, 1997).

Another way to achieve that is to use the well-known multiscale expansion method. The linear stability analysis yields the characteristic length and time scales, and the distance to the instability threshold serves as the small expansion parameter (Bena et al., 1993; Pierre-Louis et al., 1998; Gillet et al., 2001). This approach is very instructive as it sets the problem in a generic framework (e. g., Kuramoto–Sivashinsky, Korteweg–De–Wries, or Benney, depending on the regime) but we do not consider it here as it relies on a heavy formalism (the multiscale expansion method requires the successive resolution of equations at

increasing orders) that assumes an analytical expansion for the surface height, which needs to be increasingly refined to capture higher-order nonlinearities.

In contrast, in the approach we adopt here following the work of Xiang (2002) and Margetis et al. (2005), the discrete step velocity equation is interpreted as a numerical scheme for a differential equation, with the step height representing the grid constant—in a process reminiscent of the modified equation technique (Warming and Hyett, 1974)—that directly captures the relevant nonlinearities. Further, our derivation incorporates the dynamical and chemical effects, which are unaccounted for in the cited works, and ensures all terms are expanded to the same order in their Taylor-series representation. The expansion is based on the assumption that the terrace widths are small compared to the mesoscopic length scale $\mathcal{L}$ characterizing the spatial variations of step density on the vicinal surface (Margetis and Kohn, 2006). Let $\varepsilon = \ell_0/\mathcal{L}$ be the nondimensional parameter for the Taylor expansion. All functions and their derivatives are assumed to be bounded, i.e., $\mathcal{O}(1)$.

Since the equations of (3.2) constitute a free-boundary problem with time-dependent coefficients that cannot be solved analytically, we will only retain the main *advective* contributions to the dynamical effect, neglecting the transient term $\partial_t \tilde{\rho}_n$ and the velocity difference $\dot{\ell}_n$,[4] so that $(3.2)_1$ reduces to

$$0 = \partial_{uu}\tilde{\rho}_n + \chi_a \ell_n \dot{x}_n \partial_u \tilde{\rho}_n + \ell_n^2 \overline{F}. \tag{3.14}$$

The solution of (3.14) can be expressed as

$$\tilde{\rho}_n(u,t) = \tilde{\rho}_n^+ \varphi_n(u,t) + \tilde{\rho}_n^- \psi_n(u,t) + c_n(u,t), \tag{3.15}$$

where the expressions for $\varphi_n(u,t)$, $\psi_n(u,t)$ and $c_n(u,t)$ are given in Appendix F.

In the boundary conditions $(3.2)_{2,3}$, the chemical effect couples the diffusion fields on adjacent terraces. We use the interface motion equation $(3.2)_4$ to express $\tilde{\rho}_{n+1}^+$ as a function of $\dot{x}_{n+1}$ and $\tilde{\rho}_n^-$, and $\tilde{\rho}_{n-1}^-$ as a function of $\dot{x}_n$ and $\tilde{\rho}_n^+$. Inserting these expressions in $(3.2)_{2,3}$, and appealing to (3.15) to express the derivatives of $\tilde{\rho}_n$ in terms of $\tilde{\rho}_n^+$ and $\tilde{\rho}_n^-$, we obtain a linear system that can be solved for $\tilde{\rho}_n^+$ and $\tilde{\rho}_n^-$ (whose explicit expressions are given in Appendix F).

Substituting the resulting expressions in $(3.2)_4$, we obtain:

$$\begin{aligned}\dot{x}_n = {} & \mathcal{P}\Big[\frac{\ell_n + \ell_{n-1}}{2} + \frac{C_2 - C_1}{2}\delta\Big(\frac{\ell_{n-1}}{B_{n-1}}\Big)\Big] - \bar{\kappa} S \Theta\, \delta\Big(\frac{\delta(\bar{f}_{n-1})}{B_{n-1}}\Big) \\ & + \Theta C_0 \delta\Big(\frac{\delta(\dot{x}_{n-1})}{B_{n-1}}\Big) - \Theta(\chi_a - \chi_c)\frac{S+1}{2}\delta\Big(\frac{\dot{x}_n + \dot{x}_{n-1}}{B_{n-1}}\Big) + \mathcal{O}(\mathcal{P}^2, \mathcal{P}\bar{\alpha}_0),\end{aligned} \tag{3.16}$$

where, for any z_n, $\delta(z_n) := z_{n+1} - z_n$, and

$$\begin{cases} B_n := 1 + S + \bar{\kappa} S \bar{\ell}_n, \\ C_0 := (1-S)(\chi_a + \chi_c)/2 + \chi_a \chi_c \Theta(S+1), \\ C_1 := 1 + \chi_c \Theta(S+1), \\ C_2 := S - \chi_c \Theta(S+1). \end{cases} \tag{3.17}$$

4 We argue in Chapter 5 that these terms have no impact on the stability analysis at first order in $\overline{F}$ and $\bar{v}$.

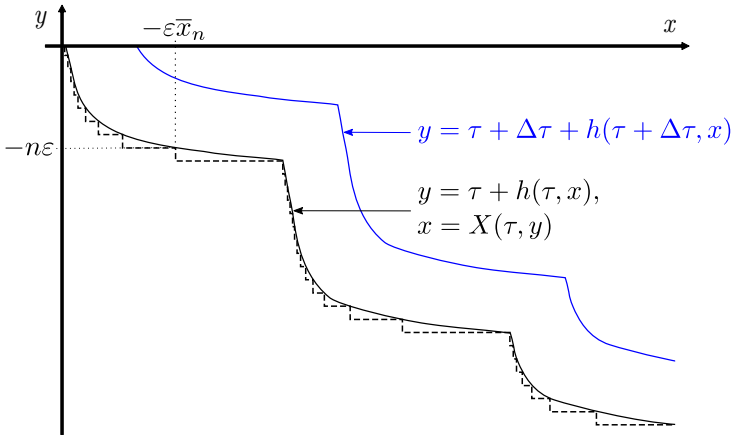

Figure 3.11: In black, correspondence between the discrete and continuous surface profiles at time τ. In blue, the surface profile at a later time $\tau + \Delta\tau$.

In the kinetic-limited regime, $\bar{\kappa} \ll 1$, so that $B_n \simeq 1 + S$. We can now proceed to the homogenization of (3.16). To approximate the profile of the vicinal surface, we introduce the continuous function $X(\tau, y)$ such that

$$x_n(t) = \varepsilon^{-1} X(\tau = \varepsilon \mathcal{P} t, y = -n\varepsilon), \tag{3.18}$$

where the space variable has been normalized and the time appropriately rescaled to reflect the change from microscopic length scale $\mathcal{L}_0$ to macroscopic length scale $\mathcal{L}$. Taylor-expanding the different terms in (3.16) up to order 3 (the dominant order of the elastic repulsion term), we get:

$$\begin{cases} \dfrac{\ell_n + \ell_{n-1}}{2} = -X_y - \dfrac{\varepsilon^2}{6} X_{y^3} + \mathcal{O}(\varepsilon^4), \\ \delta\left(\dfrac{\ell_{n-1}}{B_{n-1}}\right) = \dfrac{\varepsilon}{S+1}\left(X_{y^2} + \dfrac{\varepsilon^2}{12} X_{y^4}\right) + \mathcal{O}(\varepsilon^5), \\ \delta\left(\dfrac{\delta\bar{\mathfrak{f}}_{n-1}}{B_{n-1}}\right) = -\gamma(R)\dfrac{\bar{\alpha}_0 \varepsilon^3}{S+1}\left[\dfrac{1}{X_y^3}\right]_{y^3} + \mathcal{O}(\varepsilon^5), \\ \delta\left(\dfrac{\delta(\dot{x}_{n-1})}{B_{n-1}}\right) = \dfrac{\varepsilon^2}{S+1}\mathcal{P} X_{\tau y^2} + \mathcal{O}(\varepsilon^4), \\ \delta\left(\dfrac{\dot{x}_n + \dot{x}_{n-1}}{B_{n-1}}\right) = -\dfrac{2\varepsilon}{S+1}\mathcal{P}\left(X_{\tau y} + \dfrac{\varepsilon^2}{6} X_{\tau y^3}\right) + \mathcal{O}(\varepsilon^5). \end{cases} \tag{3.19}$$

In the limit $R \to \infty$, $\gamma(R) = \sum_{r=1}^{R} r^{-2} \to \pi^2/6 \simeq 1.64$. If the infinite sum is instead truncated at 5 terms like in the numerical simulations, $\gamma(5) \simeq 1.46$. Although this introduces an error of 11%, it has effectively no impact on the scaling law for the bunch height as H is independent of the strength of the elastic repulsion.

In order to obtain an equation for the the surface height $h(\tau, x)$, we start by introducing the nonlinear transform

$$\begin{aligned} &\tau + h(\tau, \varepsilon x_n(t)) = -n\varepsilon, \\ \text{i. e., } &\tau + h(\tau, X(\tau, y)) = y, \end{aligned} \tag{3.20}$$

such that we absorb the constant deposition term (see Figure 3.11), yielding:

$$X_\tau = -\frac{1+h_\tau}{h_x},\ X_y = \frac{1}{h_x},\ X_{yy} = \frac{1}{h_x}\left[\frac{1}{h_x}\right]_x, \tag{3.21}$$

and so on for higher-order derivatives. To eliminate the cross-derivative terms, we rearrange the terms of the equation by repeated differentiation, division by h_x, and substitutions, resulting in the sought-after PDE:

$$h_\tau - \varepsilon K_1\left[\frac{1}{h_x}\right]_x + \varepsilon^3 K_2\left[\frac{1}{h_x}(h_x^2)_{xx}\right]_x + \varepsilon^2 K_4\left[\frac{h_{xx}}{h_x^3}\right]_x + \varepsilon^3 K_5\left[\frac{1}{h_x}\left[\frac{h_{xx}}{h_x^3}\right]_x\right]_x = \mathcal{O}(\varepsilon^4), \tag{3.22}$$

where

$$\begin{cases} K_0 := \dfrac{C_0}{S+1}, \\ K_1 := \chi_a\Theta - \dfrac{1}{2}\dfrac{S-1}{S+1}, \\ K_2 := \dfrac{3}{2}\dfrac{S}{S+1}\gamma(R)\dfrac{\bar\kappa\bar\alpha_0}{\overline{F}}, \\ K_3 := \dfrac{1}{12}\left[(2\chi_a-\chi_c)\Theta - \dfrac{1}{2}\dfrac{S-1}{S+1}\right], \\ K_4 := \dfrac{1}{6} + \Theta K_0 + K_1\Theta(\chi_a-\chi_c), \\ K_5 := K_3 + \Theta K_0 K_1 + K_4\Theta(\chi_a-\chi_c). \end{cases} \tag{3.23}$$

The prevailing equation in the literature (Pimpinelli et al., 2002; Krug, 2005), based on the quasistatic BCF model, can be recovered from (3.22) by neglecting the dynamical and chemical effects ($\chi_a = \chi_c = 0$) and setting $K_5 = 0$. While the first condition ensues naturally from the definitions of χ_a and χ_c, the second amounts to neglecting a term that is of the same order as the K_2 term of elastic repulsion, which is not justified *a priori*. Numerical integration of (3.22) in the presence and absence of the K_5 term show that its impact on the bunch profile is limited to narrow regions at the upper and lower edges, with no visible effect on the bunch shape. Nevertheless, we show in the next section that the K_5 term plays an important role in the onset of instability, where its influence cannot be neglected.

In addition, using the relations (3.23) as guides, we are able to generalize the scaling laws (3.13) of H and ℓ_{min} determined in the absence of ES barrier, to the general case of an arbitrary ES barrier:

$$\begin{cases} H \simeq 2.5\,K_1^{0.7\pm0.05}\,\bar t^{1/2}, \\ \ell_{min} \simeq 1.55\left(\dfrac{K_2}{K_1}\right)^{1/3} N^{-2/3}. \end{cases} \tag{3.24}$$

3.3.2 *Linear stability analysis*

The linear-stability analysis of (3.22) is performed by setting

$$h(\tau,x) = -x + \delta h\, e^{i\hat k x + \hat\lambda\tau}, \tag{3.25}$$

where $h(\tau, x) = -x$ corresponds to the fundamental solution, and expanding (3.22) to linear order in δh. Time and space are then rescaled ($k = \varepsilon\hat{k}$ and $\lambda = \varepsilon\mathcal{P}\hat{\lambda}$) for comparison with the discrete system, yielding the dispersion relation

$$\mathrm{Re}(\lambda) = K_1 k^2 - (2K_2 + K_5)k^4. \tag{3.26}$$

We conclude from (3.26) that a step-bunching instability exists as long as $K_1 > 0$. For the quasistatic BCF model, $K_1 = (S-1)/2(S+1)$, so that an iES barrier ($S < 1$) is necessary to fulfill that condition, and its absence ($S = 1$) or the presence of a direct ES barrier ($S > 1$) leads to a stable step flow (Schwoebel and Shipsey, 1966). In contrast, the inclusion of the dynamical and chemical effects renders the recourse to an iES barrier unnecessary to explain instability, as long as the attachment/detachment asymmetry satisfies $S < (1+2\Theta)/(1-2\Theta)$.

Note that setting $S = (1-2\Theta)/(1+2\Theta)$ in the quasistatic BCF model mimics the same K_1 coefficient than setting $S = 1$ in the full model with the dynamical effect. In other words, the dynamical effect may be interpreted as an *effective* iES effect, analogously to chemical reactions (Pimpinelli and Videcoq, 2000) or diffusion anisotropy (Schelling et al., 2000). This interpretation also sheds a new light on the experimental uncertainty surrounding the nature of the ES barrier on Si(111). Indeed, the smallness of Θ implies a weak effective iES barrier, and since only indirect methods are available to determine this value, it is likely that the measurement accuracy is insufficient to conclude.

Regarding the chemical effect, the complete linear-stability analysis (Guin, 2018) shows that its destabilizing effect is strongest for the step pairing mode but that its impact is reduced in the limit of large wavelengths, which is the relevant one when passing to the continuum limit, thus explaining its absence from the dominant destabilizing contribution in (3.26).

Going back to the discrete equation (3.16) and setting $x_n = n + \mathcal{P}t + \delta x\, e^{ikn+\lambda t}$, we obtain:

$$\begin{aligned}\lambda = i\sin(k) + \Big[&4(K_1 - (\chi_a - \chi_c)\Theta - K_0\Theta\lambda) - \Theta(\chi_a - \chi_c)i\sin(k)\,\lambda \\ &+ 32\frac{\gamma_d(R,k)}{\gamma(R)}K_2\Big]\sin^2(k/2),\end{aligned} \tag{3.27}$$

with $\gamma_d(R,k) := \sum_{r=1}^{R} \dfrac{\sin^2(kr/2)}{r^4}$.

Solving for λ, taking the real part, and expanding for long wavelengths ($k \to 0$) up to $\mathcal{O}(k^5)$, we recover the exact same expression (3.26) as in the continuum limit. This confirms the validity and relevance of the continuum limit (3.22), notably regarding the new K_5 term. Indeed, as $K_5 \gtrsim K_2$ for typical values of the model parameters, it has a significant influence on the maximum growth rate $\lambda_m = (2K_2 + K_5)^{-1}(K_1/2)^2$ and the most unstable mode $k_m = \sqrt{(2K_2 + K_5)^{-1}K_1/2}$.

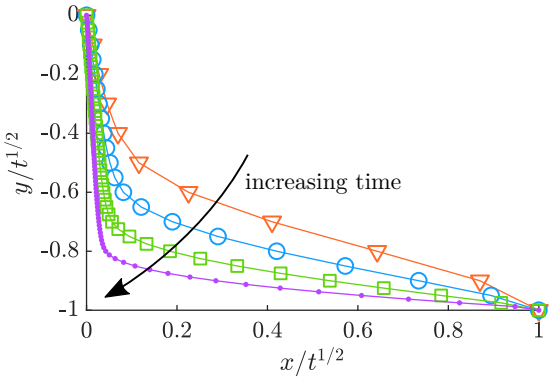

Figure 3.12: Bunch steepening. Each curve corresponds to the rescaled bunch profile after a 4-fold time increase.

3.4 ANALYTICAL SCALING LAWS

There are two scaling laws of interest to describe the asymptotic behavior of the surface profile. The scaling of H with time is an indicator of the evolution of surface roughness and the scaling of ℓ_{min} with N characterizes the bunch shape. We also look at the bunch velocity v scaling with N as an additional descriptor of the coarsening process.

3.4.1 *Bunch height H*

A common approach to obtain scaling laws from PDE's relies on identifying self-similar or self-affine solutions, depending on whether the scaling is identical or differs between the x and y directions. In the present case, the evolution of the surface profile cannot be self-affine as it would violate the vicinality constraint. Nonetheless, when limiting the analysis to a bunch, and not the whole surface profile, self-affine solutions are possible, as introduced by Pimpinelli et al. (2002) based on a simplified version of (3.22) where only the transient term h_τ, the destabilizing K_1 term and the stabilizing K_2 term are considered. We do not follow that approach here because of the ambiguous definition of the lateral extent of the bunch, as previously mentioned.

Looking for self-similar solutions of (3.22) in the form $h(\tau, x) = \tau^a \phi(\zeta)$, with $\zeta = x/\tau^a$, we find

$$\tau^{a-1}(a\phi - a\zeta\phi') - \varepsilon K_1 \tau^{-a}\left[\frac{1}{\phi'}\right]' + \tau^{-2a}\varepsilon^2 K_4\left[\frac{\phi''}{\phi'^3}\right]' + \tau^{-3a}\varepsilon^3 K_2\left[\frac{1}{\phi'}(\phi'^2)''\right]' + \tau^{-3a}\varepsilon^3 K_5\left[\frac{1}{\phi'}\left[\frac{\phi''}{\phi'^3}\right]'\right]' = 0. \quad (3.28)$$

Since this equation cannot be made scale invariant, it does not admit self-similar solutions. This is consistent with the profiles obtained from numerical simulations of the discrete step-flow equations which shows the steepening of the bunch despite rescaling it as per the expected $\tau^{1/2}$ scaling law (Figure 3.12).

Analyzing (3.28) further, we note that the K_4 and K_5 terms, which preclude scale-invariance, present a τ^{-2a} and a τ^{-3a} factors, respectively. This indicates

that they possibly become negligible at long times compared to the K_1 term exhibiting a τ^{-a} factor, provided that the associated functions $(\phi''/\phi'^3)'$ and $(1/\phi'(\phi''/\phi'^3)')'$ are regular enough. While this is the case inside the bunched and quasiflat regions, at the transition zones (which become sharper as the surface coarsens), these functions diverge, and the associated terms cannot be neglected, precluding the existence of self-similar solutions.

Nonetheless, it seems clear from Figure 3.12 that the $\tau^{1/2}$ scaling plays a crucial role, despite not obeying strict self-similarity. To see this, we modify the existing analysis to focus on the quasiflat region, so that the K_4 and K_5 terms may be neglected, and we consider asymptotic expansions for the characteristic height and length of the region of the form:

$$\begin{cases} h(\tau,x) = h_0(\tau,x) + \sum_{i\geqslant 0} \tau^{a_i}\varphi_i(\zeta), \\ \zeta = \dfrac{x}{\sum_{j\geqslant 0} c_j \tau^{b_j}}, \end{cases} \tag{3.29}$$

where $h_0(\tau,x) = -x$ represents the steady-state solution of equidistant steps, and $\forall i \in \mathbb{N}$, $a_i > a_{i-1}$, $b_i > b_{i-1}$, $\varphi_i(\zeta) = \mathcal{O}(1)$ and $c_0 = 1$. Thus,

$$h_x = -1 + \frac{\sum_{i\geqslant 0} \tau^{a_i}\varphi_i'(\zeta)}{\sum_{j\geqslant 0} c_j \tau^{b_j}}, \tag{3.30}$$

where vicinality imposes $a_0 = b_0$.[5] Next, steps being far apart in the quasiflat region, we neglect the elastic term, and (3.22) becomes:

$$\sum_{i\geqslant 0} \tau^{a_i-1}\left[a_i\varphi_i - \frac{\sum_{j\geqslant 0} b_j c_j \tau^{b_j}}{\sum_{j\geqslant 0} c_j \tau^{b_j}}\zeta\varphi'\right] - \frac{\varepsilon K_1}{\sum_{j\geqslant 0} c_j \tau^{b_j}}\left[\frac{1}{-1+\frac{\sum_{i\geqslant 0}\tau^{a_i}\varphi_i'(\zeta)}{\sum_{j\geqslant 0} c_j\tau^{b_j}}}\right]' = 0. \tag{3.31}$$

Looking at the dominant contribution, we get:

$$a_0\tau^{a_0-1}\left[\varphi_0 - \zeta\varphi_0'\right] - \varepsilon K_1 \tau^{-a_0}\left[\frac{1}{-1+\varphi_0'}\right]' = 0. \tag{3.32}$$

Hence, scale invariance imposes $a_0 - 1 = -a_0 = -1/2$ which shows that the deviation of the surface profile from the fundamental solution scales asymptotically as $\tau^{1/2}$. From geometrical arguments, one can verify that this deviation scales like the bunch height and we thus recover the scaling law reported in the literature (Krug et al., 2005; Omi et al., 2005).

3.4.2 *Minimal terrace size ℓ_{min}*

As the previous analysis is conducted in the quasiflat region, a different approach is needed to determine the scaling law for ℓ_{min} in the bunch. In the

5 Indeed, as the slope in the quasiflat region must remain finite as $\tau \to \infty$, $a_0 \leqslant b_0$ must hold. Moreover, as it cannot coincide with the -1 slope of the stable solution, strict inequality is not possible.

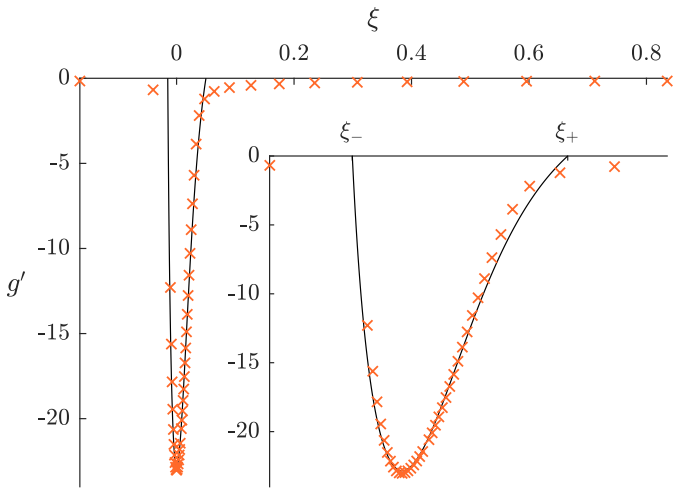

Figure 3.13: Comparison of the surface slope obtained from simulations of the discrete system under forced bunching (x) with the analytic expression (3.35), where the coefficients are given by (3.36) and v is determined from the numerical resolution of (3.34). The inset focuses on the bunched region.

stationary regime, the scaling of the bunch can be well approximated (Krug et al., 2005; Stoyanov et al., 2000) and leads, for large enough bunches, to

$$\ell_{min} \simeq \left(\frac{16}{3}\frac{K_2}{K_1}\right)^{1/3} N^{-2/3} = 4^{1/3}\left(\frac{\bar{\kappa}\bar{\alpha}_0}{\overline{F}\Theta}\right)^{1/3} N^{-2/3}. \tag{3.33}$$

This expression predicts exactly the different exponents observed for each physical parameter and the theoretical prefactor $4^{1/3} \simeq 1.58$ is in excellent agreement with the 1.6 numerical estimate found in (3.13).

However, although the scaling behavior of ℓ_{min} is accurately described in the context of the stationary approximation, a closer inspection reveals that the predicted slope of the bunch is symmetric with respect to its center, in disagreement with previous simulations (Popkov and Krug, 2005) and our own. Specifically, even though the velocity of a bunch decreases with its size, which *a priori* legitimizes the stationary approximation for large bunches, it still has a crucial influence on the bunch shape. Indeed, if the bunch velocity is included, while neglecting other dynamical contributions, the expected asymmetric bunch shape is recovered (Popkov and Krug, 2005). Nonetheless, as this adjustment only introduces a 6% correction (Popkov and Krug, 2005) in the numerical prefactor of (3.33), we argue that its validity can be extended from the stationary to the quasisteady regime.

3.4.3 *Bunch velocity*

In this section, we analytically derive an expression for the bunch velocity, which was previously only assessed via numerical simulations (Popkov and Krug, 2005). Neglecting the K_5 term in equation (3.22), which we verify numerically has no impact on the bunch shape, we apply the traveling-wave change of

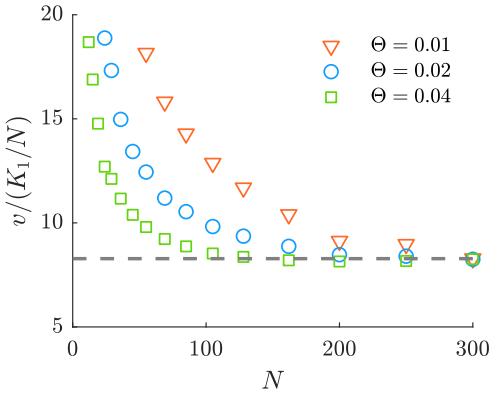

Figure 3.14: Bunch velocity v scaling with N. The asymptote is at 8.3.

variable $h(\tau, x) = g(x - v\tau) + \Omega\tau$ to transform the PDE into an ODE. Denoting derivatives with respect to $\xi = x - v\tau$ by primes, we obtain:

$$-v(1+g') - \varepsilon K_1\left[\frac{1}{g'}\right]' + \varepsilon^3 K_2\left[\frac{(g'^2)''}{g'}\right]' + \varepsilon^2 K_4\left[\frac{g''}{g'^3}\right]' = 0, \tag{3.34}$$

after identifying $\Omega = -v$ from the fundamental solution for which $g' = -1$.

Denoting M the absolute value of the maximum slope in the bunch, we use a (2,3) Padé approximant to estimate the shape of the bunch slope:

$$g'(\xi) = \frac{-M + a_1\xi + a_2\xi^2}{1 + b_1\xi + b_2\xi^2 + b_3\xi^3}, \tag{3.35}$$

where the ξ-origin is set at the point of maximum slope. The condition $g''(0) = 0$ imposes $b_1 = -a_1/M$. The remaining coefficients a_1, a_2, b_2, and b_3 are determined following the procedure detailed in Appendix G. Setting $\eta := v/(\varepsilon^3 K_2)$, we obtain, at leading order:

$$\begin{cases} a_1 \simeq A_1\eta^{1/3}M, & a_2 \simeq A_2\eta^{2/3}M, \\ b_2 \simeq B_2\eta^{2/3}, & b_3 \simeq B_3\eta, \end{cases} \tag{3.36}$$

The exact expressions for the A_i and B_i are not reported, as they consist of tedious polynomial roots with no special interest.

To compute the relationship between M and v, we use the fact that the height of the bunch is normalized to 1. When integrating the slope, we neglect the contribution of the quasiflat terraces and assume that the main contribution comes from the bunched region, i.e., the region between the roots ξ_- and ξ_+ of g' (Figure 3.13). Hence:

$$\int_{\xi_-}^{\xi_+} g'(\xi)\,\mathrm{d}\xi \simeq -1. \tag{3.37}$$

As the exact integration is unnecessarily laborious, we use a third-order Gauss quadrature (higher orders procure negligible corrections) to get an approximate expression. The dominant contribution yields:

$$M \simeq 0.303\,\eta^{1/3}. \tag{3.38}$$

Recalling that the velocity of a moving bunch mainly impacts its shape but has a negligible effect on the maximum slope M (Popkov and Krug, 2005), we finally conclude:

$$0.303^3 \frac{v}{\varepsilon^3 K_2} \simeq \frac{3}{16} \frac{K_1}{\varepsilon^2 K_2}, \tag{3.39}$$

yielding the expression

$$v \simeq 6.74 \frac{K_1}{N}. \tag{3.40}$$

While we correctly predict the scaling $v \sim K_1/N$, in agreement with (Popkov and Krug, 2005) and our own simulations, the prefactor is 20% smaller than the expected value of 8.3 derived from the numerical simulations (Figure 3.14). This can be traced back to the fact that the Padé approximant does not capture the exact bunch shape (Figure 3.13). In addition, the error is also expanded by the cubic power applied in (3.40).

3.5 KEY RESULTS

NUMERICAL SIMULATIONS We have conducted extensive numerical simulations for a wide range of physical parameters from which we have extracted the relevant scaling laws describing the coarsening behavior of step bunching. The obtained scaling laws for the bunch height H as a function of the time $\bar{t}$ (expressed in number of monolayers deposited) and for the minimal interstep distance ℓ_{min} as a function of the bunch size N are extremely robust and read

$$\begin{cases} H \simeq 2.5 K_1^{0.7 \pm 0.05} \bar{t}^{1/2}, \\ \ell_{min} \simeq 1.55 \left(\dfrac{K_2}{K_1}\right)^{1/3} N^{-2/3}, \end{cases}$$

with

$$\begin{cases} K_1 = \chi_a \Theta - \dfrac{1}{2} \dfrac{S-1}{S+1}, \\ K_2 = \dfrac{3}{2} \dfrac{S}{S+1} \dfrac{\pi^2}{6} \dfrac{\bar{\kappa} \bar{\alpha}_0}{\overline{F}}. \end{cases}$$

Crucially, we have shown that the dynamical and chemical effects can account for the onset of step bunching and for the scaling laws observed in the coarsening regime, thereby circumventing the need for an inverse Ehrlich-Schwoebel barrier required by the classical BCF model. In other words, by accounting for all the necessary mechanisms without *a priori* assumptions, we are able to explain experimental results in a unified framework, without the need to introduce additional effects.

CONTINUUM LIMIT We have conducted a coherent discrete-to-continuum derivation, leading to the following nonlinear PDE to describe the macroscopic evolution of the surface profile:

$$h_\tau - \varepsilon K_1 \left[\frac{1}{h_x}\right]_x + \varepsilon^3 K_2 \left[\frac{1}{h_x} (h_x^2)_{xx}\right]_x + \varepsilon^2 K_4 \left[\frac{h_{xx}}{h_x^3}\right]_x + \varepsilon^3 K_5 \left[\frac{1}{h_x} \left[\frac{h_{xx}}{h_x^3}\right]_x\right]_x = 0,$$

where the coefficients

$$\begin{cases} K_0 := \dfrac{\chi_a + \chi_c}{2}\dfrac{S-1}{S+1} + \chi_a\chi_c\Theta; & K_1 := \chi_a\Theta - \dfrac{1}{2}\dfrac{S-1}{S+1}; \\ K_2 := \dfrac{3}{2}\dfrac{S}{S+1}\dfrac{\pi^2}{6}\dfrac{\bar{\kappa}\bar{\alpha}_0}{\overline{F}}; & K_3 := \dfrac{1}{12}\left[(2\chi_a - \chi_c)\Theta - \dfrac{1}{2}\dfrac{S-1}{S+1}\right]; \\ K_4 := \dfrac{1}{6} + \Theta K_0 + K_1\Theta(\chi_a - \chi_c); & K_5 := K_3 + \Theta K_0 K_1 + K_4\Theta(\chi_a - \chi_c); \end{cases}$$

differ from the ones reported in the literature in that they incorporate the dynamical and chemical effects. Moreover, the K_5 term is never mentioned in the literature whereas it cannot be neglected *a priori*. While we have verified that its impact on the bunch evolution is indeed negligible, we have also shown that its influence on the onset of instability is not. We have presented a multiscale asymptotic analysis of the PDE that allows to recover the $H \sim t^{1/2}$ scaling law without introducing considerations of the ambiguously defined bunch width. We have also proposed an analytical derivation of the bunch velocity as a function of the bunch size, valid for large bunches, which was previously assessed via numerical simulations only. Based on a Padé approximation of the bunch shape, the final formula reads

$$v \simeq 6.74\frac{K_1}{N}.$$

Incidentally, the identification of the prefactors of the scaling laws offers an interesting alternative for determining microscopic parameters of the vicinal surface (e. g., the equilibrium adatom coverage Θ, the attachment/detachment coefficient $\bar{\kappa}$, the ES barrier S, or the elastic repulsion coefficient $\bar{\alpha}_0$) from macroscopic features (e. g., the bunch height H, the minimal interstep distance ℓ_{min}, the bunch size N, and the bunch velocity v).

4 LINEAR STABILITY ANALYSIS OF MEANDERING

In this chapter, we analyze the stability of vicinal surfaces with the governing equations (2.129) in the absence of electromigration ($\bar{e} = 0$).[1]

We start by establishing the general framework of the linear stability analysis in Section 4.2, which we specialize to the quasistatic case in Section 4.3 before presenting the general case with dynamics terms in Section 4.4. We interpret some experimental results in view of our findings in Section 4.5.

4.1 REVIEW OF EXISTING THEORIES

Meandering steps are a common feature in step-flow epitaxy experiments, which may have two distinct origins. While thermal fluctuations are responsible for some of the observations (Leamy et al., 1975; van Leeuwen and Mischgofsky, 1975; Voronkov, 1983), other experiments point instead towards a deterministic origin (Ino, 1989; Alfonso et al., 1993; Pierre-Louis and Misbah, 1996; Maroutian et al., 2001). Based on the BCF model, Bales and Zangwill (1990) showed that, under deposition, the straight-step configuration is unstable in the presence of a direct ES effect, and steps manifest a distinct waviness, distinguishable from the meandering due to thermal roughening (see Figure 4.1). Like most of the literature on step-flow growth, their analysis was derived under the so-called quasistatic approximation. Additionally, only the in-phase mode was considered, and the effects of step interactions (entropic and elastic) and diffusion along the step were ignored. In the following years, the model was successively refined to include the aforementioned effects.

Pimpinelli et al. (1994) extended the model to account for an arbitrary phase shift between steps, and showed that in the presence of a direct ES effect, the most unstable mode is not always in-phase like considered by Bales and Zangwill (1990) but is actually anti-phase under evaporation.

The same year, Liu and Metiu (1994) and Saito and Uwaha (1994) studied the linear stability of the system beyond the quasistatic approximation. However, Saito and Uwaha (1994) were mainly preoccupied by the effect of diffusion kinetics on step fluctuation, i. e., due to thermal noise. And while their analysis of the stability shows that the asymmetry between the forward and backward directions of the step, due to its motion, is destabilizing under both deposition and evaporation conditions, their study is restricted to an isolated step with infinitely fast symmetric attachment/detachment kinetics, where only the advective contribution of the growth velocity of a straight step is considered. Using Green's function formalism, Liu and Metiu (1994) were able to additionally take into account the transient term of the dynamics (the partial time derivative in the diffusion equation), but the rest of their analysis of the meandering

1 The case with electromigration is treated in Chapter 5.

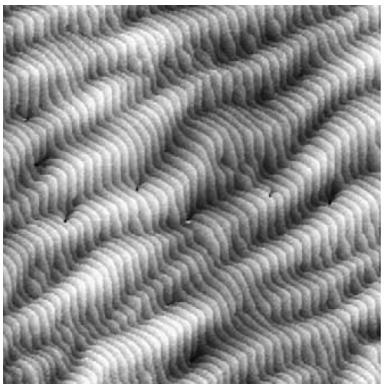

Figure 4.1: AFM image of meandering steps on Si(111) after growth of 20 nm at 3°C below the $7 \times 7 \leftrightarrow 1 \times 1$ transition temperature (reprinted from Hibino et al. (2003) with permission from Elsevier).

instability suffers from the same restrictions, as the bulk of their work is instead focused on the step-bunching instability and the impact of thermal noise. In summary, in both articles the stability analysis is restricted to very specific cases and not much discussed, with little insight on how the dynamical effect interplays with other stabilizing and destabilizing mechanisms.

In the late 90's and early 2000's, Ihle et al. (1998), Gillet et al. (2000), and Danker et al. (2003) included step-edge diffusion to the equation of mass conservation at the step. The study by Ihle et al. (1998) is very detailed and complete, as it also incorporates the contributions of elastic interactions and thermal noise in the framework of a nonlocal linear Langevin equation. However, it is centered around the scaling behavior of the temporal correlation function in global equilibrium and does not provide a stability analysis. Likewise, the studies by Gillet et al. (2000) and Danker et al. (2003) are focused on the nonlinear behavior of meanders, in a quasistatic framework, and only give a brief linear stability analysis, which is not discussed but rather serves as a stepping stone to their nonlinear derivation. Although not based on the BCF framework but rather on Kinetic Monte Carlo simulations, Nita and Pimpinelli (2005) have shown that unhindered step-edge diffusion along the step was able to explain the meandering instability observed on real Cu surfaces.

Based on a terrace-step-kink model, Caflisch et al. (1999) and Balykov and Voigt (2006) proposed a more refined approach of step-edge diffusion that accounts for step adatom and kink densities. In an effort to better incorporate atomistic processes in the mesoscopic BCF equations and extend their validity to far-from-equilibrium conditions, they describe the adatom fluxes from the terraces to the step via kinetic fluxes due to atomistic exchange processes, essentially counting all possible ways an adatom and a step adatom can be incorporated into the crystal lattice, under a mean field assumption. This approach has undeniable advantages as it combines a detailed microscopic description, whose parameters can be computed from first principles, with the computational efficiency of a continuum model. Its main interest however resides in the study of island growth, while we are concerned with a train of steps.

Few studies have been dedicated to the impact of elasticity on the stability of meanders. In their seminal work, Houchmandzadeh and Misbah (1995) showed for the first time that elasticity may destabilize straight steps; a counter-intuitive result as the interaction between straight steps of the same sign is known to be repulsive. In their analysis, the z-component of the displacement field is neglected based on an argument by Lau and Kohn (1977): "If we ignore the forces exerted by the adatom on the lattice atoms below the surface layer, then the z-component of the displacement does not contribute to the interaction energy. These forces are actually quite small; (...) the magnitudes are about 10% compared to those involving the surface atoms" Using the dipoles obtained on Si for example, we find that including the z-component causes the strength of the interaction between straight steps to increase by 16%. We also recall that their derivation implicitly relies on the integral of sine functions over $\mathbb{R}$ to be zero, which entails that infinitesimally meandering steps behave as straight steps at first order, in contrast with our results in Section 4.2.2.

In the following years, based on the results of Houchmandzadeh and Misbah (1995), Pierre-Louis and Misbah (1996) and Paulin et al. (2001) have included elasticity in their formulation. However, neither offer a stability analysis. The work of Pierre-Louis and Misbah (1996) focuses on the meander amplitude scaling and the interaction of noise and determinism, while the work of Paulin et al. (2001) is concerned with nonlinear evolution equations and scaling laws. Finally, Yeon et al. (2007) conducted a complete linear stability analysis of the standard BCF model extended to include monopole interactions between steps (that arise e. g., in heteroepitaxial growth), but used the quasistatic approximation, neglected evaporation, and did not take into account dipole interactions.

More recently, Chen (2019) considered the influence of the chemical effect on the stability of the vicinal surface, but used the quasistatic approximation and restricted the analysis to in-phase meanders.

The work of Sato and Uwaha (1999a) and Danker et al. (2003) on anisotropy is also worth mentioning, even though their focus is on the nonlinear behavior of step meanders. Sato and Uwaha (1999a) considered anisotropic attachment/detachment kinetics, and Danker et al. (2003) considered anisotropic step-edge diffusion and step stiffness, with both showing that it does not affect the onset of instability (for the case of in-phase meandering they consider) but only the subsequent coarsening pattern.

Importantly, we do not consider the possibility of nucleation along the step or on a terrace (as our model is entirely deterministic) nor the existence of a *kink ES effect*, which is the one-dimensional equivalent for the step of the ES barrier for terraces, i. e., an additional energy barrier adatoms diffusing along the step must overcome to go around a kink. Indeed, while the kink ES effect has been shown to impact the stability of the surface by several authors (Pierre-Louis et al., 1999; Politi and Krug, 2000; Kallunki et al., 2002; Kallunki and Krug, 2003), it seems to mainly concern metal surfaces like Pt(111) or Cu(001) (Ikonomov et al., 2007), which also present strong ES barriers. On semiconductor surfaces like Si(111), the existence of an ES barrier is already debated, and there is no evidence that would point to a kink ES barrier. Moreover, we recall that the core

objective of the present work is to investigate the influence of the dynamical and chemical effects on the stability of vicinal surfaces, that play a role irrespective of which additional mechanisms are considered.

In conclusion, a complete and systematic stability analysis, including all aforementioned mechanisms to study their interplay, has yet to be established. We remedy this situation here with analytic expressions for the instability growth rate in the quasistatic framework and numerical results of the complete problem with dynamics.

4.2 LINEAR STABILITY ANALYSIS

4.2.1 *General framework*

In this section, we establish the general framework for the linear stability analysis, which consists in studying the growth rate of perturbations of the principal solution, where all the steps propagate at the same velocity and the adatom density profile is identical on all terraces.

LINEAR PERTURBATION EQUATION Denoting $\tilde{\rho}^{(0)}$ the principal (steady-state) solution, in order to derive the linear perturbation equation we consider the perturbed state

$$\begin{cases} x_n(y,t) = n + \mathcal{P}t + \varepsilon \delta x_n(y,t) + \mathcal{O}(\varepsilon^2), \\ \tilde{\rho}_n(u,y,t) = \tilde{\rho}^{(0)}(u) + \varepsilon \delta\tilde{\rho}_n(u,y,t) + \mathcal{O}(\varepsilon^2), \end{cases} \tag{4.1}$$

where ε is a small parameter and we recall $u = (x - x_n(t,y))/\ell_n(t,y)$, the Lagrangian variable. Writing the perturbation as

$$\mathbf{p}_n(u,y,t) := \Big(\delta x_n(y,t), \delta\tilde{\rho}_n(u,y,t)\Big), \tag{4.2}$$

inserting (4.1) in (2.129), and collecting terms of order ε, yields a linear autonomous system for $\mathbf{p}_n$, which reads in abstract form

$$\mathcal{A}(\mathbf{p}_{n-1}, \mathbf{p}_n, \mathbf{p}_{n+1}, \mathbf{p}_{n+2}) = \mathcal{B}(\partial_t \mathbf{p}_n, \partial_t \mathbf{p}_{n+1}), \tag{4.3}$$

where $\mathcal{A}$ and $\mathcal{B}$ denote linear operator involving u-derivatives of $\delta\tilde{\rho}_n$. Consequently, the perturbation may be put in the form

$$\mathbf{p}_n(u,y,t) = \tilde{\mathbf{p}}_n(u,y)\exp(\lambda t), \tag{4.4}$$

with λ the growth rate.

FOURIER MODES Further, as the system has no explicit dependence on the coordinate y, a Fourier transform of the perturbation along y allows to write

$$\tilde{\mathbf{p}}_n(u,y) = \hat{\mathbf{p}}_n(u)\exp(iqy), \tag{4.5}$$

where q is the wavenumber of the meandering mode.

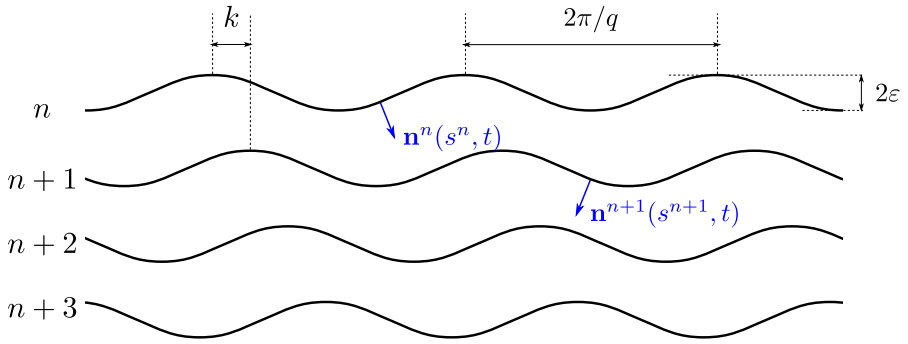

Figure 4.2: Step profile used in the linear stability analysis.

BLOCH-WAVE ANALYSIS Finally, like Guin (2018), we follow the stability method of hydrodynamics (Chandrasekhar, 1961) to write an arbitrary perturbation $\hat{\mathbf{p}}_n$ as a combination of normal modes and obtain the stability of the system by checking the stability with respect to each of these modes. Using the linearity of (4.3), and the fact that the operators $\mathcal{A}$ and $\mathcal{B}$ are n-independent (i. e., invariant under a 1-terrace translation), the perturbation is written as a combination of the normal modes given by the *Bloch waves*,

$$\hat{\mathbf{p}}_n(u) = \check{\mathbf{p}}(u)\exp(ikn), \tag{4.6}$$

where $k \in (-\pi, \pi)$ is interpreted as either the wavenumber of the step bunching mode (if $q = 0$) or the phase shift between steps (if $q \neq 0$).

To summarize, we look at the perturbed state

$$\begin{cases} x_n(y,t) = n + \mathcal{P}t + \varepsilon\exp(ikn + iqy + \lambda t) + \mathcal{O}(\varepsilon^2), \\ \tilde{\rho}_n(u,y,t) = \tilde{\rho}^{(0)}(u) + \varepsilon\tilde{\rho}^{(1)}(u)\exp(ikn + iqy + \lambda t) + \mathcal{O}(\varepsilon^2), \end{cases} \tag{4.7}$$

illustrated in Figure 4.2. The stability of the principal solution of equidistant straight steps is then entirely determined by $\mathrm{Re}(\lambda)$. Indeed, for $\mathrm{Re}(\lambda) < 0$, the amplitude of the perturbation decays and the step profiles converge to the principal solution: the system is stable. On the other hand, for $\mathrm{Re}(\lambda) > 0$, the amplitude of the perturbation increases exponentially: the system is unstable.

4.2.2 *Step-step elastic interaction*

Before we can proceed with the main stability analysis, we compute the explicit expression for the step-step elastic interaction $\mathfrak{f}$ in the case of infinitesimally perturbed meanders, whose profile is described by (4.7).

Let $\mathfrak{f}^{(m,n)}$ the elastic interaction of step m with step n. As a consequence of the superposition principle, we can decompose the elastic interaction of step n with the rest of the steps as:

$$\mathfrak{f}_n = \sum_{r\in\mathbb{Z}^*} \mathfrak{f}^{(n,n+r)}. \tag{4.8}$$

Using the results from Section 2.3.1 and Section 2.3.2, we combine (2.84) and (2.90) to obtain:

$$\begin{aligned}\mathfrak{f}^{(n,n+r)} = &- n_i^n(s^n,t)d_{p\ell}^n(s^n,t) \\ &\times \int_{\mathbb{R}} d_{jk}^{n+r}(s^{n+r},t)G_{k\ell,pij}(\mathbf{x}^{n+r}(s^{n+r},t)-\mathbf{x}^n(s^n,t))\,\mathrm{d}s^{n+r},\end{aligned} \tag{4.9}$$

where implicit summation is assumed on repeated subscript indices, s^n is the curvilinear abscissa along step n, $\mathbf{x}^n(s^n,t)$ is the position of the portion of step n at abscissa s^n, $\mathbf{n}^n(s^n,t)$ is the normal of step n at abscissa s^n, $\mathbf{d}^n(s^n,t)$ is the dipole tensor of step n at abscissa s^n, and $\mathbf{G}_{,pij}(\mathbf{x}^{n+r}(s^{n+r},t)-\mathbf{x}^n(s^n,t))$ is the third derivative of the Green's function detailed in Appendix B evaluated at $\mathbf{x}^{n+r}(s^{n+r},t)-\mathbf{x}^n(s^n,t)$.

Examining the displacement field generated by each dipole, (Pimpinelli and Villain, 1998) showed that:

- the effect of d_{zz} can be equivalently incorporated into $(d_{xx},d_{yy}) \leftarrow (d_{xx}-d_{zz}, d_{yy}-d_{zz})$;
- the effect of d_{yx}, d_{zx}, and d_{zy} can be equivalently incorporated into $d_{xy} \leftarrow d_{xy}-d_{yx}$, $d_{xz} \leftarrow d_{xz}-d_{zx}$, and $d_{yz} \leftarrow d_{yz}-d_{zy}$, respectively.

Therefore, without loss of generality, we set $d_{zz} = d_{yx} = d_{yz} = d_{zx} = 0$. Further, for steps aligned with a principal crystal direction, symmetry imposes $d_{xy} = d_{yz} = 0$. In conclusion, we find that three nonzero dipolar moments are required to describe a step aligned with a principal crystal direction: d_{xx}, d_{yy}, and d_{xz}. For the sake of simplicity, we restrict the study to these well-aligned steps.

Let $\mathfrak{f}^{(r)}$ denote the elastic interaction of step 0 with steps r and $-r$, such that

$$\mathfrak{f}^{(m,m+r)} + \mathfrak{f}^{(m,m-r)} := \mathfrak{f}^{(r)}\varepsilon\exp(ikm+iqy+\lambda t). \tag{4.10}$$

For the step profiles considered, the result of the explicit calculation is quite lengthy and we report it in Appendix C. Instead, focusing on the limit $q \ll 1$, which should be verified for all practical purposes due to the smoothening effect of step stiffness, we obtain:

$$\mathfrak{f}^{(r)}(k,q) = 12\alpha_0\frac{\sin^2(kr/2)}{(r\mathcal{L}_0)^4} + \frac{1}{2}\alpha_1\frac{\cos(kr)}{(r\mathcal{L}_0)^2}q^2 + \mathcal{O}(q^4), \tag{4.11}$$

with

$$\begin{aligned}\alpha_0 &= \frac{4(1-\nu^2)}{\pi E}(d_{xx}^2+d_{xz}^2), \\ \alpha_1 &= \frac{4(1+\nu)}{\pi E}(2d_{yy}^2-d_{xx}^2-\nu d_{xx}(4d_{yy}-3d_{xx})-(1-\nu)d_{xz}^2).\end{aligned} \tag{4.12}$$

Therefore, for $q \to 0$, we recover the formula for straight steps found in Marchenko and Parshin (1980), Stewart et al. (1994), and Tersoff et al. (1995). It is also worth noting that in contrast with Houchmandzadeh and Misbah (1995), who report, based on the interaction energy of two dipoles, no contribution of

the meandered profile to the elastic interaction at order ε (i. e., infinitesimally modulated steps behave like straight steps at first order), our own approach, which directly computes the elastic force between steps, clearly shows that this contribution is nonzero. We believe this difference ultimately stems from the fact that, in their calculation, Houchmandzadeh and Misbah (1995) seemingly assume the integral of sine functions over $\mathbb{R}$ to be zero. While this might make sense in the context of distributions, this integral is divergent in the Riemannian sense. Besides, as the elastic interaction force between steps results from differentiating the interaction energy, setting this integral to zero will result in a missing term after differentiation.

4.2.3 *Generalized eigenvalue problem*

Letting

$$\begin{cases} \tilde{\rho}_+^{(0)} := \tilde{\rho}^{(0)}(0), \\ \tilde{\rho}_-^{(0)} := \tilde{\rho}^{(0)}(1), \\ (\partial_u \tilde{\rho}^{(0)})_+ := (\partial_u \tilde{\rho}^{(0)})(0), \\ (\partial_u \tilde{\rho}^{(0)})_- := (\partial_u \tilde{\rho}^{(0)})(1), \end{cases} \tag{4.13}$$

substituting (4.7) back into (2.129) and collecting terms of order 0, we have:

$$\begin{cases} 0 = (\partial_{uu}\tilde{\rho}^{(0)}) + \chi_a \mathcal{P}(\partial_u \tilde{\rho}^{(0)}) + \overline{F} - \bar{v}\tilde{\rho}^{(0)}, \\ -\tilde{\rho}_-^{(0)}\chi_a\mathcal{P} - (\partial_u\tilde{\rho}^{(0)})_- = \bar{\kappa}\Big[\tilde{\rho}_1^{(0)} - 1 - \chi_c\Theta(\tilde{\rho}_+^{(0)} - \tilde{\rho}_-^{(0)})\Big], \\ \tilde{\rho}_+^{(0)}\chi_a\mathcal{P} + (\partial_u\tilde{\rho}^{(0)})_+ = \bar{\kappa}S\Big[\tilde{\rho}_+^{(0)} - 1 - \chi_c\Theta(\tilde{\rho}_+^{(0)} - \tilde{\rho}_-^{(0)})\Big], \\ \mathcal{P} = \bar{\kappa}\Theta(S+1)\Big[\dfrac{\tilde{\rho}_-^{(0)} + S\tilde{\rho}_+^{(0)}}{S+1} - 1 - \chi_c\Theta(\tilde{\rho}_+^{(0)} - \tilde{\rho}_-^{(0)})\Big]. \end{cases} \tag{4.14}$$

Likewise, collecting terms of order ε:

$$\begin{cases} 0 = (\partial_{uu}\tilde{\rho}^{(1)}) + \chi_a\mathcal{P}(\partial_u\tilde{\rho}^{(1)}) - (\bar{v} + q^2 + \chi_a\lambda)\tilde{\rho}^{(1)} \\ \qquad + (\partial_u\tilde{\rho}^{(0)})\Big[(\chi_a\lambda + q^2)(1 + (e^{ik}-1)u) + \chi_a\mathcal{P}(e^{ik}-1)\Big] \\ \qquad + 2(e^{ik}-1)(\overline{F} - \bar{v}\tilde{\rho}^{(0)}), \\ -\tilde{\rho}_-^{(0)}\chi_a\lambda e^{ik} - \chi_a\mathcal{P}\tilde{\rho}_-^{(1)} + (e^{ik}-1)(\partial_u\tilde{\rho}^{(0)})_- - (\partial_u\tilde{\rho}^{(1)})_- \\ \qquad = \bar{\kappa}\Big[\tilde{\rho}_-^{(1)} - \chi_c\Theta(e^{ik}\tilde{\rho}_+^{(1)} - \tilde{\rho}_-^{(1)}) - e^{ik}\mathfrak{F}_R(k,q) - \bar{\gamma}q^2e^{ik}\Big], \\ \tilde{\rho}_+^{(0)}\chi_a\lambda + \chi_a\mathcal{P}\tilde{\rho}_+^{(1)} - (e^{ik}-1)(\partial_u\tilde{\rho}^{(0)})_+ + (\partial_u\tilde{\rho}^{(1)})_+ \\ \qquad = \bar{\kappa}S\Big[\tilde{\rho}_+^{(1)} - \chi_c\Theta(\tilde{\rho}_+^{(1)} - e^{-ik}\tilde{\rho}_-^{(1)}) - \mathfrak{F}_R(k,q) - \bar{\gamma}q^2\Big], \\ \lambda = \bar{\kappa}\Theta\Big[C_1(q)e^{-ik}\tilde{\rho}_-^{(1)} + C_2(q)\tilde{\rho}_+^{(1)} \\ \qquad - (\mathfrak{F}_R(k,q) + \bar{\gamma}q^2)(S + 1 + \dfrac{\Pi}{\bar{\kappa}\Theta}q^2)\Big], \end{cases} \tag{4.15}$$

where

$$\begin{cases} C_1(q) := 1 + \chi_c \Theta(S+1) + \chi_c \dfrac{\Pi}{\bar{\kappa}} q^2, \\ C_2(q) := S - \chi_c \Theta(S+1) - \chi_c \dfrac{\Pi}{\bar{\kappa}} q^2, \\ \mathfrak{F}_R(k,q) := \displaystyle\sum_{r=1}^{R} \bar{\mathfrak{f}}^{(r)}(k,q). \end{cases} \tag{4.16}$$

Like in Chapter 3, χ_c and χ_a are introduced to follow the impact of the chemical and dynamical effect respectively.

Equation 4.15 takes the form of a generalized eigenvalue problem that can be solved analytically under the quasistatic approximation ($\chi_a = 0$) but requires a numerical treatment when the dynamics terms are included ($\chi_a = 1$). Numerical resolution of the generalized eigenvalue problem for a given (k,q) provides a set of eigenvalues (whose number depends on the numerical mesh resolution), where the one corresponding to the most unstable mode is the one with largest real part. Computing the eigenvalue with largest real part for a set of (k,q), we can determine the dispersion relation $\mathrm{Re}(\lambda(k,q))$ accounting for the dynamics terms.

The numerical resolution is based on the Chebyshev collocation method, a spectral method adapted to nonperiodic problems, whose details are given in Appendix H.

4.3 QUASISTATIC APPROXIMATION STABILITY ANALYSIS

In this section, we conduct the linear stability analysis of the steady-state solution under the quasistatic approximation, as it permits the derivation of an analytical expression for the growth rate λ of a perturbation, offering clear insights into the effect of the different mechanisms, and of their interplay, on stability. Under the quasistatic approximation, the dynamics terms are cast aside ($\chi_a = 0$). (4.14) and (4.15) reduce to

$$\begin{cases} 0 = \tilde{\rho}^{(0)}_{uu} + \overline{F} - \bar{v}\tilde{\rho}^{(0)}, \\ -(\partial\tilde{\rho}^{(0)})_- = \bar{\kappa}\left[\tilde{\rho}^{(0)}_- - 1 - \chi_c\Theta(\tilde{\rho}^{(0)}_+ - \tilde{\rho}^{(0)}_-)\right], \\ (\partial\tilde{\rho}^{(0)})_+ = \bar{\kappa}S\left[\tilde{\rho}^{(0)}_+ - 1 - \chi_c\Theta(\tilde{\rho}^{(0)}_+ - \tilde{\rho}^{(0)}_-)\right], \\ \mathcal{P} = \bar{\kappa}\Theta(S+1)\left[\dfrac{\tilde{\rho}^{(0)}_- + S\tilde{\rho}^{(0)}_+}{S+1} - 1 - \Theta(\tilde{\rho}^{(0)}_+ - \tilde{\rho}^{(0)}_-)\right], \end{cases} \tag{4.17}$$

and

$$\begin{cases} 0 = (\partial_{uu}\tilde{\rho}^{(1)}) - (\bar{\nu}+q^2)\tilde{\rho}^{(1)} + (\partial_u\tilde{\rho}^{(0)})(1+(e^{ik}-1)u)q^2 \\ \qquad + 2(e^{ik}-1)(\overline{F}-\bar{\nu}\tilde{\rho}^{(0)}), \\ (e^{ik}-1)(\partial_u\tilde{\rho}^{(0)})_- - (\partial_u\tilde{\rho}^{(1)})_- \\ \qquad = \bar{\kappa}\Big[\tilde{\rho}_-^{(1)} - \chi_c\Theta(e^{ik}\tilde{\rho}_+^{(1)} - \tilde{\rho}_-^{(1)}) - e^{ik}(\mathfrak{F}_R(k,q)+\bar{\gamma}q^2)\Big], \\ -(e^{ik}-1)(\partial_u\tilde{\rho}^{(0)})_+ + (\partial_u\tilde{\rho}^{(1)})_+ \\ \qquad = \bar{\kappa}S\Big[\tilde{\rho}_+^{(1)} - \chi_c\Theta(\tilde{\rho}_+^{(1)} - e^{-ik}\tilde{\rho}_-^{(1)}) - \mathfrak{F}_R(k,q) - \bar{\gamma}q^2\Big], \\ \lambda = \bar{\kappa}\Theta\Big[C_1(q)e^{-ik}\tilde{\rho}_-^{(1)} + C_2(q)\tilde{\rho}_+^{(1)} \\ \qquad - (\mathfrak{F}_R(k)+\bar{\gamma}q^2)(S+1+\dfrac{\Pi}{\bar{\kappa}\Theta}q^2)\Big]. \end{cases} \tag{4.18}$$

4.3.1 *Prevailing justification for the quasistatic approximation*

Before proceeding with the derivation, we briefly revisit the justification for the quasistatic approximation presented in the literature.

QUASISTATIC APPROXIMATION FOR THE STEADY-STATE SOLUTION For the steady-state solution, the idea is to compare the order of magnitude of the dynamics terms in the reaction-diffusion equation $(4.14)_1$ and in the boundary conditions $(4.14)_{2,3}$ to their diffusive counterparts. Since we are working with nondimensional quantities, we estimate $\partial_u\tilde{\rho}^{(0)} \sim 1$ and $\partial_{uu}\tilde{\rho}^{(0)} \sim 1$, noting that $\tilde{\rho}^{(0)}$ is of order 1 and typically varies over a distance of 1. Therefore, the ratio of the dynamics term over its diffusive counterpart is simply $\mathcal{P}$. Likewise, the terms $\tilde{\rho}_+^{(0)}\mathcal{P}$ and $\tilde{\rho}_+^{(0)}\mathcal{P}$ are both of order $\mathcal{P}$, compared to the diffusion currents $\partial_u\tilde{\rho}^{(0)}$ of order 1.

As such, this analysis suggests that deriving the steady-state solution under the quasistatic approximation is justified in the regime of small Péclet number $\mathcal{P} \ll 1$ (Michely and Krug, 2012). However, using the quasistatic approximation, the steady-state solution in the pure deposition regime (4.19) reveals that the reasoning above for the order of magnitude of the different terms is erroneous as the terms $(\partial_u\tilde{\rho}^{(0)})_+$ and $(\partial_u\tilde{\rho}^{(0)})_-$ show a dependence with $\overline{F}$. Since $\mathcal{P} = \overline{F}\Theta$ for pure deposition conditions, a more accurate ratio between the dynamics terms and their diffusion counterpart would actually be Θ. As the adatom coverage Θ may take values up to 0.25 (see Appendix D), it is clear that the quasistatic approximation cannot be applied to arbitrary surfaces, even in the limit $\mathcal{P} \ll 1$.

QUASISTATIC APPROXIMATION FOR THE STABILITY ANALYSIS Further, in the literature, it has been assumed that the smallness of dynamics terms, a claim we just showed is actually incorrect, is sufficient for neglecting them in the derivation of the linear stability analysis. However, this is not the case and, as demonstrated in details in Section 4.4, the contribution of the dynamics

terms does not vanish as $\mathcal{P} \to 0$. As pointed out by Guin (2018), this shortcut, which consists in neglecting the dynamics terms in the stability analysis based on their supposed smallness relative to their diffusive counterparts, led to a quasi-absence of discussion in the literature of what we refer to as the *dynamical effect* on the stability of steps.

INTEREST OF THE QUASISTATIC APPROXIMATION Although the quasistatic approximation, as explained above, is not valid simply under the condition $\mathcal{P} \ll 1$, there exist particular cases where the stability results with and without the quasistatic approximation converge.[2] Most notably, the quasistatic approximation remains of interest as it allows to derive a closed-form expression for the dispersion relation, thus facilitating the analysis of the effect of the different mechanisms on stability (unlike the general stability analysis which relies on the numerical resolution of a generalized eigenvalue problem).[3]

4.3.2 *Fundamental solution*

Integrating $(4.17)_1$ yields the function $\tilde{\rho}^{(0)}$ up to the two unknown integration constants $\tilde{\rho}_+^{(0)}$ and $\tilde{\rho}_-^{(0)}$, which are then determined via $(4.17)_{2,3}$. Finally, $(4.17)_4$ is used to derive the expression of $\mathcal{P}$.

In the general case, the analytical expressions for $\tilde{\rho}^{(0)}$ and $\mathcal{P}$ are quite lengthy and we relegate them to Appendix F. However, in the case of pure deposition ($\bar{v} = 0$), they take the simple form:

$$\tilde{\rho}^{(0)}(u,t) = -\frac{1}{2}\overline{F}u(u-1) + (\tilde{\rho}_-^{(0)} - \tilde{\rho}_+^{(0)})u + \tilde{\rho}_+^{(0)}, \tag{4.19}$$

where

$$\tilde{\rho}_+^{(0)} = 1 + \frac{\overline{F}(\bar{\kappa}C_1(0)+2)}{2\bar{\kappa}B} \quad \text{and} \quad \tilde{\rho}_-^{(0)} = 1 + \frac{\overline{F}(\bar{\kappa}C_2(0)+2)}{2\bar{\kappa}B}, \tag{4.20}$$

with

$$B := 1 + S + \bar{\kappa}S. \tag{4.21}$$

The resulting propagation velocity is

$$\mathcal{P} = \overline{F}\Theta. \tag{4.22}$$

4.3.3 *Stability results*

In the general case, the linear stability analysis results in an implicit transcendental equation for the growth rate (Gillet, 2000; Liu and Metiu, 1994), as the

2 For instance, when $\overline{F} \to 0$ (or $\bar{v} \to 0$), elasticity and step stiffness, because they are energetic mechanisms which scale independently of $\overline{F}$ and $\bar{v}$, dominate while the dynamical effect, as a kinetic mechanism which scales with $\overline{F}$ (or $\bar{v}$), becomes negligible.

3 Nevertheless, we will see in Chapter 5 that it is possible to derive an *approximate* analytical form of the dispersion relation by using a different method for the stability analysis.

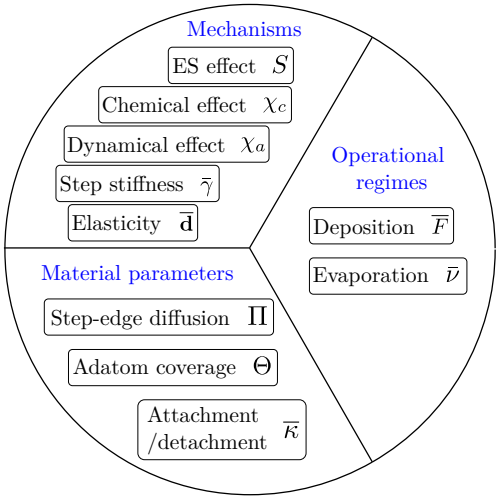

Figure 4.3: Diagram of the physical factors that determine the stability of steps, adapted from Guin (2018).

density field explicitly depends on it via the λ terms in $(4.15)_1$. Nevertheless, under the quasistatic approximation considered in this section, this dependence is absent and it is possible to derive an analytical expression for the growth rate in the form:

$$\lambda := g(k,q) - (\mathfrak{F}_R(k,q) + \bar{\gamma}q^2) f(k,q). \tag{4.23}$$

The expressions for $f(k,q)$ and $g(k,q)$ are presented and examined in detail in the next sections (see (4.24), (4.28), and (4.29)), distinguishing, as sketched in Figure 4.3, between:

1. The *mechanisms*: they are physical processes that have a stabilizing or destabilizing effect on the surface, namely the ES effect S, the chemical effect χ_c, the dynamical effect χ_a, elasticity $\overline{\mathbf{d}}$, and step stiffness $\bar{\gamma}$.
2. The *operational regimes*: they correspond to deposition and evaporation, which we consider independently. They serve to distinguish between *energetic* mechanisms, which are independent of the deposition/evaporation rates, and the *kinetic* mechanisms, which grow linearly with these rates.
3. The *material parameters*: they determine the relative weights of the different mechanisms involved and consist of the equilibrium adatom coverage Θ, the attachment/detachment coefficient $\bar{\kappa}$, and the step-edge diffusion Π.

In the stability diagrams presented, we do not directly plot λ but $\overline{\lambda} = \lambda/\mathcal{P}$ which corresponds to measuring time in terms of the number of monolayers deposited/evaporated.

STEP-STEP INTERACTION AND STEP STIFFNESS Interestingly, we note that the contributions of elastic interactions and step stiffness can be factored together. The expression for f is:

$$f(k,q) := \frac{\mathfrak{N}_1(\Lambda_q)\mathfrak{N}_2}{\mathfrak{D}} \tag{4.24}$$

where, letting $\Lambda_q := \sqrt{\bar{\nu} + q^2}$,

$$\begin{cases} \mathfrak{N}_1(x) := \bar{\kappa}(S+1)\Lambda_q \cosh(x) + (x^2 + \bar{\kappa}^2 S)\sinh(x) \\ \qquad\qquad - \chi_c \Theta \bar{\kappa}(S-1)\Lambda_q(\cosh(x) - \cos(k)), \\ \mathfrak{N}_2 := \bar{\kappa}\Lambda_q(2\bar{\kappa}S\Theta(\cosh(\Lambda_q) - \cos(k)) + \Pi q^2(S+1)\cosh(\Lambda_q)) \\ \qquad\qquad + (\bar{\kappa}(S+1)\Theta\Lambda_q^2 + \Pi q^2(\Lambda_q^2 + \bar{\kappa}^2 S))\sinh(\Lambda_q), \\ \mathfrak{D} := \mathfrak{N}_1^2 + (\chi_c \Theta \bar{\kappa}\Lambda_q(S+1))^2 \sin^2(k). \end{cases} \tag{4.25}$$

Clearly, $\mathfrak{N}_2$ and $\mathfrak{D}$ are always positive. As for $\mathfrak{N}_1$, the additional condition $\Theta \leqslant 0.5$ (always satisfied in practice) is required to obtain positiveness. Therefore, as expected, step stiffness is stabilizing and has as a smoothening effect on the step profiles by preventing the formation of high-q modes, i. e., short-wavelength meanders.

Regarding step-step elastic interactions, we see by (4.24) that their influence on stability is determined by the sign of $\mathfrak{F}_R$: $\mathfrak{F}_R > 0$ corresponds to a repulsive, stabilizing, interaction and $\mathfrak{F}_R < 0$ to an attractive, destabilizing, one. To elucidate the sign of the expression, we restrict the study to nearest-neighbor interactions, i. e., $R = 1$, and start by analyzing the influence of each dipole moment acting independently. A first important observation is that d_{xx} and d_{xz} have similar behaviors. For low enough k and q, there is a region where $\mathfrak{f}^{(1)}$ changes sign, which entails that the elastic interaction shifts from repulsive to attractive.

Regarding d_{yy}, the diagram is split into four zones. At low q, $\mathfrak{f}^{(1)}$ is positive (repulsive) for $k < \pi/2$ and negative (attractive) for $k > \pi/2$. There exists a critical value of q for which the effect of the interaction is reversed. However, it is again unlikely that such a short-wavelength meander develops as it is prevented by step stiffness for all practical purposes.

To study in more details the existence of unstable modes when all moments d_{xx}, d_{yy}, and d_{xz} are present, we set d_{xx} and explore the space $(d_{yy}/d_{xx}, d_{xz}/d_{xx})$ looking for the most unstable mode, under the assumption of *reasonable* meandering wavelength, i. e., restricting q such that $q \leqslant q_c$. We consider $q_c = 0.01$, $q_c = 0.1$ and $q_c = 1$. As the resulting diagrams are qualitatively similar, we only show the case $q_c = 1$ in Figure 4.5. Indeed, regardless of the value of q_c, we observe a band of stability, for which the elastic interaction is always repulsive, that separates two unstable regions, one with in-phase meanders, the other with anti-phase ones. Interestingly, the left boundary of this stable region is independent of q_c (for $q_c \lesssim 0.5$), while the right boundary gets pushed further to the right with decreasing q_c. Based on Equation 4.11 we can shed light on this behavior. For in-phase modes ($k = 0$), the term of order 0 vanishes, so that all contributions scale identically as q^2. Consequently, the sign of $\mathfrak{f}^{(1)}$, and thus its stabilizing/destabilizing behavior, is only determined by the sign of $\bar{\alpha}_1$, which explains why the left boundary of the stable region in Figure 4.5 is independent of q_c. On the other hand, for anti-phase modes ($k = \pi$), the term of order 0, to which only d_{xx} and d_{xz} contribute, is maximally stabilizing, whereas the destabilizing contribution of d_{yy} still scales quadratically with q. As such, for decreasing values of q_c, d_{yy} must take increasingly large values to

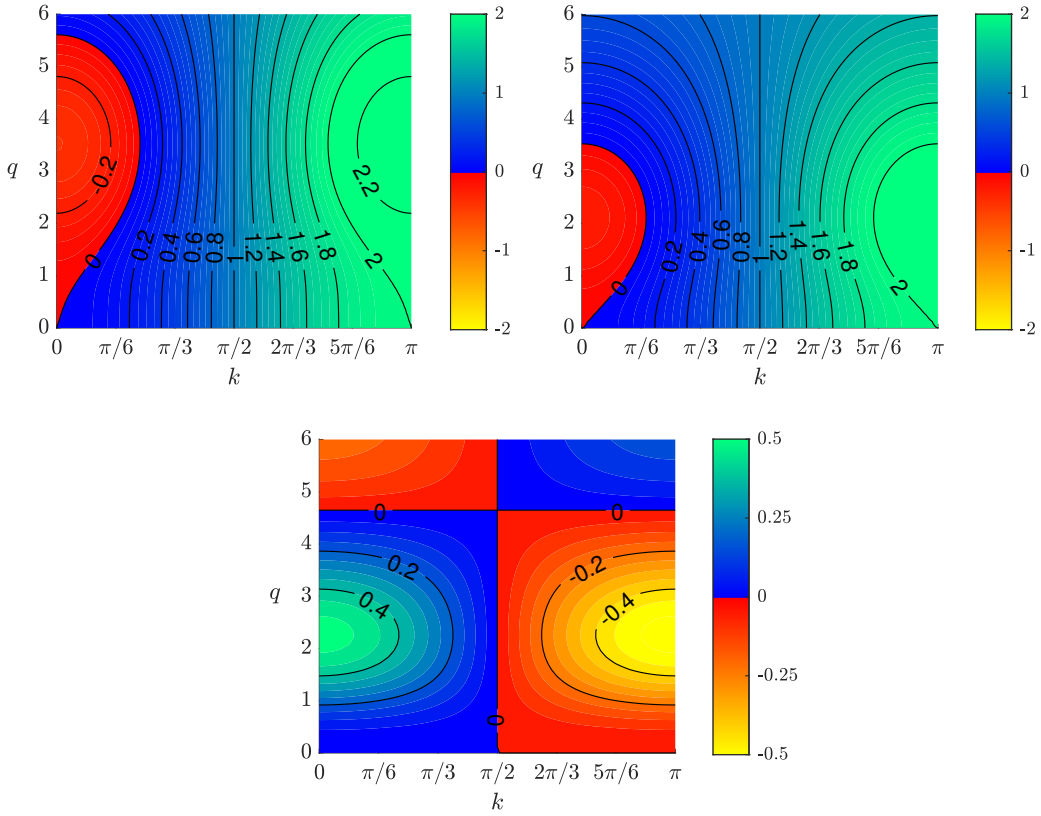

Figure 4.4: Contour plots of $\pi E/24(1-\nu^2) \times \mathfrak{f}^{(1)}$ for $\nu = 0.3$ in the presence of (a) d_{xx} only, (b) d_{xz} only, and (c) d_{yy} only. The red-yellow scale corresponds to an attractive interaction (unstable), the blue-green scale to a repulsive one (stable).

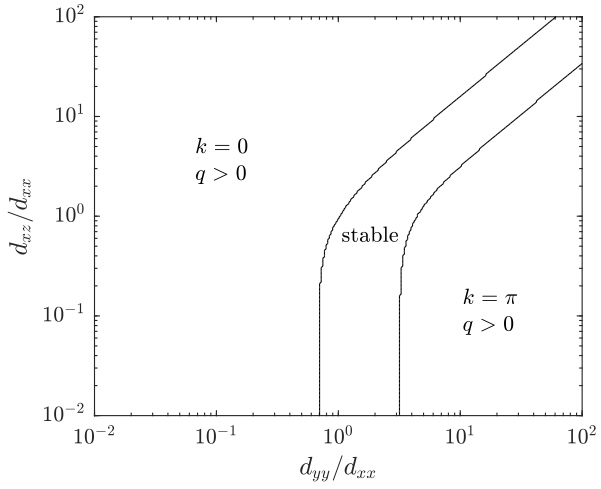

Figure 4.5: Most unstable modes of $\mathfrak{f}^{(1)}$ for $\nu = 0.3$ and $q_c = 1$.

compensate, hence why the right boundary of the stable region in Figure 4.5 is pushed to the right with decreasing q_c.

Moreover, Equation 4.11 also furnishes an explanation for the shape of the region. Indeed, the left and right boundaries essentially correspond to $\bar{\alpha}_1 = 0$ and $24\bar{\alpha}_0 - \bar{\alpha}_1 q^2 = 0$, resp., i. e., for $q_c \ll 1$

$$\begin{cases} d_{yy}^{\text{left}} &= \nu + \sqrt{\dfrac{1-\nu}{2}(1 - 2\nu + d_{xz}^2)} & \text{(left boundary)}, \\ d_{yy}^{\text{right}} &= \dfrac{2\sqrt{3(1-\nu)(1+d_{xz}^2)}}{q_c} & \text{(right boundary)}. \end{cases} \tag{4.26}$$

Note how, as expected, d_{yy}^{left} is independent of q_c while d_{yy}^{right} is proportional to q_c^{-1}. Further, for $d_{xz} \ll 1$, these expressions are independent of d_{xz}, corresponding to the vertical part of the stability band in the diagram, while for $d_{xz} \gg 1$, they scale linearly with d_{xz}, explaining the slope of 1. This again illustrates the fact that d_{xx} and d_{xz} play comparable roles. As long as either d_{xx} or d_{xz} dominates over d_{yy}, the elastic interaction destabilizes in-phase meandering, so that the determining parameter really is $\max(d_{xx}, d_{xz})$. For convenience, we assume $d_{xz} = 0$. If on the contrary d_{yy} dominates the two other dipole moments, in-phase meandering is always stable and only anti-phase meanders may be destabilized.

On Si, estimations are $d_{xx} = 15$ eV/nm and $d_{xz} = 6$ eV/nm, i. e., $d_{xz}/d_{xx} = 6/15 = 0.4$ (Stewart et al., 1994). Therefore, an attractive interaction may theoretically exist depending on the value of d_{yy}. Unfortunately, the studies dedicated to the determination of the step dipolar moments are generally restricted to straight steps, for which the moment d_{yy} plays no role, and we are not aware of any study that tries to determine this parameter. While the anisotropy required ($d_{yy}/d_{xx} \sim 0.7$) for an unstable mode to exist could be realistically reached, we will see that even in that case, the effect of the step-step interaction is mostly negligible compared to the stabilizing influence of step stiffness.

As illustrated in Figure 4.6, we verify that taking into account more neighboring steps (described by the parameter R) has no influence on the conclusion of the previous analysis. Additionally, in agreement with Guin et al. (2021b), we note that including only the nearest-neighbor in the calculation of the step-step interaction is already a very good approximation. For $R \geqslant 2$, the boundaries of the stable domain are basically indistinguishable.

In conclusion, the effect of elasticity is contingent on the ratio $r_d = \frac{\max(d_{xx}, d_{xz})}{d_{yy}}$. For $r_d \ll 1$ or $r_d \gg 1$, there exists an unstable region for which the elastic interaction is attractive while for $r_d \sim 1$ it is always repulsive, and thus stabilizing. The dispersion curves of Figure 4.7 and Figure 4.8 illustrate this result further. Once again, notice how the unstable region in the case $r_d \gg 1$ (corresponding to $(\bar{d}_{xx}, \bar{d}_{yy}) = (0.1, 0)$) has a very small growth rate, which would not lead to a developed instability in a reasonable amount of time in practice. Likewise, in the case of $r_d \ll 1$ (corresponding to $(\bar{d}_{xx}, \bar{d}_{yy}) = (0, 0.1)$), while the growth rate is not negligible in absolute terms, we show that it is still often negligible relative to step stiffness.

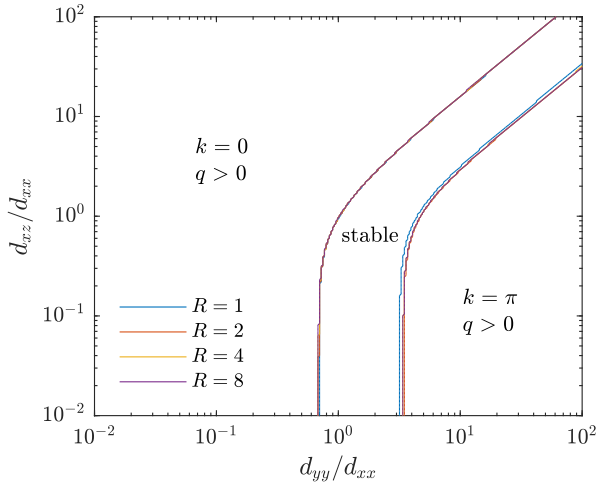

Figure 4.6: Most unstable modes of $\sum_{1\leqslant r\leqslant R} \mathfrak{f}^{(r)}$ for $\nu = 0.3$ and $q_c = 1$.

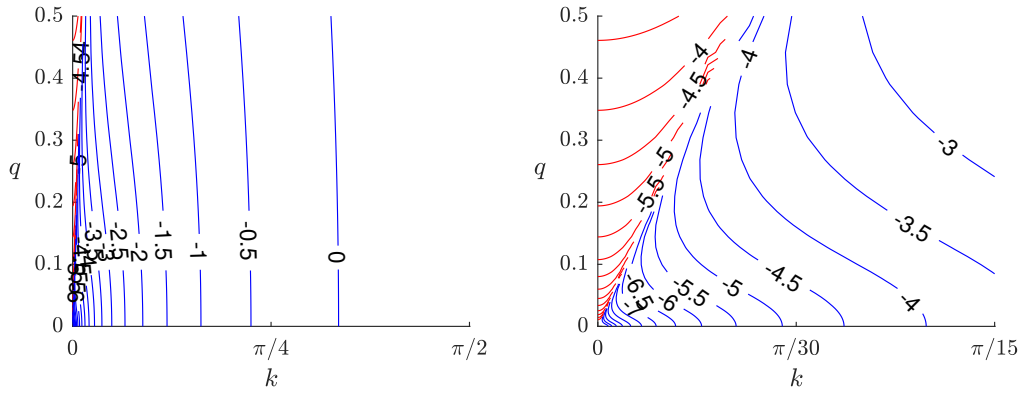

(a) $0 \leqslant k \leqslant \pi$ (b) $0 \leqslant k \leqslant \pi/10$

Figure 4.7: Dispersion curves $\mathrm{Re}(\lambda(k,q))$ associated to the elastic interaction for $(\bar{d}_{xx}, \bar{d}_{yy}) = (0.1, 0)$. The isolines show the logarithm of the absolute value of the growth rate. The red isolines correspond to a positive growth rate, i. e., an unstable system, and the blue isolines correspond to a negative growth rate, i. e., a stable system. Parameters: $\chi_a = \chi_c = 0$, $\overline{F} = 10^{-4}$, $\Theta = 0.1$, $S = 1$, $\bar{\kappa} = 1$, $\bar{\gamma} = 0$, $\Pi = 0$.

Indeed, based on dimensional analysis, $\alpha \propto Ea^4$ while $\tilde{\gamma} \propto Ea^2$ (Ihle et al., 1998; Paulin et al., 2001), and thus $\bar{\alpha}/\bar{\gamma} \sim (a/\mathcal{L}_0)^2 \ll 1$ as a is typically a few tenths of nanometers whereas $\mathcal{L}_0$ is in the range of tens of nanometers. Alternatively, using direct experimental estimates from Jeong and Williams (1999), we can determine an upper bound for the ratio, reached for semi-conductors:

$$\frac{\bar{\alpha}}{\bar{\gamma}} \sim \frac{\alpha}{\gamma \mathcal{L}_0^2} \lesssim \frac{3}{0.3 \times \mathcal{L}_0^2} = \frac{10}{\mathcal{L}_0^2}, \tag{4.27}$$

meaning that elasticity effects will be negligible compared to step stiffness in all situations, except for very narrow terraces ($\mathcal{L}_0 \lesssim 10$ nm).

To be more accurate, this conclusion applies directly to the competition between d_{yy} and step stiffness, as both effects carry a q^2 factor, but needs to

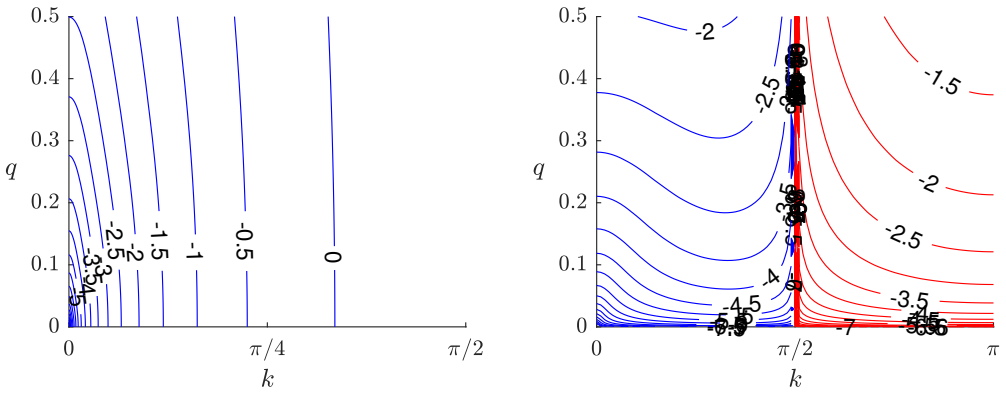

(a) $(\bar{d}_{xx}, \bar{d}_{yy}) = (0.1, 0.1)$ (b) $(\bar{d}_{xx}, \bar{d}_{yy}) = (0, 0.1)$

Figure 4.8: Dispersion curves $\mathrm{Re}(\lambda(k,q))$ associated to the elastic interaction for (a) $(\bar{d}_{xx}, \bar{d}_{yy}) = (0.1, 0.1)$ and (b) $(\bar{d}_{xx}, \bar{d}_{yy}) = (0, 0.1)$. Parameters: $\chi_a = \chi_c = 0$, $\bar{F} = 10^{-4}$, $\Theta = 0.1$, $S = 1$, $\bar{\kappa} = 1$, $\bar{\gamma} = 0$, $\Pi = 0$. [see color legend in Figure 4.7]

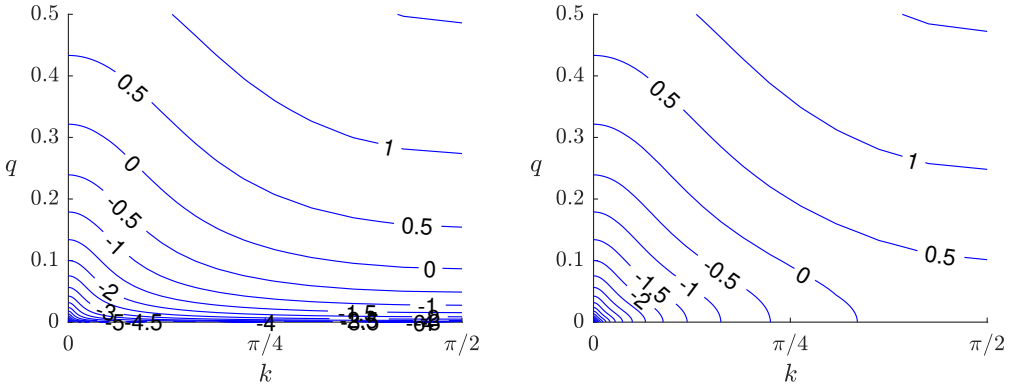

(a) $\bar{d}_{xx} = 0$ (b) $\bar{d}_{xx} = 0.1$

Figure 4.9: Dispersion curve $\mathrm{Re}(\lambda(k,q))$ associated to the total contribution of d_{xx} and step stiffness. Parameters: $\chi_a = \chi_c = 0$, $\bar{F} = 10^{-4}$, $\Theta = 0.1$, $S = 1$, $\bar{\kappa} = 1$, $\bar{d}_{yy} = 0$, $\bar{\gamma} = 10^{-2}$, $\Pi = 0$. [see color legend on Figure 4.7]

be nuanced for d_{xx}. Indeed, the elastic interaction associated to d_{xx} maximally stabilizes straight steps, i. e., the $q = 0$ mode. Consequently, as can be seen from Figure 4.9, for small enough q, the contribution of d_{xx} dominates and further stabilizes quasi-straight steps. However, beyond that small region it has minimal impact and step stiffness dominates instead.

EHRLICH-SCHWOEBEL EFFECT The results for an arbitrary Ehrlich-Schwoebel barrier, in the absence of the chemical effect, have long been known (Bales and Zangwill, 1990) and g reads:

$$\begin{aligned} g_{ES}(k,q) = &-(\overline{F}-\bar{\nu})(S-1)\frac{\Theta\bar{\kappa}^2}{\sqrt{\bar{\nu}}\mathfrak{N}_1(\sqrt{\bar{\nu}})\mathfrak{N}_1(\Lambda_q)} \\ &\times\Big[\bar{\nu}\Lambda_q(S+1)(\cosh(\sqrt{\bar{\nu}})\cosh(\Lambda_q)-\cos(k)) \\ &\quad+(\bar{\kappa}q^2S(\cosh(\sqrt{\bar{\nu}})-1)-\sqrt{\bar{\nu}}\Lambda_q\sinh(\sqrt{\bar{\nu}}))\sinh(\Lambda_q)\Big]. \end{aligned} \tag{4.28}$$

Therefore, under deposition ($\bar{\nu}=0$), a direct ES effect ($S>1$) stabilizes straight-step bunching modes (the most stabilized one being the step-pairing mode $(k,q)=(\pi,0)$) and destabilizes in-phase meandering modes ($k=0$). For an inverse ES effect ($S<1$), the opposite holds: it destabilizes straight-step bunching modes (the most destabilized one being the step-pairing mode) and stabilizes in-phase meandering modes. Under evaporation ($\overline{F}=0$), the effects of the direct and inverse ES barriers are reversed (Figure 4.10).

CHEMICAL EFFECT In the case of symmetric attachment/detachment barriers ($S=1$), g reads:

$$\begin{aligned} g_{CE}(k,q) = &\,4\chi_c\Theta\bar{\kappa}(\overline{F}-\bar{\nu})\frac{\mathfrak{N}_2\mathfrak{N}_3}{\sqrt{\bar{\nu}}\mathfrak{N}_1(\sqrt{\bar{\nu}})\mathfrak{D}} \\ &\times\Big[\sqrt{\bar{\nu}}\cosh(\sqrt{\bar{\nu}}/2)(\Lambda_q\cosh(\Lambda_q)+\bar{\kappa}\sinh(\Lambda_q)) \\ &\quad-\Lambda_q\sinh(\sqrt{\bar{\nu}}/2)(\bar{\kappa}\cosh(\Lambda_q)+\Lambda_q\sinh(\Lambda_q)) \\ &\quad-\Lambda_q\mathfrak{N}_3\cos(k)\Big], \end{aligned} \tag{4.29}$$

with

$$\mathfrak{N}_3=\sqrt{\bar{\nu}}\cosh(\sqrt{\bar{\nu}}/2)+\bar{\kappa}\sinh(\sqrt{\bar{\nu}}/2). \tag{4.30}$$

It is worth noting that under deposition, the least stable mode is anti-phase ($k=\pi$), while under evaporation, it is in-phase ($k=0$), and in that regard the chemical effect behaves qualitatively as an inverse ES barrier (see Figure 4.11).

STEP-EDGE DIFFUSION We note that step-edge diffusion has no impact on the stability by itself, in the sense that it does not affect stability when other mechanisms are disabled ($S=1$, $\chi_c=0$, $\bar{\mathbf{d}}=\mathbf{0}$, and $\bar{\gamma}=0$): it is absent from the expression of g_{ES} and its contribution in f and g_{CE}, through the term $\mathfrak{N}_2$, does not change the sign of the expression. Further, since $\mathfrak{N}_2$ can be factored out of f and g_{CE}, we conclude that even in the presence of elasticity, step-stiffness, and/or the chemical effect, step-edge diffusion still has no impact on the stability domain. As we will see, this conclusion does not hold when including an ES barrier or the dynamical effect, due to the different dependence on Π of these mechanisms. In addition, while the boundary of the instability domain in the (k,q) space may be unaffected by step-edge diffusion, the most unstable mode can be strongly impacted.

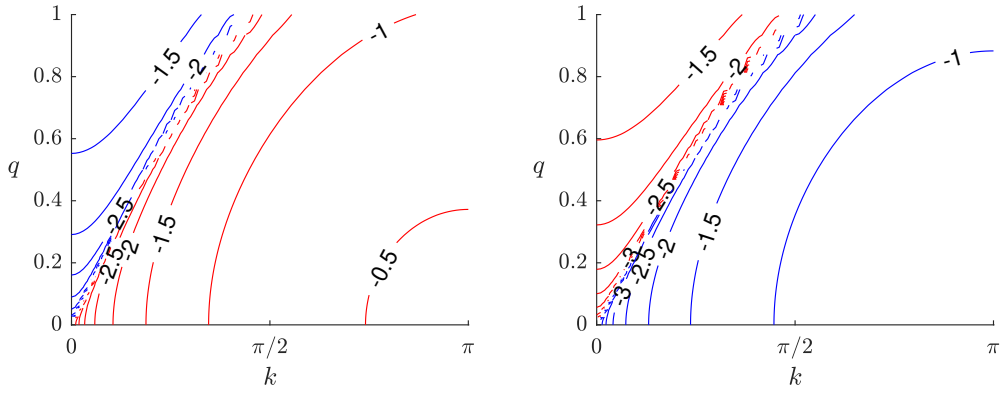

(a) Deposition, $S = 0.5$ (b) Deposition, $S = 2$

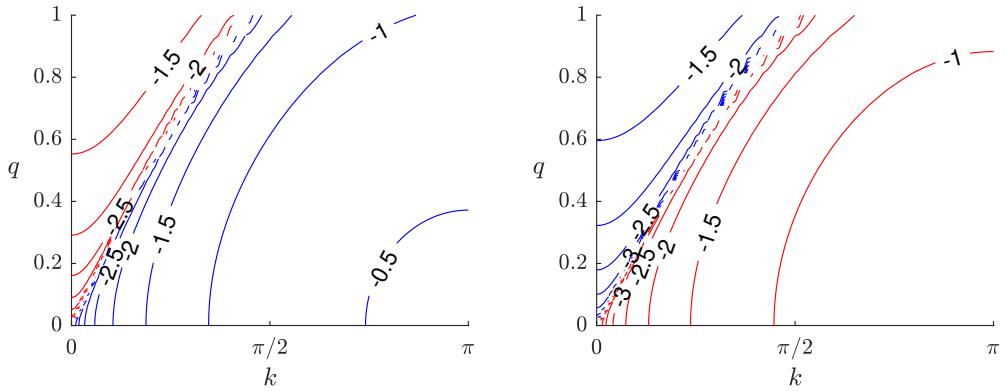

(c) Evaporation, $S = 0.5$ (d) Evaporation, $S = 2$

Figure 4.10: Dispersion curves $\mathrm{Re}(\lambda(k,q))$ associated to the ES effect, i. e., $g_{ES}(k,q)$. All mechanisms other than the ES effect are disabled: $\chi_a = \chi_c = 0$, $\overline{F} = 10^{-4}$, $\Theta = 0.1$, $\bar{\kappa} = 1$, $\tilde{\mathbf{d}} = \mathbf{0}$, $\bar{\gamma} = 0$, $\Pi = 0$. [see color legend in Figure 4.7]

4.3.4 *Influence of the operational and material parameters*

The actual stability of a vicinal surface is the result of the interplay of the different mechanisms which were studied independently in the previous section. Here, we discuss how the relative weight of each effect, ruled by the operational ($\overline{F}$ and $\bar{\nu}$) and material (Θ, $\bar{\kappa}$, and Π) parameters, affects the overall stability.

DEPOSITION $\overline{F}$ AND EVAPORATION $\bar{\nu}$ The deposition ($\overline{F}$) and evaporation ($\bar{\nu}$) parameters distinguish between the *kinetic* mechanisms, characteristic of out-of-equilibrium evolution, and the *energetic* ones. As seen from (4.24), (4.28), and (4.29), the growth rate associated with the ES effect and the chemical effect is proportional, for $\bar{\nu} \ll 1$, to $\overline{F} - \bar{\nu}$ (they are kinetic mechanisms), unlike the contribution of the elastic interaction and step stiffness which is independent of $\overline{F} - \bar{\nu}$ (for $\bar{\nu} \ll 1$), as expected from energetic mechanisms. Hence as the net deposition flux increases, kinetic mechanisms become more prominent compared to energetic mechanisms.

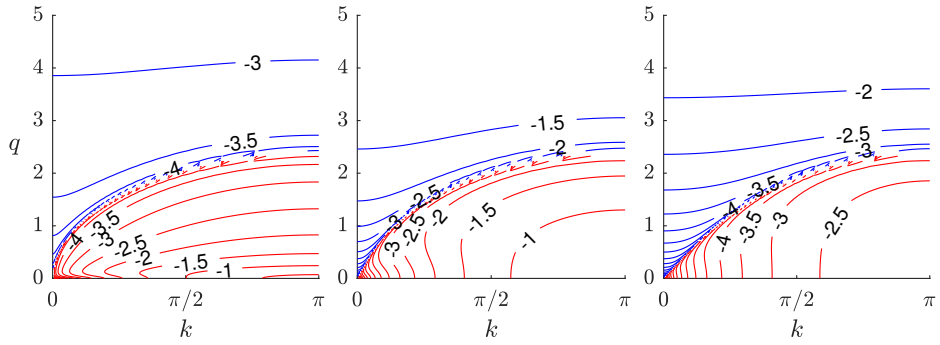

(a) Deposition ($\overline{F} = 10^{-4}, \bar{\nu} = 0$).

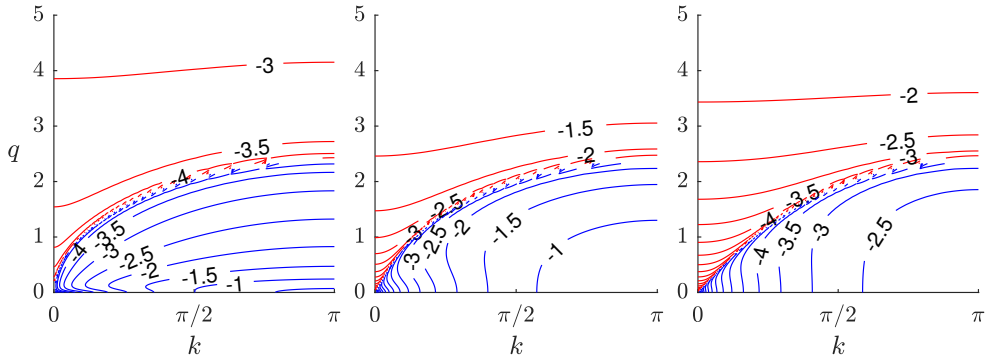

(b) Evaporation ($\overline{F} = 0, \bar{\nu} = 10^{-4}$).

Figure 4.11: Dispersion curves $\mathrm{Re}(\lambda(k,q))$ associated to the chemical effect, i.e., $g_{CE}(k,q)$. From left to right, $\bar{\kappa} = 0.01$, $\bar{\kappa} = 1$, $\bar{\kappa} = 100$. All mechanisms other than the chemical effect are disabled: $S = 1$, $\Theta = 0.1$, $\bar{\mathbf{d}} = \mathbf{0}$, $\bar{\gamma} = 0$, $\Pi = 0$. [see color legend in Figure 4.7]

EQUILIBRIUM ADATOM COVERAGE Θ The equilibrium adatom coverage Θ differentiates between the chemical effect, whose associated growth rate scales as Θ^2, and the other mechanisms, whose scaling is linear in Θ. This is consistent with the stability diagrams (Figure 4.12), as we indeed notice that for low values of Θ, the chemical effect becomes negligible. At higher values of Θ, it it interesting to note that, under deposition, the presence of the chemical effect modifies the critical S that separates in-phase meandering from straight-step pairing, while under evaporation, the critical $S = 1$ is unchanged with only an impact on the wavenumbers (k, q) of the most unstable mode. To summarize, the chemical effect will have a stronger influence on materials with a high adatom coverage such as GaAs(001) or Si(111) $-$ 1 $\times$ 1 for which experimental observations place Θ between 0.1 and 0.2.

ATTACHMENT/DETACHMENT KINETICS COEFFICIENT $\bar{\kappa}$ The scaling with the attachment/detachment kinetics coefficient $\bar{\kappa}$ is not as straightforward and we focus our attention on the two limiting cases $\bar{\kappa} \ll 1$ and $\bar{\kappa} \gg 1$. In the

4 We speak of "effective" stability in the sense that the surface might *theoretically* be unstable in the white region but with such a small growth rate ($\lambda \leqslant 10^{-5}$) that the instability would take a nonphysical amount of time to develop and can therefore not be observed.

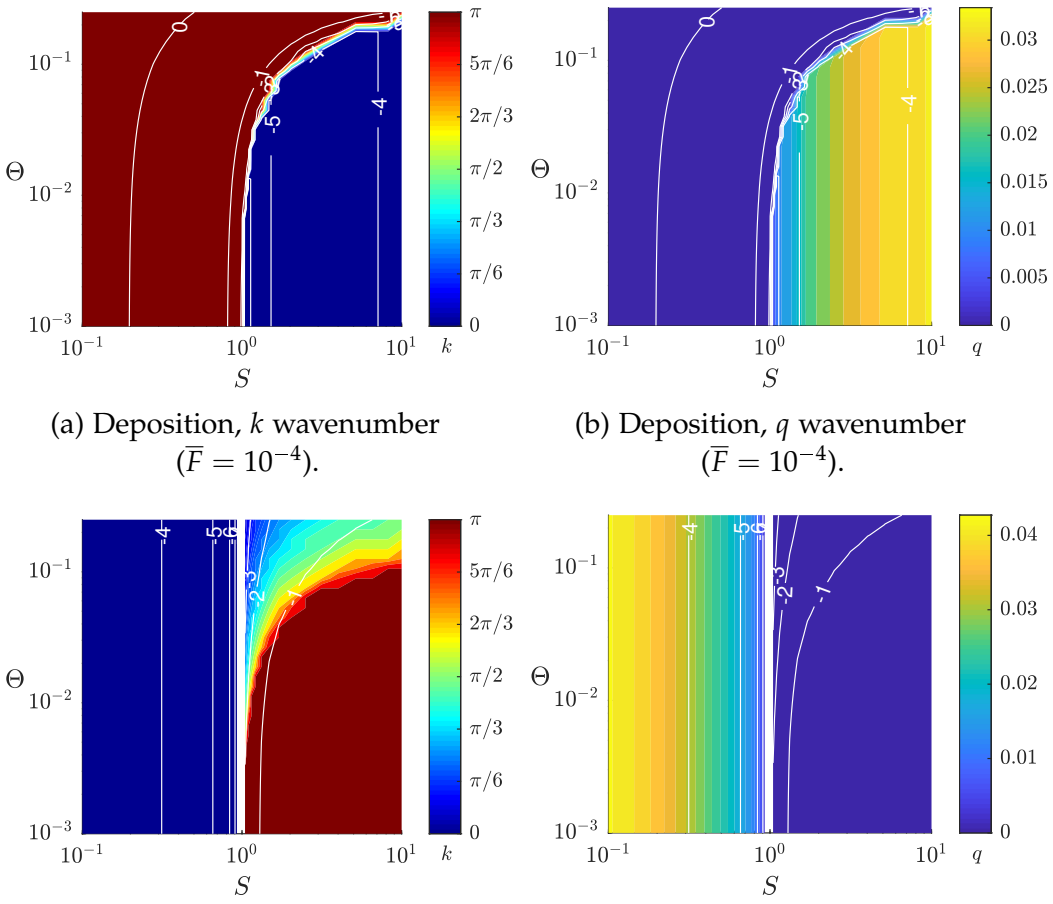

(a) Deposition, k wavenumber ($\overline{F} = 10^{-4}$).

(b) Deposition, q wavenumber ($\overline{F} = 10^{-4}$).

(c) Evaporation, k wavenumber ($\bar{\nu} = 10^{-4}$).

(d) Evaporation, q wavenumber ($\bar{\nu} = 10^{-4}$).

Figure 4.12: Stability diagrams showing the q and k wavenumbers of the most unstable mode as a function of S and Θ for pure deposition and pure evaporation conditions. The white region is "effectively" stable[4], the colored region is unstable, such that the isolines represent the logarithm of the growth rate and the color gradient represents the wavenumber. Parameters $\bar{\kappa} = 1$, $\bar{\gamma} = 10^{-2}$, $\bar{\alpha} = 0$, $\Pi = 0$.

kinetically limited regime ($\bar{\kappa} \ll 1$), ignoring step-edge diffusion, we find that the energetic mechanisms (elastic interaction and step stiffness) are linear in $\bar{\kappa}$ while the kinetic mechanisms are quadratic in $\bar{\kappa}$. In the diffusion-limited regime ($\bar{\kappa} \gg 1$), the scaling of the energetic mechanisms becomes independent of $\bar{\kappa}$ and that of the kinetic mechanisms proportional to $\bar{\kappa}^{-1}$, or even $\bar{\kappa}^{-2}$ for the bunching modes ($q = 0$) of the ES effect. Overall, the magnitude of the energetic mechanisms is always greater than that of the kinetic mechanisms, and we verify that this conclusion also holds when including step-edge diffusion, although the specific scaling relations are modified. This is consistent with the fact that the kinetic mechanisms logically have more influence when the surface evolution is kinetically controlled and become irrelevant compared to the energetic mechanisms when attachment/detachment kinetics are not the limiting process.

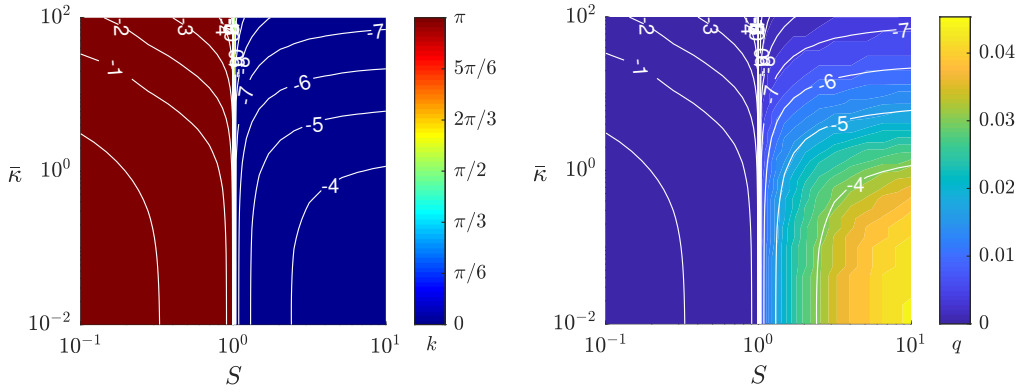

(a) Standard BCF, k wavenumber.

(b) Standard BCF, q wavenumber.

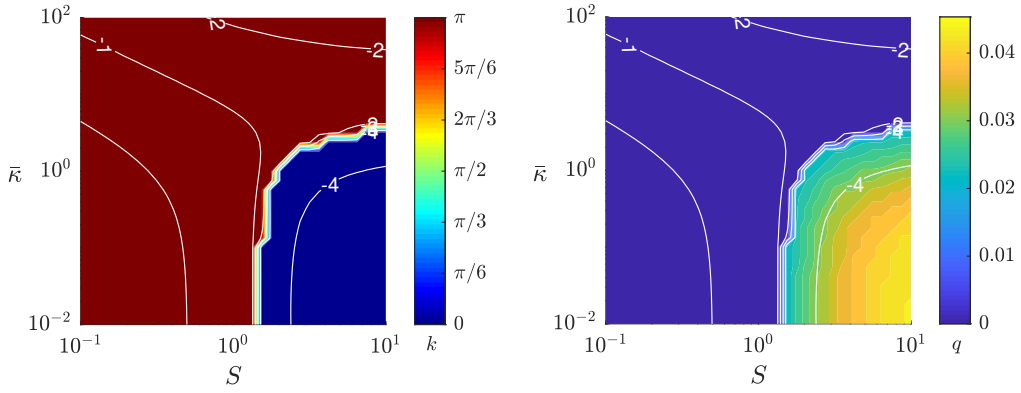

(c) Chemical effect, k wavenumber.

(d) Chemical effect, q wavenumber.

Figure 4.13: Stability diagrams showing the q and k wavenumbers of the most unstable mode as a function of S and $\bar{\kappa}$ for pure deposition with and without the chemical effect. Parameters $\overline{F} = 10^{-4}$, $\Theta = 0.1$, $\bar{\gamma} = 10^{-2}$, $\bar{\alpha} = 0$, $\Pi = 0$. [see color legend on Figure 4.12]

Taking a closer look at the stability diagrams in Figure 4.13, we can further analyze the role of $\bar{\kappa}$. For instance, in the absence of chemical effect and elastic interaction, the stability is independent of $\bar{\kappa}$, which only influences the growth rate and wavenumbers of the most unstable mode. However, with the chemical effect, the stability diagram is profoundly modified. For slow kinetic ($\bar{\kappa} \ll 1$), the critical value of S to switch from bunching to meandering is increased. And for fast kinetics ($\bar{\kappa} \gg 1$), the most unstable mode remains straight-step pairing even for a strong direct ES effect. The dispersion curves at $(S, \bar{\kappa}) = (5, 0.4)$, $(S, \bar{\kappa}) = (5, 4)$, and $(S, \bar{\kappa}) = (5, 40)$ allow to better understand the stability diagram (Figure 4.14). They show that the in-phase meandering mode is always present but for sufficiently fast kinetics and strong direct ES effect, a second, more unstable, region of straight-step pairing appears with a greater growth rate. In particular, this implies that there exists a set of parameters for which the in-phase meandering mode and the straight-step pairing mode are equally unstable.

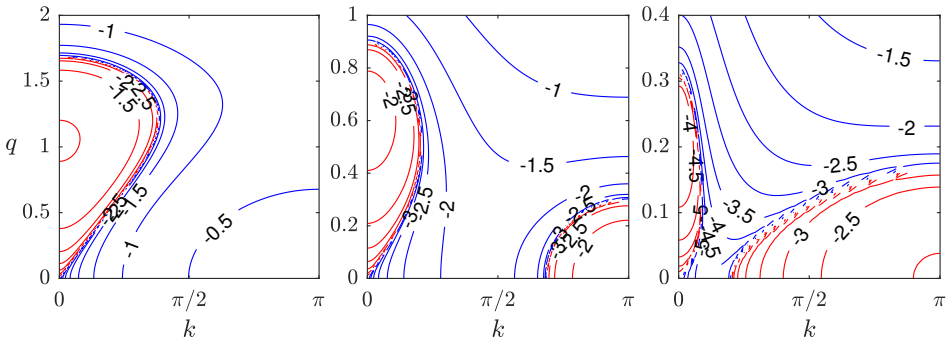

Figure 4.14: Dispersion curves associated to Figure 4.13 at points $(S, \bar{\kappa}) = (5, 0.4)$, $(S, \bar{\kappa}) = (5, 4)$, and $(S, \bar{\kappa}) = (5, 40)$, from left to right. Here, $\bar{\gamma}$ was set to 10^{-5} to make both unstable regions visible. With $\bar{\gamma} = 10^{-2}$, the diagram is qualitatively similar but the in-phase meandering unstable region is so narrow that it is barely visible when k spans $(0, \pi)$. Note the different vertical scales. [see color legend on Figure 4.7]

STEP-EDGE DIFFUSION Step-edge diffusion establishes a distinction between the ES effect, which is independent of Π, and the other mechanisms which vary linearly with Π (this is for $q > 0$ as the effect of step-edge diffusion is proportional to q^2).

Moreover, as previously mentioned, step-edge diffusion can have a strong effect on the mode of the instability. For example, under deposition, the most unstable mode is always anti-phase ($k = \pi$) but there exists a critical value of Π for which it changes from straight-step pairing ($q = 0$, $k = \pi$) to anti-phase meandering ($q > 0$, $k = \pi$) as illustrated in Figure 4.15. This is consistent with the fact that step-edge diffusion only appears in the dispersion relation combined to a positive factor multiplied by q^2, thus favoring meandering modes ($q > 0$) for the instability.

Under evaporation, step-edge diffusion does not exhibit the same special behavior as the most unstable mode is already in-phase meandering for $\Pi = 0$, and stays as such for $\Pi > 0$. Besides, for typical values of $\bar{\gamma} \sim 0.01$ and $\bar{\nu} \sim 10^{-6}$, step stiffness completely stabilizes the steps under evaporation.

4.4 GENERAL STABILITY ANALYSIS INCLUDING DYNAMICS TERMS

The impact of the dynamical effect on step-bunching has been extensively reviewed by Guin et al. (2021a). In this section, we extend this review to include meandering modes.

Under deposition, the dynamical effect always stabilizes large q wavenumbers. For smaller q wavenumbers, an unstable region is present, whose most unstable mode shifts from $k = \pi/2$ in the kinetic-limited regime $\bar{\kappa} \ll 1$ to $k \to 0$ in the diffusion-limited regime $\bar{\kappa} \gg 1$, as shown in Figure 4.16. Under evaporation, the stable and unstable domains are switched.

In the case of deposition in the diffusion-limited regime ($\bar{\kappa} \gg 1$), we should mention that, while the growth rate is theoretically positive and the system of steps is thus unstable, its value is so small that physically the associated

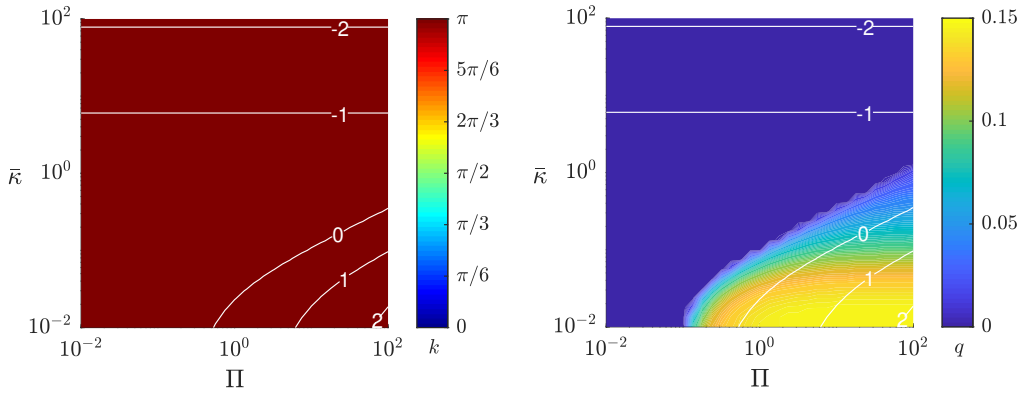

(a) k wavenumber (b) q wavenumber

Figure 4.15: Stability diagrams showing the (k, q) wavenumbers of the most unstable mode as a function of Π and $\bar{\kappa}$ for pure deposition conditions ($\bar{\nu} = 0$). Parameters $\overline{F} = 10^{-4}$, $\Theta = 0.1$, $S = 1$, $\bar{\alpha} = 0$, $\bar{\gamma} = 10^{-2}$. [see color legend on Figure 4.12]

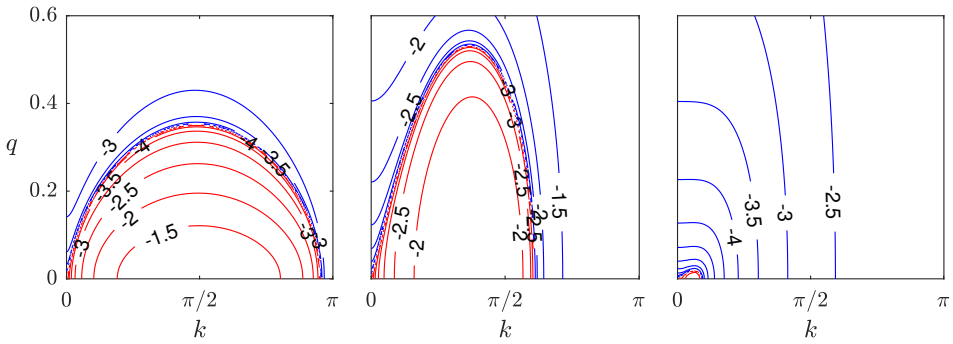

(a) Deposition ($\overline{F} = 10^{-4}$, $\bar{\nu} = 0$)

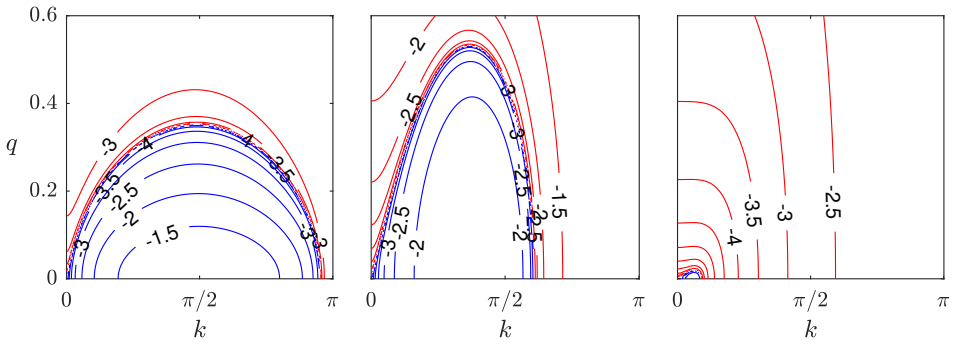

(b) Evaporation ($\overline{F} = 0$, $\bar{\nu} = 10^{-4}$)

Figure 4.16: Dispersion curves $\mathrm{Re}(\lambda(k, q))$ associated to the dynamical effect. From left to right, $\bar{\kappa} = 0.01$, $\bar{\kappa} = 1$, $\bar{\kappa} = 100$. All mechanisms other than the dynamical effect are disabled: $S = 1$, $\bar{\alpha} = 0$, $\bar{\gamma} = 0$, $\Pi = 0$, $\Theta = 0.1$, $\bar{\nu} = 10^{-4}$. [see color legend on Figure 4.7]

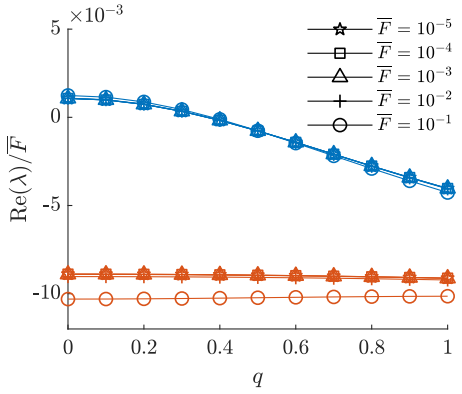

(a) Deposition: scaling with $\overline{F}$.

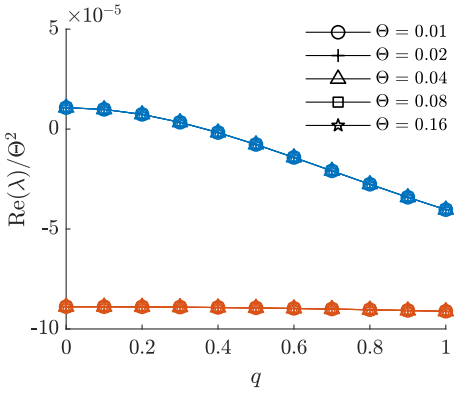

(b) Deposition: scaling with Θ.

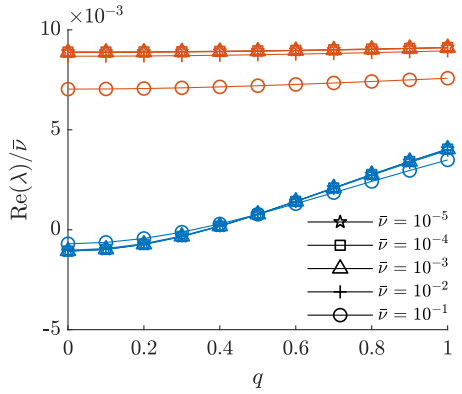

(c) Evaporation: scaling with $\bar{\nu}$.

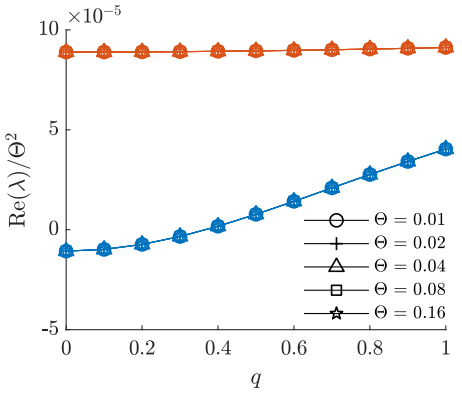

(d) Evaporation: scaling with Θ.

Figure 4.17: Scaling of the dispersion curves with $\overline{F}$, $\bar{\nu}$, and Θ ($\bar{\kappa} = 1$, $S = 1$, $\bar{\alpha} = 0$, $\bar{\gamma} = 0$, $\Pi = 0$, $\chi_a = 1$, $\chi_c = 0$). The set of blue curves correspond to $k = \pi/6$ and orange curves to $k = \pi$. Deposition ($\bar{\nu} = 0$) with (a) $\Theta = 0.1$ and (b) $\overline{F} = 10^{-4}$. Evaporation ($\overline{F} = 0$) with (c) $\Theta = 0.1$ and (d) $\bar{\nu} = 10^{-4}$.

instability might not develop in the typical time scale of the deposition. For instance, for a growth rate of 10^{-6}, the deposition of almost 7×10^5 ML (e.g., over 200 µm of Si) would be necessary to simply double the amplitude of an initial perturbation. Likewise, under evaporation, the stable region for fast attachment/detachment kinetics is likely larger in practice than portrayed in the theoretical diagram.

Like in the straight-step context, the growth rate is proportional to $\overline{F}$ ($\bar{\nu}$) under deposition (evaporation) for $\overline{F} \ll 1$ ($\bar{\nu} \ll 1$) and proportional to Θ^2 (Figure 4.17), which is the same as the chemical effect. Note that for $\overline{F} \gtrsim 10^{-1}$ and $\bar{\nu} \gtrsim 10^{-1}$ the scaling loses validity, particularly for $k = \pi$ (Figure 4.17). While no exact analytical expression is available for the growth rate when the dynamical effect is included, we derive in Chapter 5 an approximate expression using the *transpiration method* for the stability analysis that is consistent with the scaling laws observed numerically with the Chebyshev collocation method.

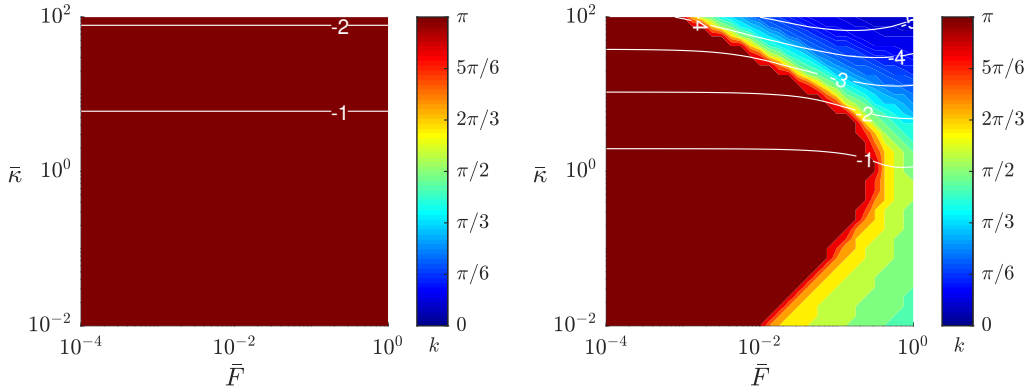

(a) Deposition, quasistatic.

(b) Deposition, dynamics.

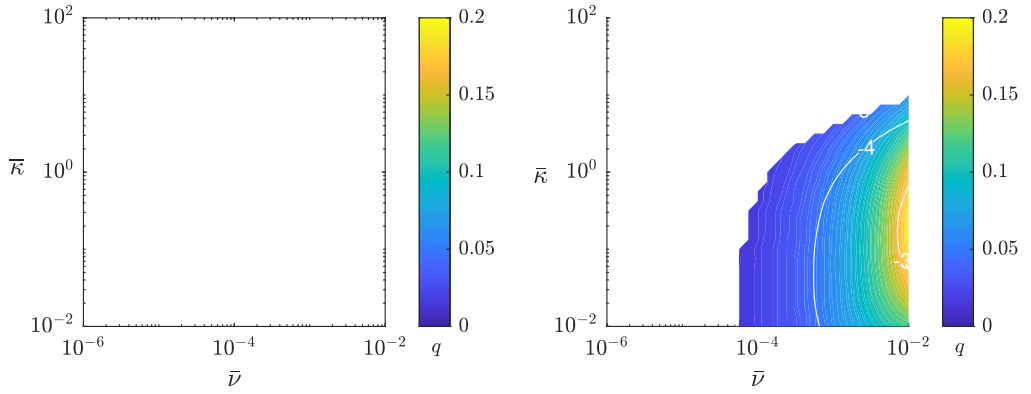

(c) Evaporation, quasistatic.

(b) Evaporation, dynamics.

Figure 4.18: Stability diagrams showing the interplay of the dynamical effect with the chemical effect ($S = 1$, $\bar{\alpha} = 0$, $\Pi = 0$, $\bar{\gamma} = 0$ for (a) and (b), and $\bar{\gamma} = 10^{-5}$ for (c) and (d)). In (a) and (b), the most unstable mode is always for $q = 0$; i. e., straight steps. In (c) and (d), the most unstable k mode is always $k = 0$; i. e., in-phase. [see color legend on Figure 4.12]

4.4.1 *Interplay between the dynamical and chemical effects*

While both the chemical and dynamical effects taken separately scale in the same fashion ($\sim \overline{F}\Theta^2$), their combined contribution exhibits a more complex behavior (Figure 4.18).

Under deposition, note the stabilizing influence of the dynamical effect at high $\bar{\kappa}$ (the growth rate is smaller than in the quasistatic case in this regime) and its destabilizing influence at low $\bar{\kappa}$. This is also evidenced by the shift in the wavenumber of the most unstable mode. Indeed, for a high enough deposition rate, k goes from π in the quasistatic context to values close to 0 in the diffusion-limited regime ($\bar{\kappa} \gg 1$), and close to $\pi/2$ in the kinetically-limited regime ($\bar{\kappa} \ll 1$), when including the dynamics terms. This is consistent with the scaling presented in Figure 4.16, and reflects the fact that the dynamical effect becomes dominant with increasing deposition rate, as expected from a kinetic mechanism.

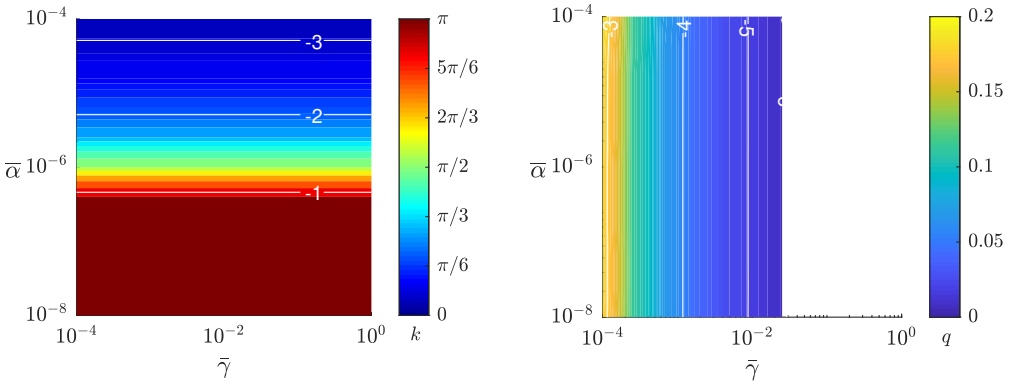

(a) Deposition: $\overline{F} = 10^{-4}$ (b) Evaporation: $\bar{v} = 10^{-4}$

Figure 4.19: Stability diagrams showing the interplay of elasticity and step stiffness (a) under deposition and (b) under evaporation. Parameters: $\chi_a = \chi_c = 1$, $\Theta = 0.1$, $S = 1$, $\bar{\kappa} = 1$. [see color legend on Figure 4.12]

Under evaporation, the surface is completely stable in the quasistatic case and the dynamical effect introduces an unstable domain of in-phase step meandering for high enough values of $\bar{v}$ and low enough values of $\bar{\kappa}$. Again, this is a testament to the destabilizing impact of the dynamical effect in the regime $\bar{\kappa} \ll 1$ and shows that the evaporation rate rules the competition between the destabilizing dynamical effect and the stabilizing step stiffness.

4.4.2 *Elasticity, step stiffness and step-edge diffusion*

Like in the quasistatic case, the most unstable mode is independent of step stiffness, which is consistent with the fact that the most unstable mode in that context is always straight-step bunching, on which step stiffness has no impact. However, with the inclusion of dynamics effect, the wavenumber of the step-bunching instability now depends on the strength of the elastic interaction. If it is weak enough, the most unstable mode is step-pairing ($k = \pi$). As the strength of the elastic interaction increases, the growth rate and wavenumber of the most unstable mode decrease (see Figure 4.19).

In the case of evaporation, the inclusion of dynamics effect makes an unstable region appear, which did not exist in the quasistatic case. The most unstable mode is always in-phase meandering, and does not depend on the strength of the elastic interaction. For a strong enough step stiffness, the system is stable. A weaker step stiffness results in a shorter wavelength for the most unstable mode, with a larger growth rate.

The introduction of step-edge diffusion modifies this behavior. For instance, under deposition, step-edge diffusion introduces a region of anti-phase meandering instability for small enough elasticity and step stiffness (Figure 4.20). In addition, step stiffness now significantly impacts the growth rate and wavenumber of the most unstable mode, for weak enough elasticity.

However, under evaporation, step-edge diffusion further stabilizes the system, so much so that while the growth rate is theoretically positive, its smallness

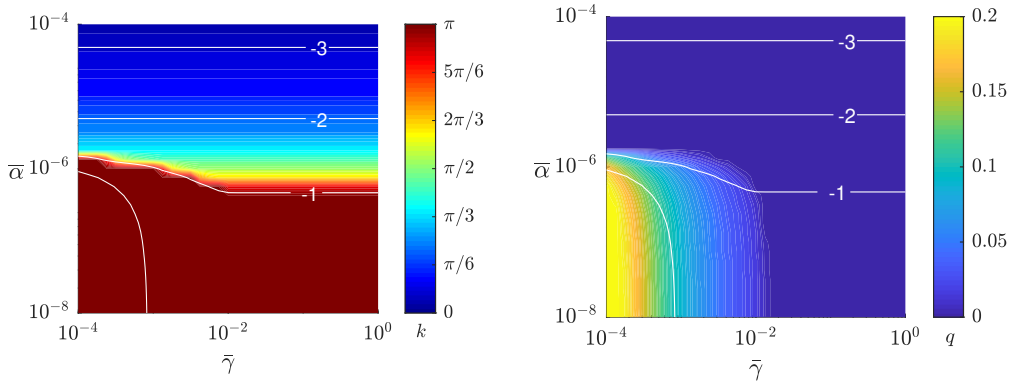

(a) k wavenumber.

(b) q wavenumber.

Figure 4.20: Stability diagrams showing the influence of step-edge diffusion under deposition. Parameters: $\chi_a = \chi_c = 1$, $\overline{F} = 10^{-4}$, $\Theta = 0.1$, $S = 1$, $\bar{\kappa} = 1$, $\Pi = 10^2$.

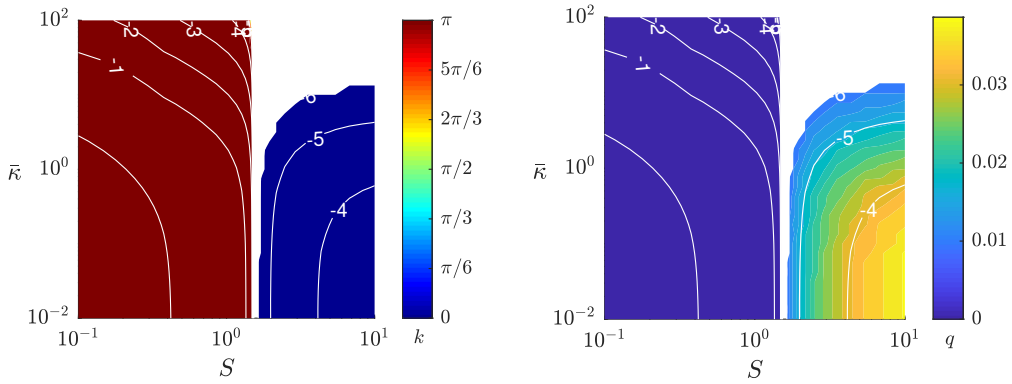

(a) k wavenumber.

(b) q wavenumber.

Figure 4.21: Stability diagrams showing the interplay of the dynamical effect with the Schwoebel effect, under deposition. Parameters: $\chi_a = \chi_c = 1$, $\overline{F} = 10^{-4}$, $\Theta = 0.1$, $\bar{\mathbf{d}} = \mathbf{0}$, $\bar{\gamma} = 10^{-2}$, $\Pi = 0$.

implies, once again, that physically the instability will likely not develop in the typical time scale of experiments.

4.4.3 *Schwoebel effect*

Under deposition, having in mind the scaling of the dynamical effect with $\bar{\kappa}$, we look at the stability diagrams of the most unstable mode as a function of S and $\bar{\kappa}$ (see Figure 4.21). Interestingly, the anti-phase meandering zone observed with chemical effect alone (see Figure 4.13) is no longer present. Instead, the diagram is very similar to the one obtained in the standard, quasistatic, BCF model except the critical value of the ES barrier S_c separating meandering ($S > S_c$) from bunching ($S < S_c$) is greater, fitting $S_c = (1 + 2\Theta)/(1 - 2\Theta)$ instead of simply $S_c = 1$.

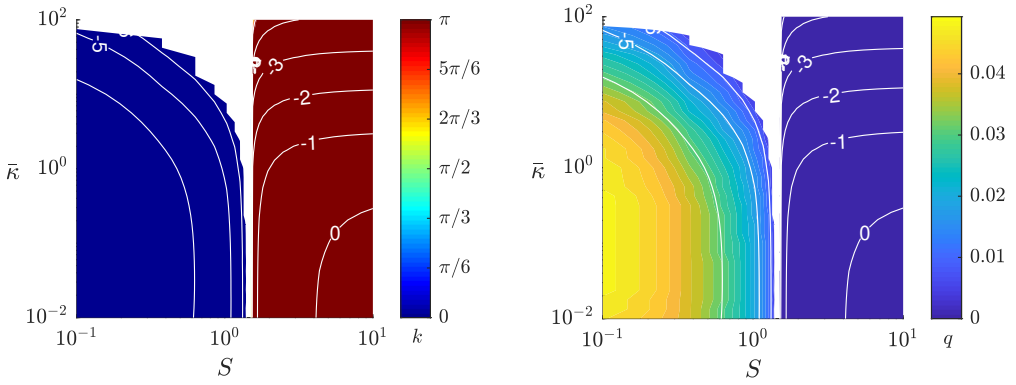

(a) k wavenumber.

(b) q wavenumber.

Figure 4.22: Stability diagrams showing the interplay of the dynamical effect with the Schwoebel effect, under evaporation. Parameters: $\chi_a = \chi_c = 1$, $\bar{\nu} = 10^{-4}$, $\Theta = 0.1$, $\bar{\mathbf{d}} = \mathbf{0}$, $\bar{\gamma} = 10^{-2}$, $\Pi = 0$.

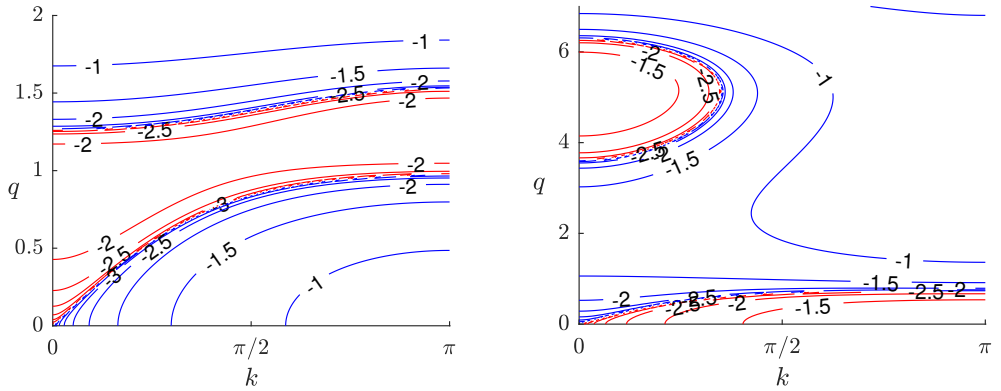

(a) Equally unstable in-phase and anti-phase meanders (deposition)

(b) Simultaneous bunching and meandering (evaporation)

Figure 4.23: Stability diagrams showing two equally unstable modes (a) under deposition, and (b) under evaporation. Parameters for (a): $\overline{F} = 10^{-4}$, $\Theta = 0.06$, $\bar{\kappa} = 1$, $S = 2$, $\bar{\mathbf{d}} = \mathbf{0}$, $\bar{\gamma} = 10^{-6}$, $\Pi = 0.1$, and for (b): $\bar{\nu} = 10^{-4}$, $\Theta = 0.1$, $S = 2$, $\bar{\kappa} = 1$, $\bar{d}_{xx} = 0.01$, $\bar{\gamma} = 10^{-7}$, $\Pi = 0.05$.

The case of evaporation is the symmetric of the case of deposition. The critical value of the ES barrier is identical at $(1 + 2\Theta)/(1 - 2\Theta)$ but the unstable meandering region is now for $S < S_c$, and the unstable bunching for $S > S_c$ (Figure 4.22).

4.4.4 *Simultaneous instabilities*

Since the Schwoebel effect and the chemodynamical effect have opposite impact on the stability, with different scaling relations (notably with respect to Θ, $\bar{\kappa}$, and Π), it should be possible to obtain stability diagram with two unstable regions, as hinted at by Figure 4.14 in the quasistatic approximation. Indeed, it is theoretically possible, both under deposition or evaporation, as illustrated

in Figure 4.23 where one can see that there exist two unstable regions whose respective maximum growth rates are equal. Under deposition, in-phase and anti-phase meanders may be equally unstable, and under evaporation, in-phase meandering and step-pairing may co-develop. It is important to emphasize that in the standard BCF model, where only the ES effect (direct or inverse) is responsible for the destabilization of the system, such a situation cannot arise. The dynamical and chemical effects can thus be added to the list of mechanisms that possibly trigger simultaneous bunching and meandering, besides heteroepitaxy (Yu et al., 2011) and diffusion anisotropy between alternating terraces Frisch and Verga (2006).

In practice however, the physically expected order of magnitude of each parameter makes this task much more challenging. For instance, for typical values of the step stiffness, its stabilizing effect dominates the destabilizing influence of the ES barrier on in-phase meandering so that a strong barrier or deposition flux (remember that it enhances the effect of kinetic mechanisms relative to energetic ones) is required, limiting the applicability of the theory to specific experimental situations.

In the pure evaporation regime, the evaporation rate is unlikely to be sufficient to allow for the chemodynamical effect to be strong enough to compete with step stiffness. In the pure deposition regime, the possibility of simultaneous instabilities still exists, although the associated growth rate is quite small (see Figure 4.24).

4.5 COMPARISON TO EXPERIMENTS

There are not many experimental results showcasing meandering of vicinal surfaces. Apart from the systematic set of studies by Maroutian et al. (2001) and Néel et al. (2003) on Cu surfaces, the other example by Omi and Ogino (2000) concerns a Si surface. More examples are available in the context of electromigration, which we review in Chapter 5.

In the case of Cu, several obstacles hinder the study of the chemodynamical effect. First, the experiments are conducted at room temperature ($T = 280$K) so that a very low adatom coverage Θ is expected, which entails a negligible influence of the chemodynamical effect based on its quadratic scaling with Θ as previously discussed. Moreover, Cu, like other metals, presents a very high ES barrier (Camarero et al., 1999; Xiang and Huang, 2008; Benlattar et al., 2017), which further undermines the impact of the chemodynamical effect.

On the other hand, on Si, the adatom coverage has been measured at a few percents (Yang and Williams, 1994) and no evidence of a strong ES barrier is found (Pimpinelli and Videcoq, 2000; Vladimirova et al., 2001; Slanina et al., 2005). However, the experimental situation remains complex as the behaviour is dependent on the steps' orientation. With $[11\bar{2}]$ steps, for temperatures between 570 and 650°C, and a deposition flux ranging from 0.01 to 0.7 nm/s, Omi and Ogino (2000) observe that initially equidistant triple-layer-high steps evolve into randomly distributed zig-zag shaped steps that eventually grow in phase after the deposited film reaches a certain thickness of around 100 nm. In a

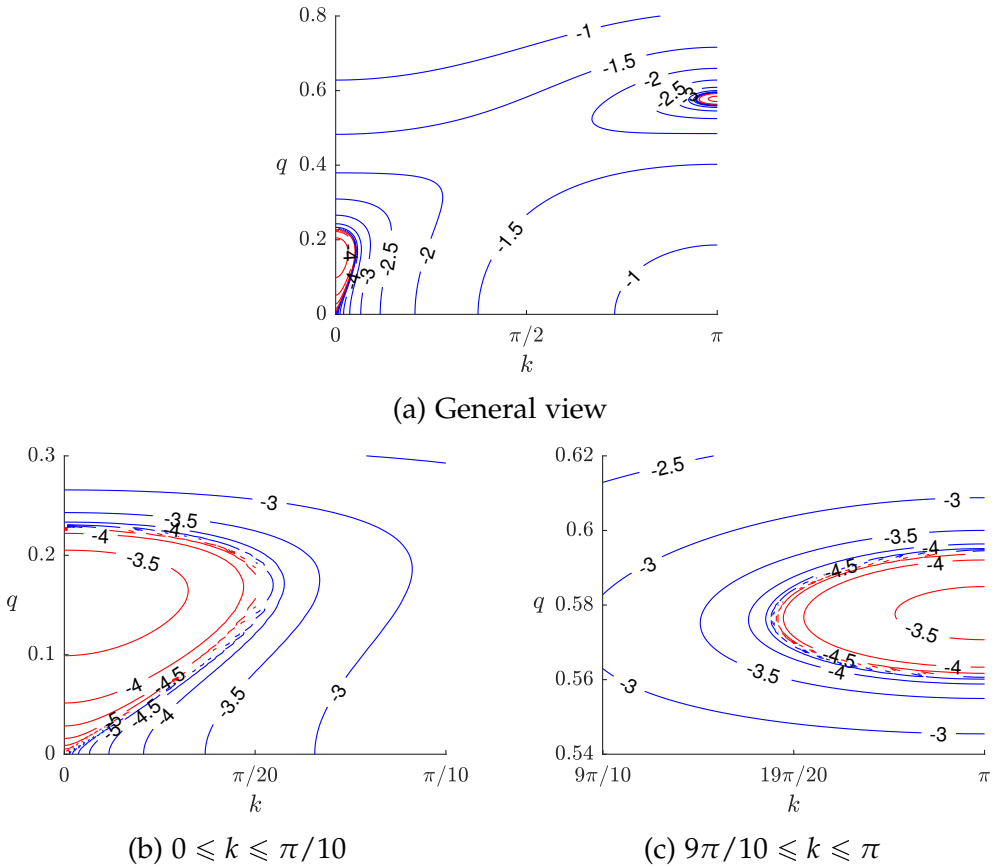

(a) General view

(b) $0 \leqslant k \leqslant \pi/10$

(c) $9\pi/10 \leqslant k \leqslant \pi$

Figure 4.24: Stability diagrams showing two equally unstable modes under deposition with physically relevant parameters. Parameters: $\overline{F} = 10^{-2}$, $\Theta = 0.1$, $\bar{\kappa} = 1$, $S = 2$, $\bar{d}_{xx} = 0.1$, $\bar{\gamma} = 10^{-3}$, $\Pi = 5/8$. [see color legend on Figure 4.11]

later work, with $[\bar{1}\bar{1}2]$ steps,[5] for temperatures between 550 and 675°C, and a deposition flux of ~ 0.01 nm/s, Omi et al. (2005) observe initially equidistant single-layer-high steps that maintain their configuration after the deposition of 100 nm. They also show that the surface stability domain is dependent on the miscut angle, such that at a given temperature, larger miscut angles tend to destabilize the surface against step bunching.[6] Despite the similar temperature range and deposition flux, the resulting morphologies are radically different, which might be an indication that the physical parameters at the step (namely the ES barrier S, the attachment/detachment coefficient $\bar{\kappa}$, step stiffness $\bar{\gamma}$, and step-edge diffusion Π) are strongly dependent on the step orientation.

5 Although $[\bar{1}\bar{1}2]$ and $[11\bar{2}]$ represent the same direction, the steps created by a miscut towards one or the other differ due to the crystallographic asymmetry of Si(111) (Suzuki and Yagi, 1997).

6 We note that there seems to be some confusion about the relation between the miscut angle and the initial terrace width in the corresponding diagram (at Fig. 3). Indeed, denoting ϕ the miscut angle and a the step height, from simple trigonometry we must have $\tan(\phi) = a/\mathcal{L}_0$. Based on the authors' observations of single-layer steps at the surface, we infer that $a = 0.314$ nm from which we derive that a 1° miscut angle corresponds to an initial terrace width of $\mathcal{L}_0 = 18$ nm. Yet, in their diagram at Fig.3, the 1° angle is associated to $\mathcal{L}_0 = 57$ nm, which is consistent with a triple-layer step instead, such that $a = 0.942$ nm.

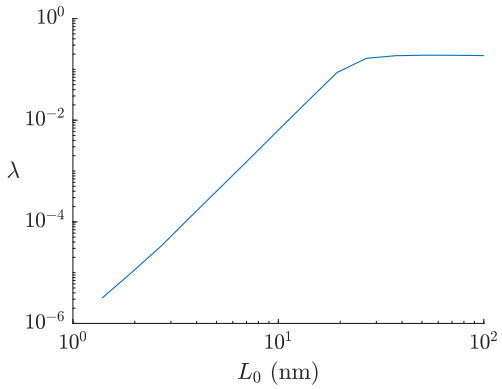

Figure 4.25: Growth rate as a function of the initial terrace width $\mathcal{L}_0$. The parameters at $\mathcal{L}_0 = 18$ nm (i. e., a miscut angle of 1°) are: $\overline{F} = 10^{-4}$, $S = 1$, $\Theta = 0.05$, $\bar{\kappa} = 10^{-2}$, $d_{xx} = 15$ eV/nm, $d_{xz} = 6$ eV/nm, $\bar{\gamma} = 10^{-2}$, $\Pi = 0$.

Bearing this in mind, we analyze the stability of a Si(111) surface based on experimental estimates of the parameters given in Appendix D. A first observation in the case of step bunching, illustrated in Figure 4.25, is that increasing the initial terrace width increases the growth rate of the instability, i. e., makes the surface more unstable, which is at odds with the experiments of Omi et al. (2005). This is expected as the step-step interaction coefficient $\bar{\alpha}_0$, whose associated mechanism is stabilizing, has the strongest scaling with $\mathcal{L}_0$ of all parameters as $\bar{\alpha}_0 \sim \mathcal{L}_0^{-3}$ which entails that the surface is more stabilized for smaller $\mathcal{L}_0$, i. e., larger miscut angles. It seems the only way to reconcile the experimental observations with the theory would be to assume that the parameters themselves depend on $\mathcal{L}_0$ and not simply their nondimensional counterpart.

In the general case, we find that the surface is unstable, against either step bunching or anti-phase meandering depending on the competition between step-edge diffusion, step-step interaction and step stiffness (see Figure 4.26). While the exact dependence of those parameters with temperature is unclear, it shows that the two instabilities of step bunching and step meandering may theoretically be triggered on Si surfaces, as observed in Omi et al. (2005) where step bunching is reported for temperatures below 800°C but step meandering develops above 800°C. However, the predicted stability diagrams do not conform with the experimental results of Omi and Ogino (2000). Indeed, because the meandering instability predicted is always anti-phase, it is stabilized by the elastic step-step interaction, so that if single-layer-high steps do not meander (Omi et al., 2005), we would expect the same behavior from triple-layer-high step as the strength of the elastic step-step interaction increases with step height (Williams et al., 1993). On the other hand, this discrepancy could also suggest that the step meandering instability observed experimentally is actually triggered by the initial step bunching (from single-layer steps to triple-layer steps) and results from nonlinear effects which are beyond the scope of our linear stability analysis. For instance, the case of step meandering acting as a precursor of step bunching has been reported by Néel et al. (2003).

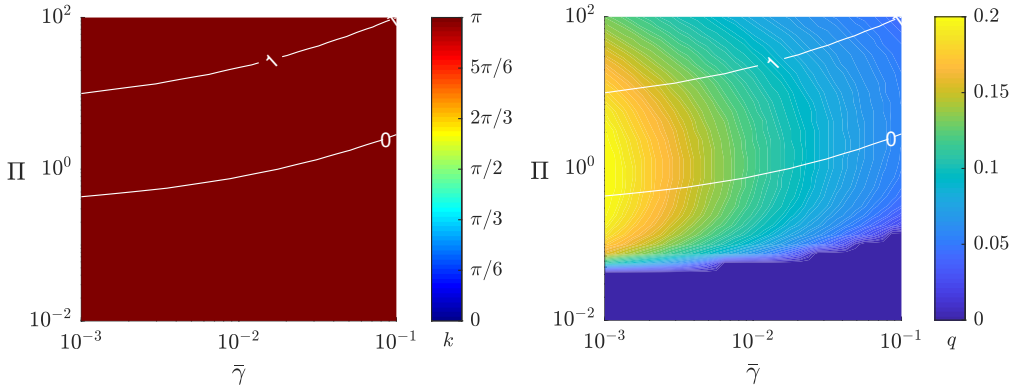

(a) $\bar{\mathbf{d}} = \mathbf{0}$, k wavenumber

(b) $\bar{\mathbf{d}} = \mathbf{0}$, q wavenumber

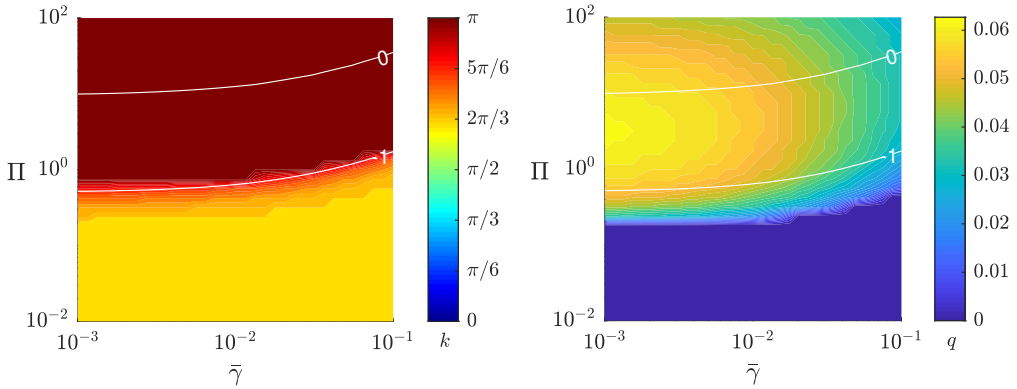

(c) $\bar{d}_{xx} = 0.15$, k wavenumber

(d) $\bar{d}_{xx} = 0.15$, q wavenumber

Figure 4.26: Stability diagrams showing the competition between step-edge diffusion and step stiffness for two values of the step-step interaction strength. Parameters: $\overline{F} = 10^{-4}$, $\Theta = 0.05$, $S = 1$, $\bar{\kappa} = 10^{-2}$.

In addition to these considerations, it is interesting to note that for temperatures between 650 and 800°C, Omi and Ogino (2000) still observe step meandering whereas Omi et al. (2005) see step bunching. In the framework of the standard BCF model, this would imply a drastic change from an inverse to a direct ES barrier. On the other hand, taking into account the chemical and dynamical effects, we observe that a slight variation of the equilibrium adatom coverage Θ (from 8% to 10%) leads to a dramatic change in the most unstable mode, from in-phase meandering to step bunching (Figure 4.27).

Given the uncertainty on several of the material parameters, it is extremely hard to interpret the experiments in light of our model and we cannot reach a definitive conclusion. What is certain is that additional experiments would be extremely welcome to offer greater accuracy on the model parameters. Nevertheless, this does not change the principal point of our work: we have provided a new instability mechanism that can trigger both step-bunching and step-meandering instabilities independently of an ES barrier, whether it be direct or inverse.

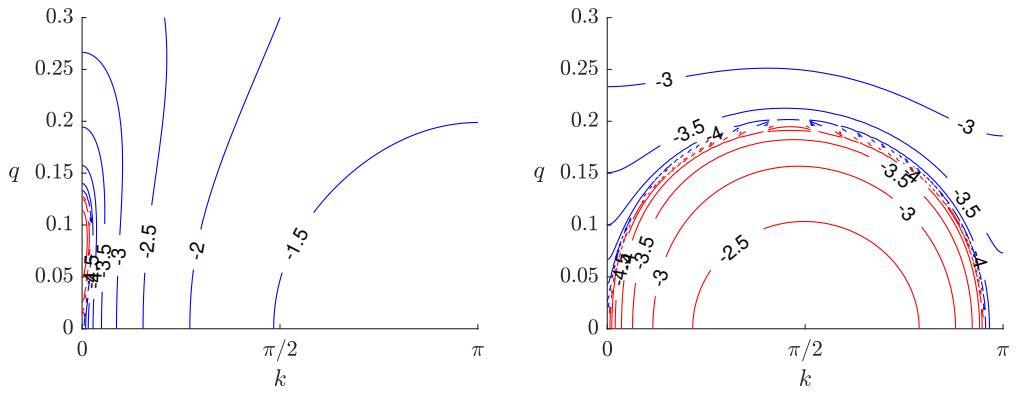

(a) $\Theta = 0.08$ (b) $\Theta = 0.1$

Figure 4.27: Stability diagrams showing a drastic switch in the most unstable mode from in-phase meandering to step bunching due to a small variation of Θ. Parameters: $\overline{F} = 10^{-3}$, $\bar{\nu} = 0$, $\bar{\kappa} = 10^{-2}$, $S = 1.5$, $\mathbf{d} = 0$, $\bar{\gamma} = 10^{-3}$, $\Pi = 0$. [see color legend on Figure 4.11]

4.6 KEY RESULTS

The stability landscape on vicinal surfaces is extremely complex, as it results from the competition between five stabilizing/destabilizing mechanisms (the ES effect S, the chemical effect χ_c, the dynamical effect χ_a, the step-step elastic interaction $\overline{\mathbf{d}}$, and the step stiffness $\bar{\gamma}$) whose relative weights are governed not only by their respective magnitude, but also by the four operational and material parameters (the deposition/evaporation rates $\overline{F}$ and $\bar{\nu}$, the equilibrium adatom coverage Θ, the attachment/detachment coefficient $\bar{\kappa}$, and the step-edge diffusion coefficient Π). Although the exact stability diagram depends on a specific choice of the set of parameters, we summarize in Table 4.1 and schematically in Figure 4.28 the impact on stability of each mechanism acting independently. Additionally, the scaling of these mechanisms with the operational and material parameters is shown in Table 4.2, at the exception of $\bar{\kappa}$ given the complexity of the associated scaling that depends on the mode, the magnitude of $\bar{\kappa}$, and the operational regime considered.

We have extended the analysis of Guin et al. (2021a) in the one-dimensional context of step bunching to the general two-dimensional context where steps are allowed to meander, and have shown that the dynamical and chemical effects have a significant impact on the stability of vicinal surfaces. On a related note, as these two effects share some common characteristics with the inverse ES effect, they could be interpreted as an effective inverse ES effect, reconciling the theories that require an inverse ES effect to trigger instability and the unlikelihood of the existence of an actual energetic inverse ES barrier.

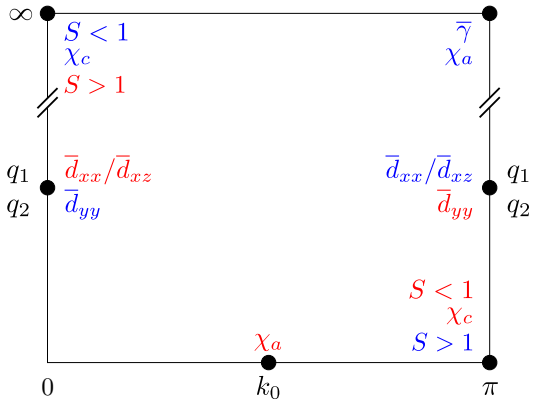

Figure 4.28: Diagram of the (k, q) space. For each mechanism, the most stabilized mode is shown in blue and the most destabilized one in red.

	$S < 1$	$S > 1$	χ_c	χ_a	$\overline{d}_{xx}/\overline{d}_{xz}$	$\overline{d}_{yy}$	$\bar{\gamma}$
$\mathcal{S}$	$(0, \infty)$	$(\pi, 0)$	$(0, \infty)$	(π, ∞)	(π, q_1)	$(0, q_2)$	(π, ∞)
$\mathcal{U}$	$(\pi, 0)$	$(0, \infty)$	$(\pi, 0)$	$(k_0, 0)$	$(0, q_1)$	(π, q_2)	

Table 4.1: Most stable and unstable mode for each mechanism taken independently. $\mathcal{S}$ denotes the most stable modes, $\mathcal{U}$ the most unstable ones, where a mode is described as (k, q). k_0, q_1, and q_2 are values such that $0 < k_0 < \pi/2$ and $0 < q_i < \infty$. Under evaporation, the most destabilized and most stabilized modes are reversed for kinetic mechanisms (first 4 columns), and unchanged for energetic mechanisms (last three columns).

	χ_c	χ_a	S	$\overline{\mathbf{d}}$ and $\bar{\gamma}$
$\overline{F}$ or $\bar{v}$	1	1	1	0
Θ	2	2	1	1
Π	1	0	0	1

Table 4.2: Scaling of each mechanism with the operational and material parameters. The numbers presented correspond to the exponents of a scaling law of the type $F^{c_1}\Theta^{c_2}(A\Pi^{c_3} + B)$. For example, the first column tells us that the growth rate associated to the chemical effect scales as $F^1\Theta^2(A\Pi^1 + B)$.

5 ELECTROMIGRATION

This chapter is dedicated to the special case of crystal growth with electromigration. Indeed, vicinal surfaces exhibit a complex behavior when subject to an electric current. While alternate-current heating of the substrate results in stable growth, a direct-current heating, depending on the current direction, the temperature, and the deposition/evaporation regime, may cause step bunching or meandering.

Of particular interest is the Si(111) -1×1 surface, whose behavior, detailed in Section 5.1, exhibits an intriguing dependence on temperature. After presenting the general stability results in Section 5.2, we derive in Section 5.3 an alternate stability analysis, the so-called *transpiration method*, which provides an approximate, but extremely accurate, analytical expression for the dispersion relation. In Section 5.4, we focus on three experiments into which the dynamical and chemical effects offer new insights.

5.1 REVIEW OF EXISTING THEORIES

First described by Latyshev et al. (1989), four different temperature regimes can be identified on Si(111) surfaces, that are characterized by the direction of the current required to trigger the step-bunching instability in free evaporation conditions. In regimes I (860°C – 960°C) and III (1200°C – 1300°C) (Homma and Aizawa, 2000; Leroy et al., 2009), step-bunching occurs at *step-down* current and is well accounted for by the standard BCF model, extended to account for the adatom drift induced by the electric current by introducing an *electromigration force* in the reaction-diffusion equation. However, the same model is incapable of describing the dynamics in regimes II (1060°C – 1200°C) and IV ($>$ 1320°C) (Homma and Aizawa, 2000; Leroy et al., 2009), where *step-up* current triggers step-bunching. Note the temperature gaps between regimes I and II, and regimes III and IV, for which no bunching occurs, irrespective of the current's direction, and which could correspond to a gradual change of step properties or adatom transport mechanism (Homma and Aizawa, 2000).

At first, the possibility of a change in the sign of the adatom effective charge was considered by Kandel and Kaxiras (1996) but ruled out by the experiments of Degawa et al. (2000), which show that the adatom drift direction corresponds to the current direction, irrespective of the temperature.

In the late 90's, it was proposed that the stability reversal in regime II is due to step permeability, whereby adatoms can hop directly from one terrace to another without attaching and detaching from a step (Stoyanov, 1998; Métois and Stoyanov, 1999). Indeed, it was shown that sufficiently permeable steps are unstable against step-bunching in the step-up direction (Stoyanov, 1998; Pierre-Louis, 2003). However, it is not clear why, as temperature increases, steps

are alternatively permeable and impermeable. Kink density at the step was suggested as a possible permeability mechanism (Sato, 2007), but is inconsistent with the fact that step-bunching does not depend on step orientation (Homma and Aizawa, 2000) while kink density does (Lin et al., 1998). Nevertheless, it should be noted that only zero azimuthal orientations $(\bar{1}\bar{1}2)$, $(11\bar{2})$ and $(0\bar{1}0)$ are considered by Homma and Aizawa (2000), which may all possess similar kink densities as they are principal crystal directions, so that their conclusion may not be generalizable to an arbitrary step orientation.

Another postulate to explain the I $\rightarrow$ II stability reversal is the transition from a state with high activation energy for desorption (Taganayaki-like adatoms) to a state with low activation energy, effectively causing a transition from local to global mass transport (Métois and Stoyanov, 1999). However, this would entail a low equilibrium coverage in regime II, which is not observed experimentally, with estimates at 0.25 ML instead (Fukaya and Shigeta, 2000; Rogilo et al., 2016).

In addition, a recent experimental study by Usov et al. (2011) on the scaling exponents of the maximal bunch slope with bunch size and applied electric field could not be explained by a self-consistent permeable-step model, but instead had to resort to out-of-equilibrium and near-equilibrium hypotheses to match the observed exponents. The transparent-step model also gives unrealistic values for the effective charges of adatoms (Fujita et al., 1999; Homma and Aizawa, 2000).

Finally, note that fast step kinetics and high permeability are essentially indistinguishable (Pierre-Louis, 2003) and could in fact be two ways of modeling the same physical process (Guin, 2018). Therefore, while appealing at first glance, the permeable-step model has many limitations and does not seem to be the right answer to explain the stability reversals.

At higher temperatures, *surface melting* was evidenced for $T \gtrsim 1200°\mathrm{C}$ (Homma et al., 1997) or $T \gtrsim 1290°\mathrm{C}$ (Fukaya and Shigeta, 2000) which could have a strong impact on the diffusion properties and attachment/detachment kinetics of adatoms. Likewise, for the high temperature ($T > 1180°\mathrm{C}$) transitions II $\rightarrow$ III and III $\rightarrow$ IV, advacancies are likely to play a role (Sitnikov et al., 2017) but theoretically were only shown to have an impact when the step spacing is large compared to the diffusion length (Misbah et al., 1995), which is not verified experimentally (Alfonso et al., 1993; Homma et al., 1997; Homma, 1998).

An alternative approach consists in considering a space-dependent diffusion coefficient or electromigration force (Zhao and Weeks, 2005; Pierre-Louis, 2006), which could emanate from different surface reconstructions in the step area and on the terrace. Matching the obtained dynamics to a BCF-type model yields a negative kinetic coefficient (Zhao and Weeks, 2005), which results in the expected stability reversal. While this is still essentially a thought experiment, the need for different reconstructed regions could conform with the existence of stable temperature gaps between some regimes.

Furthermore, the complex stability landscape on Si(111) surfaces under electromigration is not limited to step bunching. Indeed, ten years after the first observations of the peculiar behavior of step bunching by Latyshev et al.

	Evaporation		Net deposition	
	Step-down	Step-up	Step-down	Step-up
Regime I $\sim 850 - 950°C$	$SB^{2,4,6,7}$	$R^{2,4,6,7}$	$SB^{2,7}$	R^{7}
Regime II $\sim 1050 - 1200°C$	$SM^{6,8}$ $R^{1-5,7}$	SB^{1-7}	$R^{7,\star}$ $SB^{3,5,\dagger}$	$SB^{7,\star}$ $SP^{3,\dagger}$
Regime III $\sim 1200 - 1300°C$	$SB^{1-6,8}$	R^{1-6}	$SB^{3,5}$	$R^{3,9,\dagger}$ $SB^{9,\ddagger}$
Regime IV $> 1320°C$	$R^{1,4}$	$SB^{1,4}$		

Table 5.1: Compilation of the experimental observations of the stability against step bunching for Si(111) under electromigration. SB denotes step bunching (with coarsening), SP step pairing (no coarsening), R regular spacing (stable configuration) and SM step meandering. The superscripts correspond to 1. Latyshev et al. (1989), 2. Yang et al. (1996), 3. Métois and Stoyanov (1999), 4. Homma and Aizawa (2000), 5. Stoyanov et al. (2000), 6. Minoda (2003), 7. Gibbons et al. (2005), 8. Leroy et al. (2009), 9. Ranguelov et al. (2017), $\star$ "low" deposition flux (0.03 ML/s), † "moderate" deposition flux (< 1 ML/s), ‡ "high" deposition flux (5 ML/s).

(1989), Degawa et al. (1999a) found in-phase step meandering at step-down current in regime II, which was previously believed to yield a stable surface. While they used a cylindrical groove to observe at once step-up and step-down regions over a range of miscut angles (from 0 to 14°), they obtained the same result using standard vicinal surfaces (Degawa et al., 1999c). Additionally, still in regime II, (Degawa et al., 1999b) also studied the formation of in-phase step meanders in antibands during step-bunching at step-up direction of the current (thus locally step-down for the antibands). Degawa et al. (2001a) then extended the study to arbitrary directions of the direct current, such that it is not necessarily aligned with the direction perpendicular to steps, and Degawa et al. (2001b) studied the precise temperature and off-angle dependence of the instability domains. A complete review of these works can be found in Minoda (2003). All these experimental results are summarized in Table 5.1.

While it has been shown than the dynamical and chemical effects cannot explain the stability reversals observed on Si(111) vicinal surface (Guin, 2018), our objective in this chapter is to offer a reinterpretation of some experimental results for which the dynamical and chemical effects might play a crucial role. In order to reach that goal, an alternative linear stability analysis is proposed, that yields an approximate analytical expression for the growth rate which is much less computationally intensive than the Chebyshev collocation method presented in Appendix H while preserving an excellent accuracy.

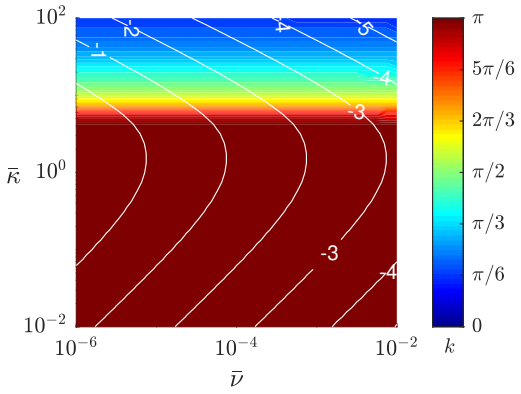

(a) BCF model ($\chi_a = \chi_c = 0$), k wavenumber

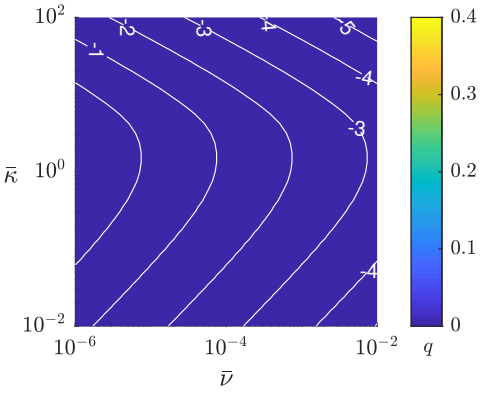

(b) BCF model ($\chi_a = \chi_c = 0$), q wavenumber

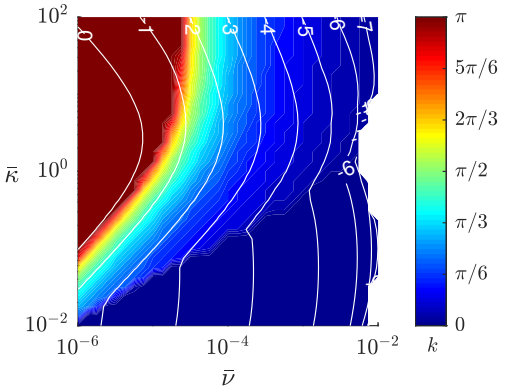

(c) Quasistatic model ($\chi_a = 0$, $\chi_c = 1$), k wavenumber

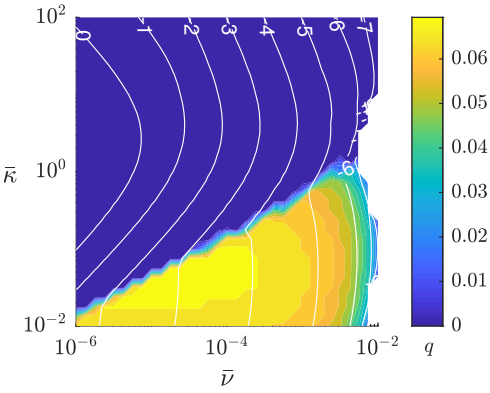

(d) Quasistatic model ($\chi_a = 0$, $\chi_c = 1$), q wavenumber

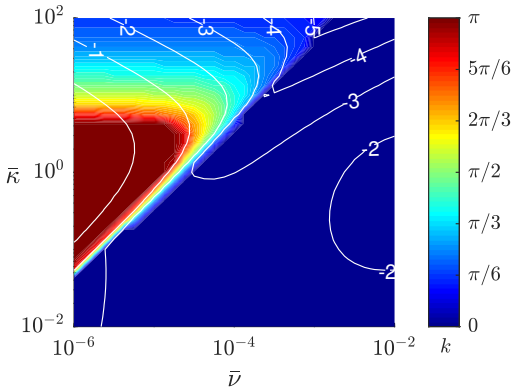

(e) Full model ($\chi_a = \chi_c = 1$), k wavenumber

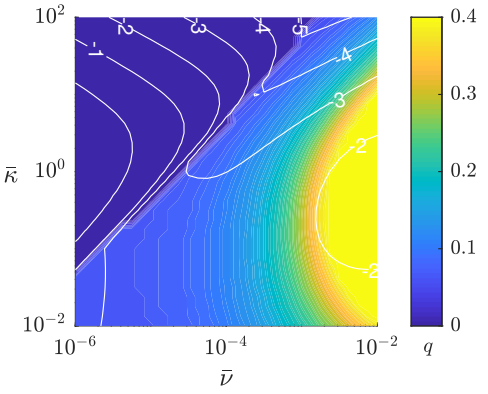

(f) Full model ($\chi_a = \chi_c = 1$), q wavenumber

Figure 5.1: Stability diagrams of (top) the BCF model, (middle) the quasistatic model, and (bottom) the full model for step-down electromigration under pure evaporation ($\overline{F} = 0$). Parameters: $\Theta = 0.2$, $S = 1$, $\bar{e} = 10^{-5}$, $\bar{d}_{xx} = 0.01$, $\bar{\gamma} = 10^{-3}$, $\Pi = 0$. [see color legend Figure 4.12]

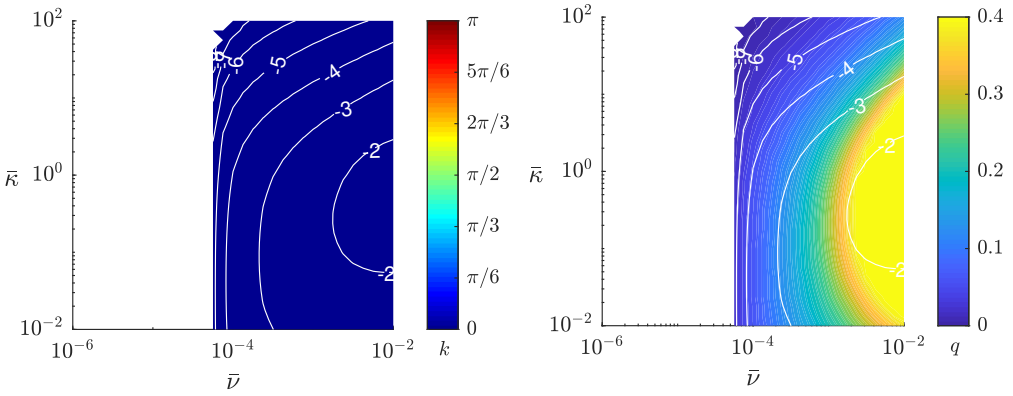

(a) Full model ($\chi_a = \chi_c = 1$), k wavenumber

(b) Full model ($\chi_a = \chi_c = 1$), q wavenumber

Figure 5.2: Stability diagrams of the full model for step-up electromigration under pure evaporation ($\overline{F} = 0$). The BCF and quasistatic models are not shown as the entire domain is stable in both cases. Parameters: $\Theta = 0.2$, $S = 1$, $\bar{e} = -10^{-5}$, $\bar{d}_{xx} = 0.01$, $\bar{\gamma} = 10^{-3}$, $\Pi = 0$. [see color legend Figure 4.12]

5.2 STABILITY RESULTS UNDER ELECTROMIGRATION

In this section, we briefly review how the stability results presented in Chapter 4 are modified by electromigration. Even under the quasistatic approximation, the expression of the growth rate is too complex to be interpreted and we instead rely on numerical results.

The general conclusions are essentially the same as in the absence of electromigration, although some interesting features appear. First, we observe that step-down current destabilizes the entire domain, no matter what model we consider (see Figure 5.1). However, while only step bunching is predicted in the BCF model, the inclusion of the chemical and dynamical effects introduces a region of step meandering in the stability diagram, as expected from their respective dispersion curves under evaporation (see Figure 4.11 and Figure 4.16). This means that a transition from step bunching to step meandering (and vice versa) may take place on the surface, depending notably on the temperature and the initial terrace width, which we study in more details in Section 5.4.2.

On the other hand, step-up electromigration acts as a stabilizing mechanism which, in the BCF model, stabilizes the whole domain. In that case, even the destabilizing influence of the chemical effect is not enough to counteract the stabilizing effect from the step-up current. However, as illustrated in Figure 5.2, the dynamical effect does have the sufficient strength to overcome the step-up current stabilization and actually induce step meandering, which once shows its significant impact on stability.

Regarding the different scaling laws, we can show that the growth rate associated to electromigration is linear with Θ and independent of Π. The dependence on the deposition/evaporation rates and attachment/detachment coefficient are more intricate and do not fit a simple power law.

5.3 LINEAR STABILITY ANALYSIS BY THE TRANSPIRATION METHOD

The ALE formulation of Section 2.4.3 combined with the Chebyshev collocation method of Appendix H allows for an exact analysis of the stability, presented in Guin et al. (2020) for the one-dimensional setting, and in Chapter 4 and Section 5.2 for the two-dimensional one, which uncovered previously neglected stability criteria relating to the dynamical and chemical effects. However, its numerical form makes a systematic study fastidious, as the stability analysis need to be run for each choice of parameters, and limits the quantitative understanding of the mechanisms to extreme regimes and general scaling laws (see Section 4.3.4). To overcome this drawback, we instead apply the so-called *transpiration technique*, which consists in an asymptotic development of the variables near their steady-state values.

For conciseness, we will restrict the derivation to straight steps, but the process is transferable to two space dimensions. We work in the comoving frame, where we denote position as $\hat{x} = x - n - \mathcal{P}t$ and concentration $\hat{\rho_n}(\hat{x}, t) = \rho_n(x, t)$. To keep notations light, we will drop the hats in the following.

The fundamental solution is $\overset{0}{x}_n = 0$ and $\rho_n(x, t) = \rho^{(0)}(x)$ where the function $\rho^{(0)}$ is given in Appendix F.[1] We consider the perturbed state:

$$\begin{aligned} x_n(t) &= \varepsilon\zeta_n(t) + \mathcal{O}(\varepsilon^2), \\ \rho_n(x, t) &= \rho^{(0)}(x) + \varepsilon\rho_n^{(1)}(x, t) + \mathcal{O}(\varepsilon^2). \end{aligned} \tag{5.1}$$

The essence of the transpiration method resides in how the boundary conditions are expressed. Because the concentrations at the steps bordering terrace n are defined at the moving points $\varepsilon\zeta_n(t)$ and $1 + \varepsilon\zeta_{n+1}(t)$, we use Taylor series to expand them around the fixed points $x = 0$ and $x = 1$.

$$\begin{aligned} \rho_n^+ = \rho_n(x_n(t), t) &= \rho_n(0, t) + \varepsilon\zeta_n(t)\partial_x\rho_n(0, t) + \mathcal{O}(\varepsilon^2) \\ &= \rho^{(0)}(0) + \varepsilon\left(\rho_n^{(1)}(0, t) + \zeta_n(t)\rho_x^{(0)}(0)\right) + \mathcal{O}(\varepsilon^2), \\ \rho_n^- = \rho_n(x_{n+1}(t), t) &= \rho_n(n + 1, t) + \varepsilon\zeta_1(t)\partial_x\rho_n(1, t) + \mathcal{O}(\varepsilon^2) \\ &= \rho^{(0)}(1) + \varepsilon\left(\rho_n^{(1)}(1, t) + \zeta_1(t)\rho_x^{(0)}(1)\right) + \mathcal{O}(\varepsilon^2). \end{aligned} \tag{5.2}$$

Since we are interested in the linear stability analysis, it suffices to study the stability with respect to the normal modes

$$\begin{cases} \zeta_n(t) = e^{ikn+\lambda t}, \\ \rho_n^{(1)}(x, t) = e^{ikn+\lambda t}\rho^{(1)}(x), \end{cases} \tag{5.3}$$

where, as in Chapter 4, λ represents the growth rate, whose real part determines the stability of the system.

1 Note that in the steady-state setting, the variable x coincides with the Lagrangian variable u.

Inserting back and collecting terms of order ε:

$$\begin{cases} 0 = \rho_{xx}^{(1)} + (\chi_a P - \bar{e})\rho_x^{(1)} - (\bar{v} + \chi_d \lambda)\rho^{(1)}, \\ (\rho^{(1)}(1) + \rho_x^{(0)}(1)e^{ik})(\chi_a P - \bar{e}) + \chi_a \rho^{(0)}(1)e^{ik}\lambda + (\rho_x^{(1)}(1) + \rho_{xx}^{(0)}(1)e^{ik}) \\ \quad = -\bar{\kappa}(\rho^{(1)}(1) + \rho_x^{(0)}(1)e^{ik} - \mathfrak{F}_R(k,0)e^{ik}) \\ \quad\quad + \chi_c \bar{\kappa}\Theta\Big[(\rho^{(1)}(0) + \rho_x^{(0)}(0))e^{ik} - (\rho^{(1)}(1) + \rho_x^{(0)}(1)e^{ik})\Big], \\ (\rho^{(1)}(0) + \rho_x^{(0)}(0))(\chi_a P - \bar{e}) + \chi_a \rho^{(0)}(0)\lambda + \rho_x^{(1)}(0) + \rho_{xx}^{(0)}(0) \\ \quad = \bar{\kappa}S(\rho^{(1)}(0) + \rho_x^{(0)}(0) - \mathfrak{F}_R(k,0)) \\ \quad\quad - \chi_c \bar{\kappa} S\Theta\Big[\rho^{(1)}(0) + \rho_x^{(0)}(0) - (\rho^{(1)}(1) + \rho_x^{(0)}(1)e^{ik})e^{-ik}\Big]. \end{cases} \tag{5.4}$$

Note that we have introduced χ_d in addition to χ_a to differentiate the transient term $\partial_t \tilde{\rho}_n$ from the advective contribution among the dynamics terms. The solution to the diffusion equation takes the form:

$$\begin{cases} \rho^{(1)}(x) = C^+ \exp(r^+ x) + C^- \exp(r^- x), \\ r^{\pm} = r^{\pm}(\lambda) = -\dfrac{\chi_a P - \bar{e}}{2} \pm \sqrt{\left(\dfrac{\chi_a P - \bar{e}}{2}\right)^2 + \bar{v} + \chi_d \lambda}, \end{cases} \tag{5.5}$$

with boundary condition written as a system

$$\mathbf{A}(\lambda)\begin{pmatrix} C^+(\lambda) \\ C^-(\lambda) \end{pmatrix} = \mathbf{b}(\lambda), \tag{5.6}$$

where

$$\begin{cases} A_{11}(\lambda) = -(\chi_a P - \bar{e} + r^+(\lambda) + \bar{\kappa})e^{r^+(\lambda)} + \chi_c \bar{\kappa}\Theta(e^{ik} - e^{r^+(\lambda)}), \\ A_{12}(\lambda) = -(\chi_a P - \bar{e} + r^-(\lambda) + \bar{\kappa})e^{r^-(\lambda)} + \chi_c \bar{\kappa}\Theta(e^{ik} - e^{r^-(\lambda)}), \\ b_1(\lambda) = \Big[(\chi_a P - \bar{e} + \bar{\kappa})\rho_x^{(0)}(1) + \chi_a \rho^{(0)}(1)\lambda + \rho_{xx}^{(0)}(1) \\ \quad\quad - \bar{\kappa}\mathfrak{F}_R(k,0) - \chi_c \bar{\kappa}\Theta(\rho_x^{(0)}(0) - \rho_x^{(0)}(1))\Big]e^{ik}, \\ A_{21}(\lambda) = (\chi_a P - \bar{e} + r^+(\lambda) - \bar{\kappa}S) + \chi_c \bar{\kappa} S\Theta(1 - e^{-ik + r^+(\lambda)}), \\ A_{22}(\lambda) = (\chi_a P - \bar{e} + r^-(\lambda) - \bar{\kappa}S) + \chi_c \bar{\kappa} S\Theta(1 - e^{-ik + r^-(\lambda)}), \\ b_2(\lambda) = (-\chi_a P + \bar{e} + \bar{\kappa}S)\rho_x^{(0)}(0) - \chi_a \rho^{(0)}(0)\lambda - \rho_{xx}^{(0)}(0) \\ \quad\quad - \bar{\kappa}S\mathfrak{F}_R(k,0) - \chi_c \bar{\kappa} S\Theta(\rho_x^{(0)}(0) - \rho_x^{(0)}(1)). \end{cases} \tag{5.7}$$

The system can easily be inverted to give C^+ and C^- as:

$$\begin{pmatrix} C^+ \\ C^- \end{pmatrix} = \frac{1}{\det(\mathbf{A})}\begin{pmatrix} A_{22}b_1 - A_{12}b_2 \\ A_{11}b_2 - A_{21}b_1 \end{pmatrix}. \tag{5.8}$$

Finally, using the interface motion we get the following analytical expression for λ:

$$\Big[1 - \chi_a \Theta(\rho^{(0)}(0) - \rho^{(0)}(1))\Big]\lambda = \Theta\Big[(r^+(\lambda) + \chi_a P - \bar{e})(1 - e^{-ik + r^+(\lambda)})C^+(\lambda) \\ + (r^-(\lambda) + \chi_a P - \bar{e})(1 - e^{-ik + r^-(\lambda)})C^-(\lambda) + \bar{v}(\rho^{(0)}(0) - \rho^{(0)}(1))\Big]. \tag{5.9}$$

In the absence of evaporation ($\bar{v} = 0$), electromigration ($\bar{e} = 0$) and the chemical effect ($\chi_c = 0$), this expression matches the one reported in Gillet (2000). In the present form, this implicit equation is unusable due to its complex nonlinearities. However, it can be simplified and made explicit under the assumptions:

$$\overline{F} \ll 1,\ \bar{v} \ll 1,\ \bar{e} \ll 1,\ \text{and}\ \bar{\alpha} \ll 1, \tag{5.10}$$

which are expected in experimental conditions. We refer to *first order* terms as terms of the form $\mathcal{O}(\overline{F})$, $\mathcal{O}(\bar{v})$, $\mathcal{O}(\bar{e})$ and $\mathcal{O}(\bar{\alpha})$. *Second order* and *third order* terms are terms of the form $\mathcal{O}(p_i p_j)$ and $\mathcal{O}(p_i p_j p_k)$ respectively, where $\{p_i, p_j, p_k\} \in \{\overline{F}, \bar{v}, \bar{e}, \bar{\alpha}\}^3$. Under those hypotheses, neglecting third and higher order terms, we establish the expression for the nondimensional fundamental velocity, i. e., the Péclet number:

$$\mathcal{P} \simeq (\overline{F} - \bar{v})\Theta - \frac{\bar{v}\Theta}{12\bar{\kappa}B}\Big\{6(C_2 - C_1)\bar{\kappa}\bar{e} + (\overline{F} - \bar{v})C_3\Big\}, \tag{5.11}$$

where

$$\begin{cases} B := 1 + S + \bar{\kappa}S, \\ C_0 := (1 - S)(\chi_a + \chi_c)/2 + \chi_a\chi_c\Theta(S + 1), \\ C_1 := 1 + \chi_c\Theta(S + 1), \\ C_2 := S - \chi_c\Theta(S + 1), \\ C_3 := (\bar{\kappa} + 4)(\bar{\kappa}S + 4) + 4(3\bar{\kappa}\Theta C_0 - 1). \end{cases} \tag{5.12}$$

Likewise, we expand (5.9) up to order 2, such that $\lambda \simeq \lambda_1 + \lambda_2$ with λ_1 and λ_2 of order 1 and 2 respectively. At first order:

$$\begin{aligned} \lambda_1 = \frac{1}{D_1}\Bigg\{ & 4S(S+1)\bar{e}\bar{\kappa}\Theta\Big(1+4\frac{\Theta}{B}C_0\sin^2(k/2)\Big)\sin^2(k/2) \\ & -48\bar{\alpha}\bar{\kappa}SB\Theta\Big(1+4\frac{\Theta}{B}C_0\sin^2(k/2)\Big)\sin^4(k/2)+2(S+1)(\overline{F}-\bar{v})\Theta\sin^2(k/2) \\ & \times\Big[(A_1-A_2)\Big(1+4\frac{\Theta}{B}C_0\sin^2(k/2)\Big)+2(\chi_c-\chi_a)B\Theta\Big(1+4\frac{\Theta}{B}C_0\Big)\sin^2(k/2)\Big]\Bigg\}, \end{aligned} \tag{5.13}$$

where

$$\begin{cases} D_1 := \big[B + 4\Theta C_0\sin^2(k/2)\big]^2 + (\chi_c - \chi_a)(S + 1)^2\Theta^2\sin^2(k), \\ A_1 := 1 + \chi_a\Theta(S + 1), \\ A_2 := S - \chi_a\Theta(S + 1). \end{cases} \tag{5.14}$$

As χ_d does not appear in this expression, we conclude that the transient term has no impact at first order, which contributes to legitimize the approximation made in Chapter 3 for the discrete-to-continuum limit of the continuum step model. Moreover, if we now look at the growth rate for each mechanism acting independently, we get, for the ES effect:

$$\lambda_1^{ES} = \frac{-2(S^2 - 1)(\overline{F} - \bar{v})\Theta\sin^2(k/2)}{B^2} \quad \propto \quad (\overline{F} - \bar{v})\Theta, \tag{5.15}$$

for the chemical effect:

$$\lambda_1^{CE} = \frac{4(\bar{\kappa}+2)(\overline{F}-\bar{v})\Theta^2\sin^4(k/2)}{(\bar{\kappa}+2)^2+4\Theta^2\sin^2(k)} \quad \propto \quad (\overline{F}-\bar{v})\Theta^2, \tag{5.16}$$

for the dynamical effect:

$$\lambda_1^{DE} = \frac{8(\overline{F}-\bar{v})\Theta^2\sin^2(k/2)\left[2-(\bar{\kappa}+2)\sin^2(k/2)\right]}{(\bar{\kappa}+2)^2-4\Theta^2\sin^2(k)} \quad \propto \quad (\overline{F}-\bar{v})\Theta^2, \tag{5.17}$$

and for the elastic step-step interaction:

$$\lambda_1^{EL} = \frac{-48\bar{a}\bar{\kappa}\Theta\sin^4(k/2)}{\bar{\kappa}+2} \quad \propto \quad \Theta, \tag{5.18}$$

so that we recover the scaling laws determined with the quasistatic approximation for the ES effect, the chemical effect, and the elastic step-step interaction (Section 4.3.4), and with the numerical resolution for the dynamical effect (Section 4.4). We are also able to provide an explanation for the discrepancy observed with the scaling laws at large values of $\overline{F}$ and $\bar{v}$. Indeed, as this is only a first order approximation, the terms in $\overline{F}^2$ and $\bar{v}^2$ become important in the large deposition/evaporation regime, invalidating the simple linear scaling law with $\overline{F}-\bar{v}$.

In the general context of $\chi_a = \chi_c = \chi = 1$, the dispersion relation simplifies to:

$$\begin{aligned}\lambda_1 = &\frac{\sin^2(k/2)}{B+4\Theta C_0\sin^2(k/2)} \\ &\times\left[2(S+1)\frac{\Theta}{B}(2\bar{\kappa}S\bar{e}+(\overline{F}-\bar{v})(A_1-A_2))-48\bar{a}\bar{\kappa}S\Theta\sin^2(k/2)\right],\end{aligned} \tag{5.19}$$

meaning there exists an unstable mode as long as:

$$2\bar{\kappa}S\bar{e}+(\overline{F}-\bar{v})(A_1-A_2)>0. \tag{5.20}$$

Further, ignoring the ES barrier ($S=1$):

$$\begin{aligned}\lambda_1 = &\frac{\sin^2(k/2)}{\bar{\kappa}+2+8\chi\Theta^2\sin^2(k/2)} \\ &\times\left[\frac{8\Theta}{\bar{\kappa}+2}(\bar{\kappa}\bar{e}+2\chi(\overline{F}-\bar{v})\Theta)-48\bar{a}\bar{\kappa}\Theta\sin^2(k/2)\right],\end{aligned} \tag{5.21}$$

and the instability condition reduces to:

$$\bar{\kappa}\bar{e}+2\chi(\overline{F}-\bar{v})\Theta>0. \tag{5.22}$$

Compared to the standard BCF model ($\chi=0$), for which stability is entirely dictated by the sign of $\bar{e}$ in the case of symmetric attachment/detachment, note how the chemodynamical effect introduces a lower bound $2\bar{v}\Theta/\bar{\kappa}$ for a step-down current to trigger instability in the evaporation regime. This qualitatively agrees with the experimental observations of O Coileain et al. (2011) and Usov

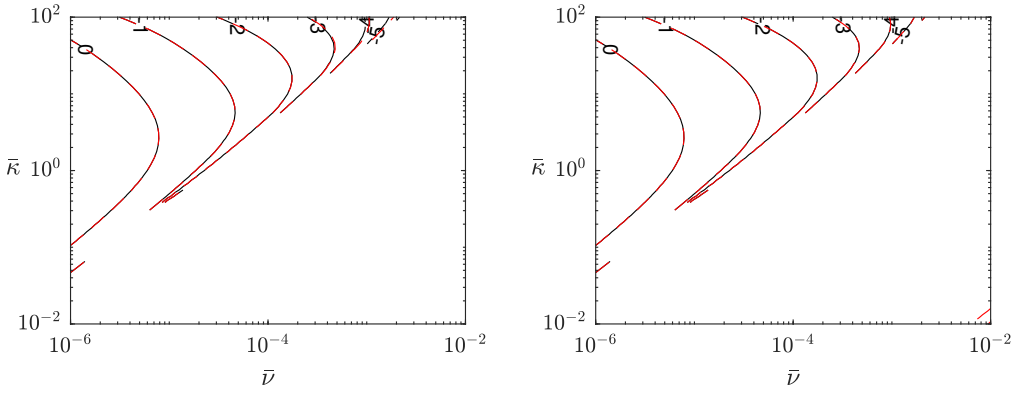

(a) Order 1, growth rate

(b) Order 2, growth rate

Figure 5.3: Superimposed stability diagrams for evaporation with electromigration obtained from the Chebyshev numerical method (black) and the transpiration method (red): (a) order 1 and (b) order 2. We do not show the k wavenumber of the most unstable mode as it is mostly constant at $k = \pi$. Parameters: $\Theta = 0.2$, $S = 1$, $\bar{e} = 10^{-5}$, $\bar{\alpha} = 10^{-8}$.

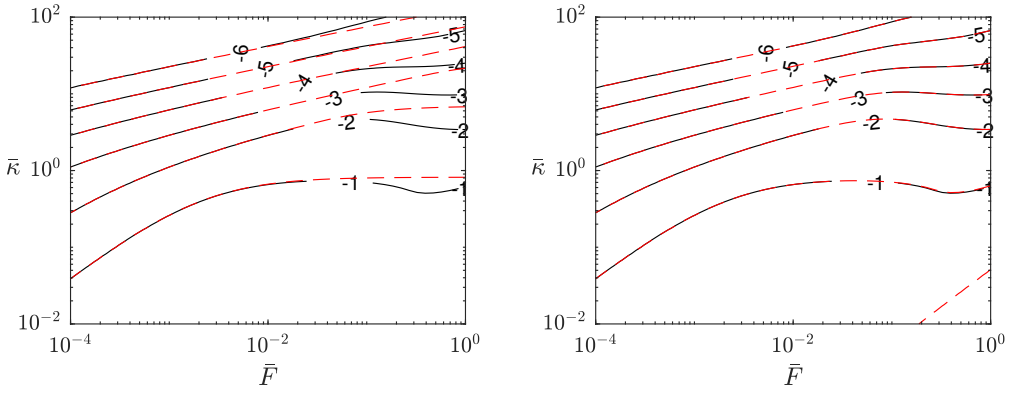

(a) Order 1, growth rate

(b) Order 2, growth rate

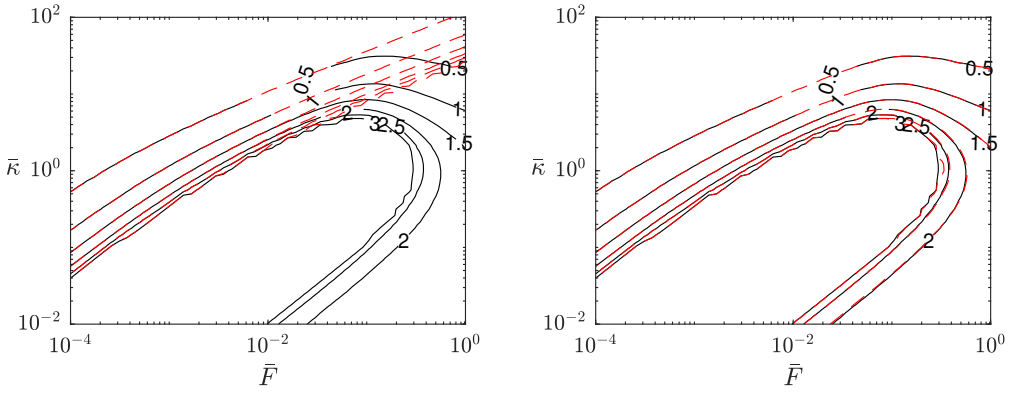

(c) Order 2, k wavenumber

(d) Order 2, k wavenumber

Figure 5.4: Superimposed stability diagrams for pure deposition ($\bar{v} = 0$) obtained from the Chebyshev numerical method (black) and the transpiration method (red): (top) order 1 and (bottom) order 2, (left) growth rate and (right) k wavenumber of the most unstable mode. Parameters: $\Theta = 0.05$, $S = 1$, $\bar{\alpha} = 10^{-5}$.

et al. (2011), which measure the strength of the electric field required to trigger instability, and is the object of a detailed analysis in Section 5.4.3. Further, in the deposition regime, we see that there exists an upper bound $2\overline{F}\Theta$ on the absolute value of the step-up current below which unstable growth will take place. This allows us to reinterpret, in Section 5.4.1, an experiment by Ranguelov et al. (2017) in the step-up regime under extreme deposition flux.

At second order, the complete expression becomes unmanageable. Given the expected value of model parameters, we only keep terms of order Θ^2 at most and assume $S = 1$. As illustrated in Figure 5.3 and Figure 5.4, this second order correction is only relevant at strong net deposition or evaporation flux, i.e. $|\overline{F} - \bar{v}| \gtrsim 10^{-2}$. Therefore, for the majority of experimental conditions, the first order expression is already an excellent approximation. We find, again in the context of $\chi_a = \chi_c = \chi = 1$:

$$\begin{aligned}\lambda_2 = \frac{1}{D_2}\Bigg\{ & \chi\bar{e}^2\frac{16}{3}\bar{\kappa}^2(\bar{\kappa}+2)^3\Theta^2\left(-24-27\bar{\kappa}-7\bar{\kappa}^2+\bar{\kappa}(\bar{\kappa}+3)\cos(k)\right)\\ & -\bar{e}\bar{v}\frac{2}{3}\bar{\kappa}^2(\bar{\kappa}+2)^5\Theta(\bar{\kappa}+6)\\ & +\chi(\overline{F}-\bar{v})^2\frac{1}{3}(\bar{\kappa}+2)^7\Theta^2(12+6\bar{\kappa}+\bar{\kappa}^2)(\cos(k)-\frac{\bar{\kappa}-2}{\bar{\kappa}+2})\\ & -\chi\bar{v}(\overline{F}-\bar{v})\frac{16}{3}(\bar{\kappa}+2)^5\Theta^2(6+6\bar{\kappa}+\bar{\kappa}^2)\\ & +\bar{e}(\overline{F}-\bar{v})\frac{2}{3}\bar{\kappa}(\bar{\kappa}+2)^6\Theta(12+6\bar{\kappa}+\bar{\kappa}^2)\Bigg\}\sin^2(k/2),\end{aligned}$$

where

$$D_2 := \bar{\kappa}\Big[(\bar{\kappa}+2)^2+4\chi^2\Theta^2\sin^2(k)\Big]D_1^3. \tag{5.23}$$

With this second order correction, the stability diagram from the approximate analytical expression coincides perfectly with the one obtained numerically from the Chebyshev collocation method. One may notice in Figure 5.3 an extraneous red line in the bottom right hand corner which seems to indicate that the analytical expression predicts an instability whereas the surface is actually stable. Nevertheless, this is not an issue as the restriction $\bar{v}/\bar{\kappa} \ll 1$, required for the validity of the near-equilibrium assumption, and which we use when Taylor expanding, is violated in that region, making it irrelevant in the present study.

5.4 REINTERPRETING EXPERIMENTAL RESULTS

5.4.1 *Extreme deposition regime in step-up electromigration*

As was demonstrated in Guin (2018), the dynamical and chemical effects do not provide a novel reversal mechanism to explain the different high-temperature regimes on Si(111). However, their inclusion in the step continuum model offers a more fitting interpretation of a recent experiment performed

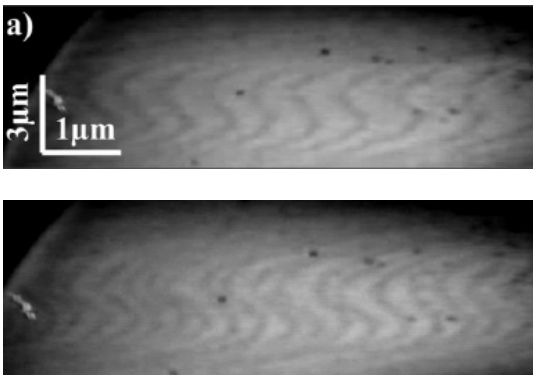

Figure 5.5: LODREM images of Si(111) at 1220°C, with step-up current and deposition flux of 5 bi-layers per second. (top) initial vicinal surface with almost equidistant monoatomic steps and (bottom) pairs of steps after 12s (reprinted from Ranguelov et al. (2017) with permission from Elsevier).

by Ranguelov et al. (2017) at a reported temperature of 1220°C under a very high deposition rate, for which a step-pairing instability is shown to develop. However, before proposing our interpretation, we need to tackle one caveat in the experimental setup to make sense of the result, as we believe the authors erroneously assume the growth to take place in regime II whereas regime III seems more logical based on their observations.

Indeed, to cite Ranguelov et al. (2017), their "experiments are done at a temperature below 1250°C and step-up direction of the electromigration force" as they claim the "vicinal surface is known to be stable in classical growth conditions, that means when exposed to 'reasonable' incident flux of silicon atoms". This last claim is accompanied by a reference to Leroy et al. (2009), which compiles different experimental results from the literature regarding the stability of Si(111) surface under electromigration. While several examples are given for the pure evaporation regime (Latyshev et al., 1989, 1990; Homma et al., 1990; Yang et al., 1996; Métois and Stoyanov, 1999; Gibbons et al., 2006), only one source is cited for a surface under net deposition (Métois and Stoyanov, 1999), disregarding the results of Gibbons et al. (2005, 2006). The conclusion drawn in Leroy et al. (2009) from that unique source is that step-bunching always occurs at step-down direction of the current, regardless of the temperature. However, even in the referenced work of Métois and Stoyanov (1999), step-pairing at step-up direction of the current is mentioned in regime II (with a net deposition flux of 0.7 ML/s) while in Gibbons et al. (2005) complete step-bunching is reported (with a net deposition flux of 0.03 ML/s), thus contradicting the argument made by Ranguelov et al. (2017) that a vicinal surface at step-up direction of the current under net deposition is classically stable.

Further, if the experiment in Ranguelov et al. (2017) truly took place in regime II, it would not be possible to conclude definitively on the origin of the instability as the surface has already been shown to be unstable at weak (Gibbons et al., 2005) and intermediate (Métois and Stoyanov, 1999) intensities of the deposition flux. However, given the uncertainty on temperature intervals (which may vary by as much as 50°C (Leroy et al., 2009)) and on the (7×7) to

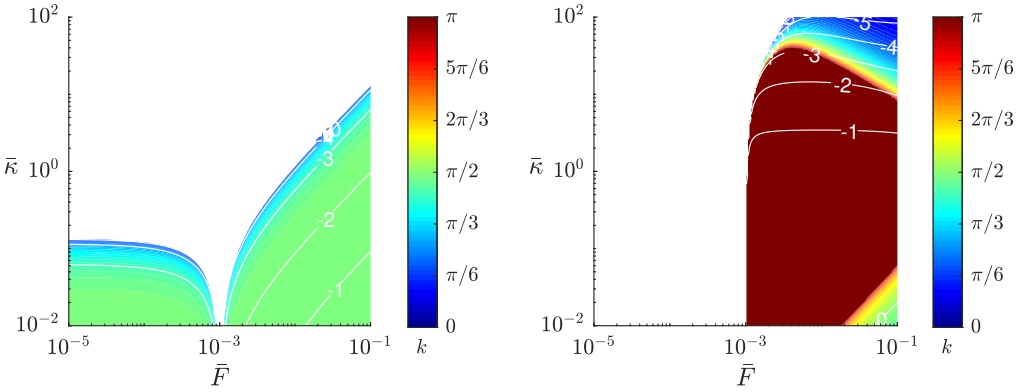

Figure 5.6: Stability diagrams of (a) the model by Ranguelov et al. (2017) and (b) our model. Colorbar for unstable mode wave-number. Contours for logarithm of growth rate. Parameters: $\Theta = 0.2$, $\bar{\nu} = 10^{-3}$, $S = 1$, $\bar{e} = -10^{-5}$, $\bar{\alpha} = 10^{-8}$.

(1×1) transition temperature (from 830°C (Telieps and Bauer, 1985) to 870°C (Bennett and Webb, 1981; Miki et al., 1992), with a dependence on the miscut angle (Phaneuf et al., 1988; Suzuki et al., 1993; Minoda, 2003)), it is possible that the surface temperature Ranguelov et al. (2017) report as 1220°C is in fact closer to 1250°C, placing it in regime III (which is classically stable for step-up current, see Table 5.1) rather than regime II. Moreover, this analysis is consistent with the fact that under mild deposition fluxes, Ranguelov et al. (2017) do not observe instability, contrary to the observations in Métois and Stoyanov (1999). Based on these explanations, we come to the conclusion that the experiment in Ranguelov et al. (2017) takes place in the regime III, and not the regime II assumed by the authors. Nevertheless, only additional experiments would resolve this interpretation uncertainty.

In regime III, at step-up current, the vicinal surface is classically observed to be stable, under both evaporation and deposition conditions, in line with the theoretical predictions of the BCF model. However, the authors show that while this is true for weak to medium deposition flux, the surface exhibits a step-pairing instability at high deposition flux (5 ML/s), shown in Figure 5.6. Based on the classical BCF framework, they derive a model without recourse to the quasistatic approximation, although fast surface diffusion and slow attachment/detachment kinetics of adatoms at the steps are assumed, which allow them to consider that the adatom density is constant across each terrace (but varies between terraces) in the absence of electromigration. To take into account the bias induced by the electromigration force, they rely on a linear approximation for the concentration profile such that the adatom density is higher at the ascending (descending) step edge for step-up (step-down) current, respectively (Ranguelov and Stoyanov, 2008).

Under these hypotheses, the authors set forth a new type of instability due to dynamics effect, that they refer to as the "kinetic memory effect". However, we find that although it predicts instability, it does not predict the correct unstable mode of step-pairing ($k = \pi$) but rather an intermediate mode $k \simeq \pi/2$ as illustrated in Figure 5.6. On the other hand, our model, which includes the

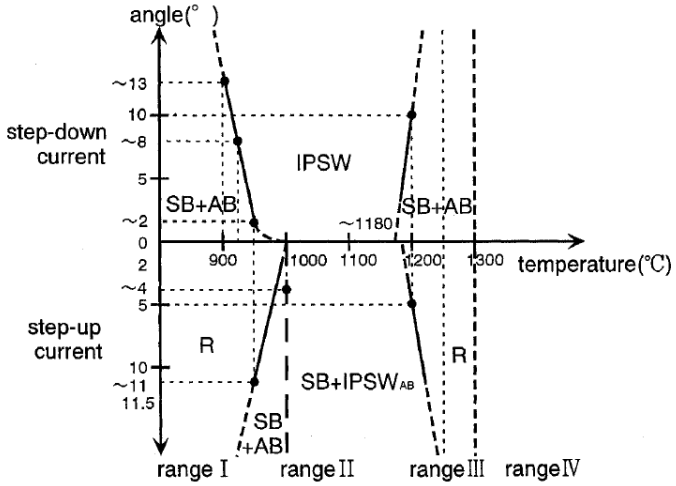

Figure 5.7: A "phase diagram" of dc-heating induced step instabilities on Si(111) showing the temperature and miscut angle dependence of step configuration (reprinted from Minoda (2003) with permission from IOP Publishing).

thermodynamically derived chemical term as well as all dynamics terms, is able to predict the step-pairing instability. The quasistatic theory actually shows an instability but only at very high kinetics (which is unlikely) and for weak deposition fluxes, which is at odds with the observations.

5.4.2 *Step-bunching to step-meandering transition*

As mentioned in the introduction, step meandering can also be observed in situations of step-down current in regime II, transitioning from step bunching in regime I. Interestingly, this transition is dependent both on the temperature and the miscut angle of the surface as can be seen from the pseudo phase diagram in Figure 5.7 taken from Minoda (2003). While the temperature dependence is challenging to accurately describe, given the uncertainty on the activation energy of the different processes, the miscut dependence is relatively accessible.

Based on experimental estimates (see Appendix D), our model indeed predicts a transition from step meandering at large miscut angles to step bunching at low miscut angles (see Figure 5.8).

Despite this qualitative agreement, this interpretation suffers from the major drawback that our model does not predict the step-bunching instability at step-up current, as expected from impermeable-step boundary conditions. We also note that the surface is predicted to be unstable against step meandering even in the absence of direct-current heating. This does not necessarily go against experimental observations of stable surfaces under alternative-current heating (Latyshev et al., 1989; Houchmandzadeh et al., 1994). Indeed, step-up current is predicted to stabilize the surface and the frequency used in the aforementioned experiments (50 Hz) is high enough that the growth rate associated to the step meandering instability is not large enough for the instability to visibly develop in the short time span when the alternative current is step-down. An

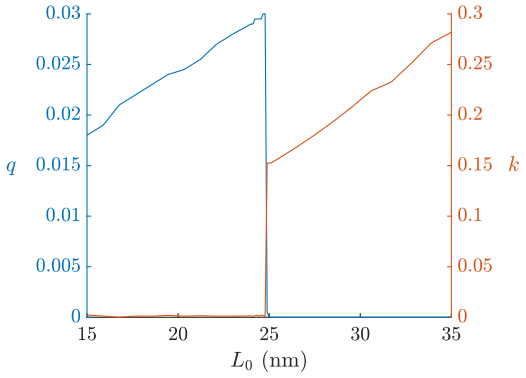

Figure 5.8: Wavenumbers k and q of the most unstable mode as a function of the initial terrace width $\mathcal{L}_0$. The parameters at $\mathcal{L}_0 = 18$ nm (i. e., a miscut angle of 1°) are: $\bar{\nu} = 10^{-6}$, $S = 1$, $\Theta = 0.2$, $\bar{\kappa} = 0.5$, $\bar{e} = 10^{-6}$, $d_{xx} = 5$ eV nm, $\bar{\gamma} = 10^{-3}$, $\Pi = 0$.

experimental setup with only radiative indirect heating would be required to clarify that point.

5.4.3 *Critical field as a function of initial step spacing*

In the experimental studies of electromigration, a minimum electric field (the *critical field*) has to be applied to the sample to trigger step bunching. From the instability condition (5.22), under pure evaporation, the expression for the critical field is:

$$\bar{e}_{cr} = 2\frac{\bar{\nu}\Theta}{\bar{\kappa}}. \tag{5.24}$$

However, this places no lower limit on the growth rate, which goes to zero as $\bar{e} \to \bar{e}_{cr}$, making it virtually undetectable in practice, as experiments must have a finite duration. Consequently, a more sensible choice would be to look at the maximum growth rate λ_m and compute $\bar{e}_{cr}$ as the minimal value of $\bar{e}$ required to put that maximum growth rate above a pre-specified threshold λ_0, dependent on the experiment's duration. Given the complexity of the expression for λ_m, we rely on a numerical resolution to determine the critical field as a function of the initial terrace length $\mathcal{L}_0$.

We aggregate different studies from the literature to compile a physical set of parameters (see Appendix D for more details)

$$\begin{cases} L_{eva} = 100\ \mu\text{m}, \\ \alpha = 0.015\ \text{eV nm}, \\ \Theta = 0.2, \\ \lambda_0 \sim 10^{-3} \text{ at } 1130°\text{C}, \lambda_0 \sim 5 \times 10^{-3} \text{ at } 1270°\text{C}, \end{cases} \tag{5.25}$$

where we have considered an instability to be detectable after a 10-fold increase of the initial perturbation of the step position.

For the -0.8 exponent, the BCF model and ours give indistinguishable results as $\bar{\kappa}^* \simeq 19$, which agrees with the general condition $\bar{\kappa}^* \gtrsim 1$ deduced from

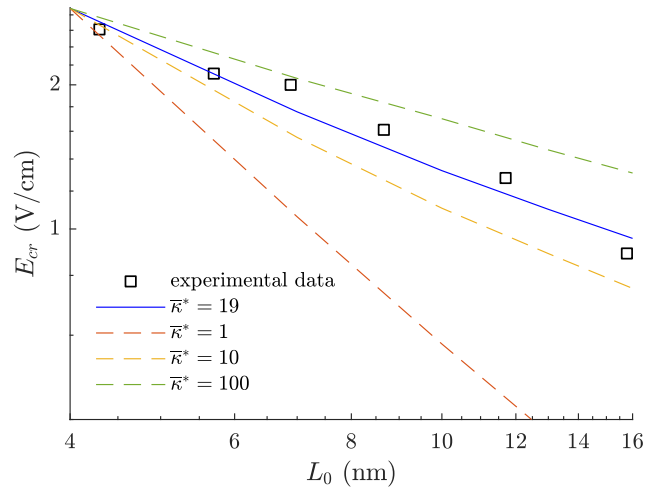

Figure 5.9: Dependence of the critical field E_{cr} on the initial interstep distance $\mathcal{L}_0$ for different values of $\bar{\kappa}^*$ (experimental data adapted from O Coileain et al. (2011) with permission from APS).

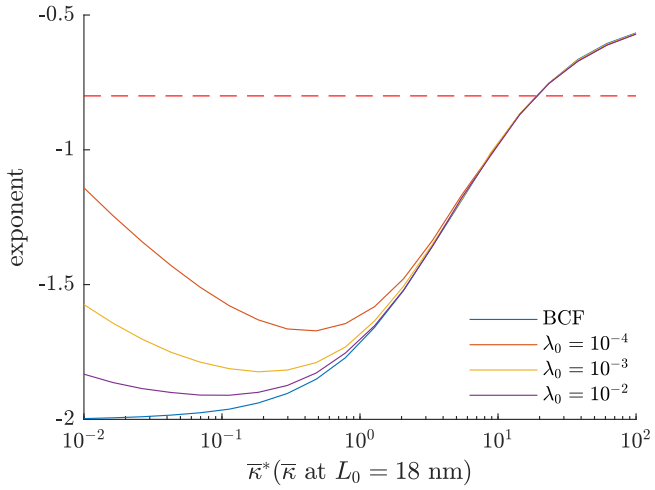

Figure 5.10: Dependence of the power-law exponent of the critical field with $\bar{\kappa}^*$ (the value of $\bar{\kappa}$ at $L = 18$ nm) for different L_d^{eva}.

Gibbons et al. (2005). Discrepancies start appearing in the attachment/detachment limited regime ($\bar{\kappa}^* \lesssim 1$), as the relation we derive depends on the various parameters L_{eva}, λ_0, or d_{xx}, while the one obtained from the BCF model does not, but instead corresponds to the limit $L_{eva} \gg 1$, $\lambda_0 \gg 1$, or $d_{xx} \gg 1$ as evidenced in Figure 5.10, Figure 5.11, and Figure 5.12. In contrast, O Coileain et al. (2011) use a formula derived in the quasistatic setting by Stoyanov (2011) who established $E_{cr} \sim \mathcal{L}_0^{-3}$ for $\bar{\kappa} \ll 1$ and $E_{cr} \sim \mathcal{L}_0^{-1}$ for $\bar{\kappa} \gg 1$, but is limited to small wavenumbers, and as such gives erroneous results for arbitrary wavenumbers, which can be the most unstable ones. Besides, they define the critical field with no consideration for the growth rate, which, as we have demonstrated, has a strong impact on the analysis. As such, even though our work does not provide

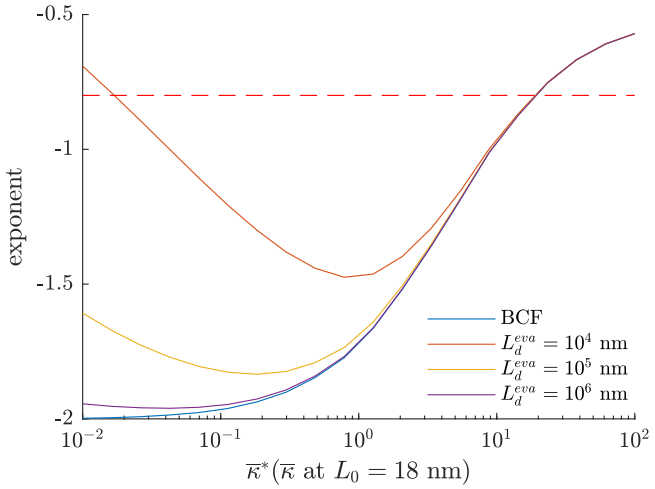

Figure 5.11: Dependence of the power-law exponent of the critical field with $\bar{\kappa}^*$ (the value of $\bar{\kappa}$ at $L = 18$ nm) for different λ_0.

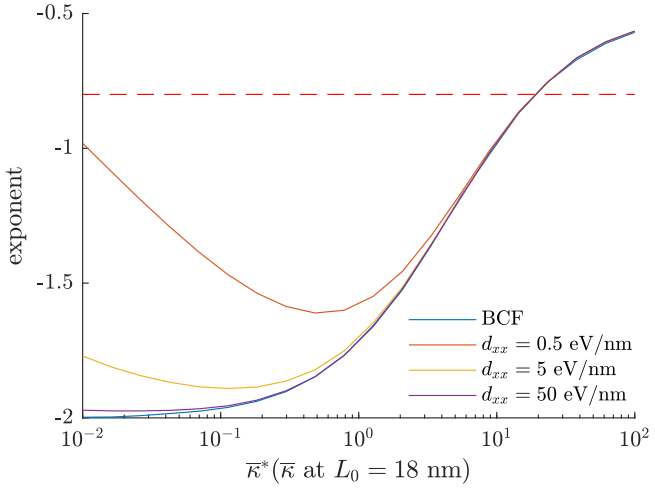

Figure 5.12: Dependence of the power-law exponent of the critical field with $\bar{\kappa}^*$ (the value of $\bar{\kappa}$ at $L = 18$ nm) for different d_{xx}.

new insights into the stability reversals, it gives a proper interpretation of the experimental results showcased in O Coileain et al. (2011).

5.5 KEY RESULTS

We have completed the linear stability analysis of Chapter 4 by studying the effects of electromigration. A step-down current destabilizes the surface towards step-bunching and a step-up current stabilizes the surface completely. However, the chemical and dynamical effects are sufficiently strong to trigger step meandering in a certain region of the parameter space. This is consistent with the fact that the equilibrium adatom coverage is usually large in electromigration experiments due to the high temperatures involved, so that the chemical and dynamical effects, which scale quadratically with Θ, dominate the electromigration effect, which only scales linearly with Θ.

The behavior of Si(111) under electromigration is extremely complex and the dynamical and chemical effects do not elucidate all the open questions regarding the stability of the surface. Nevertheless, they do provide new insights regarding some experimental results. In the extreme deposition regime, under step-up current, we were able to accurately predict the step-pairing instability observed. Under step-down current, we have shown that a transition from step-bunching to step-meandering is possible by changing the initial terrace width, in agreement with experiments. Finally, revisiting the experimentally measured relation between the critical electric field (i. e., the field required to trigger step bunching) and the initial terrace width, we have derived a robust value for the attachment/detachment kinetics coefficient, in the sense that it is not sensitive to the values of other parameters, at $\bar{\kappa}^* = 19$ (i. e., the value of $\bar{\kappa}$ at $\mathcal{L}_0 = 18$ nm). As $\bar{\kappa}^* > 1$ but we do not have $\bar{\kappa}^* \gg 1$, this places the surface in an intermediate regime between kinetics- and diffusion-limited, leaning towards the latter, in line with previous estimates.

Using the transpiration method for the linear stability analysis of the step continuum equation, we have also provided an approximate analytical expression of the growth rate including the dynamics terms, which coincides precisely with the exact numerical results from the Chebyshev collocation method, offering a clearer view of the interplay between the different mechanisms.

The fact that the stability reversals observed with increasing temperature on Si(111) still elude our complete theory seems to suggest that more complex mechanisms are at play, e. g., a dependence on the electric field of the parameters or reconstructions at the surface that introduce a space-dependence in the parameters.

6

SUMMARY AND DISCUSSION

We have proposed an overview of morphological instabilities on vicinal surfaces, from the fundamental derivation of the step-flow governing equations to the interpretation of experimental results, putting emphasis on the seldom considered chemical and dynamical effects.

Using nonequilibrium thermodynamics and the formalism of configurational forces, we have derived a generalized Gibbs–Thomson relation for the step chemical potential which accounts, from the outset, for the contribution of the elastic bulk, leading to a thermodynamically consistent generalization of the BCF model for the step dynamics equations. Furthermore, in contrast with the prevailing derivations in the literature, we do not have recourse to the quasistatic approximation, and consider all the dynamics terms, which are composed of the transient term in the reaction-diffusion equation and the advective terms in the boundary conditions. After studying in detail the dipolar representation of step-step interaction, we have shown, in the context of step-flow growth, that one dipolar moment suffices to capture the behavior of elastic interaction between steps.

Based on that model, we have studied the coarsening of step bunches via extensive numerical simulations and established scaling laws which describe the nonlinear evolution of bunches. To confirm our findings, we have conducted a discrete-to-continuum derivation leading to a nonlinear PDE to describe the macroscopic evolution of the surface profile, which allowed us to recover exactly the numerically obtained scaling laws. Importantly, we have shown that the dynamical and chemical effects can account for the onset of step bunching and for the scaling laws observed in the coarsening regime, thereby circumventing the need for an inverse Ehrlich-Schwoebel barrier required by the classical BCF model. Further, we have demonstrated how these scaling laws permit the determination of microscopic parameters of the surface from macroscopic features of the bunches. Unfortunately, they do not allow to differentiate between the different destabilizing mechanisms.

Regarding the stability analysis method, we have started by deriving a closed-form expression of the dispersion relation under the quasistatic approximation, before proposing a numerical approach taking into account all the dynamics terms, which generalizes the method developed in Guin (2018) to two dimensions. As both the function (the adatom density field) and the domain (the terraces delimited by steps) are subjected to perturbations, we have used an *arbitrary Lagrangian-Eulerian* transformation to reformulate the problem on a fixed domain. Checking the stability of the system against infinitesimal perturbations of the principal solution, we have exploited the time and space translation invariance of the resulting linear perturbation equation to write the perturbation as a combination of normal modes and obtain the stability of

the system by checking the stability with respect to each of these modes. The stability problem hence reduces to a generalized eigenvalue problem which was solved numerically using Chebyshev collocation method. Alternatively, we have also derived an approximate analytical expression for the dispersion relation with dynamics terms, using the transpiration method and Taylor expansions, which is in excellent agreement with the exact numerical results and offers a clearer view of the interplay between mechanisms.
We have then analyzed the influence on stability of all the mechanisms independently (ES effect, chemical effect, dynamical effect, elasticity, step stiffness) as well as their interplay, and discussed the influence of the operational and material parameters (deposition/evaporation rates, equilibrium adatom coverage, attachment/detachment coefficient, step-edge diffusion) on the relative weight between the mechanisms.
Like in the one-dimensional straight-step context, we have shown that the chemical and dynamical effect have a significant impact on stability, which increases with the equilibrium adatom coverage relative to the other mechanisms. Under deposition, the chemical effect maximally destabilizes the step-pairing mode and maximally stabilizes in-phase meandering. The dynamical effect maximally destabilizes a bunching mode with wavenumber $0 < k < \pi/2$ and maximally stabilizes anti-phase meandering. In both cases, the stabilizing/destabilizing nature of the effect is reversed under evaporation. We have pointed out the similarities with an inverse ES effect, and proposed that the dynamical and chemical effect may be seen as an effective inverse ES effect, reconciling the theories that require an inverse ES effect to trigger instability and the unlikelihood of the existence of an actual energetic inverse ES barrier. Furthermore, we have shown how the combination of the chemical and dynamical effect with a direct ES barrier allows for the coexistence of bunching and meandering, in contrast with the BCF model which predicts that the two instabilities are mutually exclusive.

We have also striven to provide a comparison with crystal growth experiments, combining several experimental studies to estimate the physical parameters of the problem, and quantitatively evaluate the importance of the chemical and dynamical effects. We have shown that in specific situations, these effects offer interesting alternative explanations to account for the step instabilities observed, in particular in the context of electromigration. However, the stability reversals on $\mathrm{Si}(111)$ under electromigration still remain unsolved.

The chemical and dynamical effects provide valuable new insights into the stability of vicinal surfaces and the coarsening behavior of step bunches. However, given the multiple possible origins of step instabilities and the large uncertainties surrounding many of the physical parameters, which can span several orders of magnitude, it is often difficult to ascribe the occurrence of a step instability to a precise mechanism. We had hoped that the study of step-bunching patterns would help ascertain the mechanism responsible for the instability by providing additional information compared to the onset of instability, but we have shown that while the dynamical and chemical effects can trigger step bunching without recourse to an inverse ES effect, they are

essentially indiscernible from it in the scaling laws describing the coarsening of the surface profile. In this respect, the study of the nonlinear behavior of meanders, which has successfully been used in the past to discriminate between destabilizing mechanisms based on Kinetic Monte Carlo simulations (Nita and Pimpinelli, 2005; Blel et al., 2017), could provide further insights into the influence of the dynamical and chemical effects. Additionally, while we have focused on a train of initially straight steps, a next natural step would be to investigate island stability, as was done by Kuhn et al. (2005) and Haußer et al. (2007) in the framework of the classical BCF model, and revisit the intriguing possibilities of shape control (Haußer et al., 2010; Hu et al., 2012) in light of our thermodynamically consistent model with dynamics terms. Finally, regarding electromigration, it would be interesting to derive an atomistic description of the electromigration force that could perhaps provide novel insights into the intriguing stability reversals of Si(111).

APPENDICES

A

INFLUENCE OF COUPLING IN THE CONSTITUTIVE RELATIONS

When deriving the constitutive relations for the different fluxes, we restricted the analysis to the simplest solution, neglecting all couplings. In this appendix, we investigate the influence of a possible coupling between the fluxes arriving at the step from the lower and upper terraces, which is the most likely to have an impact given how the chemical effect couples the adatom density fields of adjacent terraces. The fluxes are written:

$$\begin{cases} J^+ = \gamma^+(\mu^+ - \mu^s) + \gamma^{+-}(\mu^- - \mu^s), \\ J^- = \gamma^-(\mu^- - \mu^s) + \gamma^{-+}(\mu^+ - \mu^s), \end{cases} \tag{A.1}$$

where the dissipation inequality imposes the positiveness of γ^+ and γ^-, and the inequality $\gamma^{+-} + \gamma^{-+} \leqslant 2\sqrt{\gamma^+\gamma^-}$. Considering the simplest case $\gamma^+ = \gamma^- = \gamma$ and $\gamma^{+-} = \gamma^{-+} = c_\gamma\gamma$, the inequality becomes $c_\gamma \leqslant 1$.

As illustrated with the dispersion curves of Figure A.1, this coupling does not influence the stability domains: it is not a stabilizing/destabilizing mechanism *per se* but a material parameter that controls the relative weights of the different mechanisms. Increasing c_γ further destabilizes step pairing and stabilizes in-phase meandering. While its impact is already noticeable for coupling values of $c_\gamma \simeq 0.2$, we have no way of experimentally evaluating c_γ, and cannot conclude on whether this value is realistic. Interestingly, the effect of the coupling appears to effectively simulate a higher adatom coverage (see Figure A.2). On surfaces at low temperatures, for which the adatom coverage Θ is typically small and thus the chemodynamical effect is expected to be negligible given it scales as Θ^2 in the dispersion relation for the growth rate, the existence of this coupling could provide additional weight to the destabilizing effect of the chemical and dynamical effects.

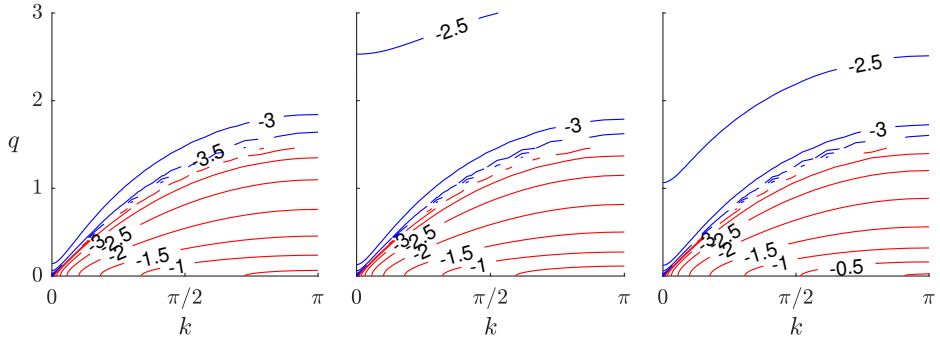

Figure A.1: Dispersion curves showing the influence of the coupling parameter c_γ. From left to right, $c_\gamma = 0$, $c_\gamma = 0.2$, and $c_\gamma = 0.5$. Parameters: $\overline{F} = 10^{-4}$, $\Theta = 0.1$, $\bar{\kappa} = 10^{-2}$. [see color legend in Figure 4.7]

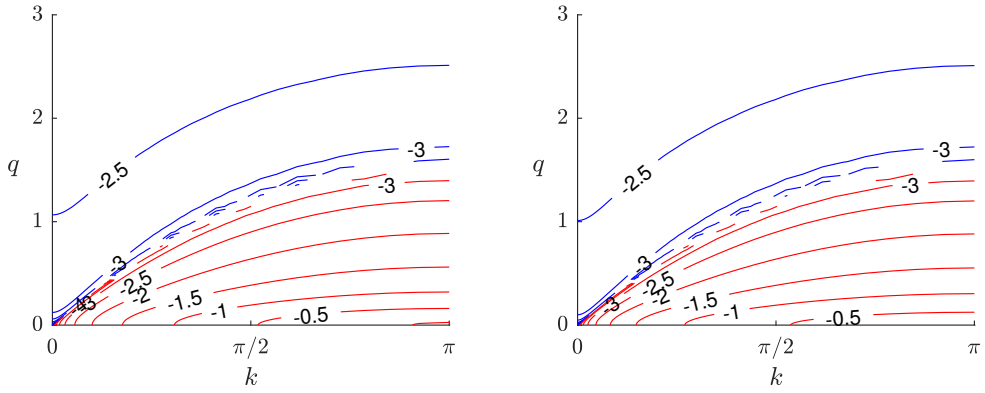

(a) $(c_\gamma, \Theta) = (0.5, 0.1)$ (b) $(c_\gamma, \Theta) = (0, 0.15)$

Figure A.2: Comparison of the dispersion curves for (a) $(c_\gamma, \Theta) = (0.5, 0.1)$ and (b) $(c_\gamma, \Theta) = (0, 0.15)$. Parameters: $\overline{F} = 10^{-4}$, $\Theta = 0.1$, $\bar{\kappa} = 10^{-2}$. [see color legend in Figure 4.7]

B

GREEN'S FUNCTION FOR A HALF-SPACE

The components of the tensor Green's function for a half space in the absence of surface stress are taken from (Lifshitz et al., 1986). They read:

$$
\begin{cases}
G_{11}(x_1,x_2,x_3) = \dfrac{1+\nu}{2\pi E}\Big(\dfrac{2(1-\nu)r+x_3}{r(r+x_3)} + \dfrac{2r(\nu r+x_3)+x_3^2}{r^3(r+x_3)^2}x_1^2\Big), \\
G_{12}(x_1,x_2,x_3) = \dfrac{1+\nu}{2\pi E}\dfrac{2r(\nu r+x_3)+x_3^2}{r^3(r+x_3)^2}x_1x_2, \\
G_{13}(x_1,x_2,x_3) = \dfrac{1+\nu}{2\pi E}\Big(\dfrac{x_3}{r^2} - \dfrac{1-2\nu}{r+x_3}\Big)\dfrac{x_1}{r}, \\
G_{21}(x_1,x_2,x_3) = \dfrac{1+\nu}{2\pi E}\dfrac{2r(\nu r+x_3)+x_3^2}{r^3(r+x_3)^2}x_1x_2, \\
G_{22}(x_1,x_2,x_3) = \dfrac{1+\nu}{2\pi E}\Big(\dfrac{2(1-\nu)r+x_3}{r(r+x_3)} + \dfrac{2r(\nu r+x_3)+x_3^2}{r^3(r+x_3)^2}x_2^2\Big), \\
G_{23}(x_1,x_2,x_3) = \dfrac{1+\nu}{2\pi E}\Big(\dfrac{x_3}{r^2} - \dfrac{1-2\nu}{r+x_3}\Big)\dfrac{x_2}{r}, \\
G_{31}(x_1,x_2,x_3) = \dfrac{1+\nu}{2\pi E}\Big(\dfrac{x_3}{r^2} + \dfrac{1-2\nu}{r+x_3}\Big)\dfrac{x_1}{r}, \\
G_{32}(x_1,x_2,x_3) = \dfrac{1+\nu}{2\pi E}\Big(\dfrac{x_3}{r^2} + \dfrac{1-2\nu}{r+x_3}\Big)\dfrac{x_2}{r}, \\
G_{33}(x_1,x_2,x_3) = \dfrac{1+\nu}{2\pi E}\Big(\dfrac{x_3^2}{r^3} + \dfrac{2(1-\nu)}{r}\Big),
\end{cases}
\tag{B.1}
$$

with $r = \sqrt{x_1^2+x_2^2+x_3^2}$.

C

FORMULA FOR THE STEP-STEP INTERACTION OF MEANDERING STEPS

Computing $\mathfrak{f}^{(r)}$ requires the calculation of complex integrals, which heavily involve Meijer G-function $G^{m,n}_{p,q}$. Denoting K_5 the 5^{th} modified Bessel function of the second kind and letting

$$M_n(r,q) = G^{2,1}_{1,3}\left(\frac{q^2r^2}{4}\middle|\begin{matrix} n-9/2 \\ 0,n,1/2 \end{matrix}\right), \tag{C.1}$$

the expression for $\mathfrak{f}^{(r)}$ takes the form:

$$\begin{aligned}\mathfrak{f}^{(r)} = \frac{4(1-\nu^2)}{\pi E(r\mathcal{L}_0)^4}\Big[& d_{xx}^2\Big(6+\frac{8}{315}\frac{1}{1-\nu}\cos(kr)\tilde{M}_{xx}(r,q)\Big) \\ & + d_{xz}^2\Big(6-\frac{8}{315}\cos(kr)\tilde{M}_{xz}(r,q)\Big) \\ & - d_{xx}d_{yy}\frac{\nu}{1-\nu}\cos(kr)\tilde{M}_{xy}(r,q) \\ & + d_{yy}^2\frac{1}{1-\nu}\cos(kr)\tilde{M}_{yy}(r,q)\Big],\end{aligned} \tag{C.2}$$

where

$$\begin{cases} \tilde{M}_{xx}(r,q) := -6(1-5\nu)M_2(r,q) + 6(7-60\nu)M_3(r,q) \\ \qquad\qquad + 16(2+15\nu)M_4(r,q) - r^5q^5K_5(rq), \\ \tilde{M}_{xz}(r,q) := 6M_2(r,q) - 42M_3(r,q) - 32M_4(r,q) + r^5q^5K_5(rq), \\ \tilde{M}_{xy}(r,q) := \frac{128}{105}M_2(r,q) - \frac{1696}{105}M_3(r,q) \\ \qquad\qquad + \frac{4352}{315}M_4(r,q) - \frac{16}{315}r^5q^5K_5(rq), \\ \tilde{M}_{yy}(r,q) := \frac{64}{315}(1+2\nu)M_2(r,q) - \frac{16}{315}(23+136\nu)M_3(r,q) \\ \qquad\qquad - \frac{16}{315}(23-159\nu)M_4(r,q) + \frac{4}{315}(1-3\nu)r^5q^5K_5(rq). \end{cases} \tag{C.3}$$

D

SELECTION OF THE MATERIAL PARAMETERS FOR SI(111)-7×7

Based on experimental estimates found in the literature, we propose physically relevant values and ranges for the nondimensional parameters of the model on the $\mathrm{Si}(111)-7\times7$ surface. In addition to a dependence on intrinsic material properties, note that many of the parameters also involve the initial terrace width $\mathcal{L}_0$. Given that $\mathcal{L}_0$ may vary between 1 nm and 1 µm , it can have a considerable impact on the value of the different parameters. Therefore, we arbitrarily pick a reference terrace width of $\mathcal{L}_0^* = 18$ nm, corresponding to a 1° miscut angle on Si, to express reference values for the different parameters, which are denoted by a star. The value for an arbitrary terrace width can then simply be obtained with a relation of the type

$$\overline{X} = \left(\frac{\mathcal{L}_0}{\mathcal{L}_0^*}\right)^p \overline{X}^*, \tag{D.1}$$

with p the power associated to the parameter considered.

Before proceeding with our review, another important remark is in order regarding the near-equilibrium assumption. Taking the steady-state solution (4.19) in the case of pure deposition, we can easily calculate the maximum density on the terrace and show that the upper bound is obtained for $S = 0$ as

$$\overline{\rho}_{\max} = 1 + \frac{\overline{F}}{2\bar{\kappa}}\Big(\bar{\kappa}(1+\chi_c\Theta+(\chi_c\Theta)^2)+2\Big), \tag{D.2}$$

meaning that for the near-equilibrium assumption to be valid, i. e., $|\overline{\rho}-1| \ll 1$, we must always verify

$$\frac{\overline{F}}{\bar{\kappa}} \ll 1 \text{ and } \overline{F} \ll 1. \tag{D.3}$$

In the case of evaporation, the calculations, although more involved, yield the exact same identities:

$$\frac{\bar{\nu}}{\bar{\kappa}} \ll 1 \text{ and } \bar{\nu} \ll 1. \tag{D.4}$$

Moreover, the deposition rate is also restricted by the constraint of step-flow regime. Indeed, as developed in Michely and Krug (2012) and Krug (2005), an excessively high deposition rate (quantitatively $\overline{F}\Theta > 1$) would lead to island nucleation, i. e., Volmer-Weber island formation growth mode.

EQUILIBRIUM ADATOM COVERAGE Θ

The equilibrium adatom coverage is usually measured by rapid quenching of the vicinal surface at equilibrium and analysis of the island coverage resulting from the crystallization of adatoms.

The Si(111) surface undergoes a phase transition from a 7×7 reconstruction at low temperatures (650 to 850°C) to a disordered 1×1 phase at high temperatures (850°C to 1200°C), each phase exhibiting distinct properties. Yang and Williams (1994) measured $\Theta = 0.041$ for a 7×7 reconstructed surface in the low temperature regime, and $\Theta = 0.2$ for the disordered 1×1 phase in the high temperature regime. More recently, Rogilo et al. (2016) found values of $\Theta = 0.14$ and $\Theta = 0.23$ at 1000°C and 1100°C, respectively. By means of medium-energy ion scattering measurements, Hibino et al. (1998) observed a fairly constant adatom coverage $\Theta \approx 0.2$ to 0.25 over the temperature range 830°C to 1200°C.

In sum, the equilibrium adatom coverage is expected to be of the order of a few percents at low temperature and around 0.2 at high temperature.

DEPOSITION RATE $\overline{F}$

The value of $\overline{F}$ is essentially tied to the terrace diffusion coefficient D, for which measurements are difficult and, as a result, often lack accuracy. The values most commonly reported for the activation energy lie between 1.1 and 1.6 eV, from experiments and first-principle calculations, across all temperature regimes (Bedair, 1974; Latyshev et al., 1990, 1996; Sato et al., 2000b; Chang and Wei, 2003). Assuming a hop frequency of 10^{13}, and a temperature range from 650°C to 1300°C, this yields D in the range 10^3 to 10^8 nm^2/S, or 10^6 to 10^8 if we only consider the activation energy of 1.1 eV. The deposition rate in experiments can be as low as 0.01 nm/s (Omi et al., 2005) and as high as 1.6 nm/s (Ranguelov et al., 2017).

As a result, one can expect $\overline{F}^*$ to range typically from $5 \times 10^{-4\pm1}$ at 650°C to 3×10^{-6} at 1250°C. This means that on surfaces with extra-wide terraces, e. g., in Ranguelov et al. (2017) where $\mathcal{L}_0 = 1$ µm, $\overline{F}$ can reach values of up to 0.1, which still complies with the near-equilibrium restrictions.

EVAPORATION RATE $\bar{\nu}$

The evaporation rate can be directly deduced from the diffusion length of adatoms, which has been measured by Rogilo et al. (2016) at 1000°C to $L_d^{eva} = 31$µm, implying $\bar{\nu}^* = 3.4 \times 10^{-7}$. Using an activation energy of 2.45 eV for $\bar{\nu}$, as determined by Rogilo et al. (2016) (and consistent with a previous estimate of 2.65 eV by Pang et al. (2008)), we find $\bar{\nu}^* = 9 \times 10^{-6}$ at 1200°C, and thus $L_d^{eva} = 6$ µm.

Measuring the velocity of a step as a function of the width of the terraces at 1200°C, Métois and Audiffren (1997) observed a linear relation up to $\mathcal{L}_0 = 10$ µm, which, based on the theoretical relation, suggests a lower bound of 10 µm for L_d^{eva}, which mostly agrees with the above estimate. It should be noted however that this relation is only valid if step motion is a direct result of attachment and detachment of adatoms to and from the step. Indeed, if the contribution of surface vacancies to the step motion is substantial, which might well be the case on Si above 1250°C, the step velocity will be proportional to

the width of the terrace regardless of how the diffusion length compares to the interstep distance (Fujita et al., 1999).

In the case of extra-wide terraces ($\mathcal{L}_0 = 1$ µm), $\bar{v}$ can reach values of up to 10^{-3}, which again complies with the near-equilibrium restrictions.

For completeness, we also report measurements of actual evaporation rates, that we use in Section 5.4.3 to translate the duration of experiments into a number of layers evaporated. Homma and Finnie (1999) found ~ 0.05 ML/s at 1130°C and ~ 1 ML/s at 1270°C, so that in O Coileain et al. (2011) the 12-hour annealing at 1130°C corresponds to ~ 2000 ML and the 6-minute annealing at 1270°C corresponds to ~ 500 ML.

ATTACHMENT/DETACHMENT COEFFICIENT $\bar{\kappa}$

As it involves microscopic kinetics at the step, measuring the attachment/detachment coefficient $\bar{\kappa}$ is particularly difficult. However, given that the kinetic length L_k must be larger than one atomic spacing, we can at least determine an upper bound of $\bar{\kappa}^* \simeq 50$.

In the low temperature regime, based on the study of the size of nucleated islands, Chung and Altman (2002) estimated that any of the values $L_k = 61, 330,$ or 910 nm produced a good fit with experimental observations at 527°C. More recently, analyzing the critical terrace width for adatom nucleation, Rogilo et al. (2013) estimated $L_k \sim 4 \times 10^4$ at 700°C. Given the wide spread in the values, an accurate value for $\bar{\kappa}$ is out of reach. Nevertheless, these results do suggest that $\bar{\kappa} \ll 1$ in the low temperature regime, i. e., the surface kinetics is controlled by the attachment/detachment processes.

The work of Rogilo et al. (2013) also suggests that the growth mode switches to diffusion-limited beyond 720°C, which the experiments by Gibbons et al. (2005) at 940, 1090, and 1290°C seem to indicate as well. Their work focuses on the scaling of the quantity $\ell_{min} N^{2/3}$ which they show does not depend on the initial terrace width down to $\mathcal{L}_0 = 20$ nm.[1] A comparison with theoretically derived expressions shows that this is consistent with diffusion-limited kinetics, and thus implies $L_k < 20$ nm, i. e., $\bar{\kappa}^* \gtrsim 1$.

This value would also be consistent with our own estimate of $\bar{\kappa}^* \simeq 19$, which we detail in Section 5.4.3 and is based on the experimental work of O Coileain et al. (2011).

EHRLICH-SCHWOEBEL BARRIER S

On Si(111) $-$ 7 × 7, measurements of the Schwoebel effect have been performed by different techniques—comparison in the growth and decay rates of islands and holes (Ichimiya et al., 1996), denuded zones around steps (Voigtländer et al., 1995; Rogilo et al., 2013), island nucleation distributions (Chung and Altman, 2002)—and lead to contradictory conclusions, i. e., , a direct, negligible or inverse ES effect. As a result, we use the general range of S between 0.1 and 10 for the discussions relative to this surface.

1 We recall that ℓ_{min} is the minimal interstep distance in a bunch and N the size of the bunch.

DIPOLAR TENSOR $\bar{\mathbf{d}}$

The only available dipole moments in the literature are d_{xx} and d_{xz}, as the measurements and calculations are carried out on a straight step for which d_{yy} plays no role. Combining experimental measurements of the displacement field of a step with atomistic simulations, Stewart et al. (1994) determined $d_{xz} = 6\text{eV/nm}$ and $d_{xx} = 15\text{eV/nm}$ on a $\text{Si}(111) - 7 \times 7$ surface.

Based on a nearest-neighbour square-lattice model with elastic step-step interactions whose two parameters are fitted to match experimental observations, Williams et al. (1993) determine, on $\text{Si}(111) - 7 \times 7$, $\alpha_0 = 0.08$ eV nm for $[\bar{2}11]$ single-layer steps and $\alpha_0 = 0.72$ eV nm for $[2\bar{1}\bar{1}]$ triple-layer steps, and, on $\text{Si}(111) - 1 \times 1$, $\alpha_0 = 0.03$ eV nm. Based on the average values of Young's modulus $E = 165$ GPa $= 1030$ eV nm^{-3} and Poisson coefficient $\nu = 0.22$ for Si, this allows to compute, assuming $d_{xz} = 0$: $d_{xx} = 8$ eV/nm, 25 eV/nm, and 5 eV/nm, respectively, which conform well with the estimate of Stewart et al. (1994).

Being deterministic, our model does not account for the entropic repulsion between steps due to thermal wandering, which, like the elastic repulsion, scales as the inverse of the squared distance between steps, so that their cumulative effect can be described by an "effective" α_0. While its influence is negligible at 900°C, and step interaction is mainly energetic, Akutsu and Akutsu (1999) showed, via simulations of a two-dimensional honeycomb lattice-gas model with both nearest- and next-nearest-neighbour interactions, that entropic repulsion dominates step interaction at higher temperatures, with estimates of α_0 ranging from 0.12 to 0.46 eV nm. Translating these values into the dipolar moment yields $d_{xx} = 10 - 20$ eV/nm.

In sum, d_{xx} is always of the order of a few eV/nm, but we note that since $\bar{\alpha}_0 \propto \mathcal{L}_0^{-3}$, $\mathcal{L}_0$ is actually the crucial parameter that determines the strength of step-step interaction, which may vary over several decades and may a have small or large effect on the stability depending on the initial miscut angle.

ELECTROMIGRATION FORCE $\bar{e}$

The value of $\bar{e}$ is essentially contingent on the effective charge q_e, for which various estimates, as a fraction of the elementary charge, are, at around 950°C:

1. 0.001 (Métois and Audiffren, 1997), from the critical alternative-current frequency above which step bunching is observed,
2. 0.006 (Fu et al., 1997) or 0.01 (Williams et al., 1996), from the decay rate of metastable step bunch structures,
3. 0.1 or $0.02 - 0.06$ (depending on the choice of elastic repulsion coefficient) (Homma and Aizawa, 2000), from the scaling between bunch slope and bunch height,

and, at around 1250°C:

1. 0.07 (Rodyakina et al., 2011), from the position of antisteps as a function of the distance between bunches,

2. 0.35 (Fujita et al., 1999), from the scaling between bunch slope and bunch height, 0.13 (Thürmer et al., 1999), from the S-shape of steps between bunches.

All these estimates suggest an effective charge of the order of one hundredth of the elementary charge at 950°C and of the order of one tenth at 1250°C.

The electric field being of the order of $e = 5$ V/cm typically, this means $\bar{e}^* = 8 \times 10^{-7\pm1}$, depending on the true value of the effective charge, which varies by at most 25% over the range of temperatures from 950 to 1250°C.

STEP STIFFNESS $\bar{\gamma}$

As step stiffness quantifies the tendency of steps to maintain their straightness, its value is typically determined from the analysis of the standard deviation of the step position due to thermal wandering. For an isolated step, Alfonso et al. (1992) obtained $\tilde{\gamma} = 0.69$ eV/nm.

Using their square-lattice model, Williams et al. (1993) are able to determine $\tilde{\gamma} = 0.55$ eV/nm for $[\bar{2}11]$ steps, $\tilde{\gamma} = 1.2$ eV/nm for $[2\bar{1}\bar{1}]$ steps, and $\tilde{\gamma} = 0.4$eV/nm for the 1×1 phase at 800°C (which is a little surprising as the $7 \times 7 \leftrightarrow 1 \times 1$ takes place at around 830°C).

Likewise, with their simulations of a two-dimensional honeycomb lattice-gas model, Akutsu and Akutsu (1999) showed $\tilde{\gamma} = 0.1$ eV/nm for $[\bar{2}11]$ steps and $\tilde{\gamma} = 3$ eV/nm for $[2\bar{1}\bar{1}]$ steps at 700°C, and $\tilde{\gamma} = 0.03$ eV/nm for the 1×1 phase at 1000°C in agreement with the experimental estimate of Bartelt et al. (1993).

In conclusion, we expect $\bar{\gamma}^* \sim 0.1$ at low temperatures and $\bar{\gamma}^* \sim 2 \times 10^{-3}$ at high temperatures.

STEP-EDGE DIFFUSION Π

Like for the attachment/detachment coefficient, step-edge diffusion, because it involves microscopic processes at the step, is particularly difficult to measure. As a matter of fact, we have not found any experimental value in the literature of Si(111) surfaces. The works dedicated to the study of the influence of step-edge diffusion on the surface evolution are mostly theoretical and qualitative.

The only quantitative result is a suggestion by Bartelt et al. (1993) that, at 900°C, step-edge diffusion plays no role for large-wavelength meanders, as the theoretical prediction derived ignoring step-edge diffusion fit the experimental data points very well.

As a result, when discussing step-edge diffusion, we explore the range $\Pi \in [10^{-2}, 10^{2}]$.

E

JACOBIAN OF THE FEM SYSTEM OF GOVERNING EQUATIONS

The system (3.9) obtained after discretization with the finite element method of the governing equations may be rewritten as

$$\dot{\mathbf{q}} = \mathcal{F}(\mathbf{q}), \tag{E.1}$$

where we have concatenated the step positions and the node values of the adatom density fields in $\mathbf{q} = (x_1, ..., x_{N_s}, \breve{\rho}\big|_1, ..., \breve{\rho}\big|_{N_s})$, recalling $\breve{\rho}\big|_n = (\breve{\rho}_n^{(\mu)})_{\mu\in\{1,..,N\}}$ with N the number of nodes per terrace. We also introduce an alternative, subscript only, indexing as $\breve{\rho}_{(n-1)N+\mu} = \breve{\rho}_n^{(\mu)}$, and $\breve{\rho} = (\breve{\rho}\big|_n)_{n\in\{1,...,N_s\}}$ the global vector of all node values of the adatom density.

Our objective is to derive the jacobian $J^{\mathcal{F}}$ of $\mathcal{F}$, which we decompose into four submatrices as

$$J^{\mathcal{F}} = \begin{pmatrix} \dfrac{\partial \dot{x}_i}{\partial x_j} \in \mathbb{R}^{N_s\times N_s} & \dfrac{\partial \dot{x}_i}{\partial \breve{\rho}_J} \in \mathbb{R}^{N_s\times N_sN} \\ \dfrac{\partial \dot{\breve{\rho}}_I}{\partial x_j} \in \mathbb{R}^{N_sN\times N_s} & \dfrac{\partial \dot{\breve{\rho}}_I}{\partial \breve{\rho}_J} \in \mathbb{R}^{N_sN\times N_sN} \end{pmatrix}. \tag{E.2}$$

By convention, we use greek letters for indices in $\{1, ..., N\}$, lower case letters for indices in $\{1, ..., N_s\}$, and upper case letters for indices in $\{1, ..., N \times N_s\}$. Denoting $\delta_{i,j}$ the Kronecker delta, we start by computing two recurring jacobian submatrices:

$$\begin{cases} \dfrac{\partial \bar{\mathrm{f}}_i}{\partial x_j} = 3\bar{\alpha}_0 \displaystyle\sum_r \frac{\delta_{i,j+r} - \delta_{i,j}}{(x_{i+r} - x_i)^4}, \\ \dfrac{\partial \dot{x}_i}{\partial \breve{\rho}_J} = \bar{\kappa}\Big(C_2\delta_{J,(i-1)N+1} + C_1\delta_{J,(i-1)N}\Big). \end{cases} \tag{E.3}$$

Using the fact that

$$\frac{\partial \dot{x}_i}{\partial x_j} = \bar{\kappa}\Theta(S+1)\frac{\partial \bar{\mathrm{f}}_i}{\partial x_j}, \tag{E.4}$$

the top two submatrices can now been determined.

For the bottom two submatrices, we recall the decomposition

$$\dot{\breve{\rho}}\big|_n = (\mathbf{D}^{(2)} + \mathbf{D}^{(1)} + \mathbf{D}^{(u)})\breve{\rho}\big|_n + \overline{F}\mathbf{B}, \tag{E.5}$$

and, letting $\mathbf{I}_{N_s}$ the identity matrix of size N_s, $\mathbf{V}_{N_s} = (1, ..., 1)$ a vector of length N_s, and $\otimes$ the Kronecker product, we introduce the global matrices

$$\begin{cases} \breve{\mathbf{D}}^{(2)} = \mathbf{I}_{N_s} \otimes \mathbf{D}^{(2)}, \\ \breve{\mathbf{D}}^{(1)} = \mathbf{I}_{N_s} \otimes \mathbf{D}^{(1)}, \\ \breve{\mathbf{D}}^{(u)} = \mathbf{I}_{N_s} \otimes \mathbf{D}^{(u)}, \\ \breve{\mathbf{B}} = \mathbf{V}_{N_s} \otimes \mathbf{B}, \end{cases} \tag{E.6}$$

such that

$$\check{\dot{\rho}} = (\check{\mathbf{D}}^{(2)} + \check{\mathbf{D}}^{(1)} + \check{\mathbf{D}}^{(u)})\check{\rho} + \overline{F}\check{\mathbf{B}}. \tag{E.7}$$

We can then compute the local jacobian of each term on the nth terrace, before reconstructing the complete jacobian. Letting

$$\begin{cases} \mu = I - (n-1)N, \\ \nu = J - (n-1)N, \\ b_n^{(0)} = \tilde{J}_n^+ - \tilde{\rho}_n^+ \dot{x}_n, \\ b_n^{(1)} = \tilde{J}_{n+1}^- - \tilde{\rho}_n^- \dot{x}_{n+1}, \end{cases} \tag{E.8}$$

and summing on the repeated index $\lambda \in \{1, ..., N\}$, we find:

$$\begin{cases} \left.\dfrac{\partial(\check{\mathbf{D}}^{(2)}\check{\rho})_I}{\partial x_j}\right|_n = \dfrac{\partial}{\partial x_j}\left[-\dfrac{1}{\ell_n^2}(\mathbf{D}^{(2)}\check{\rho}\big|_n)_\mu\right] \\ \qquad\qquad = \dfrac{2}{\ell_n^3}(\delta_{j,n+1} - \delta_{j,n})(\mathbf{D}^{(2)}\check{\rho}\big|_n)_\mu, \\ \left.\dfrac{\partial(\check{\mathbf{D}}^{(1)}\check{\rho})_I}{\partial x_j}\right|_n = \dfrac{\partial}{\partial x_j}\left[\dfrac{\dot{x}_n}{\ell_n}(\mathbf{D}^{(1)}\check{\rho}\big|_n)_\mu\right] \\ \qquad\qquad = \left[\dfrac{1}{\ell_n}\dfrac{\partial \dot{x}_n}{\partial x_j} - \dfrac{\dot{x}_n}{\ell_n^2}(\delta_{j,n+1} - \delta_{j,n})\right](\mathbf{D}^{(1)}\check{\rho}\big|_n)_\mu, \\ \left.\dfrac{\partial(\check{\mathbf{D}}^{(u)}\rho)_I}{\partial x_j}\right|_n = \dfrac{\partial}{\partial x_j}\left[\dfrac{\dot{x}_{n+1} - \dot{x}_n}{\ell_n}(\mathbf{D}^{(u)}\check{\rho}\big|_n)_\mu\right] \\ \qquad\qquad = \left[\dfrac{1}{\ell_n}\dfrac{\partial(\dot{x}_{n+1} - \dot{x}_n)}{\partial x_j}\right. \\ \qquad\qquad\qquad \left. - \dfrac{\dot{x}_{n+1} - \dot{x}_n}{\ell_n^2}(\delta_{j,n+1} - \delta_{j,n})\right](\mathbf{D}^{(u)}\check{\rho}\big|_n)_\mu, \\ \left.\dfrac{\partial\check{\mathbf{B}}_I}{\partial x_j}\right|_n = \dfrac{\partial}{\partial x_j}\left[\dfrac{1}{\ell_n}(-b_n^{(0)}\delta_{I,(n-1)N+1} + b_n^{(1)}\delta_{I,nN})\right] \\ \qquad\qquad = \dfrac{1}{\ell_n}\left[-\bar{\kappa}S\dfrac{\partial\bar{\mathfrak{f}}_i}{\partial x_j} + \tilde{\rho}_n^+\dfrac{\partial\dot{x}_i}{\partial x_j}\right. \\ \qquad\qquad\qquad \left. - \dfrac{1}{\ell_n}(\delta_{j,n+1} - \delta_{j,n})b_n^{(0)}\right]\delta_{I,(n-1)N+1} \\ \qquad\qquad + \dfrac{1}{\ell_n}\left[\bar{\kappa}\dfrac{\partial\bar{\mathfrak{f}}_{i+1}}{\partial x_j} + \tilde{\rho}_n^-\dfrac{\partial\dot{x}_{i+1}}{\partial x_j}\right. \\ \qquad\qquad\qquad \left. + \dfrac{1}{\ell_n}(\delta_{j,n+1} - \delta_{j,n})b_n^{(1)}\right]\delta_{I,nN}, \end{cases} \tag{E.9}$$

and

$$
\begin{cases}
\left.\dfrac{\partial(\breve{\mathbf{D}}^{(2)}\rho)_I}{\partial\breve{\rho}_J}\right|_n = -\dfrac{1}{\ell_n^2}D^{(2)}_{\mu\lambda}\dfrac{\partial\breve{\rho}_n^{(\lambda)}}{\partial\tilde{\rho}_J} = -\dfrac{1}{\ell_n^2}D^{(2)}_{\mu\lambda}\delta_{J,(n-1)N+\lambda} \\
\qquad\qquad = -\dfrac{1}{\ell_n^2}D^{(2)}_{\mu\nu}, \\
\left.\dfrac{\partial(\breve{\mathbf{D}}^{(1)}\breve{\rho})_I}{\partial\breve{\rho}_J}\right|_n = \dfrac{1}{\ell_n}\left[\dfrac{\partial\dot{x}_n}{\partial\breve{\rho}_J}(\mathbf{D}^{(1)}\breve{\rho}\big|_n)_\mu + \dot{x}_n D^{(1)}_{\mu\nu}\right], \\
\left.\dfrac{\partial(\breve{\mathbf{D}}^{(u)}\breve{\rho})_I}{\partial\breve{\rho}_J}\right|_n = \dfrac{1}{\ell_n}\left[\dfrac{\partial(\dot{x}_{n+1}-\dot{x}_n)}{\partial\breve{\rho}_J}(\mathbf{D}^{(u)}\breve{\rho}\big|_n)_\mu + (\dot{x}_{n+1}-\dot{x}_n)D^{(u)}_{\mu\nu}\right], \\
\left.\dfrac{\partial\breve{\mathbf{B}}_I}{\partial\breve{\rho}_J}\right|_n = \dfrac{-\bar{\kappa}S}{\ell_n}\Big[(1-\Theta-\dot{x}_n)\delta_{J,(n-1)N_s+1} \\
\qquad\qquad + \Theta\delta_{J,(n-1)N} - \tilde{\rho}_n^+\dfrac{\partial\dot{x}_n}{\partial\breve{\rho}_J}\Big]\delta_{I,(n-1)N+1} \\
\qquad + \dfrac{\bar{\kappa}}{\ell_n}\Big[-(1+\Theta+\dot{x}_{n+1})\delta_{J,nN} \\
\qquad\qquad \Theta\delta_{J,nN+1} - \tilde{\rho}_n^-\dfrac{\partial\dot{x}_{n+1}}{\partial\breve{\rho}_J}\Big]\delta_{I,nN},
\end{cases}
\tag{E.10}
$$

thus completing the jacobian.

F

PARTICULAR SOLUTIONS OF THE STEP-FLOW FREE-BOUNDARY PROBLEM

Fundamental solution

In the context of linear stability analysis, we investigate the stability of the step-flow free-boundary problem to perturbations of the fundamental solution, i. e., the solution of Equation 4.14, which takes the form:

$$\tilde{\rho}^{(0)}(u) = (\tilde{\rho}^{+} - \frac{\overline{F}}{\bar{\nu}})f^{+}(u) + (\tilde{\rho}^{-} - \frac{\overline{F}}{\bar{\nu}})f^{-}(u) + \frac{\overline{F}}{\bar{\nu}}, \tag{F.1}$$

where

$$\begin{cases} \Lambda = \sqrt{\bar{\nu} + \left(\dfrac{\chi_a V_0}{2}\right)^2}, \\ f^{+}(u) = \exp(-\dfrac{1}{2}\chi_a V_0 u)\dfrac{\sinh(\Lambda(1-u))}{\sinh(\Lambda)}, \\ f^{-}(u) = \exp(\dfrac{1}{2}\chi_a V_0 (1-u))\dfrac{\sinh(\Lambda u)}{\sinh(\Lambda)}. \end{cases} \tag{F.2}$$

The boundary conditions give a linear system for the two unknowns $\tilde{\rho}^{+}$ and $\tilde{\rho}^{-}$ in the form

$$\mathbf{A}\begin{pmatrix} \tilde{\rho}^{+} \\ \tilde{\rho}^{-} \end{pmatrix} = \mathbf{b}, \tag{F.3}$$

where

$$\begin{cases} A_{11} = -\bar{\kappa}S(1-\chi_c\Theta) - \Lambda\coth(\Lambda) + \chi_a\dfrac{V_0}{2}, \\ A_{12} = -\bar{\kappa}S\chi_c\Theta + \exp(\chi_a\dfrac{V_0}{2})\dfrac{\Lambda}{\sinh\Lambda}, \\ A_{21} = \bar{\kappa}\chi_c\Theta + \exp(-\chi_a\dfrac{V_0}{2})\dfrac{\Lambda}{\sinh\Lambda}, \\ A_{22} = -\bar{\kappa}(1+\chi_c\Theta) - \Lambda\coth(\Lambda) - \chi_a\dfrac{V_0}{2}, \\ b_1 = \bar{\kappa}S + \dfrac{\overline{F}}{\bar{\nu}}\Big(\Lambda\coth(\Lambda) + \chi_a\dfrac{V_0}{2} - \exp(\chi_a\dfrac{V_0}{2})\dfrac{\Lambda}{\sinh(\Lambda)}\Big), \\ b_2 = \bar{\kappa} + \dfrac{\overline{F}}{\bar{\nu}}\Big(\Lambda\coth(\Lambda) - \chi_a\dfrac{V_0}{2} - \exp(-\chi_a\dfrac{V_0}{2})\dfrac{\Lambda}{\sinh(\Lambda)}\Big), \end{cases} \tag{F.4}$$

and therefore

$$\begin{cases} \tilde{\rho}^{+} = \dfrac{1}{\det(\mathbf{A})}(A_{22}b_1 - A_{12}b_2), \\ \tilde{\rho}^{-} = \dfrac{1}{\det(\mathbf{A})}(A_{11}b_2 - A_{21}b_2). \end{cases} \tag{F.5}$$

Under the quasistatic approximation ($\chi_a = 0$), in the limit of pure deposition ($\bar{v} \to 0$), we recover the expressions presented in Section 4.3.2.

Regarding the fundamental step velocity $\mathcal{P}$, we can verify that in the case of pure deposition ($\bar{v} = 0$) we get

$$\mathcal{P} = \overline{F}\Theta. \tag{F.6}$$

In the general case with evaporation, the expression is not as straightforward:

$$\mathcal{P} = (\overline{F} - \bar{v})\Theta \frac{\bar{\kappa}S\mathcal{C}(\bar{v}) + (S+1)\mathcal{S}(\bar{v})}{(S+1)(1+\frac{\bar{v}}{2}\mathcal{C}(\bar{v})) + (\frac{\bar{v}}{\bar{\kappa}} + \bar{\kappa}S)\mathcal{S}(\bar{v}) - \chi_c\Theta(S-1)\frac{\bar{v}}{2}\mathcal{C}(\bar{v})}. \tag{F.7}$$

with

$$\mathcal{C}(x) = 2\frac{\cosh(\sqrt{x}) - 1}{x}, \quad \mathcal{S}(x) = \frac{\sinh(\sqrt{x})}{\sqrt{x}}. \tag{F.8}$$

In the limit $\bar{v} \ll 1$, $\mathcal{C}(x) \to 1$, $\mathcal{S}(x) \to 1$, and we find

$$\mathcal{P} \simeq (\overline{F} - \bar{v})\Theta. \tag{F.9}$$

Approximate solution neglecting the transient term

The functions ψ_n, φ_n, and c_n introduced in (3.15) are given by

$$\begin{cases} \psi_n(u,t) = \dfrac{\exp(-\chi_a \dot{x}_n \ell_n u) - 1}{\exp(-\chi_a \dot{x}_n \ell_n) - 1}, \\ \varphi_n(u,t) = 1 - \psi_n(u,t), \\ c_n(u,t) = F\dfrac{\ell_n}{\chi_a \dot{x}_n}(\psi_n(u,t) - u). \end{cases} \tag{F.10}$$

From the boundary conditions, the linear system for the two unknowns $\tilde{\rho}_n^+$ and $\tilde{\rho}_n^-$ reads

$$\mathbf{A}_n \begin{pmatrix} \tilde{\rho}_n^+ \\ \tilde{\rho}_n^- \end{pmatrix} = \mathbf{b}_n, \tag{F.11}$$

where

$$\begin{cases} A_{n,11} = \dfrac{1}{\ell_n}\varphi_n'(0) - \dfrac{\bar{\kappa}S}{C_1} + \chi_a \dot{x}_n, \quad A_{n,12} = \dfrac{1}{\ell_n}\psi_n'(0), \\ A_{n,21} = \dfrac{1}{\ell_n}\varphi_n'(1), \quad A_{n,22} = \dfrac{1}{\ell_n}\psi_n'(1) + \dfrac{\bar{\kappa}S}{C_2} + \chi_a \dot{x}_{n+1}, \\ b_{n,1} = \dfrac{1}{\ell_n}c_n'(0) - \dfrac{\bar{\kappa}S}{C_1}(\bar{f}_n - 1) - \dfrac{\chi_c S}{C_1}\dot{x}_n, \\ b_{n,2} = \dfrac{1}{\ell_n}c_n'(1) + \dfrac{\bar{\kappa}S}{C_2}(\bar{f}_{n+1} - 1) - \dfrac{\chi_c}{C_2}\dot{x}_{n+1}, \end{cases} \tag{F.12}$$

and like before

$$\begin{cases} \tilde{\rho}_n^+ = \dfrac{1}{\det(\mathbf{A}_n)}(A_{n,22}b_{n,1} - A_{n,12}b_{n,2}), \\ \tilde{\rho}_n^- = \dfrac{1}{\det(\mathbf{A}_n)}(A_{n,11}b_{n,1} - A_{n,21}b_{n,2}). \end{cases} \tag{F.13}$$

G

PADÉ APPROXIMANT OF THE BUNCH PROFILE

The coefficients a_1, a_2, b_2, and b_3 in (3.35) are determined as follows. We substitute (3.35) in (3.34), Taylor-expand in ξ, and look at the four lowest orders, which yields a nonlinear system of four equations with the four coefficients as unknowns.

As this system is impossible to solve analytically, we instead solve an approximated version. We proceed by first solving the system numerically for a wide range of model parameters to determine the dominant scaling of the unknown coefficients with ε, and find

$$\begin{cases} a_1 \sim \varepsilon^{-5/3}, & a_2 \sim \varepsilon^{-8/3}, \\ b_2 \sim \varepsilon^{-2}, & b_3 \sim \varepsilon^{-3}. \end{cases} \tag{G.1}$$

Next, using these scaling relations and $M = \ell_{min}^{-1} \sim \varepsilon^{-2/3}$, we approximate each equation of the system by its two leading contributions in ε:

$$\begin{cases} -v(1+M) + \dfrac{12K_2}{M}\Sigma_2\varepsilon^2 = 0, \\ -16K_2(-3a_1\Sigma_2 + M\Sigma_1(a_2 + 4Mb_2))\varepsilon^2 = 0, \\ -120K_2M^2a_1^2\Sigma_2\varepsilon^2 + M^5\Sigma_1 v + 24K_2M^3(a_1\Sigma_1(3a_2 + 13Mb_2)\varepsilon^2 \\ \quad + M^2b_3(8a_2 + 13Mb_2))\varepsilon^2 = 0, \\ -M^3\Sigma_2 v + 8K_2(30a_1^3\Sigma_2 - 5Ma_1^2\Sigma_1(5a_2 + 23Mb_2) \\ \quad - 2M^3a_1b_3(47a_2 + 77Mb_2) + M^2(-4a_2^2(a_2 - Mb_2) \\ \qquad + 50M^2a_2b_2^2 + 3M^3(14b_2^3 - 13b_3^2)))\varepsilon^2 = 0. \end{cases} \tag{G.2}$$

where

$$\begin{cases} \Sigma_1 = a_2 + Mb_2, \\ \Sigma_2 = a_1\Sigma_1 + M^2b_3. \end{cases} \tag{G.3}$$

This approximate system can now be solved analytically and yields (3.36) at leading order in ε.

H

THE CHEBYSHEV COLLOCATION METHOD

The Chebyshev collocation method is used to solve the generalized eigenvalue problem Equation 4.15, written in the form

$$\mathcal{A}_k \check{\mathbf{p}} = \lambda \mathcal{B}_k \check{\mathbf{p}}, \tag{H.1}$$

where the expressions for $\mathcal{A}_k$ and $\mathcal{B}_k$ can be deduced from (4.15).

A detailed description of the resolution process is given in Guin (2018), whose principal steps we summarize here:

1. Consider a function $f \in \mathbb{C}^{(0,1)}$ and let its Chebyshev series approximation f_N truncated at order N,

$$f_N := \sum_{n=0}^{N} \check{f}_n \check{T}_n, \tag{H.2}$$

where $\check{f}_n$ are the Chebyshev coefficients and $\check{T}_n$ denote the Chebyshev polynomials shown in Figure H.1 and defined on $(0,1)$ by

$$\check{T}_0(u) = 1, \quad \check{T}_1(u) = 2u - 1, \tag{H.3}$$

and the recurrence relationship

$$\check{T}_n - (4u-2)\check{T}_{n-1} + \check{T}_{n-2} = 0. \tag{H.4}$$

2. The coefficients $\check{f}_n$ are obtained by the *collocation method* from the $N+1$ equations deriving from the interpolation of f on the Gauss-Lobatto points $(u_0, ..., u_N)$,

$$f_N(u_n) = \sum_{j=0}^{N} \check{f}_j \check{T}_j(u_n) = f(u_n), \tag{H.5}$$

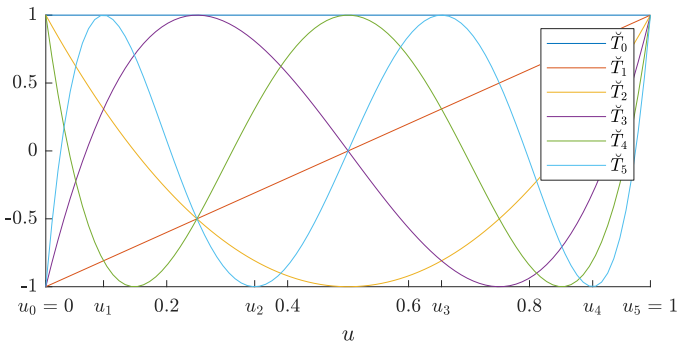

Figure H.1: Representation of the first six Chebyshev polynomials $\check{T}_n$ along with the six Gauss-Lobatto points for $N = 5$.

where the Gauss-Lobatto mesh is composed of the $N+1$ points defined by

$$u_n = \frac{1}{2}\left(\cos(\frac{(N-n)\pi}{N}) + 1\right), \text{ for } n = 0...N, \tag{H.6}$$

illustrated on Figure H.1 for $N = 5$.

3. The first and second derivatives of f can be approximated by

$$f'_N(u_n) = \check{D}_{n,j} f_N(u_j) \text{ and } f''_N(u_n) = (\check{D}^2)_{n,j} f_N(u_j), \tag{H.7}$$

with $\check{\mathbf{D}}$ an appropriate differentiation matrix.

4. The operators $\mathcal{A}_k$ and $\mathcal{B}_k$ are decomposed as a sum of operators acting separately on $\delta\check{x}$, $\delta\check{\rho}$, and its derivatives, and then approximated using the $(N+2)\times(N+2)$ matrices $\check{\mathbf{A}}_k$ and $\check{\mathbf{B}}_k$:

$$\begin{cases} \check{\mathbf{A}}_k \check{\mathbf{p}} = \check{\mathbf{A}}^1_k(\check{\mathbf{D}}^2)\delta\check{\rho} + \check{\mathbf{A}}^2_k\check{\mathbf{D}}\delta\check{\rho} + \check{\mathbf{A}}^3_k\delta\check{\rho} + \check{\mathbf{A}}^4_k\delta\check{x}, \\ \check{\mathbf{B}}_k \check{\mathbf{p}} = \check{\mathbf{B}}^1_k\delta\check{\rho} + \check{\mathbf{B}}^2_k\delta\check{x}. \end{cases} \tag{H.8}$$

where $\delta\check{\rho} = (\delta\check{\rho}(u_0), ..., \delta\check{\rho}(u_N))$ and $\check{\mathbf{p}} = (\delta\check{x}, \delta\check{\rho})$.

5. We can now finally solve the discretized $(N+2)\times(N+2)$ version of the generalized eigenvalue problem

$$\check{\mathbf{A}}_k \check{\mathbf{p}} = \lambda \check{\mathbf{B}}_k \check{\mathbf{p}}, \tag{H.9}$$

and obtain the leading eigenvalue which corresponds to the most critical growth rate.

BIBLIOGRAPHY

Akutsu, N. and Y. Akutsu (1999). "Statistical Mechanical Calculation of Anisotropic Step Stiffness of a Two-Dimensional Hexagonal Lattice-Gas Model with next-Nearest-Neighbour Interactions: Application to Si(111) Surface." In: 11.35, pp. 6635–6652. DOI: 10.1088/0953-8984/11/35/302 (cit. on pp. 128, 129).

Alfonso, C., J. M. Bermond, J. C. Heyraud, and J. J. Métois (1992). "The Meandering of Steps and the Terrace Width Distribution on Clean Si(111): An in-Situ Experiment Using Reflection Electron Microscopy." In: *Surface Science* 262.3, pp. 371–381. DOI: 10.1016/0039-6028(92)90133-Q (cit. on p. 129).

Alfonso, C., J. C. Heyraud, and J. J. Métois (1993). "About the Sublimation of Si Surfaces Vicinal of {111}." In: *Surface Science Letters* 291.1, pp. L745–L749. DOI: 10.1016/0167-2584(93)90280-V (cit. on pp. 37, 61, 96).

Bales, G. S. and A. Zangwill (1990). "Morphological Instability of a Terrace Edge during Step-Flow Growth." In: *Physical Review B* 41.9, pp. 5500–5508. DOI: 10.1103/PhysRevB.41.5500 (cit. on pp. 61, 77).

Balykov, L. and A. Voigt (2006). "A Kinetic Model for Step Flow Growth in Molecular Beam Epitaxy." In: *Surface Science* 600.17, pp. 3436–3445. DOI: 10.1016/j.susc.2006.06.031 (cit. on p. 62).

Bänsch, E., F. Haußer, O. Lakkis, B. Li, and A. Voigt (2004). "Finite Element Method for Epitaxial Growth with Attachment–Detachment Kinetics." In: *Journal of Computational Physics* 194.2, pp. 409–434. DOI: 10.1016/j.jcp.2003.09.029 (cit. on pp. 6, 38).

Bartelt, N. C., J. L. Goldberg, T. L. Einstein, E. D. Williams, J. C. Heyraud, and J. J. Métois (1993). "Brownian Motion of Steps on Si(111)." In: *Physical Review B* 48.20, pp. 15453–15456. DOI: 10.1103/PhysRevB.48.15453 (cit. on p. 129).

Bauer, E. (1958). "Phänomenologische Theorie der Kristallabscheidung an Oberflächen. I." In: *Zeitschrift für Kristallographie - Crystalline Materials* 110.1-6, pp. 372–394. DOI: 10.1524/zkri.1958.110.16.372 (cit. on p. 1).

Bedair, S. M. (1974). "Activation Energy for Migration on Silicon (111) Face." In: *Surface Science* 42.2, pp. 595–599. DOI: 10.1016/0039-6028(74)90042-9 (cit. on p. 126).

Bena, I., C. Misbah, and A. Valance (1993). "Nonlinear Evolution of a Terrace Edge during Step-Flow Growth." In: *Physical Review B* 47.12, pp. 7408–7419. DOI: 10.1103/PhysRevB.47.7408 (cit. on p. 49).

Benlattar, M., E. Elkoraychy, K. Sbiaai, M. Mazroui, and Y. Boughaleb (2017). "Ehrlich–Schwöbel Barriers and Adsorption of Au, Cu and Ag Stepped (100) Surfaces." In: *Modern Physics Letters B*. DOI: 10.1142/S0217984917500373 (cit. on p. 89).

Bennett, P. A. and M. W. Webb (1981). "The Si(111)7 × 7 to 1 × 1 Transition." In: *Surface Science* 104.1, pp. 74–104. DOI: 10.1016/0039-6028(81)90125-4 (cit. on p. 107).

Benoit–Maréchal, L., M. E. Jabbour, and N. Triantafyllidis (2021). "Scaling Laws for Step Bunching on Vicinal Surfaces: Role of the Dynamical and Chemical Effects." In: *Physical Review E* 104.3, p. 034802. DOI: 10.1103/PhysRevE.104.034802 (cit. on p. xi).

Blel, S., A. B. Hamouda, B. Mahjoub, and T. L. Einstein (2017). "Competing Growth Processes Induced by Next-Nearest-Neighbor Interactions: Effects on Meandering Wavelength and Stiffness." In: *Physical Review B* 95.8, p. 085404. DOI: 10.1103/PhysRevB.95.085404 (cit. on p. 115).

Burton, W. K., N. Cabrera, and F. C. Frank (1951). "The Growth of Crystals and the Equilibrium Structure of Their Surfaces." In: *Philosophical Transactions of the Royal Society of London. Series A, Mathematical and Physical Sciences* 243.866, pp. 299–358. DOI: 10.1098/rsta.1951.0006 (cit. on p. 5).

CVODE Solver Description (n.d.) (cit. on p. 40).

Caflisch, R. E., W. E, M. F. Gyure, B. Merriman, and C. Ratsch (1999). "Kinetic Model for a Step Edge in Epitaxial Growth." In: *Physical Review E* 59.6, pp. 6879–6887. DOI: 10.1103/PhysRevE.59.6879 (cit. on p. 62).

Camarero, J. et al. (1999). "Epitaxial Growth of Metals with High Ehrlich–Schwoebel Barriers and the Effect of Surfactants." In: *Applied Physics A* 69.5, pp. 553–557. DOI: 10.1007/s003390051469 (cit. on p. 89).

Cermelli, P. and M. E. Jabbour (2007). "Possible Mechanism for the Onset of Step-Bunching Instabilities during the Epitaxy of Single-Species Crystalline Films." In: *Physical Review B* 75.16, p. 165409. DOI: 10.1103/PhysRevB.75.165409 (cit. on pp. 6, 35).

Cermelli, P. and M. Jabbour (2005). "Multispecies Epitaxial Growth on Vicinal Surfaces with Chemical Reactions and Diffusion." In: *Proceedings of the Royal Society A: Mathematical, Physical and Engineering Sciences* 461.2063, pp. 3483–3504. DOI: 10.1098/rspa.2005.1495 (cit. on pp. 5, 9).

Chandrasekhar, S. (1961). *Hydrodynamic and Hydromagnetic Stability*. London: Oxford University Press (cit. on p. 65).

Chang, C. M. and C. M. Wei (2003). "Diffusion of an Adsorbed Si Atom on the Si(111) $-$ 7 $\times$ 7) Surface." In: *Physical Review B* 67.3, p. 033309. DOI: 10.1103/PhysRevB.67.033309 (cit. on p. 126).

Chang, J., O. Pierre-Louis, and C. Misbah (2006). "Birth and Morphological Evolution of Step Bunches under Electromigration." In: *Physical Review Letters* 96.19, p. 195901. DOI: 10.1103/PhysRevLett.96.195901 (cit. on p. 35).

Chen, Y. (2019). "Revisiting the Meandering Instability During Step-Flow Epitaxy." In: *Applied Sciences* 9.22, p. 4840. DOI: 10.3390/app9224840 (cit. on pp. 6, 63).

Chernov, A. A. (1961). "THE SPIRAL GROWTH OF CRYSTALS." In: *Soviet Physics Uspekhi* 4.1, p. 116. DOI: 10.1070/PU1961v004n01ABEH003328 (cit. on p. 5).

Chung, W. F. and M. S. Altman (2002). "Kinetic Length, Step Permeability, and Kinetic Coefficient Asymmetry on the Si(111)(7 $\times$ 7) Surface." In: *Physical Review B* 66.7, p. 075338. DOI: 10.1103/PhysRevB.66.075338 (cit. on pp. 47, 48, 127).

Cohen, S. D., R. D. Schroll, T. L. Einstein, J.-J. Métois, H. Gebremariam, H. L. Richards, and E. D. Williams (2002). "Si(111) Step Fluctuations at High Temperature: Anomalous Step-Step Repulsion." In: *Physical Review B* 66.11, p. 115310. DOI: 10.1103/PhysRevB.66.115310 (cit. on p. 37).

Coleman, B. D. and W. Noll (1963). "The Thermodynamics of Elastic Materials with Heat Conduction and Viscosity." In: *Archive for Rational Mechanics and Analysis* 13.1, pp. 167–178. DOI: 10.1007/BF01262690 (cit. on p. 21).

Danker, G., O. Pierre-Louis, K. Kassner, and C. Misbah (2003). "Interrupted Coarsening of Anisotropic Step Meander." In: *Physical Review E* 68.2, p. 020601. DOI: 10.1103/PhysRevE.68.020601 (cit. on pp. 62, 63).

Davis, S. H. (2001). *Theory of Solidification*. Cambridge Monographs on Mechanics. Cambridge: Cambridge University Press. DOI: 10.1017/CBO9780511546747 (cit. on p. 23).

Degawa, M., H. Minoda, Y. Tanishiro, and K. Yagi (1999a). "DC-heating-induced Antiband Formation and Subsequent Step Wandering on Si(111) Studied by in-Situ REM." In: *Surface Review and Letters* 06.06, pp. 977–984. DOI: 10.1142/S0218625X99001050 (cit. on p. 97).

Degawa, M., H. Minoda, Y. Tanishiro, and K. Yagi (1999b). "Temperature Dependence of Period of Step Wandering Formed on Si(111) Vicinal Surfaces by DC Heating." In: 11.48, pp. L551–L556. DOI: 10.1088/0953-8984/11/48/105 (cit. on p. 97).

Degawa, M., H. Minoda, Y. Tanishiro, and K. Yagi (2000). "Direct-Current-Induced Drift Direction of Silicon Adatoms on Si(111) – (1 × 1) Surfaces." In: *Surface Science* 461.1, pp. L528–L536. DOI: 10.1016/S0039-6028(00)00593-8 (cit. on p. 95).

Degawa, M., H. Minoda, Y. Tanishiro, and K. Yagi (2001a). "In-Phase Step Wandering on Si(111) Vicinal Surfaces: Effect of Direct Current Heating Tilted from the Step-down Direction." In: *Physical Review B* 63.4, p. 045309. DOI: 10.1103/PhysRevB.63.045309 (cit. on p. 97).

Degawa, M., H. Nishimura, Y. Tanishiro, H. Minoda, and K. Yagi (1999c). "Direct Current Heating Induced Giant Step Bunching and Wandering on Si(111) and (001) Vicinal Surfaces." In: *Japanese Journal of Applied Physics* 38.3B, p. L308. DOI: 10.1143/JJAP.38.L308 (cit. on p. 97).

Degawa, M., K. Thürmer, I. Morishima, H. Minoda, K. Yagi, and E. D. Williams (2001b). "Initial Stage of In-Phase Step Wandering on Si(111) Vicinal Surfaces." In: *Surface Science* 487.1, pp. 171–179. DOI: 10.1016/S0039-6028(01)01089-5 (cit. on p. 97).

Dufay, M., J.-M. Debierre, and T. Frisch (2007). "Electromigration-Induced Step Meandering on Vicinal Surfaces: Nonlinear Evolution Equation." In: *Physical Review B* 75.4, p. 045413. DOI: 10.1103/PhysRevB.75.045413 (cit. on p. 6).

Eshelby, J. D. and N. F. Mott (1951). "The Force on an Elastic Singularity." In: *Philosophical Transactions of the Royal Society of London. Series A, Mathematical and Physical Sciences* 244.877, pp. 87–112. DOI: 10.1098/rsta.1951.0016 (cit. on p. 9).

Fried, E. and M. E. Gurtin (2003). "The Role of the Configurational Force Balance in the Nonequilibrium Epitaxy of Films." In: *Journal of the Mechanics*

and Physics of Solids 51.3, pp. 487–517. DOI: 10.1016/S0022-5096(02)00077-7 (cit. on pp. 11, 17).

Fried, E. and M. E. Gurtin (2004). "A Unified Treatment of Evolving Interfaces Accounting for Small Deformations and Atomic Transport with Emphasis on Grain-Boundaries and Epitaxy." In: *Advances in Applied Mechanics*. Vol. 40. Elsevier, pp. 1–177. DOI: 10.1016/S0065-2156(04)40001-5 (cit. on pp. 9, 11, 17).

Frisch, T. and A. Verga (2006). "Effect of Step Stiffness and Diffusion Anisotropy on the Meandering of a Growing Vicinal Surface." In: *Physical Review Letters* 96.16, p. 166104. DOI: 10.1103/PhysRevLett.96.166104 (cit. on p. 89).

Fu, E. S., D. J. Liu, M. D. Johnson, J. D. Weeks, and E. D. Williams (1997). "The Effective Charge in Surface Electromigration." In: *Surface Science* 385.2, pp. 259–269. DOI: 10.1016/S0039-6028(97)00188-X (cit. on pp. 3, 128).

Fujita, K., M. Ichikawa, and S. S. Stoyanov (1999). "Size-Scaling Exponents of Current-Induced Step Bunching on Silicon Surfaces." In: *Physical Review B* 60.23, pp. 16006–16012. DOI: 10.1103/PhysRevB.60.16006 (cit. on pp. 96, 127, 129).

Fukaya, Y. and Y. Shigeta (2000). "New Phase and Surface Melting of Si(111) at High Temperature above the $7 \times 7 - 1 \times 1$ Phase Transition." In: *Physical Review Letters* 85.24, pp. 5150–5153. DOI: 10.1103/PhysRevLett.85.5150 (cit. on p. 96).

Ghez, R., H. G. Cohen, and J. B. Keller (1993). "The Stability of Growing or Evaporating Crystals." In: *Journal of Applied Physics* 73.8, pp. 3685–3693. DOI: 10.1063/1.352928 (cit. on p. 6).

Gibbons, B. J., J. Noffsinger, and J. P. Pelz (2005). "Influence of Si Deposition on the Electromigration Induced Step Bunching Instability on Si(111)." In: *Surface Science* 575.1, pp. L51–L56. DOI: 10.1016/j.susc.2004.11.020 (cit. on pp. 97, 106, 110, 127).

Gibbons, B. J., S. Schaepe, and J. P. Pelz (2006). "Evidence for Diffusion-Limited Kinetics during Electromigration-Induced Step Bunching on Si(111)." In: *Surface Science* 600.12, pp. 2417–2424. DOI: 10.1016/j.susc.2006.03.046 (cit. on p. 106).

Gillet, F. (2000). "Dynamique Non Linéaire de Surfaces Vicinales Hors de l'équilibre." PhD thesis. Grenoble, France: Université Joseph Fourier (cit. on pp. 35, 36, 70, 102).

Gillet, F., Z. Csahok, and C. Misbah (2001). "Continuum Nonlinear Surface Evolution Equation for Conserved Step-Bunching Dynamics." In: *Physical Review B* 63.24, p. 241401. DOI: 10.1103/PhysRevB.63.241401 (cit. on p. 49).

Gillet, F., O. Pierre-Louis, and C. Misbah (2000). "Non-Linear Evolution of Step Meander during Growth of a Vicinal Surface with No Desorption." In: *The European Physical Journal B - Condensed Matter and Complex Systems* 18.3, pp. 519–534. DOI: 10.1007/s100510070042 (cit. on pp. 6, 62).

Guin, L., M. E. Jabbour, L. Shaabani-Ardali, L. Benoit-Maréchal, and N. Triantafyllidis (2020). "Stability of Vicinal Surfaces: Beyond the Quasistatic Approximation." In: *Physical Review Letters* 124.3, p. 036101. DOI: 10.1103/PhysRevLett.124.036101 (cit. on pp. xi, 6, 35, 44, 100).

Guin, L., M. E. Jabbour, L. Shaabani-Ardali, and N. Triantafyllidis (2021a). "Revisiting Step Instabilities on Crystal Surfaces. Part II: General Theory." In: *Journal of the Mechanics and Physics of Solids* 156, p. 104582. DOI: 10.1016/j.jmps.2021.104582 (cit. on pp. 6, 35, 44, 82, 93).

Guin, L., M. E. Jabbour, and N. Triantafyllidis (2021b). "Revisiting Step Instabilities on Crystal Surfaces. Part I: The Quasistatic Approximation." In: *Journal of the Mechanics and Physics of Solids* 156, p. 104574. DOI: 10.1016/j.jmps.2021.104574 (cit. on pp. 6, 35, 74).

Guin, L. (2018). "Electromechanical Couplings and Growth Instabilities in Semiconductors." PhD thesis. Université Paris-Saclay (cit. on pp. 3, 6, 9, 47, 53, 65, 70, 71, 96, 97, 105, 113, 139).

Gurtin, M. E. (1995). "The Nature of Configurational Forces." In: *Archive for Rational Mechanics and Analysis* 131.1, pp. 67–100. DOI: 10.1007/BF00386071 (cit. on pp. 16, 17, 34).

Gurtin, M. E. (2000). *Configurational Forces As Basic Concepts of Continuum Physics*. Springer. New York (cit. on p. 17).

Haußer, F., M. E. Jabbour, and A. Voigt (2007). "A Step-Flow Model for the Heteroepitaxial Growth of Strained, Substitutional, Binary Alloy Films with Phase Segregation: I. Theory." In: *Multiscale Modeling & Simulation* 6.1, pp. 158–189. DOI: 10.1137/06065355X (cit. on pp. 9, 10, 115).

Haußer, F., S. Rasche, and A. Voigt (2010). "The Influence of Electric Fields on Nanostructures—Simulation and Control." In: *Mathematics and Computers in Simulation*. Multiscale Modeling of Moving Interfaces in Materials 80.7, pp. 1449–1457. DOI: 10.1016/j.matcom.2009.05.009 (cit. on p. 115).

Hibino, H., Y. Homma, M. Uwaha, and T. Ogino (2003). "Step Wandering Induced by Homoepitaxy on Si(111) during âĂIJ1 × 1âĂİ–7 × 7 Phase Transition." In: *Surface Science* 527.1, pp. L222–L228. DOI: 10.1016/S0039-6028(03)00012-8 (cit. on p. 62).

Hibino, H., K. Sumitomo, T. Fukuda, Y. Homma, and T. Ogino (1998). "Disordering of Si(111) at High Temperatures." In: *Physical Review B* 58.19, pp. 12587–12589. DOI: 10.1103/PhysRevB.58.12587 (cit. on p. 126).

Homma, Y. (1998). "Sublimation and Phase Transitions on Si(111) Observed by Ultra High Vacuum Scanning Electron Microscopy." In: *Surface Review and Letters* 05.03n04, pp. 685–691. DOI: 10.1142/S0218625X98001043 (cit. on p. 96).

Homma, Y. and N. Aizawa (2000). "Electric-Current-Induced Step Bunching on Si(111)." In: *Physical Review B* 62.12, pp. 8323–8329. DOI: 10.1103/PhysRevB.62.8323 (cit. on pp. 3, 44, 95–97, 128).

Homma, Y. and P. Finnie (1999). "Steps on Subliming Si(111) Surfaces." In: *Journal of Physics: Condensed Matter* 11.49, pp. 9879–9888. DOI: 10.1088/0953-8984/11/49/306 (cit. on p. 127).

Homma, Y., H. Hibino, T. Ogino, and N. Aizawa (1997). "Sublimation of the Si(111) Surface in Ultrahigh Vacuum." In: *Physical Review B* 55.16, R10237–R10240. DOI: 10.1103/PhysRevB.55.R10237 (cit. on p. 96).

Homma, Y., R. J. Mcclelland, and H. Hibino (1990). "DC-Resistive-Heating-Induced Step Bunching on Vicinal Si(111)." In: *Japanese Journal of Applied Physics* 29.12A, p. L2254. DOI: 10.1143/JJAP.29.L2254 (cit. on p. 106).

Houchmandzadeh, B. and C. Misbah (1995). "Elastic Interaction Between Modulated Steps on a Vicinal Surface." In: *Journal de Physique I* 5.6, pp. 685–698. DOI: 10.1051/jp1:1995160 (cit. on pp. 9, 63, 66, 67).

Houchmandzadeh, B., C. Misbah, and A. Pimpinelli (1994). "A Theoretical Study of Step Bunching Dynamics in the Presence of an Alternating Heating Current." In: *Journal de Physique I* 4.12, pp. 1843–1853. DOI: 10.1051/jp1:1994225 (cit. on p. 108).

Hu, Z., J. S. Lowengrub, S. M. Wise, and A. Voigt (2012). "Phase-Field Modeling of Epitaxial Growth: Applications to Step Trains and Island Dynamics." In: *Physica D: Nonlinear Phenomena* 241.2, pp. 77–94. DOI: 10.1016/j.physd.2011.09.004 (cit. on pp. 38, 115).

Ichimiya, A., K. Hayashi, E. D. Williams, T. L. Einstein, M. Uwaha, and K. Watanabe (2000). "Decay of Silicon Mounds: Scaling Laws and Description with Continuum Step Parameters." In: *Physical Review Letters* 84.16, pp. 3662–3665. DOI: 10.1103/PhysRevLett.84.3662 (cit. on p. 47).

Ichimiya, A., Y. Tanaka, and K. Ishiyama (1996). "Quantitative Measurements of Thermal Relaxation of Isolated Silicon Hillocks and Craters on the Si(111) $-$ (7×7) Surface by Scanning Tunneling Microscopy." In: *Physical Review Letters* 76.25, pp. 4721–4724. DOI: 10.1103/PhysRevLett.76.4721 (cit. on pp. 48, 127).

Ihle, T., C. Misbah, and O. Pierre-Louis (1998). "Equilibrium Step Dynamics on Vicinal Surfaces Revisited." In: *Physical Review B* 58.4, pp. 2289–2309. DOI: 10.1103/PhysRevB.58.2289 (cit. on pp. 62, 75).

Ikonomov, J., K. Starbova, and M. Giesen (2007). "Island Coalescence and Diffusion along Kinked Steps on Cu(001): Evidence for a Large Kink Ehrlich–Schwoebel Barrier." In: *Surface Science* 601.5, pp. 1403–1408. DOI: 10.1016/j.susc.2007.01.004 (cit. on p. 63).

Ino, S. (1989). *Reflection High-Energy Electron Diffraction and Reflection Electron Imaing of Surfaces*. Ed. by P. Larsen and P. Dobson. Springer US (cit. on p. 61).

Ishizaki, J.-y., K. O. K. Ohkuri, and T. F. T. Fukui (1996). "Simulation and Observation of the Step Bunching Process Grown on GaAs (001) Vicinal Surface by Metalorganic Vapor Phase Epitaxy." In: *Japanese Journal of Applied Physics* 35.2S, p. 1280. DOI: 10.1143/JJAP.35.1280 (cit. on p. 48).

Jabbour, M. E. (2005). "Epitaxy of Binary Compounds and Alloys." In: *Journal of Elasticity* 80.1, pp. 153–182. DOI: 10.1007/s10659-005-9030-4 (cit. on pp. 5, 9).

Jeong, H.-C. and E. D. Williams (1999). "Steps on Surfaces: Experiment and Theory." In: *Surface Science Reports* 34.6, pp. 171–294. DOI: 10.1016/S0167-5729(98)00010-7 (cit. on p. 75).

Johnson, M. D., K. T. Leung, A. Birch, B. G. Orr, and J. Tersoff (1996). "Adatom Concentration on GaAs(001) during MBE Annealing." In: *Surface Science* 350.1, pp. 254–258. DOI: 10.1016/0039-6028(95)01110-2 (cit. on p. 47).

Johnson, M. D., C. Orme, A. W. Hunt, D. Graff, J. Sudijono, L. M. Sander, and B. G. Orr (1994). "Stable and Unstable Growth in Molecular Beam Epitaxy." In: *Physical Review Letters* 72.1, pp. 116–119. DOI: 10.1103/PhysRevLett.72.116 (cit. on p. 49).

Jung, T. M., R. J. Phaneuf, and E. D. Williams (1994). "Sublimation and Phase Transitions on Singular and Vicinal Si(111) Surfaces." In: *Surface Science* 301.1, pp. 129–135. DOI: 10.1016/0039-6028(94)91294-7 (cit. on p. 37).

Kallunki, J. and J. Krug (2003). "Effect of Kink-Rounding Barriers on Step Edge Fluctuations." In: *Surface Science* 523.3, pp. L53–L58. DOI: 10.1016/S0039-6028(02)02435-4 (cit. on p. 63).

Kallunki, J., J. Krug, and M. Kotrla (2002). "Competing Mechanisms for Step Meandering in Unstable Growth." In: *Physical Review B* 65.20, p. 205411. DOI: 10.1103/PhysRevB.65.205411 (cit. on p. 63).

Kandel, D. and E. Kaxiras (1996). "Microscopic Theory of Electromigration on Semiconductor Surfaces." In: *Physical Review Letters* 76.7, pp. 1114–1117. DOI: 10.1103/PhysRevLett.76.1114 (cit. on p. 95).

Keller, J. B., H. G. Cohen, and G. J. Merchant (1993). "The Stability of Rapidly Growing or Evaporating Crystals." In: *Journal of Applied Physics* 73.8, pp. 3694–3697. DOI: 10.1063/1.352929 (cit. on p. 6).

Koguchi, H. (2008). "Surface Green Function With Surface Stresses and Surface Elasticity Using Stroh's Formalism." In: *Journal of Applied Mechanics* 75.6. DOI: 10.1115/1.2967893 (cit. on p. 25).

Kosolobov, S. and A. Latyshev (2011). "Step Bunching on Silicon Surface Under Electromigration." In: *Nanophenomena at Surfaces: Fundamentals of Exotic Condensed Matter Properties*. Ed. by M. Michailov. Springer Series in Surface Sciences. Berlin, Heidelberg: Springer, pp. 239–258. DOI: 10.1007/978-3-642-16510-8_11 (cit. on p. 3).

Krug, J., V. Tonchev, S. Stoyanov, and A. Pimpinelli (2005). "Scaling Properties of Step Bunches Induced by Sublimation and Related Mechanisms." In: *Physical Review B* 71.4, p. 045412. DOI: 10.1103/PhysRevB.71.045412 (cit. on pp. 35, 46, 49, 55, 56).

Krug, J. (1997). "Continuum Equations for Step Flow Growth." In: *Dynamics of Fluctuating Interfaces and Related Phenomena*. Ed. by D. Kim and B. Kahng. World Scientific (cit. on p. 49).

Krug, J. (2005). "Introduction to Step Dynamics and Step Instabilities." In: *Multiscale Modeiling in Epitaxial Growth*. Ed. by A. Voigt. Basel: Birkhäuser Basel, pp. 69–95 (cit. on pp. 30, 52, 125).

Krzyżewski, F., M. Załuska-Kotur, A. Krasteva, H. Popova, and V. Tonchev (2017). "Step Bunching and Macrostep Formation in 1D Atomistic Scale Model of Unstable Vicinal Crystal Growth." In: *Journal of Crystal Growth*. The 8th International Workshop on Modeling in Crystal Growth 474, pp. 135–139. DOI: 10.1016/j.jcrysgro.2016.11.121 (cit. on p. 46).

Kuhn, P., J. Krug, F. Hausser, and A. Voigt (2005). "Complex Shape Evolution of Electromigration-Driven Single-Layer Islands." In: *Physical Review Letters* 94.16, p. 166105. DOI: 10.1103/PhysRevLett.94.166105 (cit. on p. 115).

Lai, Z.-W. and S. Das Sarma (1991). "Kinetic Growth with Surface Relaxation: Continuum versus Atomistic Models." In: *Physical Review Letters* 66.18, pp. 2348–2351. DOI: 10.1103/PhysRevLett.66.2348 (cit. on p. 49).

Latyshev, A. V., A. L. Aseev, A. B. Krasilnikov, and S. I. Stenin (1989). "Transformations on Clean Si(111) Stepped Surface during Sublimation." In: *Surface Science* 213.1, pp. 157–169. DOI: 10.1016/0039-6028(89)90256-2 (cit. on pp. 95–97, 106, 108).

Latyshev, A. V., A. L. Aseev, A. B. Krasilnikov, and S. I. Stenin (1990). "Reflection Electron Microscopy Study of Structural Transformations on a Clean Silicon Surface in Sublimation, Phase Transition and Homoepitaxy." In: *Surface Science* 227.1, pp. 24–34. DOI: 10.1016/0039-6028(90)90387-N (cit. on pp. 106, 126).

Latyshev, A. V., L. I. Fedina, S. S. Kosolobov, S. V. Sitnikov, D. I. Rogilo, E. E. Rodyakina, D. A. Nasimov, D. V. Sheglov, and A. L. Aseev (2017). "8 - Atomic Processes on the Silicon Surface." In: *Advances in Semiconductor Nanostructures*. Ed. by A. V. Latyshev, A. V. Dvurechenskii, and A. L. Aseev. Elsevier, pp. 189–221. DOI: 10.1016/B978-0-12-810512-2.00008-1 (cit. on p. 1).

Latyshev, A. V., A. B. Krasilnikov, and A. L. Aseev (1996). "Self-Diffusion on Si(111) Surfaces." In: *Physical Review B* 54.4, pp. 2586–2589. DOI: 10.1103/PhysRevB.54.2586 (cit. on p. 126).

Lau, K. H. and W. Kohn (1977). "Elastic Interaction of Two Atoms Adsorbed on a Solid Surface." In: *Surface Science* 65.2, pp. 607–618. DOI: 10.1016/0039-6028(77)90469-1 (cit. on p. 63).

Leamy, H., G. Gilmer, and K. Jackson (1975). "Statistical Thermodynamics of Clean Surfaces." In: *Surface of Materials*. Ed. by J. Blakely. Vol. 1, p. 121 (cit. on p. 61).

Leroy, F., D. Karashanova, M. Dufay, J. M. Debierre, T. Frisch, J. J. Métois, and P. Müller (2009). "Step Bunching to Step-Meandering Transition Induced by Electromigration on Si(111) Vicinal Surface." In: *Surface Science* 603.3, pp. 507–512. DOI: 10.1016/j.susc.2008.12.016 (cit. on pp. 95, 97, 106).

Lifshitz, E. M., A. M. Kosevich, and L. P. Pitaevskii (1986). "CHAPTER I - FUNDAMENTAL EQUATIONS." In: *Theory of Elasticity (Third Edition)*. Ed. by E. M. Lifshitz, A. M. Kosevich, and L. P. Pitaevskii. Oxford: Butterworth-Heinemann, pp. 1–37. DOI: 10.1016/B978-0-08-057069-3.50008-5 (cit. on p. 121).

Lin, J.-L., D. Y. Petrovykh, J. Viernow, F. K. Men, D. J. Seo, and F. J. Himpsel (1998). "Formation of Regular Step Arrays on Si(111)7 × 7." In: *Journal of Applied Physics* 84.1, pp. 255–260. DOI: 10.1063/1.368077 (cit. on p. 96).

Liu, D.-J., E. S. Fu, M. D. Johnson, J. D. Weeks, and E. D. Williams (1996). "Relaxation of the Step Profile for Different Microscopic Mechanisms." In: *Journal of Vacuum Science & Technology B: Microelectronics and Nanometer Structures Processing, Measurement, and Phenomena* 14.4, pp. 2799–2808. DOI: 10.1116/1.588836 (cit. on p. 3).

Liu, D.-J., J. D. Weeks, and D. Kandel (1998). "Current-Induced Step Bending Instability on Vicinal Surfaces." In: *Physical Review Letters* 81.13, pp. 2743–2746. DOI: 10.1103/PhysRevLett.81.2743 (cit. on p. 3).

Liu, F. and H. Metiu (1994). "Stability and Kinetics of Step Motion on Crystal Surfaces." In: *Physical Review E* 49.4, pp. 2601–2616. DOI: 10.1103/PhysRevE.49.2601 (cit. on pp. 38, 61, 70).

Luo, T., Y. Xiang, and N. K. Yip (2016). "Energy Scaling and Asymptotic Properties of Step Bunching in Epitaxial Growth with Elasticity Effects." In: *Multiscale Modeling & Simulation*. DOI: 10.1137/15M1041821 (cit. on p. 9).

Marchenko, V. and A. Parshin (1980). "Elastic Properties of Crystal Surfaces." In: *Journal of Experimental and Theoretical Physics* 52, p. 129 (cit. on pp. 9, 37, 66).

Margetis, D., M. J. Aziz, and H. A. Stone (2005). "Continuum Approach to Self-Similarity and Scaling in Morphological Relaxation of a Crystal with a Facet." In: *Physical Review B* 71.16, p. 165432. DOI: 10.1103/PhysRevB.71.165432 (cit. on p. 50).

Margetis, D. and R. V. Kohn (2006). "Continuum Relaxation of Interacting Steps on Crystal Surfaces in $2+1$ Dimensions." In: *Multiscale Modeling & Simulation* 5.3, pp. 729–758. DOI: 10.1137/06065297X (cit. on p. 50).

Maroutian, T., L. Douillard, and H.-J. Ernst (2001). "Morphological Instability of Cu Vicinal Surfaces during Step-Flow Growth." In: *Physical Review B* 64.16, p. 165401. DOI: 10.1103/PhysRevB.64.165401 (cit. on pp. 61, 89).

Métois, J.-J. and M. Audiffren (1997). "An Experimental Study of Step Dynamics under the Influence of Electromigration: Si(111)." In: *International Journal of Modern Physics B* 11.31, pp. 3691–3702. DOI: 10.1142/S0217979297001878 (cit. on pp. 126, 128).

Métois, J. J. and S. Stoyanov (1999). "Impact of the Growth on the Stability–Instability Transition at Si(111) during Step Bunching Induced by Electromigration." In: *Surface Science* 440.3, pp. 407–419. DOI: 10.1016/S0039-6028(99)00817-1 (cit. on pp. 3, 95–97, 106, 107).

Michely, T. and J. Krug (2012). *Islands, Mounts and Atoms*. Vol. 42. Springer Science & Business Media (cit. on pp. 1, 35, 69, 125).

Miki, K., Y. Morita, H. Tokumoto, T. Sato, M. Iwatsuki, M. Suzuki, and T. Fukuda (1992). "Real-Time Observation of the Si(111) : $(7 \times 7) - -(1 \times 1)$ Phase Transition by Scanning Tunneling Microscopy." In: *Ultramicroscopy* 42–44, pp. 851–857. DOI: 10.1016/0304-3991(92)90368-T (cit. on p. 107).

Minoda, H. (2003). "Direct Current Heating Effects on Si(111)vicinal Surfaces." In: *Journal of Physics: Condensed Matter* 15.47, S3255–S3280. DOI: 10.1088/0953-8984/15/47/005 (cit. on pp. 97, 107, 108).

Misbah, C. and O. Pierre-Louis (1996). "Pulses and Disorder in a Continuum Version of Step-Bunching Dynamics." In: *Physical Review E* 53.5, R4318–R4321. DOI: 10.1103/PhysRevE.53.R4318 (cit. on p. 35).

Misbah, C., O. Pierre-Louis, and A. Pimpinelli (1995). "Advacancy-Induced Step Bunching on Vicinal Surfaces." In: *Physical Review B* 51.23, pp. 17283–17286. DOI: 10.1103/PhysRevB.51.17283 (cit. on p. 96).

Misbah, C., O. Pierre-Louis, and Y. Saito (2010). "Crystal Surfaces in and out of Equilibrium: A Modern View." In: *Reviews of Modern Physics* 82.1, pp. 981–1040. DOI: 10.1103/RevModPhys.82.981 (cit. on p. 4).

Mysliveček, J, C Schelling, F Schäffler, G Springholz, P Šmilauer, J Krug, and B Voigtländer (2002). "On the Microscopic Origin of the Kinetic Step Bunching Instability on Vicinal Si(001)." In: *Surface Science* 520.3, pp. 193–206. DOI: 10.1016/S0039-6028(02)02273-2 (cit. on p. 4).

Natori, A. N. A. (1994). "Step Structure Transformation Induced by DC on Vicinal Si(111)." In: *Japanese Journal of Applied Physics* 33.6R, p. 3538. DOI: 10.1143/JJAP.33.3538 (cit. on pp. 9, 35).

Néel, N., T. Maroutian, L. Douillard, and H.-J. Ernst (2003). "From Meandering to Faceting, Is Step Flow Growth Ever Stable?" In: *Physical Review Letters* 91.22, p. 226103. DOI: 10.1103/PhysRevLett.91.226103 (cit. on pp. 89, 91).

Nita, F. and A. Pimpinelli (2005). "When Smoothening Makes It Rough: Unhindered Step-Edge Diffusion and the Meandering Instability on Metal Surfaces." In: *Physical Review Letters* 95.10, p. 106104. DOI: 10.1103/PhysRevLett.95.106104 (cit. on pp. 62, 115).

O Coileain, C., V. Usov, I. V. Shvets, and S. Stoyanov (2011). "Critical Field Behavior and Antiband Instability under Controlled Surface Electromigration on Si(111)." In: *Physical Review B* 84.7, p. 075318. DOI: 10.1103/PhysRevB.84.075318 (cit. on pp. 103, 110, 111, 127).

Omi, H., Y. Homma, V. Tonchev, and A. Pimpinelli (2005). "New Types of Unstable Step-Flow Growth on Si(111) $-$ (7×7) during Molecular Beam Epitaxy: Scaling and Universality." In: *Physical Review Letters* 95.21, p. 216101. DOI: 10.1103/PhysRevLett.95.216101 (cit. on pp. 3, 6, 37, 48, 55, 90–92, 126).

Omi, H. and T. Ogino (2000). "Growth-Induced Atomic Step Ordering on Patterned and Non-Patterned Si(111)." In: *Thin Solid Films* 380.1, pp. 15–19. DOI: 10.1016/S0040-6090(00)01461-9 (cit. on pp. 89, 91, 92).

Otto, F., P. Penzler, A. Rätz, T. Rump, and A. Voigt (2003). "A Diffuse-Interface Approximation for Step Flow in Epitaxial Growth." In: *Nonlinearity* 17.2, pp. 477–491. DOI: 10.1088/0951-7715/17/2/006 (cit. on p. 38).

Pang, A. B., K. L. Man, M. S. Altman, T. J. Stasevich, F. Szalma, and T. L. Einstein (2008). "Step Line Tension and Step Morphological Evolution on the Si(111)1 $\times$ 1 Surface." In: *Physical Review B* 77.11, p. 115424. DOI: 10.1103/PhysRevB.77.115424 (cit. on p. 126).

Paulin, S., F. Gillet, O. Pierre-Louis, and C. Misbah (2001). "Unstable Step Meandering with Elastic Interactions." In: *Physical Review Letters* 86.24, pp. 5538–5541. DOI: 10.1103/PhysRevLett.86.5538 (cit. on pp. 9, 63, 75).

Phaneuf, R. J., E. D. Williams, and N. C. Bartelt (1988). "Temperature Dependence of Vicinal Si(111) Surfaces." In: *Physical Review B* 38.3, pp. 1984–1993. DOI: 10.1103/PhysRevB.38.1984 (cit. on p. 107).

Pierre-Louis, O. (2003). "Step Bunching with General Step Kinetics: Stability Analysis and Macroscopic Models." In: *Surface Science* 529.1, pp. 114–134. DOI: 10.1016/S0039-6028(03)00075-X (cit. on pp. 3, 9, 95, 96).

Pierre-Louis, O. (2006). "Local Electromigration Model for Crystal Surfaces." In: *Physical Review Letters* 96.13, p. 135901. DOI: 10.1103/PhysRevLett.96.135901 (cit. on p. 96).

Pierre-Louis, O., M. R. D'Orsogna, and T. L. Einstein (1999). "Edge Diffusion during Growth: The Kink Ehrlich-Schwoebel Effect and Resulting Instabilities."

In: *Physical Review Letters* 82.18, pp. 3661–3664. DOI: 10.1103/PhysRevLett.82.3661 (cit. on p. 63).

Pierre-Louis, O. and J.-J. Métois (2004). "Kinetic Step Pairing." In: *Physical Review Letters* 93.16, p. 165901. DOI: 10.1103/PhysRevLett.93.165901 (cit. on p. 3).

Pierre-Louis, O. and C. Misbah (1996). "Out-of-Equilibrium Step Meandering on a Vicinal Surface." In: *Physical Review Letters* 76.25, pp. 4761–4764. DOI: 10.1103/PhysRevLett.76.4761 (cit. on pp. 61, 63).

Pierre-Louis, O., C. Misbah, Y. Saito, J. Krug, and P. Politi (1998). "New Nonlinear Evolution Equation for Steps during Molecular Beam Epitaxy on Vicinal Surfaces." In: *Physical Review Letters* 80.19, pp. 4221–4224. DOI: 10.1103/PhysRevLett.80.4221 (cit. on p. 49).

Pimpinelli, A., I. Elkinani, A. Karma, C. Misbah, and J. Villain (1994). "Step Motions on High-Temperature Vicinal Surfaces." In: *Journal of Physics: Condensed Matter* 6.14, pp. 2661–2680. DOI: 10.1088/0953-8984/6/14/005 (cit. on p. 61).

Pimpinelli, A., V. Tonchev, A. Videcoq, and M. Vladimirova (2002). "Scaling and Universality of Self-Organized Patterns on Unstable Vicinal Surfaces." In: *Physical Review Letters* 88.20, p. 206103. DOI: 10.1103/PhysRevLett.88.206103 (cit. on pp. 48, 52, 54).

Pimpinelli, A. and A. Videcoq (2000). "Novel Mechanism for the Onset of Morphological Instabilities during Chemical Vapour Epitaxial Growth." In: *Surface Science* 445.1, pp. L23–L28. DOI: 10.1016/S0039-6028(99)01100-0 (cit. on pp. 48, 53, 89).

Pimpinelli, A. and J. Villain (1998). *Physics of Crystal Growth*. Collection Alea-Saclay: Monographs and Texts in Statistical Physics. Cambridge: Cambridge University Press. DOI: 10.1017/CBO9780511622526 (cit. on p. 66).

Politi, P. and J. Krug (2000). "Crystal Symmetry, Step-Edge Diffusion, and Unstable Growth." In: *Surface Science* 446.1, pp. 89–97. DOI: 10.1016/S0039-6028(99)01104-8 (cit. on p. 63).

Popkov, V. and J. Krug (2005). "Shape and Scaling of Moving Step Bunches." In: *EPL (Europhysics Letters)* 72.6, p. 1025. DOI: 10.1209/epl/i2005-10335-4 (cit. on pp. 49, 56, 58).

Ranguelov, B. and S. Stoyanov (2007). "Evaporation and Growth of Crystals: Propagation of Step-Density Compression Waves at Vicinal Surfaces." In: *Physical Review B* 76.3, p. 035443. DOI: 10.1103/PhysRevB.76.035443 (cit. on pp. 6, 35).

Ranguelov, B. and S. Stoyanov (2008). "Instabilities at Vicinal Crystal Surfaces: Competition between Electromigration of Adatoms and Kinetic Memory Effect." In: *Physical Review B* 77.20, p. 205406. DOI: 10.1103/PhysRevB.77.205406 (cit. on p. 107).

Ranguelov, B., P. Müller, J.-J. Metois, and S. Stoyanov (2017). "Step Density Waves on Growing Vicinal Crystal Surfaces – Theory and Experiment." In: *Journal of Crystal Growth*. SI: CRYS_ECCG5 457, pp. 184–187. DOI: 10.1016/j.jcrysgro.2016.06.041 (cit. on pp. 97, 105–107, 126).

Rodyakina, E. E., S. S. Kosolobov, and A. V. Latyshev (2011). "Drift of Adatoms on the (111) Silicon Surface under Electromigration Conditions." In: *JETP Letters* 94.2, p. 147. DOI: 10.1134/S0021364011140128 (cit. on p. 129).

Rogilo, D. I., L. I. Fedina, S. S. Kosolobov, B. S. Ranguelov, and A. V. Latyshev (2013). "Critical Terrace Width for Two-Dimensional Nucleation during Si Growth on Si(111) – 7 × 7 Surface." In: *Physical Review Letters* 111.3, p. 036105. DOI: 10.1103/PhysRevLett.111.036105 (cit. on pp. 48, 127).

Rogilo, D. I., N. E. Rybin, L. I. Fedina, and A. V. Latyshev (2016). "Adatom Concentration Distribution on an Extrawide Si(111) Terrace during Sublimation." In: *Optoelectronics, Instrumentation and Data Processing* 52.5, pp. 501–507. DOI: 10.3103/S8756699016050125 (cit. on pp. 96, 126).

Ronda, A and I Berbezier (2004). "Self-Patterned Si Surfaces as Templates for Ge Islands Ordering." In: *Physica E: Low-dimensional Systems and Nanostructures*. Proceedings of the Fifth International Workshop on Epitaxial Semiconductors on Patterned Substrates and Novel Index Surfaces (ESPS-NIS) 23.3, pp. 370–376. DOI: 10.1016/j.physe.2003.12.136 (cit. on p. 4).

Royer, L. (1928). "Recherches expérimentales sur l'épitaxie ou orientation mutuelle de cristaux d'espèces différentes." In: *Bulletin de Minéralogie* 51.1, pp. 7–159. DOI: 10.3406/bulmi.1928.4034 (cit. on p. 1).

Saito, Y. and M. Uwaha (1994). "Fluctuation and Instability of Steps in a Diffusion Field." In: *Physical Review B* 49.15, pp. 10677–10692. DOI: 10.1103/PhysRevB.49.10677 (cit. on p. 61).

Sato, M. (2007). "Effect of Step Permeability on Step Instabilities Due to Alternation of Kinetic Coefficients on a Growing Vicinal Face." In: *The European Physical Journal B* 59.3, pp. 311–318. DOI: 10.1140/epjb/e2007-00295-y (cit. on p. 96).

Sato, M. and M. Uwaha (1999a). "Change of Wandering Pattern with Anisotropy in Step Kinetics." In: *Journal of Crystal Growth* 198–199, pp. 38–42. DOI: 10.1016/S0022-0248(98)01111-7 (cit. on p. 63).

Sato, M. and M. Uwaha (1999b). "Growth of Step Bunches Formed by the Drift of Adatoms." In: *Surface Science* 442.2, pp. 318–328. DOI: 10.1016/S0039-6028(99)00932-2 (cit. on pp. 35, 44).

Sato, M., M. Uwaha, and Y. Saito (2000a). "Instabilities of Steps Induced by the Drift of Adatoms and Effect of the Step Permeability." In: *Physical Review B* 62.12, pp. 8452–8472. DOI: 10.1103/PhysRevB.62.8452 (cit. on p. 35).

Sato, T., S. Kitamura, and M. Iwatsuki (2000b). "Surface Diffusion of Adsorbed Si Atoms on the Si(111)7 × 7 Surface Studied by Atom-Tracking Scanning Tunneling Microscopy." In: *Journal of Vacuum Science & Technology A* 18.3, pp. 960–964. DOI: 10.1116/1.582283 (cit. on p. 126).

Schelling, C, G Springholz, and F Schäffler (2000). "New Kinetic Growth Instabilities in Si(001) Homoepitaxy." In: *Thin Solid Films* 369.1, pp. 1–4. DOI: 10.1016/S0040-6090(00)00823-3 (cit. on pp. 48, 53).

Schwoebel, R. L. (1969). "Step Motion on Crystal Surfaces. II." In: *Journal of Applied Physics* 40.2, pp. 614–618. DOI: 10.1063/1.1657442 (cit. on p. 5).

Schwoebel, R. L. and E. J. Shipsey (1966). "Step Motion on Crystal Surfaces." In: *Journal of Applied Physics* 37.10, pp. 3682–3686. DOI: 10.1063/1.1707904 (cit. on p. 53).

Sitnikov, S. V., A. V. Latyshev, and S. S. Kosolobov (2017). "Advacancy-Mediated Atomic Steps Kinetics and Two-Dimensional Negative Island Nucleation on Ultra-Flat Si(111) Surface." In: *Journal of Crystal Growth*. SI: CRYS_ECCG5 457, pp. 196–201. DOI: 10.1016/j.jcrysgro.2016.05.048 (cit. on p. 96).

Slanina, F., J. Krug, and M. Kotrla (2005). "Kinetics of Step Bunching during Growth: A Minimal Model." In: *Physical Review E* 71.4, p. 041605. DOI: 10.1103/PhysRevE.71.041605 (cit. on pp. 46, 48, 89).

Šmilauer, P. and D. D. Vvedensky (1995). "Coarsening and Slope Evolution during Unstable Spitaxial Growth." In: *Physical Review B* 52.19, pp. 14263–14272. DOI: 10.1103/PhysRevB.52.14263 (cit. on p. 4).

Stewart, J., O. Pohland, and J. M. Gibson (1994). "Elastic-Displacement Field of an Isolated Surface Step." In: *Physical Review B* 49.19, pp. 13848–13858. DOI: 10.1103/PhysRevB.49.13848 (cit. on pp. 27, 37, 66, 74, 128).

Stoyanov, S. (1998). "New Type of Step Bunching Instability at Vicinal Surfaces in Crystal Evaporation Affected by Electromigration." In: *Surface Science* 416.1, pp. 200–213. DOI: 10.1016/S0039-6028(98)00582-2 (cit. on pp. 3, 95).

Stoyanov, S. (2011). "Step-Bunching Instabilities of Vicinal Surfaces During Growth and Sublimation of Crystals – the Role of Electromigration of Adatoms." In: *Nanophenomena at Surfaces: Fundamentals of Exotic Condensed Matter Properties*. Ed. by M. Michailov. Springer Series in Surface Sciences. Berlin, Heidelberg: Springer, pp. 259–275. DOI: 10.1007/978-3-642-16510-8_12 (cit. on p. 110).

Stoyanov, S., J. J. Métois, and V. Tonchev (2000). "Current Induced Bunches of Steps on the Si(111) Surface – a Key to Measuring the Temperature Dependence of the Step Interaction Coefficient." In: *Surface Science* 465.3, pp. 227–242. DOI: 10.1016/S0039-6028(00)00652-X (cit. on pp. 56, 97).

Stoyanov, S. S. S. (1991). "Electromigration Induced Step Bunching on Si Surfaces – How Does It Depend on the Temperature and Heating Current Direction?" In: *Japanese Journal of Applied Physics* 30.1R, p. 1. DOI: 10.1143/JJAP.30.1 (cit. on p. 3).

Suzuki, M., H. Hibino, Y. Homma, T. Fukuda, T. Sato, M. Iwatsuki, K. Miki, and H. Tokumoto (1993). "Real-Time Observation of $(1 \times 1) - (7 \times 7)$ Phase Transition on Vicinal Si<script>(111) Surfaces by Scanning Tunneling Microscopy." In: *Japanese Journal of Applied Physics* 32.7R, p. 3247. DOI: 10.1143/JJAP.32.3247 (cit. on p. 107).

Suzuki, T. and K. Yagi (1997). "REM Study of the Si(111) Vicinal Surfaces." In: *Surface Review and Letters* 04.03, pp. 543–549. DOI: 10.1142/S0218625X97000523 (cit. on p. 90).

Telieps, W. and E. Bauer (1985). "The $(7 \times 7) \leftrightarrow (1 \times 1)$ Phase Transition on Si(111)." In: *Surface Science* 162.1, pp. 163–168. DOI: 10.1016/0039-6028(85)90890-8 (cit. on p. 107).

Tersoff, J., Y. H. Phang, Z. Zhang, and M. G. Lagally (1995). "Step-Bunching Instability of Vicinal Surfaces under Stress." In: *Physical Review Letters* 75.14, pp. 2730–2733. DOI: 10.1103/PhysRevLett.75.2730 (cit. on pp. 9, 37, 66).

The Julia Programming Language (n.d.) (cit. on p. 40).

Thürmer, K., D.-J. Liu, E. D. Williams, and J. D. Weeks (1999). "Onset of Step Antibanding Instability Due to Surface Electromigration." In: *Physical Review Letters* 83.26, pp. 5531–5534. DOI: 10.1103/PhysRevLett.83.5531 (cit. on pp. 3, 129).

Toktarbaiuly, O. et al. (2018). "Step Bunching with Both Directions of the Current: Vicinal W(110) Surfaces versus Atomistic-Scale Model." In: *Physical Review B* 97.3, p. 035436. DOI: 10.1103/PhysRevB.97.035436 (cit. on p. 44).

Tonchev, V. (2012). "Classification of Step Bunching Phenomena." In: *Bugarian Chemical Communications* 44 (cit. on p. 47).

Torabi, S., J. Lowengrub, A. Voigt, and S. Wise (2009). "A New Phase-Field Model for Strongly Anisotropic Systems." In: *Proceedings of the Royal Society A: Mathematical, Physical and Engineering Sciences* 465.2105, pp. 1337–1359. DOI: 10.1098/rspa.2008.0385 (cit. on p. 38).

Usov, V., C. O Coileain, and I. V. Shvets (2011). "Experimental Quantitative Study into the Effects of Electromigration Field Moderation on Step Bunching Instability Development on Si(111)." In: *Physical Review B* 83.15, p. 155321. DOI: 10.1103/PhysRevB.83.155321 (cit. on pp. 96, 103).

Vladimirova, M., A. De Vita, and A. Pimpinelli (2001). "Dimer Diffusion as a Driving Mechanism of the Step Bunching Instability during Homoepitaxial Growth." In: *Physical Review B* 64.24, p. 245420. DOI: 10.1103/PhysRevB.64.245420 (cit. on pp. 48, 89).

Voigtländer, B., A. Zinner, T. Weber, and H. P. Bonzel (1995). "Modification of Growth Kinetics in Surfactant-Mediated Epitaxy." In: *Physical Review B* 51.12, pp. 7583–7591. DOI: 10.1103/PhysRevB.51.7583 (cit. on pp. 48, 127).

Voronkov, V. (1983). "Statistics of Surfaces, Steps and Two-Dimensional Nuclei: A Macroscopic Approach." In: *Crystals*. Ed. by A. Chernov and H. Müller-Krumbhaar. Vol. 9, p. 75 (cit. on p. 61).

Warming, R. F and B. J Hyett (1974). "The Modified Equation Approach to the Stability and Accuracy Analysis of Finite-Difference Methods." In: *Journal of Computational Physics* 14.2, pp. 159–179. DOI: 10.1016/0021-9991(74)90011-4 (cit. on p. 50).

Williams, E. D., E. S. Fu, and B. Li (1996). "Evolution of Morphology During Etching of Si." In: *MRS Online Proceedings Library* 466.1, pp. 157–166. DOI: 10.1557/PROC-466-157 (cit. on p. 128).

Williams, E. D., R. J. Phaneuf, J. Wei, N. C. Bartelt, and T. L. Einstein (1993). "Thermodynamics and Statistical Mechanics of the Faceting of Stepped Si(111)." In: *Surface Science* 294.3, pp. 219–242. DOI: 10.1016/0039-6028(93)90110-6 (cit. on pp. 91, 128, 129).

Wise, S. M., J. S. Lowengrub, J. S. Kim, K. Thornton, P. W. Voorhees, and W. C. Johnson (2005). "Quantum Dot Formation on a Strain-Patterned Epitaxial Thin Film." In: *Applied Physics Letters* 87.13, p. 133102. DOI: 10.1063/1.2061852 (cit. on p. 4).

Xiang, S. K. and H. Huang (2008). "Ab Initio Determination of Ehrlich–Schwoebel Barriers on Cu {111}." In: *Applied Physics Letters* 92.10, p. 101923. DOI: 10.1063/1.2891106 (cit. on p. 89).

Xiang, Y. (2002). "Derivation of a Continuum Model for Epitaxial Growth with Elasticity on Vicinal Surface." In: *SIAM Journal on Applied Mathematics* 63.1, pp. 241–258. DOI: 10.1137/S003613990139828X (cit. on pp. 9, 50).

Yang, Y. N., E. S. Fu, and E. D. Williams (1996). "An STM Study of Current-Induced Step Bunching on Si(111)." In: *Surface Science* 356.1, pp. 101–111. DOI: 10.1016/0039-6028(96)00033-7 (cit. on pp. 97, 106).

Yang, Y.-N. and E. D. Williams (1994). "High Atom Density in the "1 × 1"phase and Origin of the Metastable Reconstructions on Si(111)." In: *Physical Review Letters* 72.12, pp. 1862–1865. DOI: 10.1103/PhysRevLett.72.1862 (cit. on pp. 47, 89, 126).

Yeon, D.-H., P.-R. Cha, J. S. Lowengrub, A. Voigt, and K. Thornton (2007). "Linear Stability Analysis for Step Meandering Instabilities with Elastic Interactions and Ehrlich-Schwoebel Barriers." In: *Physical Review E* 76.1, p. 011601. DOI: 10.1103/PhysRevE.76.011601 (cit. on p. 63).

Yu, Y.-M., A. Voigt, X. Guo, and Y. Liu (2011). "Simultaneous Step Meandering and Bunching Instabilities Controlled by Ehrlich-Schwoebel Barrier and Elastic Interaction." In: *Applied Physics Letters* 99.26, p. 263106. DOI: 10.1063/1.3666781 (cit. on p. 89).

Zhao, T. and J. D. Weeks (2005). "A Two-Region Diffusion Model for Current-Induced Instabilities of Step Patterns on Vicinal Si(111) Surfaces." In: *Surface Science* 580.1, pp. 107–121. DOI: 10.1016/j.susc.2005.02.015 (cit. on p. 96).

van Leeuwen, C. and F. H. Mischgofsky (1975). "The Structure of a Single Step on the Surface of a Kossel Crystal in Equilibrium: A Monte Carlo Simulation." In: *Journal of Applied Physics* 46.3, pp. 1056–1062. DOI: 10.1063/1.322210 (cit. on p. 61).

ECOLE DOCTORALE

Titre : Instabilités morphologiques des surfaces vicinales pendant la croissance épitaxiale

Mots clés : couplage chimico-mécanique, stabilité, écoulement de marches, épitaxie, mise en paquet, mûrissement, méandrage

Résumé : L'étude de la dynamique des marches sur les surfaces vicinales est un problème de longue date dans le domaine de la croissance cristalline, qui remonte aux travaux précurseurs de Burton, Cabrera et Frank (BCF) en 1951. Sur ces surfaces, le cristal croît par écoulement de marches, qui peuvent développer des instabilités rompant la configuration initiale de marches droites et équidistantes. La mise en paquet correspond à des situations où se développe à la surface un motif de larges terrasses séparées par des paquets de marches, et le méandrage à des situations où les marches développe une ondulation disctinctive.

En utilisant le formalisme de la thermodynamique hors-équilibre et des forces configurationnelles, nous établissons une relation de Gibbs–Thomson généralisée pour le potentiel chimique des marches qui inclut la contribution du substrat élastique et incorpore le couplage nécessaire entre les champs de diffusion de terrasses adjacentes (*l'effet chimique*). Cela conduit à un problème à frontière libre qui généralise le modèle BCF, et où les termes dynamiques sont pleinement pris en compte. Ce faisant, nous contournons l'approximation quasi-statique qui prévaut dans la littérature existante.

Les lois d'échelle régissant le mûrissement de la mise en paquet sont identifiées par simulation numérique, et corroborées analytiquement en prenant la limite continue des équations de l'écoulement de marches. Surtout, nous démontrons que les effets chimique et dynamique à eux seuls suffisent à expliquer les lois d'échelle observées expérimentalement pour le mûrissement des paquets.

Avec pour dessein une analyse générale de la stabilité, nous discutons de l'influence de chaque mécanisme, agissant indépendamment ou de concert, sur les instabilités de mise en paquet et de méandrage, et nous démontrons l'impact significatif des effets chimique et dynamique. Nous mettons ainsi en évidence la possible coexistence des instabilités de mise en paquet et de méandrage, contrairement au modèle BCF qui prévoit que les deux instabilités sont mutuellement exclusives.

À la lumière de ces résultats, nous montrons que les effets chimique et dynamique offrent des alternatives intéressantes pour expliquer les instabilités observées dans certaines expériences, notamment dans le cadre de l'électromigration sous un flux de déposition extrême pour laquelle nous prédisons correctement l'instabilité d'appariement des marches auparavant inexpliquée. Toutefois, une explication complète des inversions de stabilité observées sur Si(111) sous électromigration reste un problème ouvert car les effets chimique et dynamique n'affectent pas la dépendance de la stabilité à la direction du courant d'électromigration.

Title : Morphological instabilities of vicinal surfaces during epitaxial growth

Keywords : chemomechanical coupling, stability, step flow, epitaxy, bunching, coarsening, meandering

Abstract : The study of step dynamics on vicinal surfaces is a long-standing problem in crystal growth, dating back to the seminal work of Burton, Cabrera, and Frank (BCF) in 1951. On these surfaces, the crystal grows by step flow, i.e., by propagation of the atomic steps, which may develop instabilities breaking the regularly spaced, straight-step initial configuration. Step bunching corresponds to situations where steps coalesce together resulting in an alternating pattern of bunches and wide atomic terraces, and step meandering to situations where steps develop a distinct waviness.

Using nonequilibrium thermodynamics and the formalism of configurational forces, we derive a generalized Gibbs–Thomson relation for the step chemical potential which accounts, from the outset, for the contribution of the elastic bulk and incorporates the necessary coupling between the diffusion fields on adjacent terraces (the *chemical effect*). This leads to a free-boundary problem that generalizes the BCF model for the governing equations of step flow where full account is taken of the dynamics terms. In doing so, we circumvent the quasistatic approximation that prevails in the existing literature.

Through comprehensive numerical simulations, scaling laws governing the coarsening behavior of step bunches are identified, and corroborated analytically by the discrete-to-continuum limit of the step-flow equations. Importantly, we demonstrate that the chemical and dynamical effects can account for the scaling laws experimentally observed in the coarsening regime.

In the context of a general stability analysis, we discuss the influence on step bunching and step meandering of all the mechanisms independently, as well as their interplay, and we demonstrate the significant impact of the chemical and dynamical effects. Consequently, we set forth the possible coexistence of bunching and meandering, in contrast with the BCF model which predicts that the two instabilities are mutually exclusive.

In light of these findings, we show that the chemical and dynamical effects offer interesting alternative explanations to account for the step instabilities observed in some experiments, notably in the setting of electromigration under extreme deposition flux for which we correctly predict the unexplained step pairing instability. A full accounting of the stability reversals observed on Si(111) under electromigration remains an open problem as the chemical and dynamical effects do not modify the stability dependence on the direction of the current.

Institut Polytechnique de Paris
91120 Palaiseau, France